DEMOCRITUS UNIVERSITY OF THRACE

Nuclear Spectroscopic Techniques for studying Biological Systems at ISOLDE

by

Stavroula Pallada

A thesis submitted in partial fulfillment for the degree of Doctor of Philosophy

in the

School of Health Sciences

June 19, 2020

"I have not yet lost a feeling of wonder, and of delight, that this delicate motion should reside in all the things around us, revealing itself only to him who looks for it. I remember, in the winter of our first experiments, just seven years ago, looking on snow with new eyes. There the snow lay around my doorstep — great heaps of protons quietly precessing in the earth's magnetic field. To see the world for a moment as something rich and strange is the private reward of many a discovery."

-Edward M. Purcell (1952 Nobel Price in Physics) on the discovery of NMR.

Abstract

Perturbed Angular Correlation of γ-rays technique (PAC) and β-decay Nuclear Magnetic Resonance (β-NMR) are two very sensitive spectroscopic techniques, partly due to the use of radioactive isotopes. Nevertheless, they are not very frequently used among life-scientists due to both, the use of short-lived radioactive isotopes requiring on-line production and the complexity of the experimental setups that are required. Conventional NMR on the other hand is one of the most used and versatile techniques for studying the structure and dynamics of biochemical systems but lacks sensitivity. The three techniques belong to the family of hyperfine interactions. They allow for measuring the interactions of the extranuclear electric and magnetic fields with the nuclear moments of the ensemble of nuclei under study. Thus, they can give insights to the local structure and dynamics for different time scales of the investigated systems.

The first part of this work focuses on the PAC spectroscopy with heavy metal radioactive ions to explore the local electronic and molecular structure at the PAC probe site. Firstly, we focused on proving that a Cu isotope can be used to study the hyperfine interactions using the PAC technique. The $^{68m}Cu^{+}$ produced at ISOLDE-CERN was tested as the first Cu isotope and as a result its magnetic dipole moment, μ, and the quadrupole moment, Q, was reported for the first time. This work was successful and clearly demonstrated that $^{68m}Cu/^{68}Cu$ is a unique probe for hyperfine interactions in areas such as condensed and soft matter physics but it is unlikely that this isotope can be used for measurements of NQIs of copper bound to biomolecules. Furthermore, ^{111m}Cd PAC experiments were performed on a metalloregulatory protein found in two different bacteria, the CadC. We investigated the interactions between the ^{111m}Cd(II) heavy metal ion and the CadC protein. It is shown experimentally that two co-existing metal site structures in Listeria monocytogenes bacteria are in continuous rapid exchange for temperatures higher than -196°C, the CdS_4 and CdS_3O. Furthermore, it is shown

that the binding site of CadC with Cd(II) and the dynamic exchange between the two sites is not affected by the binding of CadC with a DNA molecule.

The second part of this thesis presents the numerous conventional ^{25}Mg and ^{23}Na NMR measurements in ionic liquids, that took place at the University of Copenhagen with a 11.74 T magnet. A thorough analysis and comparison of the ^{25}Mg and ^{23}Na and the respective ^{1}H NMR experimental spectra are presented. The NMR measurements that constituted the reference for the β-detected NMR measurements were conducted later at ISOLDE-CERN.

The third and most challenging part of this thesis was the design, building and put into operation of the experimental setup that could host liquid samples for applying the β-detected NMR technique in biologically related liquids while using the radioactive beams from the ISOLDE targets. This work included the participation in building a new laser polarisation beamline at ISOLDE-CERN dedicated to β-NMR experiments for studies in biochemistry and biophysics. The new vacuum compatible liquid handling system (LHS) tested off-line and on-line with ILs and radioactive beams was one of the main technical aspects if this work. Tests showed that the system is reliable and allowed for measuring the first NMR chemical shifts from non-aqueous, ionic liquid hosts paving the way to applications in chemistry and biochemistry. The results of the beamline commissioning and the NMR chemical shifts measured from different ILs are presented in this thesis.

Περίληψη

Η παρούσα διατριβή επικεντρώνεται στην μελέτη και την κατανόηση των αλλαγών της διαμορφωτικής γεωμετρίας συγκεκριμένων πρωτεινών και αμινοξέων όταν τα παραπάνω αλληλεπιδρούν με μεταλλικά ιόντα. Ο ρόλος των μεταλλικών ιόντων σε αυτη την αλληλεπίδραση με βιολογικά συστήματα μελετάται επι μακρών. Χρόνο με το χρόνο αναγνωρίζεται όλο και περισσότερο η συμμετοχή των μεταλλικών στοιχείων στις κυταρρικές και υποκυτταρικές λειτουργίες.

Τα μεταλλικά ιόντα μπορούν να διαχωριστού σε δύο κύριες κατηγορίες, σε συσχετισμό με τον σκοπό της παρούσας διδακτορικής εργασίας; τα βαρέα και τοξικά για τον οργανισμό μέταλλα (όπως το Cd(II), Hg(II), Pb(II) κλπ) και τα απολύτως απαραίτητα κατιόντα για της φυσιολογικές διεργασίες του ζωντανού οργανισμού (όπως τα Na(I), K(I), Mg(I), Ca(II) and Zn(II)). Ο ρόλος των μεταλλικών ιόντων ως προς την αναγκαιότητά τους για την ομαλή λειτουργία των βιολογικών συστημάτων έχει μελετηθεί και συνοψίζεται από διαφορετικές ομάδες ερευνητών [1–3]. Παρόλο το συνεχώς αυξανόμενο ενδιαφέρον για τέτοιου είδους μελέτες, η ερευνητική κοινότητα είναι ακόμα μακριά από την πλήρη κατανόηση και λεπτομερή περιγραφή όλων των μηχανισμών που που υπόκεινται τα βιολογικά συστήματα όταν έρχονται σε επαφή με ορισμένα μεταλλικά ιόντα.

Με την εξέλιξη της τεχνολογίας και την εμφάνιση καινούριων τεχνικών, μπορούμε να εξετάσουμε εις βαθος τον πραγματικό ρόλο που παίζουν τα ανόργανα άλατα στους έμβυους οργανισμούς. Κατά τη διάρκεια της διδακτορικής εργασίας χρησιμοποιήθηκαν τρεις πειραματικές φασματοσκοπικές τεχνικές. Και οι τρεις αυτές τεχνικές μελετούν το φαινόμενο της υπέρλεπτης υφής. Πιο συγκεκριμένα χρησιμοποιώντας ραδιενεργά ισότοπα, συγκεκριμένων μεταλλικών ιόντων (^{68m}Cu και ^{111m}Cd), εφαρμόστηκε η φασματοσκοπική τεχνική της Χρονοεξαρτώμενης Διαταραγμένης Γωνιακής Συσχέτισης ακτίνων γάμμα (Perturbed Angular Correlation of γ rays technique η σε συντομογραφια PAC) οι οποίες εκπέμπονται σε σύμπτωση κατά τη διάρκεια

της ραδιενεργούς διάσπασης. Εν συνεχεία, αναπτύχθηκε και χρησιμοποιήθηκε στο ISOLDE-CERN μια υβριδική φασματοσκοπική τεχνική η οποία συνδιάζει την ταυτόχρονη εκπομπή ηλεκτρονίων κατά των πυρηνικό συντονισμό των ραδιενεργών πυρήνων από τους οποίους προέρχονται, η οποία ονομάζεται β-Πυρηνικός Μαγνητικός Συντονισμός (β NMR).

Η φασματοσκοπία της Χρονοεξαρτώμενης Διαταραγμενης Γωνιακής Συσχέτισης (PAC) χρησιμοποιείται κατα κύριο λόγο για την ανίχνευση των αλληλεπιδράσεων μεταξύ των πυρηνικών ροπών ενός ισοτόπου ανιχνευτή (probe) και των ηλεκτρομαγνητικών πεδίων που δημιουργούνται σε άμμεση γειτνίαση, λόγο του υλικού στο οποίο εμφυτεύεται [3, 4]. Η συμβατική τεχνική του Πυρηνικού Μαγνητικού Συντονισμού, χρησιμοποιείται ευρέως για την διερεύνηση των γεωμετριών διαμόρφωσης ρευστών και στερεών δειγμάτων καθώς παρέχει σε βάθος πληροφόρηση ως προς το ηλεκτρονιακό περιβάλλον του υλικού όπου εναποτίθενται τα ραδιενεργά ισότοπα. Σε αυτή την τεχνική χρησιμοποιούνται ραδιενεργά ισότοπα τα οποία υποβάλλονται σε ένα ισχυρό εξωτερικό μαγνητικό πεδίο, B_0. Η μαγνητική διπολική ροπή, μ, ενός συνόλου πυρήνων αλληλεπιδρά με το B_0. Σύμφωνα με τη θερμοκρασία περιβάλλοντος και τη μαγνητική ενεργειακή κατάσταση Zeeman, οι πλυθησμοί των πυρηνικών σπιν μεταβάλλονται και κατευθύνονται είτε προς είτε ενάντια στο εφαρμοζόμενο μαγνητικό πεδίο. Γνωρίζοντας την αναμενόμενη συχνότητα συντονισμού, συχνόντητα Larmor, των πυρηνικών σπιν γύρω απο το B_0, μπορούμε να προσδιορίσμουμε τα πιθανά διαφορετικά περιβάλλοντα που αλληλεπιδρούν με το ίδιο είδος πυρήνων. Λόγω της περιορισμένης ευαισθησίας της τεχνικής σε θερμοκρασίες δωματίου, η οποία μπορεί να βελτιωθεί μέχρι έναν βαθμό αν εφαρμόσουμε πολύ χαμηλές θερμοκρασίες η πολύ αυξημένο μαγνητικό πεδίο, B_0, υπάρχει ανάγκη για την ανάπτηξη διαφορετικών φασματοσκοπικών τεχνικών. Για το λόγο αυτό, το 2012 στο ISOLE-CERN, η μη συμβατική β-NMR τεχνική εφαρμοστηκε για πρώτη φορά χρησιμοποιώντας ένα υργό δείγμα [5]. Η β-NMR τεχνική βασίζεται στην ανισότροπη εκπομπή των β^- σωματιδίων κατά την β-διάσπαση οπτικά πολωμένων πυρηνικών σπιν. Για το λόγο αυτο η β-NMR τεχνική υπερισχύει σε ευαισθησία της συμβατικής NMR τεχνικής, επιτρέποντας τη λήψη πολύ καλών πειραματικών φασμάτων με τη χρήση ελάχιστης ποσοτήτας βιολογικού υλικού μειώνοντας επίσης τον χρόνο καταγραφής. Με την τεχνική αυτή η πόλωση των πυρηνικών σπιν δεν γίνεται με τον συμβατικό τρόπο, με πολύ ισχυρά στατικά μαγνητικά πεδία, αλλά με τη χρήση δέσμης λέιζερ.

Η διδακτορική αυτή διατριβή εκπονήθηκε υπό τη συνεργασιά του Τμήματος Ιατρικής του Δημοκρίτειου πανεπιστημίου Θράκης με το τμήμα χημείας του πανεπιστημίου

της Κοπενχαγης στη Δανία και τον Ευρωπαικό Οργανισμό Πυρηνικής Ενέργειας (CERN) στη Γενεύη της Ελβετίας. Το ISOLDE (Isotope On-Line Separator Device) είναι ένα από τα πιο ισχυρά εργαστήρια πυρηνικής φυσικής στον κόσμο και εξειδικεύεται στην παραγωγή και στην μελέτη ενός τεράστιου εύρους ραδιενεργών ισοτόπων με σκοπό την έρευνα στην πυρηνική φυσική, την επιστήμη των υλικών, της φυσική των στερεών και τις βιοεπιστήμες.

Όπως φαίνεται στην Εικόνα 1 το ISOLDE λαμβάνει τα πρωτόνια του απο το Proton-Synchrotron Booster (PSB). Ο PSB αποτελείται από τέσσερα υπερσυγχρονισμένα σύγχροτρα που λαμβάνουν τη δέσμη πρωτονίων ενέργειας 50 MeV απο τον γραμμικό επιταχυντή 2 (Linac 2) και την επιταχύνουν στα 1.4 Gev με μία μέση ένταση δέσμης 2 μA πριν την εισαγωγή της στο ISOLDE.

0.0.1 Παραγωγή ραδιενεργών ιόντων

Η υψηλής ενέργειας δέσμη πρωτονίων ενέργειας 1.4 GeV ακτινοβολεί έναν βαρύ στόχο όπως φαίνεται στην Εικόνα 2(a). Ο στόχος διατηρείται σε μια υψηλή θερμοκρασία ώστε τα παραγώμενα ραδιενεργά άτομα να διαχέονται εύκολα στο εξωτερικό των στόχων και να μεταφέρονται στις διαφορετικές πηγές ιόντων. Στο ISOLDE συνήθως χρησιμοποιούνται μεταλλικοί στόχοι, στερεοί μεταλλικοί στόχοι, καρβίδια και οξείδια. Τα ραδιενεργά άτομα παράγονται μέσω αντιδράσεων εξουδετέρωσης, θραυσματοποίησης ή σχάσης, Εικόνα 2(b) [7].

Ένα τυποποιημένο δοχείο στόχου ειναι κατασκευασμένο απο κύλινδρο Τανταλίου (Ta) μήκους 20 cm και διαμέτρου 2 cm. Με ωμική θέρμανση εώς 1000 A μπορεί να φτάσει μέχρι τους 2500 ^{o}C έτσι ώστε τα προιόντα της πυρηνικής αντίδρασης να μπορούν να εξαχθούν γρήγορα από τον στόχο. Υπό την προυπόθεση ότι η θερμοκρασία διατηρείται σταθερη, τα περισσότερα απο τα παραγόμενα ραδιονουκλίδια μπορούν να φτάσουν στην πηγή ιόντων που συνδέονται με τον στόχο μέσω μιας γραμμής μεταφοράς. Υπάρχουν τρεία ήδη ιονισμού των ατόμων στον ISOLDE. Η πηγή θερμού πλάσματος, χρησιμοποιείται για τον ιονισμό λιγότερο πτητικών στοιχείων χωρίς την παροχή οποιαδήποτε χημικής εκλεκτικότητας. Η πηγή θερμής επιφάνειας χρησιμοποιείται κυρίως για τον ιονισμό αλκαλικών μετάλλων και μορίων με χαμηλό δυναμικό ιονισμού, ενώ τα ισοβαρή με υψηλότερο δυναμικό ιονισμού ιονίζονται πολύ λιγότερο αποτελεσματικά. Αυτό παρέχει μια χημική εκλεκτικότητα. Η τελευταία μέθοδος εκλεκτικού ιονισμού είναι ο ιονισμός συντονισμού με διέγερση μέσω λέιζερ γνωστή και ως RILIS (Resonance Ionisation Laser Ion Source).

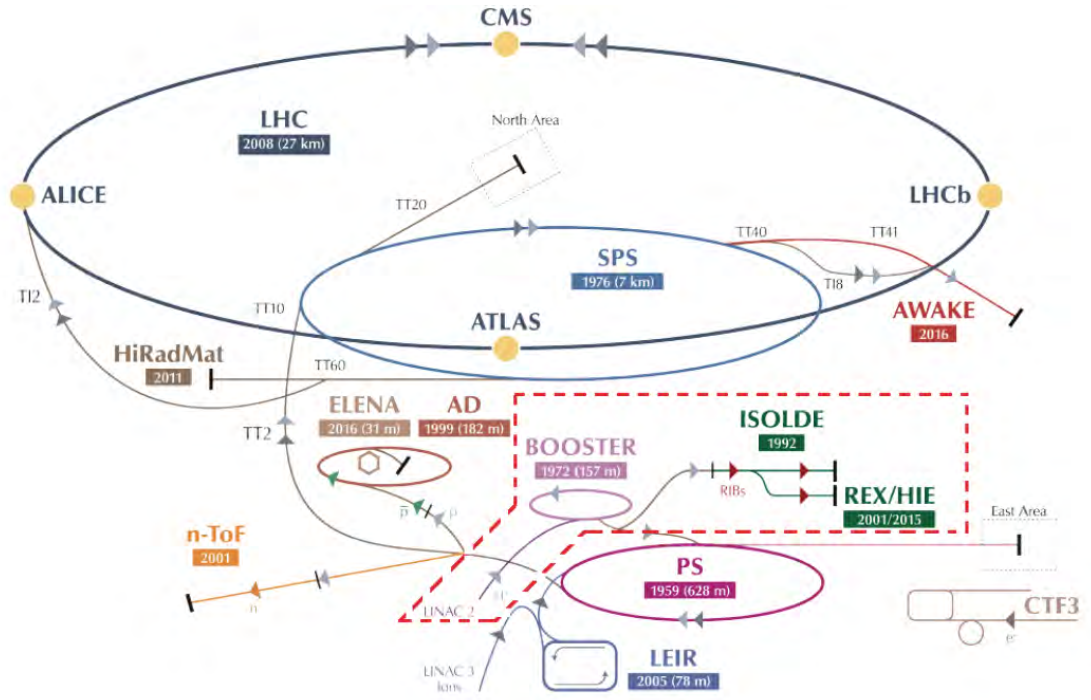

FIGURE 1: Το σύστημα επιταχυντών του CERN. Η κόκκινη διακεκωμένη γραμμη υποδεικνύει τους επιταχυντές που χρησιμοποιούνται για την παραγωγή της δεσμης πρωτονιων 1.4 GeV που παρέχεται στο ISOLDE και η τοποθεσία του ISOLDE [6].

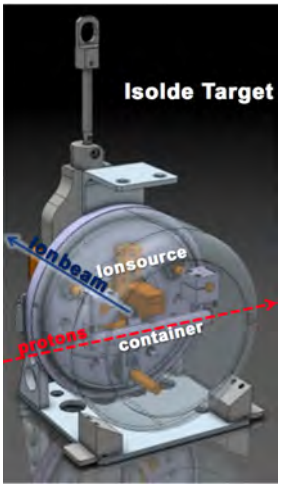

(a) Τυπικός στόχος του ISOLDE και πηγή ιονισμών για την παραγωγή ραδιενεργών ιόντων.

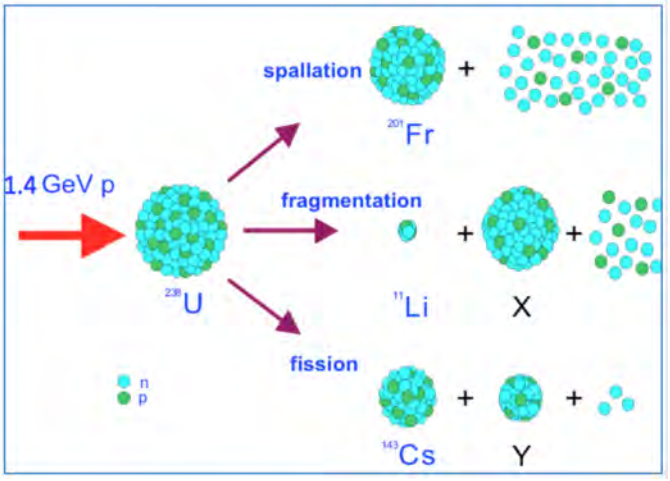

(b) Πυρηνικές αντιδράσεις για την παραγωγή ισοτόπων στο ISOLDE.

FIGURE 2: Κανάλια παραγωγής ραδιενεργών ισοτόπων στο ISOLDE.

Η πληθώρα συνδιασμών πηγων-στόχων επιτρέπουν την παραγωγή και τον διαχωρισμό πάνω από 1300 ραδιοισοτόπων με περισσότερα από 80 διαφορετικά χημικά στοιχεία. Στην Εικονα 3 παρουσιάζονται όλα τα χημικά στοιχεία που παράγονται επι του παρόντος στο ISOLDE, συμπεριλαμβανομένων αυτών που είναι βιολογικά ενδιαφέροντα.

Τα ισότοπα που χρησιμοποιήθηκαν για την εργασία και παράχθηκαν στο ISOLDE ήταν τα ^{68m}Cu, ^{26}Na, ^{27}Na και ^{28}Na.

0.0.2 Διαχωριστές δέσμης στο ISOLDE

Το ISOLDE διαθέτει δύο σταθμούς παραγωγής ισοτόπων με δύο διαχωριστές δέσμης, Εικόνα Fig. 4. Ο διαχωριστής δέσμης γενικού σκοπού (GPS) αποτελείται απο έναν μαγνήτη με ακτίνα κάμψης 1.5 m και γωνία κάμψης 70°C. Η ανάλυση που επιτυγχάνεται με τον GPS είναι περίπου m/δm 800 [8]. Η δέσμη ιόντων που περνάει απο τόν GPS μπορεί να παραδοθεί ταυτόχρονα σε τρεις πειραματικές γραμμές, Εικόνα 4.

Ο διαχωριστής δέσμης υψηλής ανάλυσης (HRS) αποτελείται απο δύο μαγνήτες κάμψης, έναν στις 90°C και έναν στις 60°C, για μεγαλύτερη αβλαλυση μάζας. Και οι δύο μαγνήτες είναι C-type και έχουν ακτίνα κάμψης 1 m. Η συνολική ανάλυση και των δύο μαγνητών είναι 6000 [8]. Αν και για τους σκοπούς αυτής της εργασίας δεν ήταν απαραίτητη ένα τόσο υψηλό επίπεδο μασικής ανάλυσης, ο HRS χρησιμοποιήθηκε κατά την πρώτη β NMR πειραματική εκστρατεία με τα πρώτα υγρά δείγματα.

Χρησιμοποιήθηκε επίσης η γραμμή GLM για τη συλλογή ραδιενέργειας για τα πειράματα με την τεχνική της Διαταραχής Γωνιακής Συσχέτισης των ακτίνων γ (PAC), ενώ για τα β NMR πειράματα χρησιμοποιήθηκε η κεντρική γραμμή (CBL).

0.1 Πανεπιστημιακό νοσοκομείο Κοπενχάγης

Επικουρικά των πειραμάτων στο ISOLDE μία σειρά πειραμάτων έλαβαν χώρα στο Χημικό τμήμα του πανεπιστημίου της Κοπενχαγης. ^{111m}Cd παρήχθη στο κύκλοτρο Scanditronic MC32 του πανεπιστημιακού νοσοκομείου της Κοπενχαγης, Εικόνα 5. Το κύκλοτρο χρησιμοποιείται κυρίως για την παραγωγή ισοτόπων για PET (Positron Emission Tomography) ^{18}F, ^{13}N and ^{11}C και κάποια SPECT (Single Photon Emission Computed Tomography) που χρησιμοποιούνται για διαγνωστικούς σκοπούς. Ερευνητικά σε συνεργασία με το πανεπιστήμιο της Κοπενχάγης παράγονται αρκετά

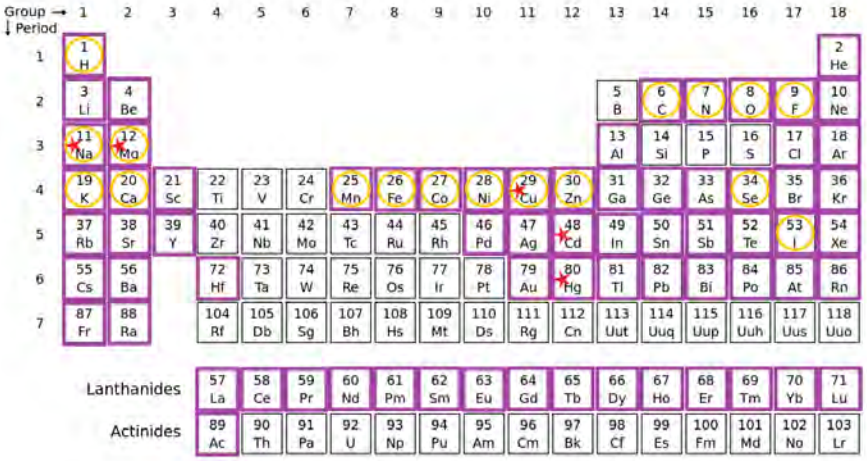

FIGURE 3: Τα χημικά στοιχεία που εξάγονται και ιονίζονται στο ISOLDE. Οι κίτρινοι κύκλοι σηματοδοτούν τα βιολογικώς συναφή στοιχεία και τα κόκκινα αστέρια υποδεικνύουν τα ισότοπα που χρησιμοποιήθηκαν στην τρέχουσα εργασία. Τα πειράματα με Hg(II) δεν παρουσιάζονται εδώ.

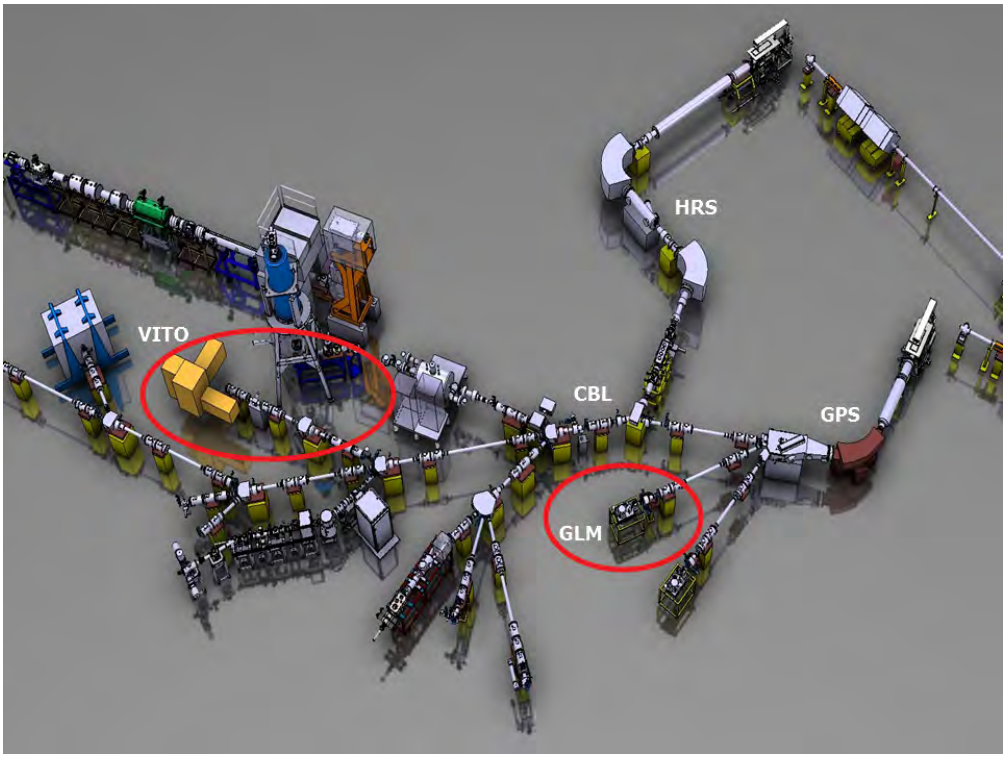

FIGURE 4: Η διάταξη της εγκατάστασης του τμήματος της χαμηλής ενέργειας του ISOLDE και των διαχωριστών δέσμεων [9]. Οι κόκκινοι κύκλοι ορίζουν τον διαχωριστή και την πειραματική γραμμή VITO (Versatile Ion Polarised Technique On-line) που χρησιμοποιήθηκαν για τη διδακτορική διατριβή.

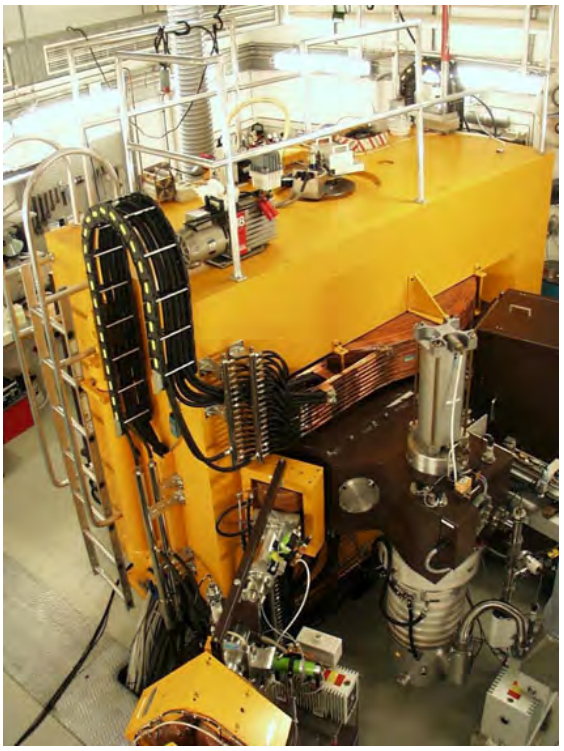

FIGURE 5: Scanditronix MC32 κύκλοτρο του Πανεπιστημιακού νοσοκομείου της Κοπενχάγης, Ringospitalet, Δανία [11]

ισότοπα όπως το ^{111m}Cd και το ^{211}At. Στα πειράματα μας στόχοι ^{108}Pd ακτινοβολήθηκαν με α σωματίδια και έλαβε χώρα η πυρηνική αντίδραση (α, n) ^{111m}Cd [10].

Οι ακτινοβολημένοι στόχοι μεταφέρθηκαν στο πανεπιστήμιο της Κοπενχαγης και περίπου 600 MBq ^{111m}Cd εξήχθησαν και χρησιμοποιήηκαν για τα πειράματα.

0.2 Καινουριο PAC ισότοπο, το ^{68m}Cu

Το 2015 αμέσως μετά το Long Shutdown 1 (LS1) του CERN, σε συνεργασία με τον Abel Fenta, επίσης διδακτορικό φοιτητή, κατασκευάσαμε μία γραμμή όπως αυτή φαίνεται και περιγράφεται στίς Εικόνες 6 and 7. Για να τεστάρουμε την καινούρια γραμμή αποφασίσθηκε να διεξάγουμε μετρήσεις με on-line PAC τεχνική [12], σε ένα ισότοπο το οποίο δεν είχε μετρηθεί ποτέ ξανά με αυτή την τεχνική, το ^{68m}Cu, 3.3 .

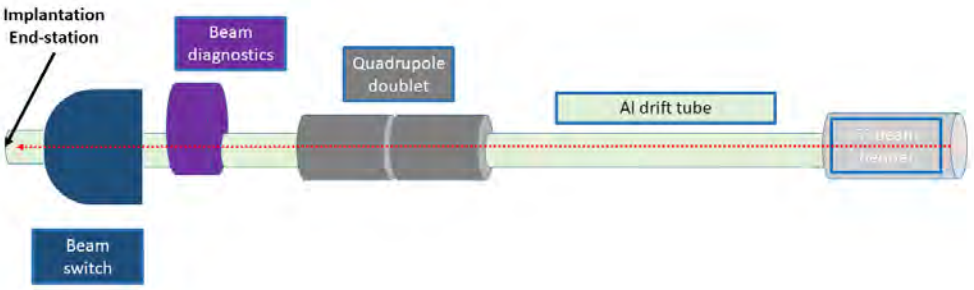

FIGURE 6: Γραφική αναπαράσταση της γραμμής VITO στη φάση 1 (2015).

FIGURE 7: Πάνω όψη της γραμμής VITO στη φάση 1.

Τα πειράματα έγιναν πάνω σε στερεά δείγματα, κοβάλτιο, αλουμίνιο και οξείδιο του χαλκού. Η πειραματική διάταξη στην πλευρά της καταγραφής των δεδομένων αποτελούνταν από τέσσερις ανιχνευτές σπηνθιρισμών με πολύ καλή ενεργειακή και χρονική ικανότητα σε γεωμετρία όπως φαίνεται στις Εικόνες 8 και Fig. 9 [13, 14].

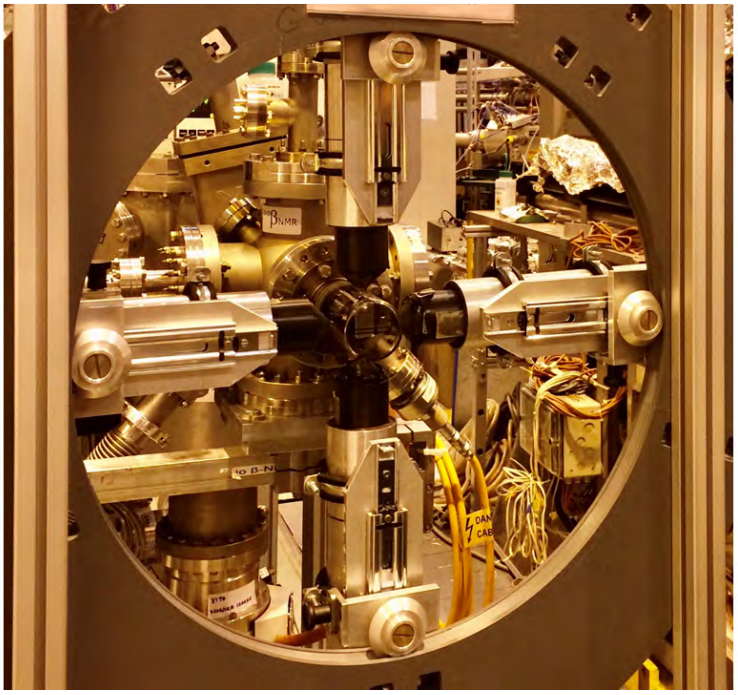

FIGURE 8: Μπροστά όψη του θαλάμου εμφύτευσης της ακτινοβολίας, φτιαγμένο από χαλαζία, τοποθετημένο στη μεση του συστήματος ανιχνευσης των τεσσάρων ανιχνευτών, $LaBr_3$.

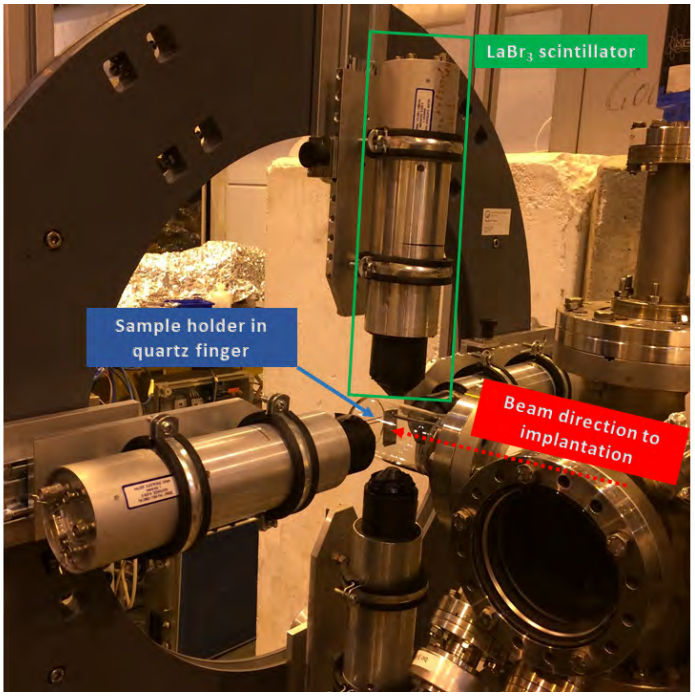

FIGURE 9: Πίσω όψη του συστήματος $LaBr_3$ PAC ανιχνευτών.

Τα αποτελέσματα των τριών PAC μετρήσεων παρουσιάζονται στο Διάγραμμα 10 [15].

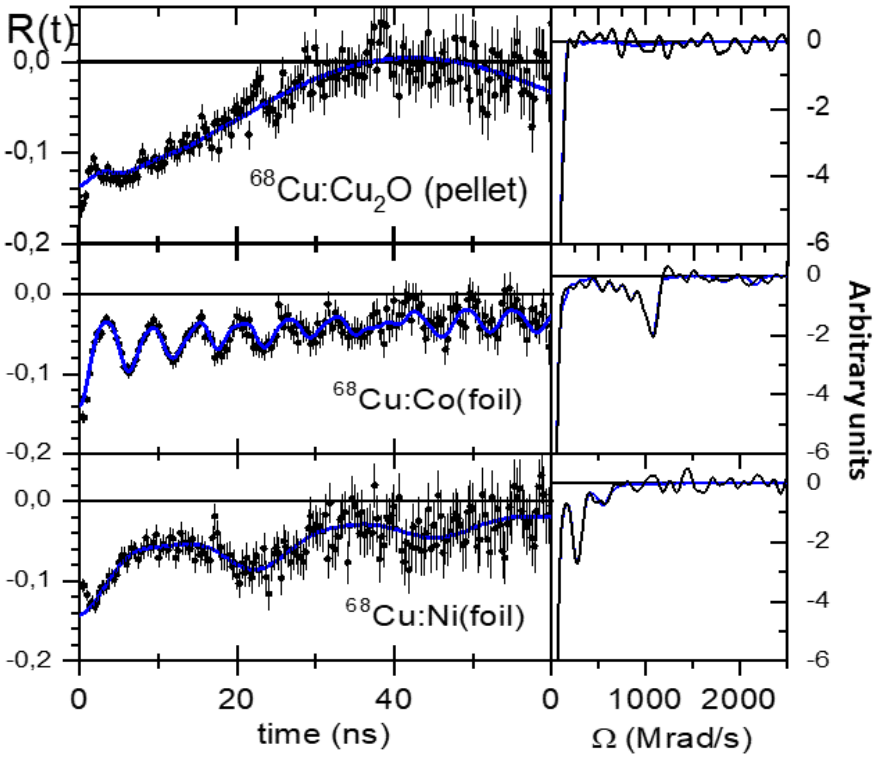

FIGURE 10: PAC πειραματικά φασματα της διαταραχής της εκπομπής των φωτονίων, R(t), και τα αντιστοιχα φάσματα μετά από μετασχηματισμό Fourier.

Οι ποιο σημαντικές παράμετροι μετά την αναλυση των δεδομένων συνοψίζονται στον Πίνακα 1 [15].

TABLE 1: Πειραματικές παράμετροι που εξήχθησαν μετά την αναλυση των φασματικων δεδομένων [15]

Host	A^{eff}_{22}	f(1)%	ω_0 (Mrad/s)	ω_L (Mrad/s)
Cu_2O	-0.13(1)	89	21.3(4)	-
Co	-0.13(1)	22	-	1079.1(34)
Ni	-0.13(1)	44	-	273.7(48)

Στο τέλος αυτής της ερευνητικής δουλειάς υπολογίσαμε για πρώτη φορά τις πυρηνικές ροπές του ^{68m}Cu ισοτόπου. Η ηλεκτρική τετραπολική ροπή υπολογίστηκε $|\mathbf{Q(^{68}Cu, 2^+, 84.1\ keV)}|=\mathbf{0.110(3)b}$ και η μαγνητική διπολική ροπή $\mu=\mathbf{2.857(6)}\mu_\mathbf{N}$.

0.3 ^{111m}Cd PAC πειραματα στην μεταλλοπρωτείνη CadC

Εν συνεχεία, μελετήθηκε η συμπεριφορά μίας μεταλλοπρωτείνης, ανεκτικής στο βαρύ και τοξικό ^{111m}Cd, την CadC. Τα πειράματα έγιναν πάνω σε υγρά δείγματα που περιείχαν βακτήρια με τη συγκεκριμένη πρωτείνη, Listeria monocytogenes και S. aureus pI258 σε διαφορετικές θερμοκρασίες και διαφορετικά pH. Το σύστημα ανίχνευσης που χρησιμοποιήθηκε φαίνεται στην Εικόνα 11 και αποτελείται από έξι ανιχνευτές σπινθηρισμών BaF_2.

FIGURE 11: Το PAC σύστημα έξι ανιχνευτών BaF_2 του χημικού τμήματος του πανεπιστημίου της Κοπενχάγης, Δανία.

Τα πειραματικά αποτελέσματα της PAC φασματοσκοπίας σε διαφορετικές θερμοκρασίες για pH 7 για το L. monocytogenes WT CadC συνοψίζονται στον Πίνακα 2.

TABLE 2: Παράμετροι πυρηνικών τετραπολικών αλληλεπιδράσεων για το L. monocytogenes CadC όταν προσδένεται με το ^{111m}Cd. Σταθερές πειραματικές συνθήκες 50 μM CadC, 0.2 eq Cd(II), 55% w/w γλυκόζη και pH=7.

sample	T [°C]	ω_0[rad/ns]	η	site [%]	linewidth *100	$1/\tau_c$ [us^{-1}]	A*100	chi^2
WT L. monocytogenes	-196	0.067(3)	0.49(7)	100	40.6(4)	$\infty[F]$	11.6 (0.5)	0.84
WT L. monocytogenes	1	0.070(0.5)	0.82(2)	59	8.0 (1)	351	5.7(0.3)	1.07
		0.162(5)	0.45(4)	41	16.3(3)		4.0(0.5)	
WT L. monocytogenes	30	0.063(0.3)	1	54	17(2)	290	5.6(0.8)	1.20
		0.198(3)	0.3(3)	46	14.2(2)		4.8(0.7)	
C10G L. monocytogenes	1	0.186(0.6)	0.25(0.9)	100	4.6(0.5)	238	7.1(0.3)	1.10

[F] παράμετροι που κρατήθηκαν υποχρεωτικά σταθεροί κατά την αφορμογή του Winfit προγράμματος.

Η γραφική αναπαράσταση των φασμάτων R(t) και των αντιστοιχων μετασχηματισμών Fourier στον χώρο των συχνοτήτων φαίνονται στην Εικόνα 12.

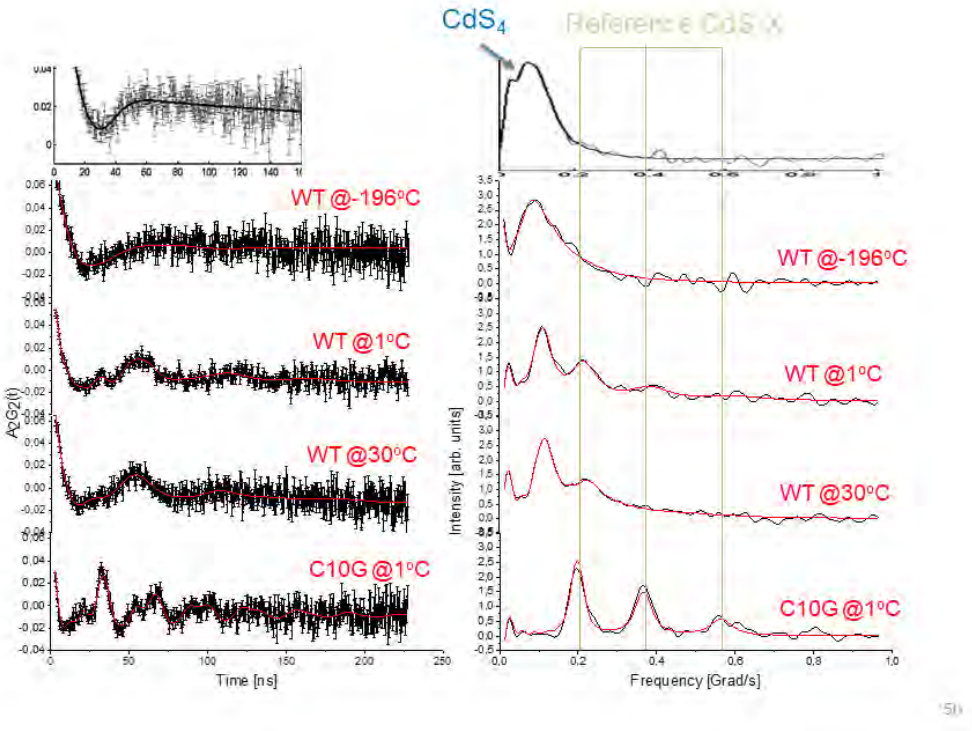

FIGURE 12: Φάσματα R(t) και τα αντιστοιχα FFT για διαφορετικές θερμοκρασίες, όταν το βακτηρίο L. monocytogenes CadC προσδένεται με την μεταλλοπρωτείνη Cd(II) σε pH 7.

Συγκρίνοντας τα πειρακατικά αποτελέσματα με προηγούμενες μελέτες [16] (πάνω φασματα της Εικόνας 12), διαφαίνεται ότι υπάρχει η ταυτόχρονη συνήπαρξη δύο

διαφορετικών γεωμετριών, CdS_4 και CdS_3O. Φαίνεται ότι το τέταρτο άτομο του S αποσυνδέεται από το ^{111m}Cd και ενα μόριο O, από τη διαλυμένη ουσία (το νερό) που χρησιμοποιήθηκε κατά τη προετοιμασία των δειγμάτων, παίρνει τη θέση του.

Πολύ σημαντικό είναι το αποτέλεσμα ότι για το δεύτερο βακτήριο, S. aureus pI258, η σύνδεσή της πρωτείνης CadC με ένα DNA μόριο δεν φαίνεται να αλλάζει την αλληλεπίδραση της πρωτείνης με το μέταλλο. Με τη χρήση Monte Carlo προσομοίωσης, αποδείχθηκε ότι η κινητική μεταξύ των δύο διαφορετικων γεωμετριών είναι της τάξης του 1 ns, καθιστώντας κατάλληλη την PAC τεχνική για τη μελέτη τέτοιους ήδους βιολογικών συστημάτων, όταν άλλες τεχνικές, όπως για παράδειγμα η κλασσική NMR τεχνική αδυνατεί να παρατηρήσει τέτοια φαινομενα. Η NMR τεχνική λειτουργεί στο φάσμα των ms καθιστώντας τις πιο γρήγορες χημικές εναλλαγές αόρατες.

0.4 ^{23}Na και ^{25}Mg NMR

Σε αυτό το σημείο μόνο τα συνολικά συγκριτικά αποτελέσματα των NMR μετρήσεων παρουσιάζονται για χάρη συντομίας. Τέσσερα διαφορετικά ιονικά υγρά μελετήθηκαν με την NMR τεχνική, BMIM_Ac, BMIM_SCN, EMIM_Ac and EMIM_DCA, με σκοπό να βρεθούν τα κατάλληλα υγρά που θα μπορούσαν να χρησιμοποιηθούν στα μελλονικά β NMR πειράματα. Τα αποτελέσματα των φασμάτων υπό την μορφή χημικής μετατώπισης (chemical shift) παρουσιάζονται στο Διάγραμμα 13.

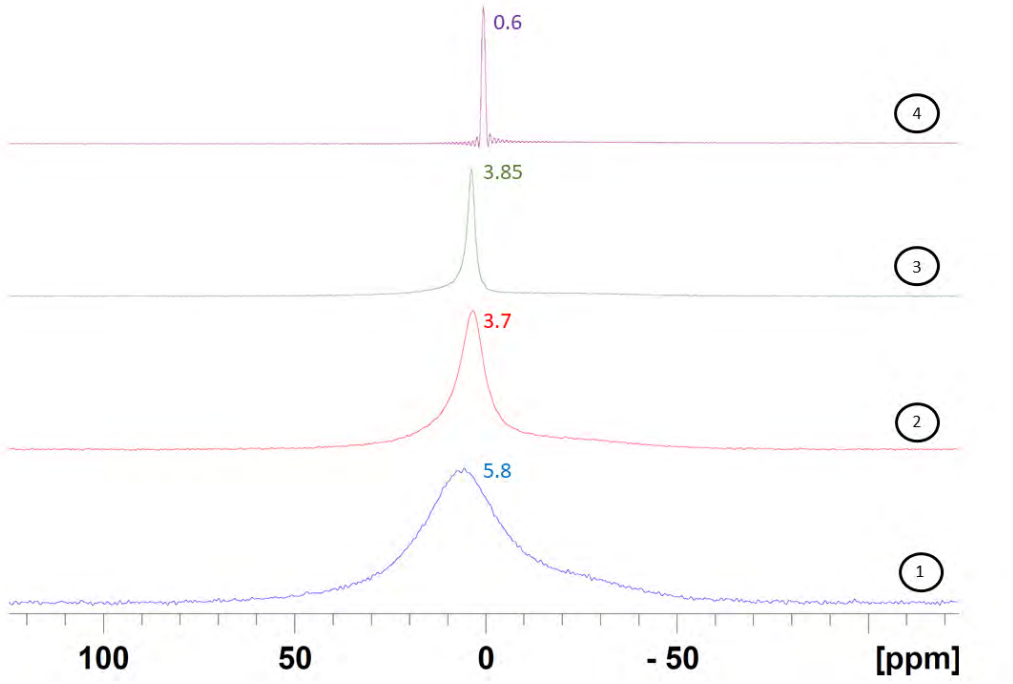

FIGURE 13: ^{23}Na NMR φάσματα 1. 0.3 M NaAc σε BMIM_Ac, 2. 0.3 M NaAc σε EMIM_Ac, 3. 0.3 M NaSCN σε BMIM_SCN και 4. 0.3 M NaDCA σε EMIM_DCA.

Φαίνεται μία γενική τάση μεταξύ της θέσης και του πλάτους του σήματος. Το EMIM_Ac δίνει ένα σήμα πιό στενό από το BMIM_Ac, ~ 9 (± 0.06) ppm σε σχέση με $\sim 25(\pm 0.09)$ ppm. Το EMIM_DCA δίνει το πιο καθορισμένο NMR σήμα με FWHM $0.84(\pm 0.03)$ ppm στα 0.6 ppm ενώ το BMIM_SCN έχει ενα πλάτος $\sim 2.6(\pm 0.02)$ ppm. Για τα λεπτομερή αποτελέσματα της ανάλυσης παρακαλώ ανατρέξτε στον Πίνακα 7.2.

Στη συνέχεια αντίστοιχες ^{25}Mg NMR μετρήσεις έγιναν στα εξής ιοντικά υγρά BMIM_SCN, BMIM_Ac, EMIM_Ac και EMIM_DCA. Τα συλλογικά συγκριτικά αποτελέσματα συνοψίζονται στο Διάγραμμα 14.

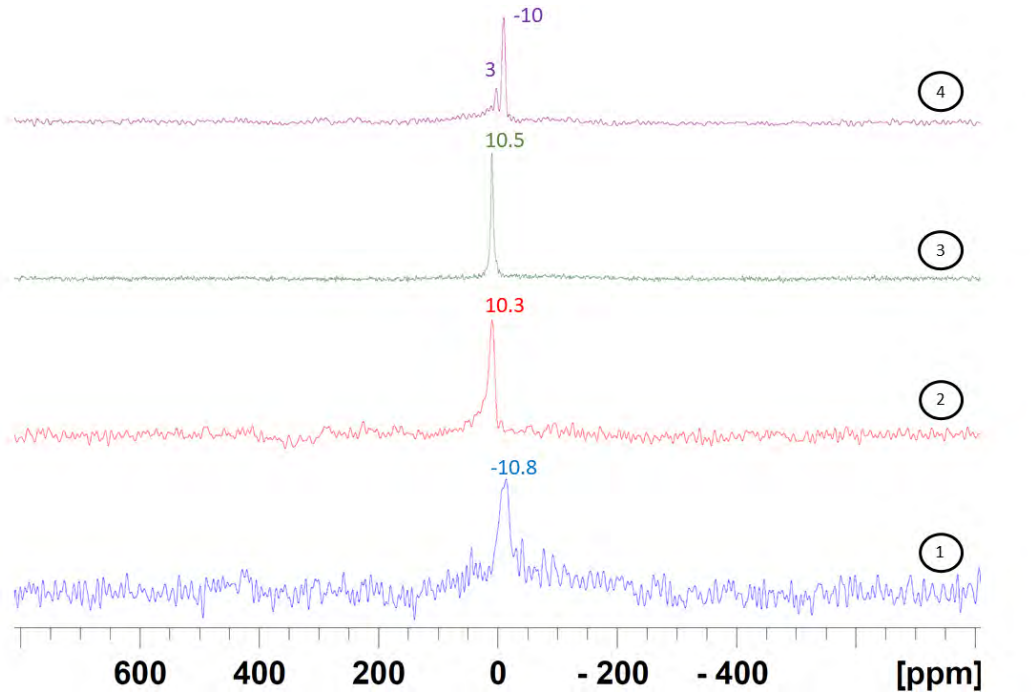

FIGURE 14: ^{25}Mg NMR φασματα 1. 0.3 M $MgCl_2$ σε BMIM_SCN, 2. 0.3 M $MgCl_2$_anhydrous σε BMIM_Ac, 3. 0.3 M $MgCl_2$_anhydrous σε EMIM_Ac, 4. $MgCl_2$_anhydrous σε EMIM_DCA.

Οι πιο σημαντικές παρατηρήσεις ανήκουν στα φάσματα 1 και 4. Παρατηρείται ότι τα κυρίως ^{25}Mg NMR σήματα από τα BMIM_Ac και BMIM_SCN δείγματα απέχουν 22 ppm. Το EMIM_DCA εμφανίζει τουλάχιστον δύο ξεκάθαρα σήματα στα 3 και στα -10 ppm. ΑΥτό σημαίνει ότι τουλάχιστον δυο διαφορετικά χημικά περιβάλλοντα υπάρχουν σε αργή μεταξύ τους εναλλαγή (ms). Και τα δύο σήματα έχουν FWHM 6 ppm. Για τα λεπτομερή αποτελέσματα της ανάλυσης παρακαλώ ανατρέξτε στον Πίνακα 7.4.

0.5 Η β NMR τεχνική

Τέλος, ένα μεγάλο μέρος αυτού του διδακτορικού αφιερώθηκε στην ανάπτυξη της β-NMR τεχνικής και την εφαρμογή της σε υγρά συστήματα. Για την πραγματοποίηση αυτού του στόχου, χρειάστηκε να αφιερωθεί πολύς χρόνος σε τεχνικές εργασίες, βιβλιογραφική έρευνα καθώς και τέστ των συστημάτων σε off-line εργαστηρια. Παρακάτω παρουσιάζονται όλα τα συστήματα τα οποία κατασκευάστηκαν τους τελευταίους μήνες της διδακτορικής αυτής διατριβής από μία πολύ μικρή ομάδα φοιτήτων και έναν μεταδιδακτορικό.

Στην εικόνα 6.4 παρουσιάζεται η τρισδιάστατη αναπαράσταση της γραμμής όπου μπορεί να εφαρμοστεί η πόλωση με λέιζερ στη ραδιενεργή δέσμη ιόντων όπως έρχεται από το ISOLDE (κίτρινο και κόκκινο βέλος δεξιά) και να μετρηθεί η ασυμμετρία της εκπομπής των β σωματιδίων στον ηλεκτρομαγνήτη με μέγιστο μαγνητικό πεδίο 0.65 T.

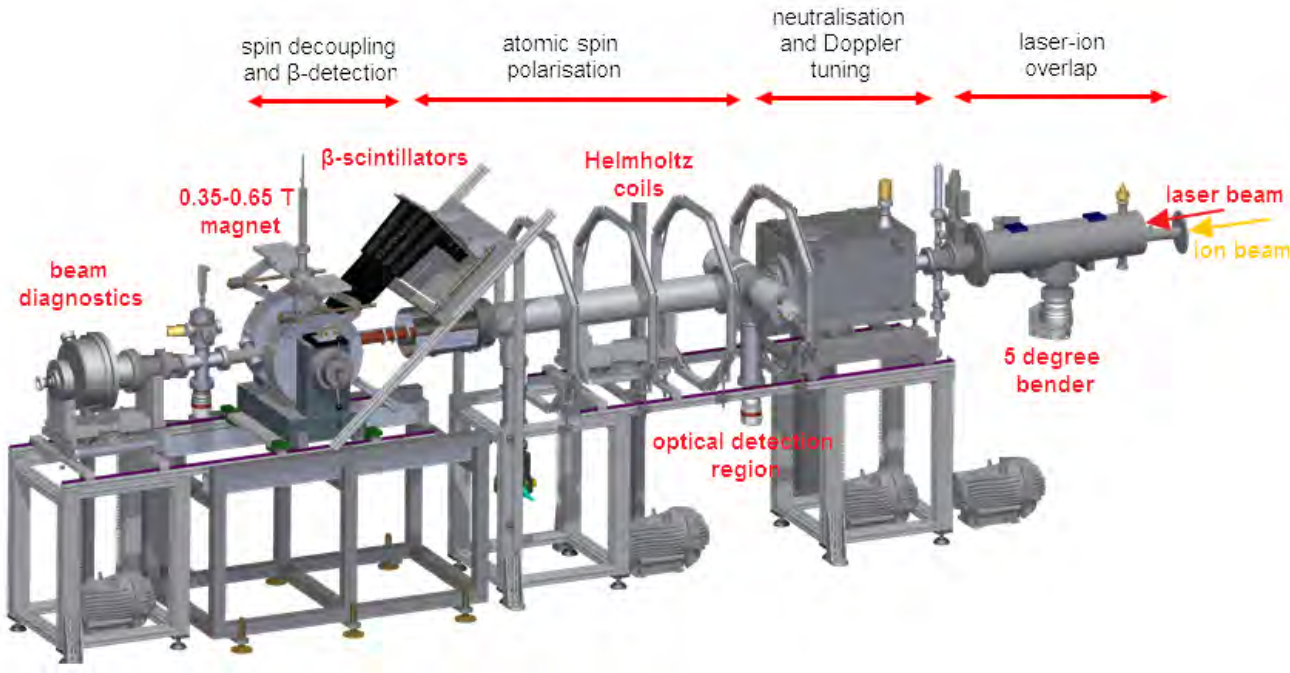

FIGURE 15: β NMR σύστημα στην καινούρια δέσμη του ISOLDE. Το 3D σχέδιο παραχωρήθηκε απο τον Dr. Frank Wienholtz.

Η πραγματική μορφή της γραμμής κατα τη διάρκεια των πειραμάτων της διδακτορικής εργασίας παρουσιάζεται στην Εικόνα 6.5.

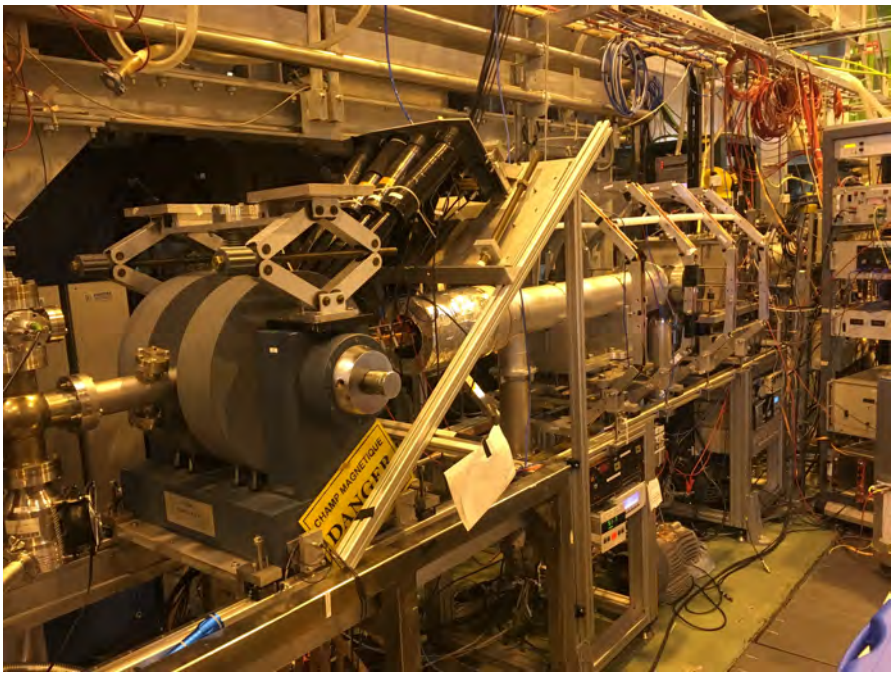

FIGURE 16: Η καινούρια δέσμη στο ISOLDE, όπως χρησιμοποιήθηκε για τα πειράματα β ασυμμετρίας NMR.

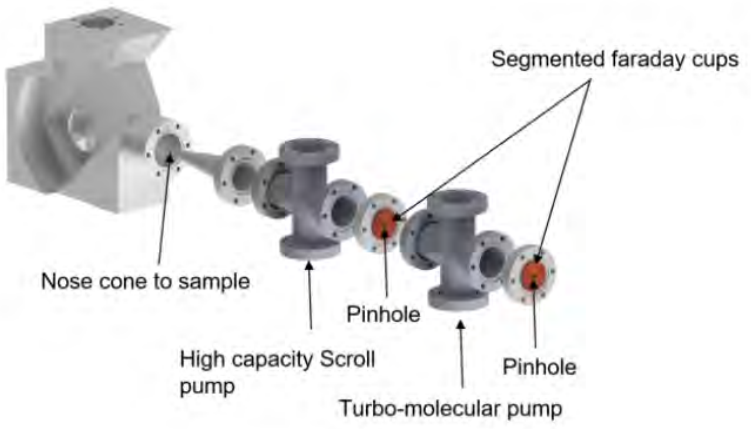

FIGURE 17: Πειραματικός θάλαμος κενού και διαφορικό σύστημα πίεσης, με σκοπό τη μελλοντική χρήση υδάτινων δειγμάτων. Το 3D σχέδιο παραχωρήθηκε απο τον Dr. Frank Wienholtz.

Το σύστημα χειρισμού των υγρών δειγμάτων για τη σωστή μεταφορά τους στο σημείο μέτρησης μέσα σε μεγάλο κενό, 10^{-6} mbar παρουσιάζεται στην Εικόνα 8.12.

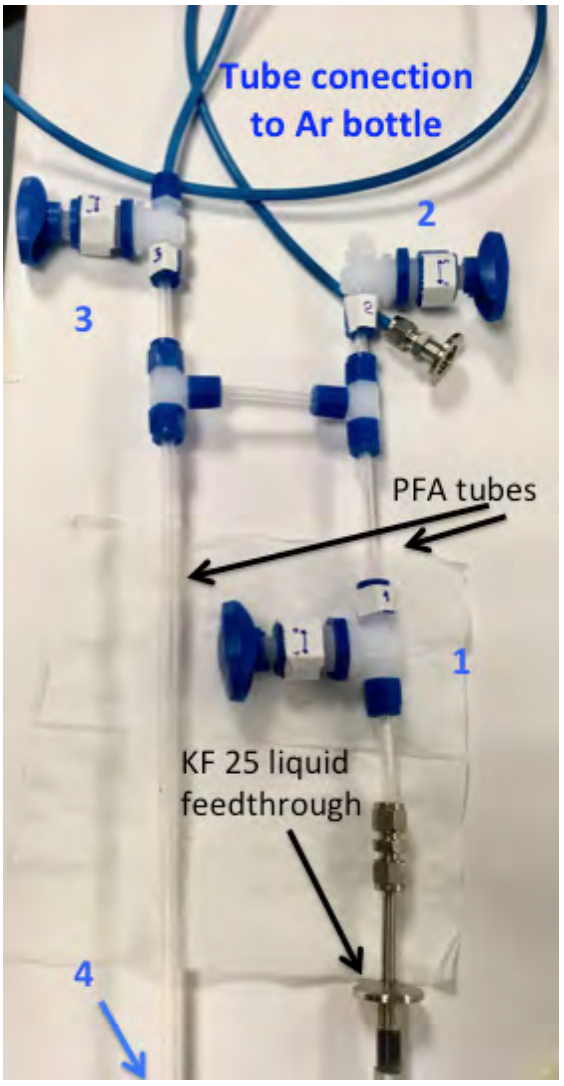

FIGURE 18: Σύστημα χειρισμού υγρών (Liquid Handling System (LHS)) με PFA Swagelok βαλβίδες.

Σύστημα χειρισμού των υγρών δειγμάτων για τη σωστή μεταφορά τους στο σημείο μέτρησης μέσα σε μεγάλο κενό, 10^{-6} mbar με τη χρήση κατάλληλου υποστρώματος (Mica) για τη σωστή υποστήριξη του δείγματος για αρκετές ώρες .

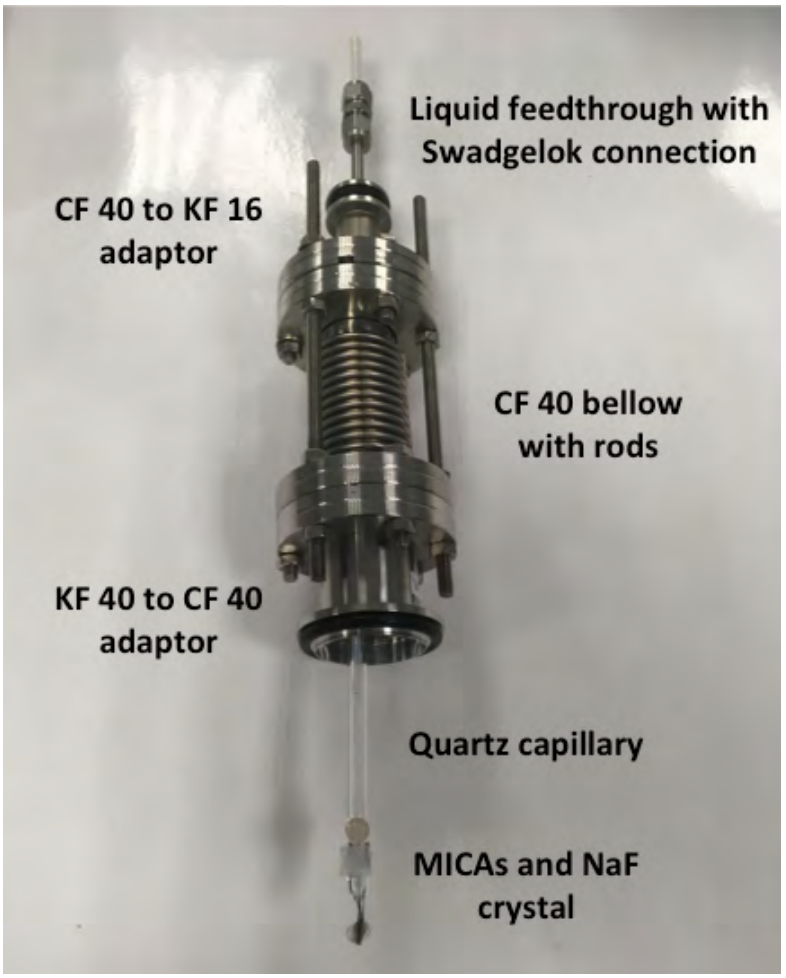

FIGURE 19: Γυάλινος σωλήνας συνδεδεμένος με το σύστημα χειρισμού υγρών και ένα μεταλλικό bellow.

Τέλος, παραθέτονται το πρώτο β NMR σήμα σε ένα κρύσταλλο NaF και το αντίστοιχο σήμα από ένα ιονικό υγρό (BMIM_HCOO). Είναι ορατή η τεράστια διαφορά μεταξύ των πλατών των δύο αυτών σημάτων. Είναι επίσης η απόδειξη ότι το σύστημα λειτουργεί όταν εισάγουμε υργά δείγματα. Επιπλέον μετρήσεις έχουν γίνει και με άλλα υγρά δείγματα. Τα αποτελέσματα αυτων των μετρήσεων βρίσκονται στο ξενόγλωσσο μέρος της διατριβής, καθώς και στο Appencix D.

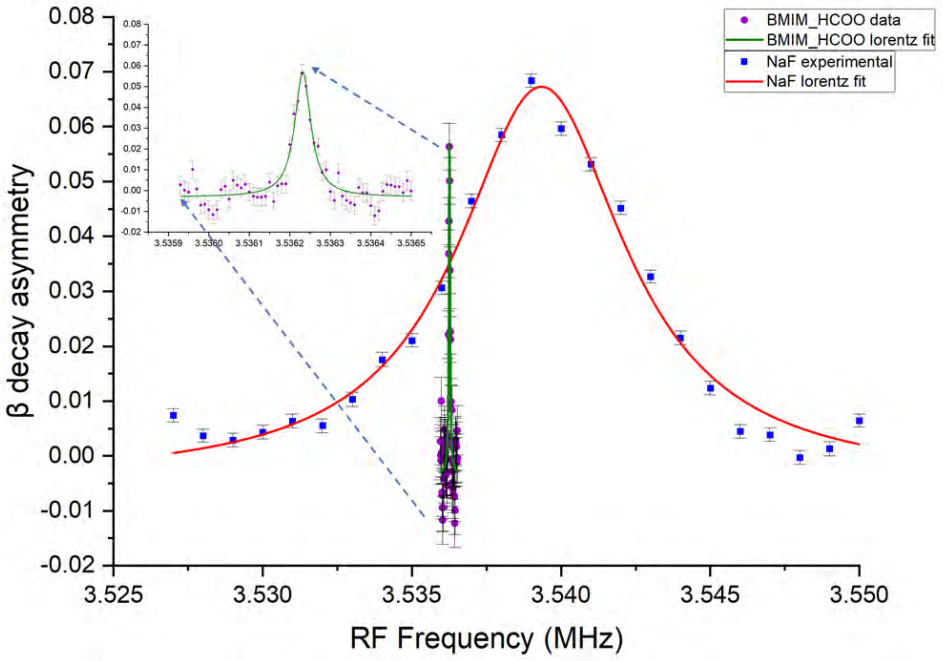

FIGURE 20: β NMR σήματα από ^{26}Na που εναποτέθηκαν σε κρύσταλλο NaF και σε ενα BMIM_HCOO ιονικό υγρό.

Acknowledgements

This manuscript summarises my research work developed during the last years within a collaboration between the Democritus University of Thrace, Greece, the University of Copenhagen, Denmark and the ISOLDE-CERN facility. I am sincerely grateful to a countless number of people which supported me during my PhD years but unfortunately here I can only name some.

First and foremost, I am sincerely grateful to Dr. Magdalena Kowalsa, my CERN supervisor, for supporting my work for helping me with all the difficulties I had to face during and after my PhD years, for making the β-NMR project possible and for being a great mentor to me. Also, I am sincerely grateful to my Universities' supervisors, Prof. Ioannis Seimenis and Prof. Lars Hemmingsen. I would like to thank Ioannis Seimenis for his support and help, without him my dream of joining CERN would have probably stayed just a dream. I am specially indebt to Lars Hemmingsen who guided me in my first steps in my research at CERN, who provided me with alternatives, when my experiments at CERN were failing due to technical problems the first 2 years of my PhD, who hosted me at the University of Copenhagen several times and put me in contact with experts who helped me with this PhD work and many more. Special thanks to my first supervisors at CERN Dr. Monika Stachura and Prof. Maria José Garcia Borge.

To my CERN colleagues, Dr. Abel Fenta, Dr. Mokhles Gerami, Dr. Mark Bissell, Robert Harding, Dr. Frank Wienholtz, Dalibor Zakoucky, Luca Cerato, Jared Croese, Dr. Torben Molholt, Dr. Marcello Barbosa, Dr. Wouter Gins, Michał Walczak, Joanna Wolak, Mikołaj Baranowski and all the other people that I have worked with during the years and the many different projects, I thank them for their collaboration and for making the difficult night-shifts funnier and successful. I would like to thank especially Dr. Joao Guilherme Correia for his kind support and guidance, for introducing me to the world of materials science, for letting me have hands-on experience setting up the PAC spectrometers in the new SSP lab, for his availability, his good ideas and help for the ^{68m}Cu PAC project. I would also like to thank Dr. Juliana Schell for her precious help with the coordination of the ISOLDE chemistry lab. I could never forget to thank the Physics coordinator Dr. Karl Johnston for all the help with the physics program, for his flexibility and good intentions to provide beamtimes equally to all the groups of ISOLDE for his good advice and his support throughout all my stay at CERN.

To the members of the chemistry department of the the University of Copenhagen, without whom this PhD thesis would not be the same. Special thanks to Prof. Stephan Sauer, Prof. Peter Thulstrup and Marianne Lund. I would like to thank Dr. Flemming Larsen for his supervision and help into the interpretation of all the NMR experiments carried out at the Department of Food and Science at the University of Copenhagen.

To the colleagues from the Department of Inorganic and Analytical Chemistry at the University of Szeged, Prof. Attila Jancso, Dr. Daniel Szunyogh and Ria Balogh, for their help and collaboration during the numerous successful and unsuccessful PAC beamtimes at CERN.

To my friends Dr. Elpida Iliopoulou, Dr. Eleni Vagena, Anastastios Kanellakopoulos and Varvara Lagaki for their unconditional support, for the coffee breaks and the late nights at CERN we shared together. Thank you for making this time as joyful as possible and to you Tassos thank you for always helping me in the lab, even during nights and weekends...

Last but not least, to my father Panagiotis Palladas, thanks for being next to me always, providing me any kind of support but especially for believing in me. To my second father, Anastasios Pedakis. To my chosen family, my "sister", Maria Touranakou thanks for being present always even when we were living in different countries, without you this PhD would not be finished. To my husband Manoel Barros Marin for being always positive and inspiring and for being patient with me during the long periods that I had to be away from home.

The Greek State Scholarships Foundation (I.K.Y), Project scholarships I.K.Y. from resources of "Education and Lifelong Learning", the European Social Fund (ESF) NSRF, 2007/2013 is acknowledged for awarding me a PhD Scholarship.

Contents

List of Figures

List of Tables

To my father Panagiotis Palladas, who always believes in me

Chapter 1

Introduction

The current PhD thesis focuses on studying and understanding the conformational geometry changes of specific proteins and amino acids when they interact with metal ions. The role of metal ions in biological systems has been studied for a long time. It is increasingly recognised that metals are involved in cellular and subcellular functions.

Metal ions can be classified into two main categories relative to the scope of the current work, the toxic heavy metal ions (i.e Cd(II), Hg(II), Pb(II) etc) and the essential cations for biological processes (Na(I), K(I), Mg(I), Ca(II) and Zn(II)). Their role in biological systems have been studied and summarised by several groups [1–3] but we are still far away from understanding and describing the underlying mechanisms that the biological systems undergo when they bind with the several metal ions.

With the development of new and sophisticated techniques to study biological and biochemical systems the true role of inorganic salts in living systems can be revealed. Radioactive isotopes from elements of both categories were studied with three different spectroscopic techniques that belong to the family of hyperfine interactions. The Perturbed Angular Correlation of gamma ray (PAC) spectroscopy, the Nuclear Magnetic Resonance (NMR) spectroscopy and the β-detected Nuclear Magnetic Resonance (β-NMR) spectroscopy. PAC spectroscopy detects the interactions between the nuclear moments of a given isotope, usually called the probe isotope, and its local surroundings, the host environment [3, 4]. The NMR technique, alike PAC, is widely used for probing the molecular conformation in solids and liquids since it can provide information of the chemical environment in the

vicinity of the probe nuclei. In the case of conventional NMR, stable isotopes with I>0 are used and are immersed into a strong magnetic field, B_0. The magnetic dipole moment of an ensemble of nuclei interacts with the external applied B_0 and depending on the ambient temperature and the Zeeman energy level there is a change in the nuclear spin populations for and against the magnetic field direction. From the characteristic precession frequency of the nuclear spins around the B_0, known as Larmor frequency, one can determine the potential different chemical environments surrounding the same kind of probes. Due to the sensitivity limitations of the NMR technique, that can be improved up to a certain limit if very low temperatures or very high applied B_0, the β-detected NMR spectroscopic technique was first tested in liquids in 2012 at ISOLDE-CERN [5]. The technique relies on the anisotropic emission of β^- particles during the β-decay of optically spin-polarised nuclei. Both NMR and β-detected NMR techniques can be used for studying the dynamics of liquid samples and the coordination geometry of biological complexes while using stable and radioactive isotopes respectively. The β-detected NMR is winning in sensitivity providing the use of substantially minimal quantities of biological materials while improving the nuclear polarisation using laser light instead of static magnetic fields. She is also useful when corresponding stable isotopes do not exist for conventional NMR. Within the current work, a dedicated beamline for β-NMR studies in biological liquids and a liquid handling system were developed and commissioned. Detailed descriptions of the new dedicated beamline at ISOLDE-CERN can be found in [33, 34] and the new liquid handling system is described in detail at 8.6.1.

With the Perturbed Angular Correlation of gamma rays spectroscopic technique (PAC) two different experiments were conducted within the scope of the current thesis. First the study of the interaction between the ^{111m}Cd metal ion and a Cadmium resistant transcriptional regulatory protein, named CadC. PAC was used for the first time on-line in order to prove the feasibility and the potential interest for biological studies with the ^{68m}Cu probe isotope. The latter allowed the determination of the nuclear moments (magnetic dipole moment (μ and electric quadrupole moment (Q)) of the intermediate state using different host solid environments proving the feasibility of using the ^{68m}Cu as a potential PAC probe chemistry and potentially biochemistry [15]. The second part of the PhD thesis was dedicated to ^{25}Mg and ^{23}Na NMR studies and characterisation of immidazolium Ionic Liquids (ILs) as possible hosts for the β-detected NMR experiments in biologically related liquids. ILs were selected as the most appropriate liquid host environments

due to the very low vapour pressure that they exhibit, making them easily used to beamline's very high vacuum conditions. Furthermore, the ILs' green nature make them potentially biologically compatible allowing us to use them for at least the first experiments with selected biological complexes. Some very simple biological systems were also studied in combination with ILs with NMR. Following the conventional NMR measurements in ILs and after commissioning the new β-NMR beamline, the liquid handling system and the spectroscopic acquisition setup, ^{26}Na β-detected NMR experiments were performed on different ILs paving the way for the first application of β-detected NMR in biological samples. The next future steps in biological liquid β NMR at ISOLDE-CERN include the interaction investigations of the alkali metal ion Na(I) with guanine rich DNA sequences, the G-quadruplexes [35], and with crown ethers such as the 15-crown-5.

Chapter 2

Facilities

2.1 The ISOLDE facility

The radioactive ion beams of ^{68m}Cu, ^{111m}Cd, ^{26}Na, ^{27}Na and ^{28}Na used for the different projects of the current PhD thesis were produced and delivered by the Isotope mass Separator On-Line Device (ISOLDE) facility at the European Organisation for Nuclear Research (CERN). The ISOLDE facility is a unique production source of a large variety of low energy beams of exotic radioactive nuclei dedicated for experiments in the fields of nuclear and atomic physics, solid-state physics, materials science and life sciences.

As shown in the dashed red box of Fig. 2.1 the ISOLDE facility receives protons from the Proton-Synchrotron Booster (PSB). PSB is made up of four superimposed synchrotron rings that receive proton beams from the linear accelerator Linac 2 at 50 MeV and accelerate them to 1.4 Gev with an average intensity up to 2 μA before the injection to the ISOLDE facility.

2.1.1 Radioactive Ions production

The high energy 1.4 GeV primary proton beam irradiates a fixed thick target as shown in Fig. 2.2(a), which is kept at an elevated temperature so that the produced radioactive atoms diffuse easily out of it into different dedicated ion sources. The type of targets used at ISOLDE are metal targets, solid metal targets, carbides

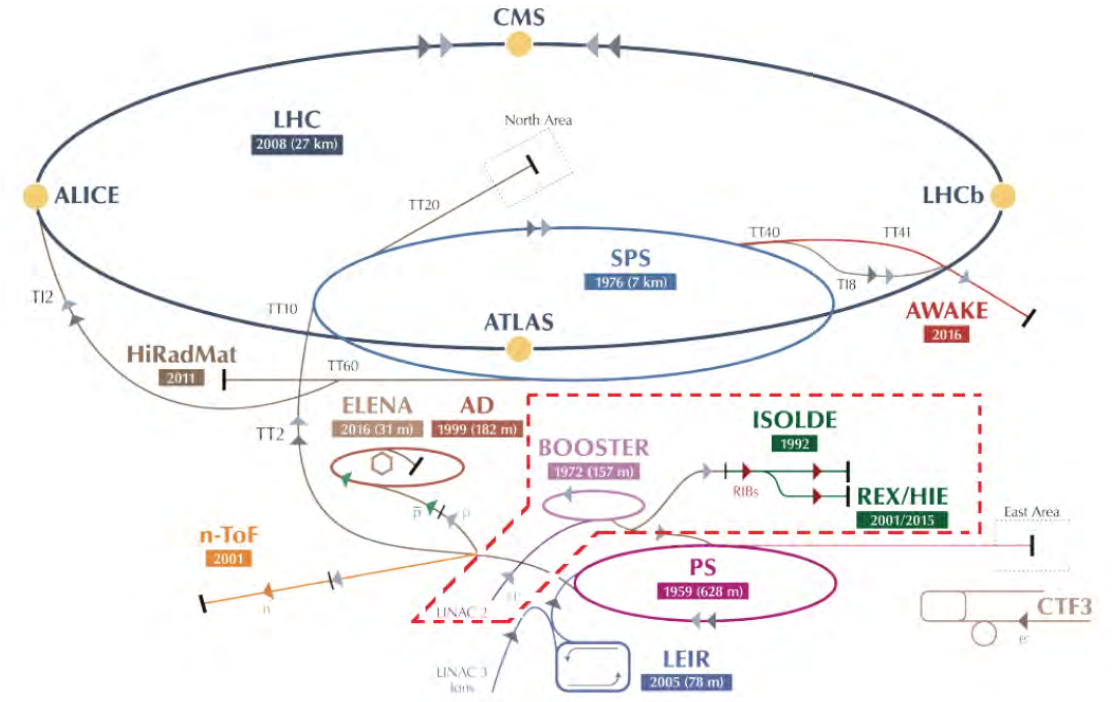

FIGURE 2.1: The current CERN accelerator complex. The red dashed box indicates the accelerators used for the production of the 1.4 GeV proton beams delivered to ISOLDE and ISOLDE itself. The layout was adapted from [6]

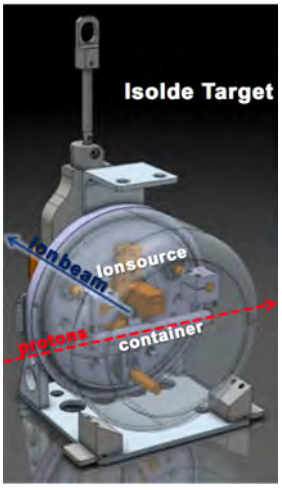

(a) Standard ISOLDE target and ion source unit for radioactive ion production

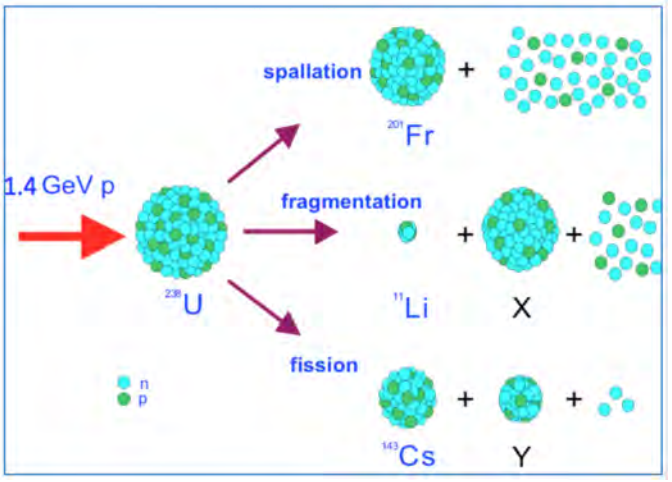

(b) Nuclear reactions for isotopes production at ISOLDE

FIGURE 2.2: ISOLDE radioactive ion production channels

and oxides. The radioactive atoms are produced via spallation, fragmentation or fission reactions, Fig. 2.2(b) [7].

The production via spallation or fragmentation requires a target heavier than the desired element (i.e. $Z_{target} > Z_{product}$ and $N_{target} > N_{product}$). Neutron-rich nuclei

of medium mass about $60 < A < 170$ are mainly produced in fission actinides. These targets provide high cross-sections for the production of light neutron-rich nuclei such as heavy Na isotopes [7].

A standard ISOLDE target container is made of Ta cylinder that is 20 cm long and has a diameter of 2 cm. By ohmic heating up to 1000 A it can be brought up to 2500 °C so that the nuclear reaction products can be quickly extracted from the target. Provided that the high temperature is maintained, most of the produced radionuclides can arrive to the ion source that is connected with the target via a transfer line. The ionisation can take place using three different types of ion sources. The hot plasma source is used for ionisation of less volatile elements without providing any chemical selectivity. The hot surface source is used mainly for ionisation of alkali metals and molecules with low ionisation potential while the isobars with higher ionisation potential are ionised much less efficiently which provides chemical selectivity. The last method for selective ionisation used at ISOLDE is the resonance ionisation by laser excitation known as RILIS (Resonance Ionisation Laser Ion Source). This method is applied to the less volatile metals with high ionisation potential and uses laser light that is tuned to the characteristic transition in the atomic level scheme of the desired element [7]. After the ionisation of the produced atoms, the ions are extracted by the ion-source and they are accelerated to energies of 30-60 keV by an applied voltage.

The numerous combinations of target-ion sources allow for producing and separating over 1300 radioisotopes of more than 80 different chemical elements. In Fig. 2.3 all the chemical elements that are currently produced at ISOLDE including those which are biologically interesting are shown.

2.1.2 Production of isotopes of interest

The isotopes used for the current work that were produced at the ISOLDE facility were the following ^{68m}Cu, ^{26}Na, ^{27}Na and ^{28}Na. The $^{68m}Cu^{+}$ ion beam was produced in a UC_x target and RILIS ionisation. The target/ion source parameters were optimised to enhance ^{68m}Cu/^{68}Cu and suppress the surface ionised ^{68}Ga, so that the ratio of extracted ions of Cu to Ga was about 80.

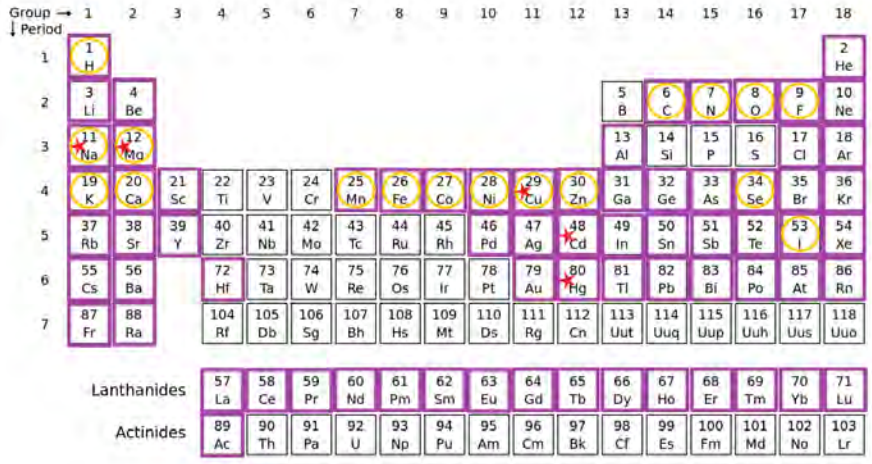

FIGURE 2.3: Chemical elements extracted and ionised at ISOLDE. Yellow circles mark the biologically relevant elements and the red stars indicate the isotopes used in the current work. Hg experiments will not be presented on this work.

2.1.3 ISOLDE separators

The ISOLDE facility has two isotope production stations with two on-line separators, as shown in Fig. 2.4. The General Purpose Separator (GPS) consists of at H-magnet type with a bending radius of 1.5 m and a bending angle of 70°C. The resolution achieved with GPS, m/δm is approximately 800 [8]. The ion beam that passes through the GPS can be delivered simultaneously in three beamlines (Fig. 2.4).

The High Resolution Separator (HRS) consists of two bending magnets, a 90°C and a 60°C magnet, for higher mass resolution. Both magnets are C-type and they have a bending radius of 1 m. The overall resolution of both magnets is approximately 6000 [8]. Even though for the purposes of the current thesis such high mass resolution was not necessary, HRS was used for the commissioning campaign of the laser polarisation beamline and for the first liquid β-NMR (marked as VITO in Fig. 2.4) that will be described in the β-NMR chapter.

In the current work, the GLM beamline was used for the radioactivity collections for the Perturbed Angular Correlation of gamma rays (PAC) technique while the Central Beamline (CBL) was used for the β NMR experiments and PAC experiments with the short-lived ^{68m}Cu. More details concerning the implantation sites and the beamlines will be given to the respective chapters.

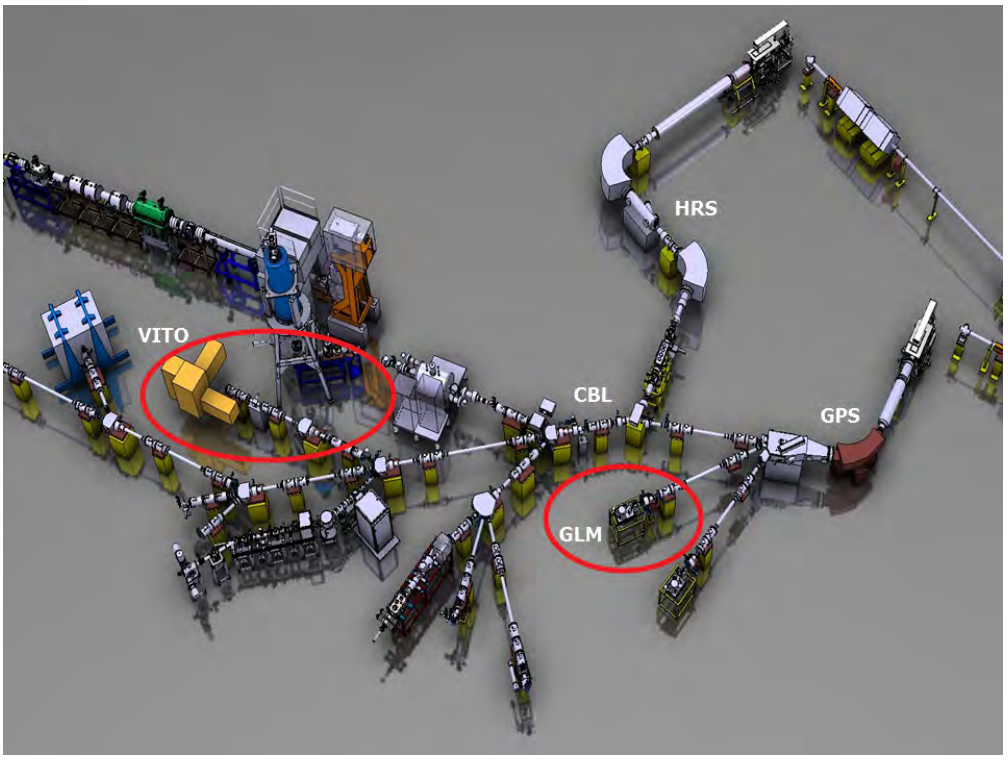

FIGURE 2.4: ISOLDE facility layout of the low energy part and the GPS and HRS separators, adopted from [9]. The red circles mark the GLM and VITO beamlines used for the experimental campaigns of the current PhD thesis.

2.2 University Hospital of Copenhagen

Additionally to the experiments conducted at the ISOLDE facility, a series of experiments took place at the Chemistry Department of the University of Copenhagen. ^{111m}Cd was produced at the Scanditronic MC32 cyclotron unit of the University Hospital of Copenhagen, Fig. 2.5. The cyclotron is dedicated to the production of Positron Emission Tomography (PET) isotopes such as ^{18}F, ^{13}N and ^{11}C and some Single Photon Emission Computed Tomography (SPECT) isotopes used for diagnostic purposes. For research purposes, in collaboration with the University of Copenhagen, several unique isotopes such as ^{111m}Cd and ^{211}At are produced. In the case of this thesis, ^{108}Pd targets were irradiated by α particles and the nuclear reaction ^{108}Pd (α, n) ^{111m}Cd took place [10].

The irradiated targets were transported to the University of Copenhagen and approximately 600 MBq of ^{111m}Cd were extracted and used for the experiments.

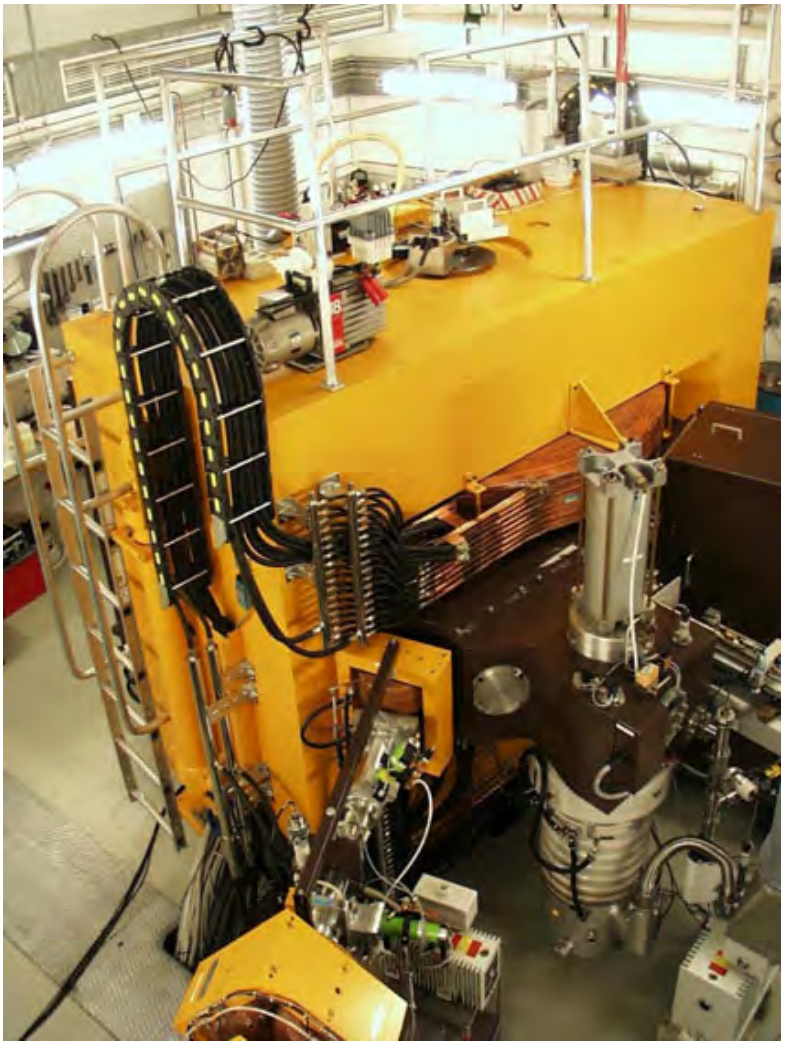

FIGURE 2.5: Scanditronix MC32 cyclotron at the University Hospital of Copenhagen, Ringospitalet in Denmark [11]

Chapter 3

Perturbed Angular Correlation of γ rays

The Perturbed Angular Correlation of γ rays technique (PAC) is a powerful tool for studying the local electric and magnetic fields of probe nuclei through hyperfine interactions, along with Nuclear Magnetic Resonance (NMR) [36] and β detected NMR [28], Nuclear Quadrupole Resonance (NQR) [37], Mossbauer spectroscopy [38], Muon Spin Rotation (μSR) [39] etc. In this work both the electric and magnetic interactions are studied for different solid state systems while only the electric interactions are present in biological systems. The PAC technique has been used in chemistry, biochemistry and biophysics [28, 40, 41] and it was first applied in biological macromolecules in solutions in 1968 [42]. The PAC spectroscopy has being used at the ISOLDE-CERN facility over the past 35 years for nuclear physics, solid-state physics and more recently for biophysics studies [43].

3.1 Basics of PAC

Nuclei with oriented (polarised) spins have a probability of radiation emission in a certain direction due to the conservation of the total angular momentum that is depended on the orientation of the nuclear spin, I [44]. The basic requirement for a PAC measurement is having appropriately excited nuclei at place of measurement. These nuclei are either metastable, implanted directly in the material under examination, or they are produced by the radioactive decay of the mother nuclide after being introduced in the material. It is necessary to select radioactive nuclei

with an excited state of an appropriate halflife for off-line experiments (typically a few hours) that decay to the ground state energy level emitting two successive γ-rays with an intermediate state of several ns halflife during the nuclear decay. The first γ photon is emitted and sets an oriented ensemble of nuclear states in the intermediate state of the gamma cascade. The second one while the intermediate energy level is depopulated during the transition to the ground state. An example of such a cascade is shown in Fig. 3.1.

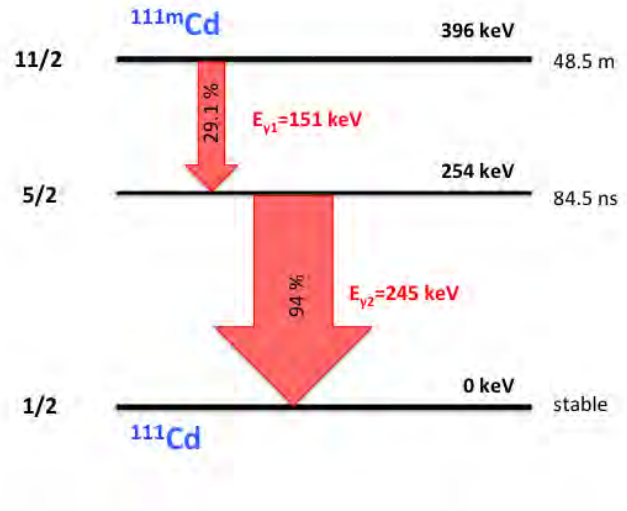

FIGURE 3.1: The decay scheme of ^{111m}Cd/^{111}Cd. The arrows indicate the population and depopulation transitions of the intermediate state interesting for the PAC experiment. Width and length of the arrows are proportional to intensity and energy, respectively.

The general expression of the angular correlation between the two γ photons, γ_1 and γ_2, is given by Eq. 3.1 [45].

$$W(\theta) = \sum_{k=even}^{k_{\max}} A_{\mathrm{kk}} P_{\mathrm{k}}(cos\theta) \tag{3.1}$$

with A_{kk}= $A_k(\gamma_1)A_k(\gamma_2)$ the angular correlation coefficients that depend on the angular momenta of the state and the transitions' multipolarities. Due to the conservation of the angular momentum Eq. 3.1 is finite. For the particular case of I=5/2 the upper summation limit is k_{max}=4 and for randomly oriented molecules in the first order approximation leading to Eq. 3.4 [3].

$$W(\theta) = 1 + A_{22}P_2(cos\theta) = 1 + A_2(1)A_2(2)(\frac{3}{2}cos^2\theta - \frac{1}{2}) \tag{3.2}$$

where θ is the angle between the direction of the emission between the two γ rays, $A_2(1)$ and $A_2(2)$ are the anisotropy coefficients that depend on the angular momenta involved in the first and second transitions and $P_2\cos(\theta)$ is the second Legendre polynomial [3]

$$P_2(cos\theta) = \frac{1}{2}(3cos^2\theta - 1) \tag{3.3}$$

If the intermediate nuclear level has a short half-life, τ_N, the perturbed angular correlation function becomes

$$W(\theta, t) = e^{\frac{-t}{\tau_N}}(1 + A_2(1)A_2(2)G_{22}(t)(\frac{3}{2}cos^2\theta - \frac{1}{2}) \tag{3.4}$$

where $G_{22}(t)$ is the time-dependent perturbation factor that contains information concerning the interaction of the nuclear moments with its environment.

3.1.1 Electrical Quadrupole Interactions

For an isotropic EFG the G_{22} is constant and equal to 1 and thus there is no time-dependence. In case an anisotropic EFG is present and the nuclei are quadrupolar with I=5/2 in the intermediate energy state, the G_{22} is given by Eq. 3.5 [46].

$$G_{22}(t) = \alpha_0 + \alpha_1 cos(\omega_1 t) + \alpha_2 cos(\omega_2 t) + \alpha_3 cos(\omega_3 t) \tag{3.5}$$

ω_1, ω_2 and ω_3 are the transition frequencies between the three magnetic sublevels m_F. The three frequencies are not independent since ω_3=ω_1+ω_2. α_0, α_1, α_2 and α_3 are the relevant amplitudes of the transitions that depend on the asymmetry of the EFG, η, Eq. 3.9, and the strength of the electric field, ω_0, Eq. 3.6 [46].

$$\omega_0 = \frac{12\pi|eQV_{ZZ}|}{40h} \tag{3.6}$$

For a nucleus with I=5/2, the intermediate nuclear level split into three doubly degenerate Zeeman magnetic sublevels with m_F=±5/2, m_F=±3/2 and m_F=±1/2. The energy difference between these magnetic sublevels is given by the Eq. 3.7 [3]

$$E_{m_F} = \frac{eQV_{zz}(3m^2 - I(I+1))}{4I(2I-1)} \tag{3.7}$$

and depends on the electric field gradient (EFG) around the nucleus and the quadrupole moment, Q. From Eq. 3.7 one can see that the magnetic sublevels with same value and different sign (e.g +5/2 and -5/2) will have the same energy. For the same isotopes, if the EFGs created around the nuclei change the quadrupole interaction (NQI) changes as well. The NQI is very sensitive to minor changes in structure, bonding and dynamics and can be best described by a second-rank tensor in Cartesian space as

$$\mathrm{V}=\begin{pmatrix} V_{xx} & V_t xy & V_{xz} \\ V_{yx} & V_{yy} & V_{yz} \\ V_{zx} & V_{zy} & V_{zz} \end{pmatrix}$$

Each component describes the gradient of the electric field vector components with respect to the position in an arbitrary reference frame [47]. The tensor is traceless due to the Laplace equation (V_{xx}+V_{yy}+V_{zz}=0), symmetric V_{uv}=V_{vu} and diagonal into its own principal axis system,

$$\mathrm{V}=\begin{pmatrix} V_{xx} & 0 & 0 \\ 0 & V_{yy} & 0 \\ 0 & 0 & V_{zz} \end{pmatrix}$$

with the following convention

$$|V_{zz}| \geq |V_{yy}| \geq |V_{xx}| \tag{3.8}$$

The EFG tensor is traceless and there are only two independent principal components that need to be known in order to characterise it:

1. eq=V_{zz}
2. the axial asymmetry parameter η

where V_{zz} is the largest EFG component and the η asymmetry parameter which takes values only from 0 to 1.

$$\eta = \frac{V_{yy} - V_{xx}}{V_{zz}} \tag{3.9}$$

The η=0 describes axial symmetric EFGs and is very common for quadrupolar nuclei in terminal bonding situations, while η=1 describes the highest asymmetry situation.

The quadrupole frequency, ω_Q is another relevant parameter for describing the EQI, given by Eq. 3.10

$$\omega_Q = \frac{eQV_{ZZ}}{4I(2I-1)\hbar} = \frac{2\pi\nu_Q}{4I(2I-1)} \tag{3.10}$$

with Q being the intermediate energy level's nuclear quadrupole moment and I its nuclear spin. ν_Q is the quadrupole interaction frequency.

Considering ω_0 as the lowest transition frequency (ω_0=kω_Q) and the smallest frequency that occurs in a PAC measurement, we distinguish the integer and half-integer nuclear spins as follows from Eq. 3.6 and Eq. 3.10 [48]:

Half-integer nuclear spins (such as I=5/2 for ^{111}Cd) k=6 :

$$\omega_0 = 6 * \omega_Q \tag{3.11}$$

Integer nuclear spins (such as I=2 for ^{68}Cu) k=3:

$$\omega_0 = 3 * \omega_Q \tag{3.12}$$

3.1.2 Magnetic Dipole Interactions

In case the magnetic dipole moment, μ, of the probe nucleus with I=5/2 interacts with a static magnetic field created by the host material (magnetic and ferromagnetic solid materials) there is a Magnetic Dipole Interaction that causes again a time dependent perturbation given by Eq. 3.13

$$G_{22}(t) = \frac{1 + 2cos(\omega_L t) + 2cos(2\omega_L t)}{5} \tag{3.13}$$

The Larmor frequency, ω_L, is proportional to the external magnetic field, B, (in this case to the hyperfine magnetic field, H) and is given by Eq. 3.14

$$\omega_L = \frac{|g\mu_N H|}{\hbar} \tag{3.14}$$

,where the g factor is relative to the isotope used, μ_N is the nuclear magneton and I the nuclear spin of the intermediate level.

3.1.3 Liquid dynamics studied by PAC

In biological samples the EFG is time dependent if the samples are not immobilised by e.g. freezing and they remain in the liquid form. Due to the conformation alterations of the molecules during the lifetime of the intermediate nuclear state, the emission of the γ_1 and γ_2 may be perturbed due to the hyperfine interactions of the nuclei with the EFG. The perturbation factor $G_{22}(t)$ should be modified for non-static EFGs, taking into account the magnitude of the molecular rotational correlation time, τ_c, and the size of the nuclear quadrupole interaction, eQ, in the intermediate energy state [4].

Brownian rotation diffusion of a particle in a solution has a characteristic time constant that is called rotational correlation time, τ_c. According to Stokes-Einstein rotational diffusion, assuming that the molecule is spherical, the correlation time is given by Eq. 3.15 [49]. In solution the τ_c is the average time that a molecule takes to rotate one radian and normally they are in the order of ps.

$$\tau_c = \frac{4\pi r^3 * \xi}{k_B * T} \tag{3.15}$$

, where r is the effective hydrodynamic radius of the molecule under study, ξ is the viscosity of the solvent, T is the absolute sample temperature in K and k_B is the Boltzmann's constant.

For slow reorientation of the molecules in the sample where $\omega_0\tau_c >> 1$ the perturbation function $G_{22}{}^{rot}(t)$ become exponentially damped and is given by Eq. 3.16

[49], where $G_{22}(t)$ is the perturbation function of the static interaction and is given by Eq. 3.5

$$G_{22}^{rot}(t) = G_{22}(t) * exp - (\frac{t}{\tau_c}) \tag{3.16}$$

For fast reorientation of the molecules in the sample where $\omega_0\tau_c << 1$, with short correlation times, and for the typical case of intermediate state I=5/2, the perturbation function becomes [49]:

$$G_{22}^{rot}(t) = exp(-2.8{\omega_0}^2 t\tau_c(1+\eta^2/3)) \tag{3.17}$$

When the molecules have correlation times in the intermediate region, $\omega_0\tau_c \approx 1$, the $G_{22}(t)$ cannot be described analytically. A Monte Carlo simulation approach can be implemented for simulating PAC spectra of dynamic EFG of any origin by Danielsen et al [29].

From a PAC measurement we are always interested to determine the perturbation function, $R(t)=A_{22}G_{22}(t)$ which is given by Eq. 3.18 [3].

$$A_{22}G_{22}(t)_{\text{exp}} = 2\frac{N(180^o,t) - N(90^o,t)}{N(180^o,t) + 2N(90^o,t)} \tag{3.18}$$

, where $N(\theta,t)$ are the coincidence counts of the two successive γ-rays emitted (γ_1 and γ_2) detected by two detectors positioned at right angles to each other and θ is either 90° or 180°. The typical PAC instruments consist of six scintillation detectors (such as BaF_2) which are positioned at right angles to each other, resulting to the acquisition of six 180° and twenty four 90° coincidence spectra.

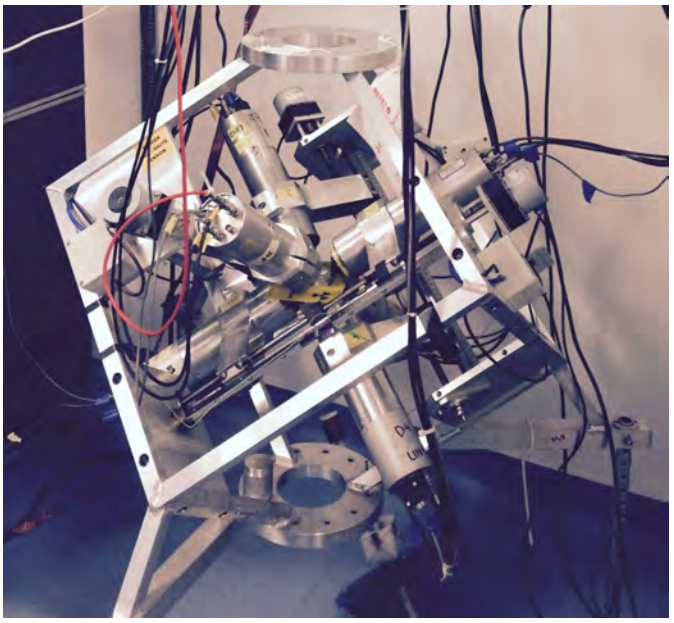

FIGURE 3.2: A typical PAC instrument: An array of six scintillation detectors at right angles to each other.

After the coincidences acquisition the $A_{22}G_{22}(t)$ is Fourier transformed for easier visualisation of the frequencies between the hyperfine energy levels. For extracting quantitative results from the FT spectra the $A_{22}G_{22}(t)$ is fitted to the analytical function given by Eq. 3.19 [3]

$$A_{22}G_{22}(t)_{\text{theor}} = B_0 + A_{22}^{eff} \sum_i f^{\text{i}} G_{22}^i(\omega_0, \eta, \delta\omega_0/\omega_0, \tau_{\text{c}}) \tag{3.19}$$

, where B_0 is a constant background, $A_{22}{}^{\text{eff}}$ is the measured amplitude of the anisotropy of the angular emission between γ_1 and γ_2 and depends on the nuclear properties of the probe nucleus as well as the geometry of the experimental setup. i is the index of the sum that runs over all the existing coordination geometries in the sample and f^{i} is the relative fraction of every structure and NQI. $\delta\omega_0/\ \omega_0$ is the linewidth of each signal of the PAC spectrum, Lorentzian or Gaussian. Alike other spectroscopic techniques, thin linewidths represent a well-defined and relatively stable coordination geometry, while a relatively large linewidth can represent flexible structures that undergo dynamic interactions that alter their geometry.

3.2 Experimental considerations

3.2.1 The PAC probes

The necessary requirements of a good PAC probe are summarised in the following list [3]:

1. The most suitable PAC probes are those who are solely decaying through Isomeric Transition (IT), from an excited state via emission of two correlated γ-rays.
    - The intermediate energy state is necessary to have a reasonably long half-life (1 μs to 2 ns) so that the probe isotope has adequate time to sense the extranuclear fields (EFG and MF) and has the time to interact with them.
    - At least one full period of ω_1 observable has to take place.
    - At the same time the half-life must not be too long. Otherwise the probability of recording accidental γ-rays coincidences increases, creating an elevated background noise spectrum.
2. The two emitted γ photons should have sufficiently different energies in order to be well distinguished when detected.
3. The nuclear moments of the probe nucleus (Q and μ) and the anisotropy (A_{22}) of the angular correlation between γ_1 and γ_2 have to be large enough to allow the measurement of the perturbation function R(t).
4. The nuclear spin of the intermediate energy level has to $I > 1$, since I=0 or 1/2 does not exhibit Nuclear Quadrupole Interactions (NQI).
5. The parent isotopes should be readily produced and they must have long enough half-lifes in order to be practical to work with.
6. The parent isotopes must be produced with low to non contamination from other isotopes and with high activity.

The most important characteristics of potential probe isotopes that could be used within the scope of the current work, for chemistry and biochemistry PAC experiments, are shown in Table. 3.1.

TABLE 3.1: Characteristic parameters of selected PAC isotopes [28]

Isotope	$T_{1/2}$	Decay mode	Probe isotope	γ_1/γ_2 cascade E (keV)	Intermediate state I	$T_{1/2}$ Intermediate state	Q (b)	μ	Anisotropy A_{22}
^{68m}Cu*	3.75 min	IT	^{68}Cu	637-84	2+	7.84(8) ns	(-)0.110(3)	(+)2.857(6)	0.05
^{111m}Cd*	48 min	IT	^{111}Cd	151-245	5/2+	84.5(4) ns	+0.68(2)	-0.7656(25)	0.1786
^{111}Ag	7.45 d	β^-	^{111}Cd	97-245	5/2+	84.5(4) ns	+0.68(2)	-0.7656(25)	0.1786
^{111}In	2.8 d	EC	^{111}Cd	171-245	5/2+	84.5(4) ns	+0.68(2)	-0.7656(25)	-0.0714
^{199m}Hg	42.4 d	IT	^{199}Hg	374-158	5/2-	2.46(3) ns	+0.95(9)	+0.88(3)	0.221

*Isotopes used in the current work

The detailed decay schemes of the isotopes used in the current work are shown in Fig. 3.1 and Fig. 3.3 and are taken by [17].

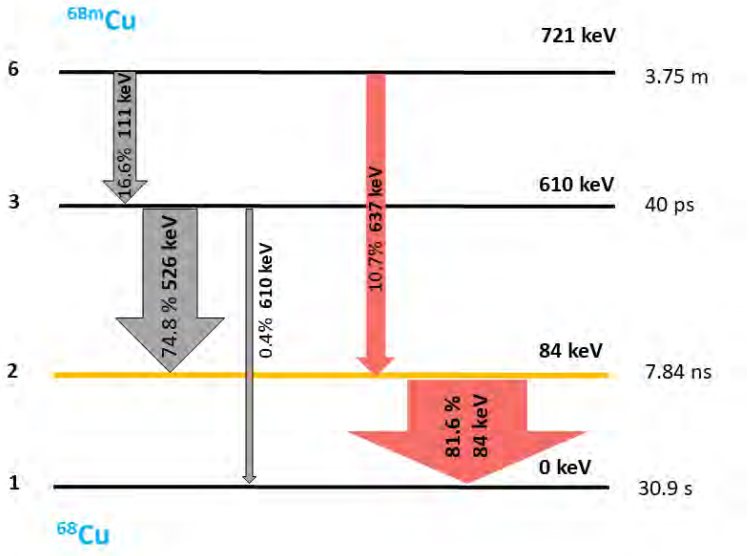

FIGURE 3.3: Decay scheme for ^{68m}Cu-^{68}Cu [17].

Chapter 4

Experimental PAC results

In the beginning of the current PhD work, in 2014, a collaboration between the Solid State Physics Group and the Biophysics group of ISOLDE-CERN was established. One of the main goals of this collaboration was to build and commission a new beamline called VITO (Versatile Ion-Polarised Techniques Online), dedicated to produce laser-spin-polarised radioactive atomic and ion beams. VITO was concepted to be dedicated to multidisciplinary experiments in the areas of nuclear and solid state physics, fundamental interaction physics and biophysics [50, 51]. In its initial configuration, VITO had an open-end station available for travelling experiments, such as On-line PAC experiments. The first PAC experiments with radioactive ^{68m}Cu ion beams proposed by [12] will be presented in the following section. This project was shared between my self and an other PhD student of the Solid State Physics CERN group, Abel Fenta.

4.1 The ^{68m}Cu used as a new PAC probe

In order to test the feasibility of using copper as a probe isotope for PAC studies, the ^{68m}Cu was selected as the test case isotope due to the several preferential characteristics. It has good production yields from the ISOLDE targets (1x10^8 from UC_x target), it is easily ionised by RILIS and has favourable physical properties that are summarised in [12]. As it is shown in Fig. 3.3, the isotope decays through a cascade of photons with suitable energies (637 keV and 84 keV), the intermediate energie state has a nuclear spin 2+ with a 7.84 ns half-life and the anisotropy

was expected to be as high as 15%, [12]. The nuclear moments (magnetic dipole moment and quadrupole moment) of ^{68m}Cu were until that time unknown.

Since the lifetime of ^{68m}Cu is too short to collect and carry out offline chemical sample preparation, the feasibility experiments were conducted by implanting the radioactive Cu(I) into different solid foils at room temperature and high vacuum conditions. The ion beam of ^{68m}Cu, with 30 keV energy, was directed to the central end station of the VITO beamline, Fig. 2.4. The VITO beamline elements as presented in Fig. 4.1 and 4.2 comprise, from left to right (direction of beam propagation), of: a 5° beam deflector, a 2 m long drift tube, two quadrupole doublets, a beam diagnostics box (a wire scanner and a Faraday cup) and a beam switch.

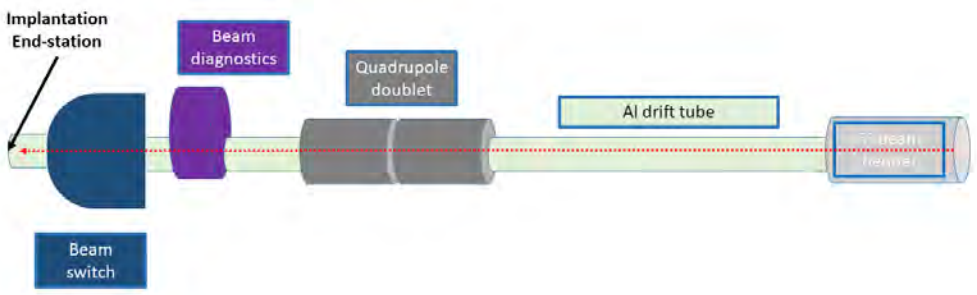

FIGURE 4.1: Graphical representation of the VITO beamline at phase 1 (2015) showing the one end-station, when no laser polarisation of ions or atoms was possible.

FIGURE 4.2: Top view of VITO beamline at phase 1.

The experimental setup where the implantation of ^{68m}Cu and the on-line PAC measurements in different host environments took place is shown in Fig. 4.3 and Fig. 4.4. A quartz finger, vacuum compatible collection chamber of 2mm wall thickness was used for direct visualisation of the sample holder and for minimising the gamma transmission through the chamber. The detection PAC setup used during the experiments consisted of four $LaBr_3$ gamma scintillator detectors positioned in a plane perpendicular to the direction of the beam propagation. Each detector was placed at 90° and 180° in respect to each other at approximately equal distances from the implantation foil. The data acquisition was performed with the digital and FPGA signal processing [13, 14].

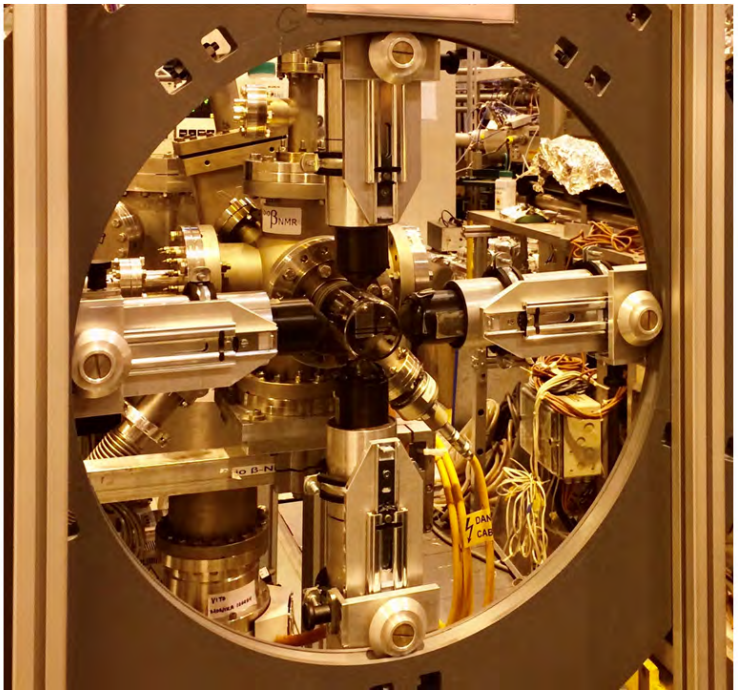

FIGURE 4.3: Front view of the implantation chamber made of quartz in the middle of the detection PAC experimental setup of $LaBr_3$

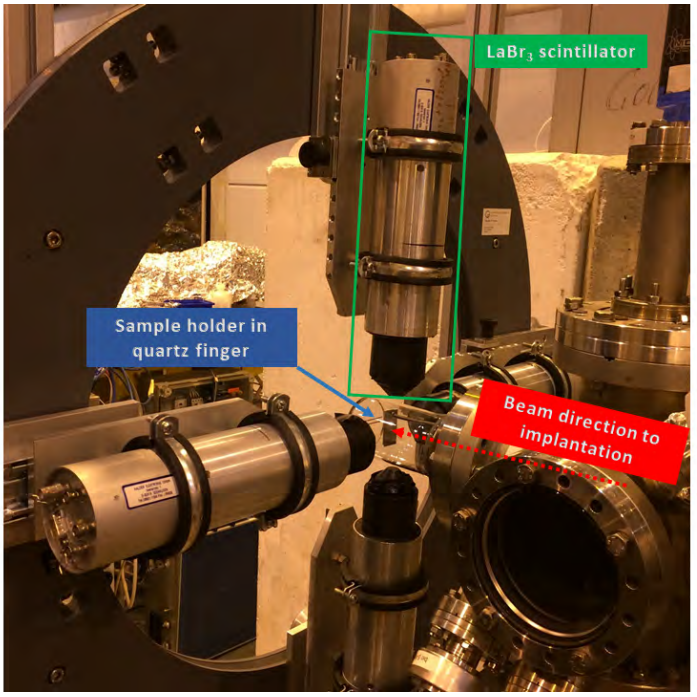

FIGURE 4.4: Back view of the 4 $LaBr_3$ PAC detectors, the vacuum quartz implantation chamber and the sample holder supporting the host material

Three solid state samples, a Cobalt and a Nickel foil plus a Cu_2O pellet were used as the host material and were placed approximately at the geometrical centre

of the experimental setup. For the three samples the experimental conditions were, room temperature, high vacuum of approximately 10^{-6} mbar and maximum number of implanted atoms 2x10^{11}b [15]. The γ_1-γ_2 coincidences, $N_{ij}(\theta,t)$ were measured as a function of time between the detection of the two γ rays for every detector combination (i, j). The experimental perturbation functions R(t) given by Eq. 3.18 were acquired for ^{68}Cu implanted in three different samples (Co, Ni and Cu_2O) and are illustrated at Fig. 4.5 [15].

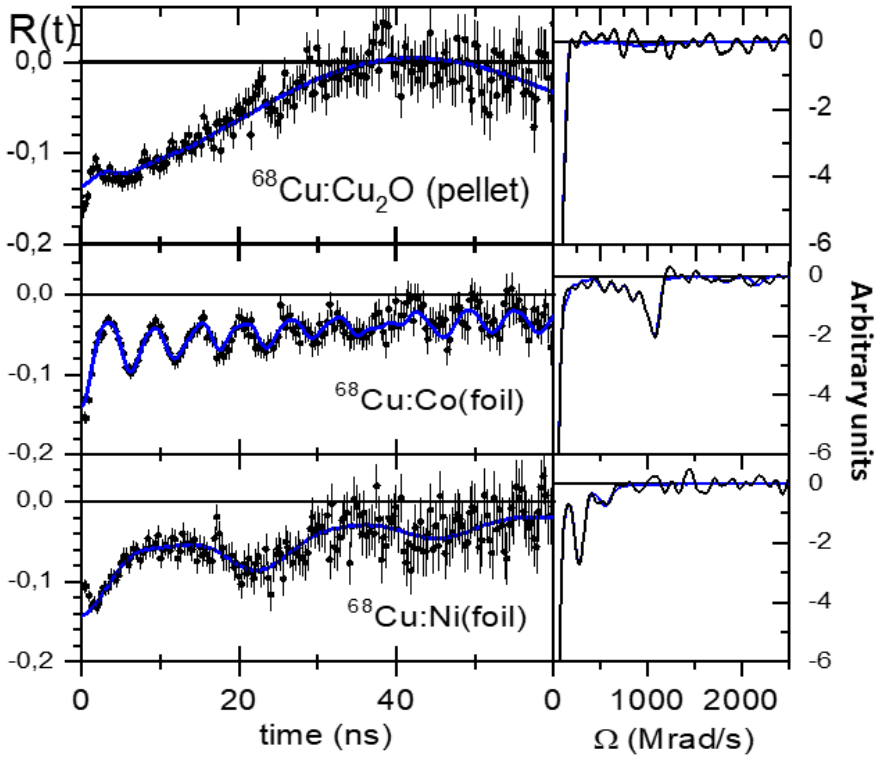

FIGURE 4.5: PAC experimental R(t) spectra (data points with error bars (black) and fit (red) and the corresponding Fourier transforms

The most important extracted experimental parameters by the fitting procedure are summarised in Table. 4.1 [15].

Cu_2O, due to its simple cubic structure, was selected in order to measure the NQI and to determine the quadrupole moment of the ^{68}Cu intermediate state. Cu is linearly coordinated with two O atoms and O have a tetrahedral coordination

TABLE 4.1: Experimental parameters from fitting analysis of R(t) experimental function [15]

Host	A^{eff}_{22}	f(1)%	ω_0 (Mrad/s)	ω_L (Mrad/s)
Cu_2O	-0.13(1)	89	21.3(4)	-
Co	-0.13(1)	22	-	1079.1(34)
Ni	-0.13(1)	44	-	273.7(48)

with Cu atoms. Due to the low coordination number, the Cu binding site has a strong EFG and high axial symmetry η=0. From the fitting of the experimental R(t) we concluded to a predominant fraction of ^{68}Cu of 89(3)% with ω_0=21.3(3) Mrad/s and η=0. From Eq. 3.10 and Eq. 3.12 we calculated the quadrupole interaction frequency, ν_Q=27.14(44) MHz. From previous NQR measurements [52] we adopted the $\nu_Q(^{65}Cu, I=3/2)$=48.138(12) MHz for ^{65}Cu implanted in Cu_2O and we calculated the ratio $^{68}Cu/^{65}Cu$=0.5638. Knowing the quadrupole moment of the ^{65}Cu nucleus, $Q(^{65}, I=3/2)$=-0.195(4)b [53], and using the quadrupole coupling constant ratio we calculated the quadrupole moment of the ^{68}Cu, $I=2^+$ state, $\mathbf{|Q(^{68}Cu,\ 2^+,\ 84.1\ keV)|=0.110(3)b}$.

For measuring the magnetic hyperfine interaction we initially used a cobalt foil to determine the magnetic dipole moment of ^{68}Cu and then a nickel foil in order to confirm our result. More precisely in the case of the Co host, we had to introduce three fractions of ^{68}Cu in order to fit the experimental R(t) function. The fraction of atoms f_1=22(1)% was assigned to interact with the unperturbed lattice sites of the hcp structure of Co and to interact with a strong magnetic field. From the fitting of this signal we extracted the Larmor frequency ω_L= 1079.1(34) Mrad/s. The second fraction, f_2=32(1)% atoms, was assigned to interactions with defects that were created during the implantation procedure of the radioactive ^{68m}Cu atoms in the Co foil. Last, the third fraction of the signal was most probably originating by ^{68m}Cu atoms implanted in the Al sample holder that we used during the experiments due to not optimal beam focusing on the host sample. f_1 was the main component of the signal, with a ω_L= 1079.1(34) Mrad/s (for ^{68}Cu in Co). From previous NMR measurements at room temperature [54] the Larmor frequency for ^{63}Cu in Co was ω_L= 1117.8(3) Mrad/s and for ^{65}Cu in Co was ω_L= 1198.2(3) Mrad/s. Using the known g factors of both isotopes respectively $g(^{63}Cu)$=1.480(0) and $g(^{65}Cu)$=1.580(5) [55] and from Eq. 3.14 we calculated the g factor of ^{68}Cu from Eq. 4.1.

$$g(^{68}Cu) = g_{\rm i}\omega_{\rm L}/\omega_{\rm Li} \tag{4.1}$$

with the i index referring to the ^{63}Cu and ^{65}Cu isotopes' parameters and $\omega_{\rm L}$ the Larmor frequency of ^{68}Cu as extracted by the fit of the experimental spectrum of this work. The final value of the g factor of ^{68}Cu was obtained by averaging the two slightly different values resulting from the two calculations and is g=1.429(6). From Eq. 5.2 and Eq. 5.1 we calculated the dipole moment $\mu(\mathbf{^{68}Cu})=\mathbf{2.859(13)}\mu_{\mathbf{N}}$.

Finally, an independent PAC measurement was carried out with a Ni foil in order to crosscheck the calculation of $\mu(^{68}$Cu. From the fitting of the experimental R(t) function two different interaction sites were distinguished. The fraction f_1=44(2)% is assigned to the Cu atoms who interacted with the hyperfine magnetic field of Ni and a Larmor frequency $\omega_{\rm L}$=273.7(48)Mrad/s was extracted by the spectrum. A second higher fraction, f_2=56(3)%, of Cu atoms was again implanted in the Al sample holder and thus was neglected from our calculations. As described in our publication [15] and the references therein, we extracted graphically the Larmor frequencies of ^{62}Cu when implanted in a Ni host at different temperatures, $\omega_{\rm L}$=153.8(17)Mrad/s for 105 K and $\omega_{\rm L}$=135.5(10)Mrad/s for 304 K. From Eq. 3.14 the hyperfine magnetic field was calculated, H=-4.08(10)T and using the experimental $\omega_{\rm L}$=273.7(48) Mrad/s we obtained the g=1.402(43) resulting to a magnetic moment of the $\mu(\mathbf{68Cu,\ I=2+})=\mathbf{2.804(85)}\mu_{\mathbf{N}}$.

The final value of the magnetic dipole moment of the 68Cu isotope that we proposed was the average (error weighted) value of the two independent measurements and and is $\mu=\mathbf{2.857(6)}\mu_{\mathbf{N}}$.

With the current work we clearly demonstrated that the ^{68m}Cu/^{68}Cu IT transition can be used as a probe for PAC experiments. From the calculated nuclear moments we found a relatively short quadrupole moment, Q=0.110(3) b which in combination with the very short half-life of the intermediate energy level (7.84 ns) makes it difficult to record one full oscillation in the perturbation function, even if a Large EFG is present. Therefore, this copper isotope may not be used for elucidating Cu(I) coordination geometries in metalloproteins but can serve as a unique copper probe for condensed and soft matter physics.

4.2 ^{111m}Cd(II) PAC studies of CadC binding

Metalloregulatory proteins or metal sensor proteins control the expression of genes providing organisms with a defence against the heavy metal toxicity [56]. Some pathogenic bacteria have evolved in regulating and managing the heavy metal ions in their microenvironment for their survival. This adaptive behaviour could be of great interest for intracellular survival for mammals. CadC is one of the metal receptor proteins that senses a wide range of metal ions such as Cd(II), Pb(II) and Zn(II) [57, 58]. In this part of the thesis, the ^{111m}Cd PAC spectroscopy was applied to elucidate the function CadC by determining the metal site structure and the dynamics on the ns scale of the binding site and to explore the effect of CadC binding to DNA on the metal site.

Previous ^{113}Cd NMR experiments in CadC gave an indication of two co-existing possible metal site structures that change between a CdS_4 and a CdS_3X complex [57] attracting our interest for further investigation.

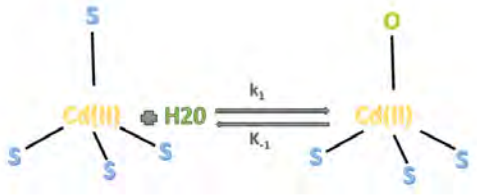

FIGURE 4.6: Representation of proposed reaction scheme of Cd(II) with CadC when H_2O is used as solvent

The proposed reaction shown in Fig. 4.6 was tested experimentally with ^{111m}Cd PAC on the CadC of two different bacteria, the Listeria Monocytogenes (L. monocytogenes) and the Staphylococcus aureus (S. aureus) pI258. A previous ^{111m}Cd PAC work [16] shows the expected FFT spectra of pure CdS_4 and CdS_3X complexes for two special designed peptides (α_3DIV-L21C and α_3DIV-H72C). The PAC FFT spectra from [16] constituted the reference spectra for the CdS_4 and CdS_3O species.

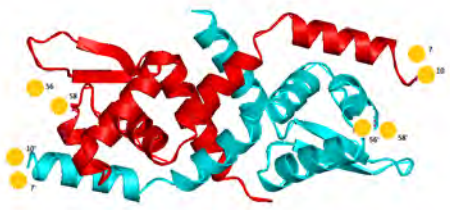

FIGURE 4.7: Crystal structure and binding sites of L. monocytogenes WT (designed with PyMOL)

4.2.1 Experimental conditions

Sample preparation of ^{111m}Cd and CadC bacteria

The radioactive ^{111m}Cd with a decay scheme 3.1 was produced by the PET and Cyclotron Unit of the University Hospital of Copenhagen in Denmark, 2.5 and a radioactivity of approximately 600 MBq was shipped to the Chemical Institute of the Faculty of Life Sciences were the PAC measurements took place. The radioactive probe was first chemically separated by the ^{208}Pb as described previously by [59] and the radioactivity was fragmented for preparing the different samples used for the experiments. The chemical separation of the ^{111m}Cd from ^{208}Pb was carried out by the laboratory assistant Marianne Lund Jensen the day of the experiments.

Two type of bacteria were used for these experiments, the Listeria monocytogenes (L. monocytogenes) CadC Wild Type and the Staphylococcus aureus (S. aureus) pI258 CadC that were kindly provided the Agriculture and Life Sciences Texas A&M University, Department of Biochemistry and Biophysics and the Indiana University Bloomington, Department of Chemistry. The chemical structure of L. monocytogenes is presented in Fig. 4.7 and the one of S. Aureus pI258 can be found in [57]. The sample preparations with the bacteria and the radioactive probe were carried out by the laboratory assistant Marianne Lund Jensen the day of the experiments.

The PAC spectrometer

The ^{111m}Cd PAC experiments were carried out at the Chemistry department of University of Copenhagen in Denmark. The PAC spectrometer used for the current project, presented in Fig. 4.8, consists of six BaF_2 scintillation detectors. The six

detectors are placed in a 4π geometry at 90° and 180° with respect to each other and they are placed as close as possible to the sample in equal distances from the center of the sample. The energy and temporal resolution of the detectors (11.5-12.5% and 650 ps respectively) were adequate to easily distinguish the emission of γ_1 and γ_2 [60]. The experimental setup has a temperature control system, consisted of a Peltier element, that was very useful for the current work since it allowed for temperature series measurements from -196°C to more than 50°C for studying the dynamics of the binding sites of CadC.

FIGURE 4.8: The six BaF_2 scintillator detectors PAC system at the University of Copenhagen, Chemistry department in Denmark

4.2.2 Experimental results

The experiments with the CadC bacteria were carried out at different temperatures. Table 4.2 summarises the parameters fitted to ^{111m}Cd PAC data for different sample temperatures using the code WINFIT developed at Leipzing University by F. Heinrich ad T. Butz. The experimental conditions kept at 50 μM CadC, 0.2 eq Cd(II), pH=7 and addition of sucrose 55% w/w in order to slow down the rotational diffusion of the molecules.

TABLE 4.2: NQI parameters for the ^{111m}Cd PAC experiments on the L. monocytogenes CadC. Experimental conditions 50 μM CadC, 0.2 eq Cd(II), 55% w/w sucrose and pH=7.

sample	T [°C]	ω_0[rad/ns]	η	site [%]	linewidth *100	$1/\tau_c$ [us^{-1}]	A*100	chi^2
WT L. monocytogenes	-196	0.067(3)	0.49(7)	100	40.6(4)	$\infty[F]$	11.6 (0.5)	0.84
WT L. monocytogenes	1	0.070(0.5)	0.82(2)	59	8.0 (1)	351	5.7(0.3)	1.07
		0.162(5)	0.45(4)	41	16.3(3)		4.0(0.5)	
WT L. monocytogenes	30	0.063(0.3)	1	54	17(2)	290	5.6(0.8)	1.20
		0.198(3)	0.3(3)	46	14.2(2)		4.8(0.7)	
C10G L. monocytogenes	1	0.186(0.6)	0.25(0.9)	100	4.6(0.5)	238	7.1(0.3)	1.10

[F] denotes parameters kept fixed during the fitting procedure in the Winfit program

The experimental perturbation functions R(t) and the respective Fourier transforms (FFT) for the different temperatures are presented in Fig. 4.9.

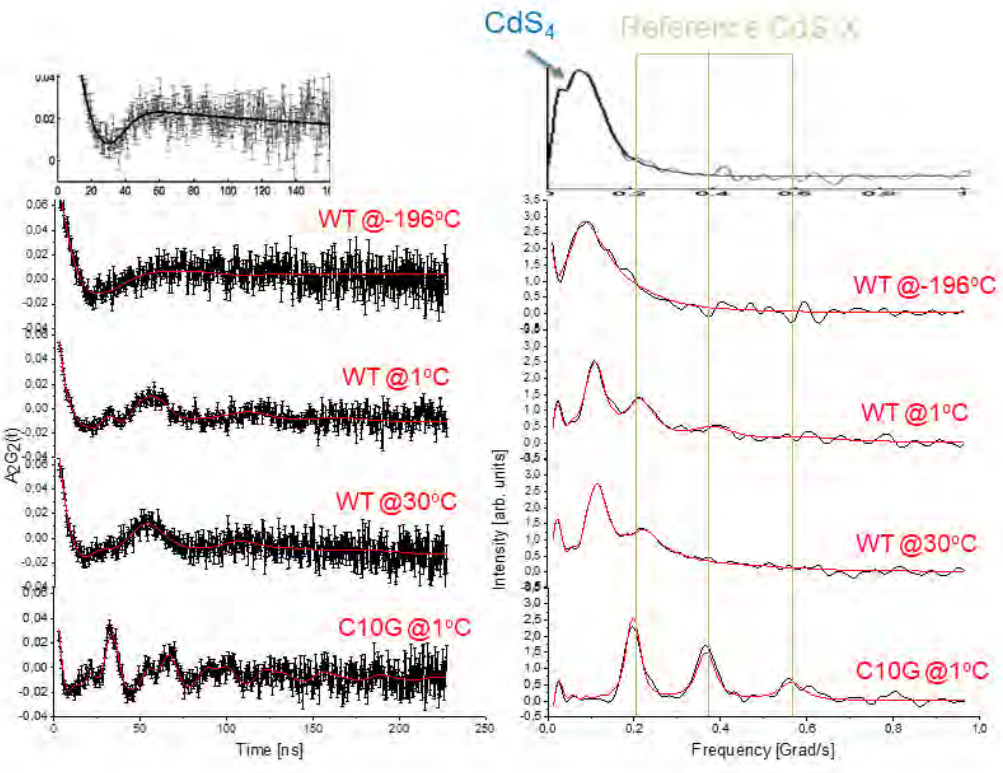

FIGURE 4.9: The experimental Perturbation Function R(t) and the respective Fourier transform (FFT) for the wild type (WT) L. monocytogenes at at various T.

Comparing the FFT experimental spectra of L. monocytogenes CadC bound with Cd(II) of this work with the spectra for CdS_4 and CdS_3O found in [16] Fig. 4.9,

it is shown that a rapid exchange between two species CdS_4 and CdS_3O is very probable. With the temperature increase the fraction of the CdS_3O is increasing, while when the sample is frozen instantaneously with LN and due to the absence of dynamics the CdS_4 metal site structure dominates. This indicates that CdS_4 is enthalpically stabilised with respect to CdS_3O structure as expected since Cd-S bonds are stronger than Cd-O bonds.

We repeated the ^{111m}Cd PAC measurements with L. monocytogenes CadC lowering the pH of the samples from 7 to 6.5. The pH was decreased in order to increase the H^+ ions in the sample expecting to shift the chemical reaction to the CdS_3O. The rest experimental conditions remained unchanged, 50 μM CadC, 0.2 eq Cd(II) and addition of sucrose 55% w/w. The experimental perturbation functions R(t) and the respective FFT for the different temperatures at pH 6.5 are presented in Fig. 4.10, Fig. **??** and Fig. **??** and the experimental results after the fitting the code WINFIT are summarised at Table. 4.3.

TABLE 4.3: NQI parameters for the ^{111m}Cd PAC experiments on the L. monocytogenes CadC. Experimental conditions 50 μM CadC, 0.2 eq Cd(II), 55% w/w sucrose and pH=6.5.

sample	T [°C]	ω_0[rad/ns]	η	site [%]	linewidth *100	$1/\tau_c$ [us^{-1}]	A*100	chi^2
WT L. monocytogenes	-196	0.067(1)	0.20(23)	76	47.3(5.5)	∞	9.1(1)	0.76
		0.198[F]	0	24	23.4(12)		2.9(2)	
WT L. monocytogenes	-20	0.066[F]	1	27	82 (39)	344	4.2(3)	0.80
		0.192[F]	0.33(6.5)	73	30(6.5)		11(3.5)	
WT L. monocytogenes	30	0.066[F]	1	21	34(17)	147	3.1(14)	0.77
		0.198[F]	0.33(7)	79	27(7)		26.8(7)	

[F] denotes parameters which were kept fixed during the fitting procedure in the Winfit program.

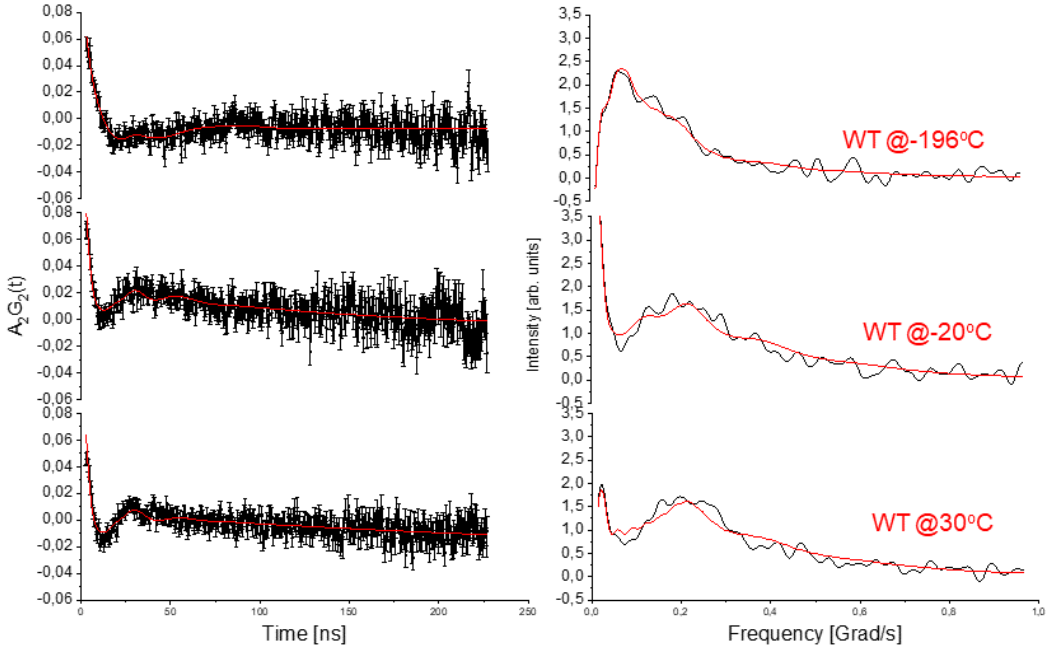

52

FIGURE 4.10: The experimental Perturbation Function R(t) and the Fourier transform (FFT) for the WT L. motocytogenes at pH 6.5 for different T.

Comparing the results from Table. 4.2 and Table 4.3 one can see that upon lowering the pH there is a shift of higher fractions of sites towards higher ω_o and thus ω_Q frequencies. At the same time we observe a considerable line broadening that could be potentially originating by faster exchange dynamics between the two species, CdS_4 and CdS_3O. For easier visualisation of the differences between the different pH, Fig. 4.11 shows the FFT spectra of -196 °C and 30°C for pH 7 and pH 6.5 respectively.

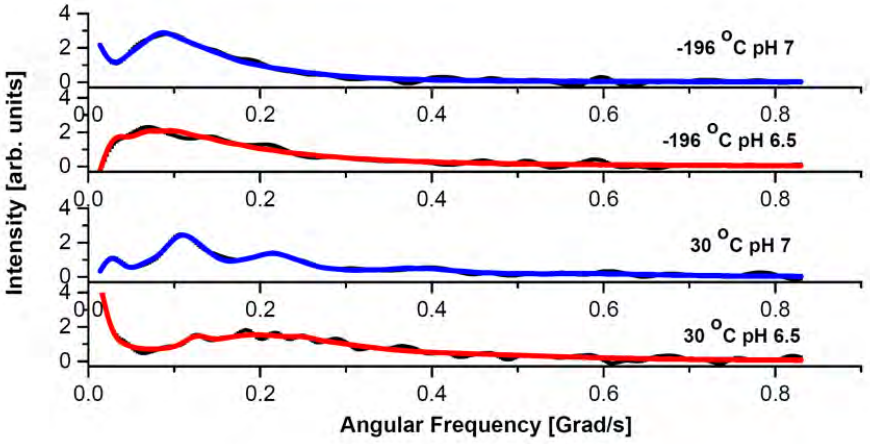

FIGURE 4.11: Comparison of FFT spectra for the WT L. motocytogenes at -196 °C and 30°C for pH 7 and pH 6.5.

Due to time constraints and the limited radioactivity, we measured only at 1°C the ^{111m}Cd spectrum of CadC in S. Aureus. In addition a sample with 100 μM DNA dissolved and bound with the CadC in the S. Aureus was measured with PAC under the same pH 7 and temperature, 1 °C. From the detailed results of the spectral analysis presented in Table. 4.4 and Fig. 4.12 it is concluded that the metal site structure and the exchange rate between the two species CdS_3O and CdS_4 appear not to be affected by the DNA binding to CadC.

TABLE 4.4: NQI parameters for the ^{111m}Cd PAC experiments on the S. aureus pI258 CadC. Experimental conditions 50 μM CadC, 0.2 eq Cd(II), 55% w/w sucrose and pH=7

sample	T [°C]	ω_0[rad/ns]	η	site [%]	linewidth *100	$1/\tau_c$ [us^{-1}]	A*100	chi^2
WT S. Aureus	1	0.078(0.11)	0.88(4)	47	9.8(1)	2325	4.9(0.2)	1.07
		0.181(1)	0.42(1)	53	7.8(0.7)		5.5(0.4)	
WT S. Aureus + 100μM DNA	1	0.072(0.2)	0.95(11)	53	11.2(2)	476	5.7(0.2)	1.09
		0.183(0.1)	0.40(1)	47	7.2(0.7)		5.0(0.3)	

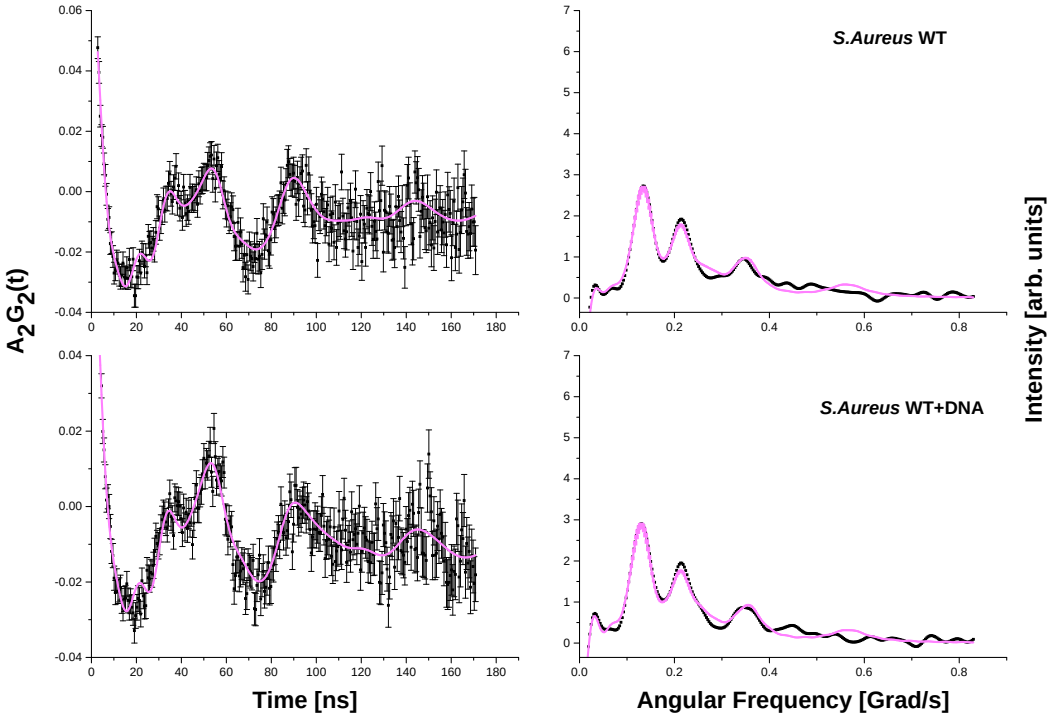

FIGURE 4.12: Comparison of R(t) and FFT spectra for the WT S. Aureus pI258 CadC and the WT S. Aureus pI258 + 100 μM DNA at 1°C.

Last, an attempt to simulate the exchange dynamics between the two suggested coordination species at 1°C for S. aureus pI258 CadC was made using the PAC simulator, a Monte Carlo Program dedicated to simulate PAC dynamic spectra [29]. The simulated spectra were in good agreement with the R(t) and FFT experimental spectra of ^{111m}Cd PAC in CadC of S.Aureus pI258 for lifetimes of Cd binding at the CdS_4 site, τ_1=1 ns, and τ_1=0.5 ns for the CdS_3O. In Table. 4.5 the input parameters to the PAC simulator are presented. In Fig. 4.13 the experimental and simulated R(t) and FFT spectra are presented.

TABLE 4.5: Input parameters for dynamic PAC simulations of ^{111m}Cd [29] binding to S. Aureus pI258 CadC at 1°C

Site	CdS_4	CdS_3O
τ[ns]	1	0.5
ω[Grad/s]	0.066	0.186
η	0.83	0.25
(α,β,γ)	(0,0,0)	(0,0,0)

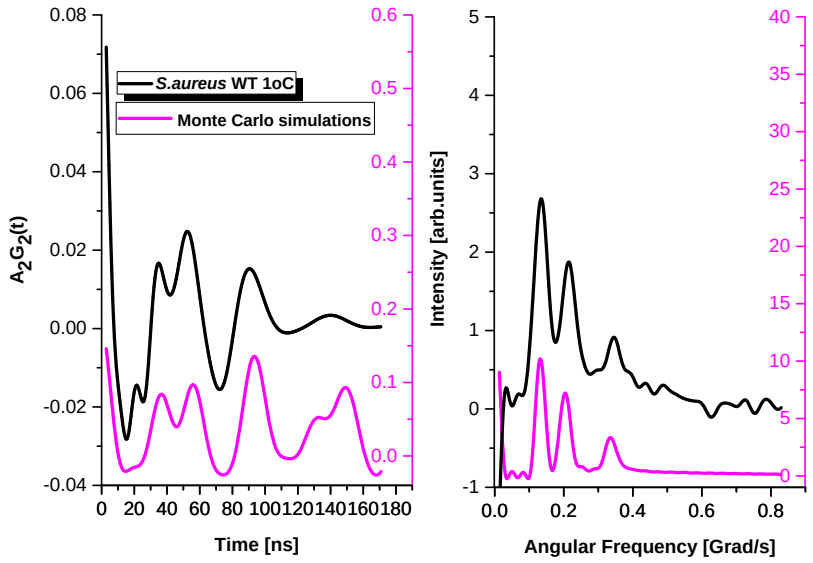

FIGURE 4.13: Comparison of R(t) and FFT spectra for the WT S. Aureus pI258 CadC and the WT S. Aureus pI258 CadC + 100 μM DNA at 1°C.

Temperature-dependent ^{111m}Cd PAC spectroscopy was used to explore the kinetics of the reaction proposed in Fig. 4.6 for the CadC bacteria L. monocytogenes. The ^{111m}Cd PAC spectra in Fig. 4.9 clearly demonstrate the temperature dependence of the NQI. At -196 °C the CdS_4 geometry dominates. For 1 °C a second NQI signal appears reflecting the coexistence with a CdS_3O species that starts dominating as the temperature further increases. When lowering the pH to 6.5, we observed the shift to the right, CdS_3O as expected, since we increased the H atoms.

A possible co-existence of the two species was observed at the PAC measurements of S. aureus pI258 CadC. From the studies performed with these bacteria we clearly showed that the DNA binding to the CadC protein does not alter the binding and the dynamics of Cd(II). Also, with Monte Carlo simulations we achieved to simulate the exchange dynamics between the two species. The life-time of the resident Cd ion on both chemical species was very short in the order of ns, showing that it would be impossible to observe it with a conventional spectroscopic technique, i.e NMR. The phenomena that NMR can study are in the range of ms. These results demonstrate that ^{111m}Cd PAC can be used for monitoring the dynamics of CadC proteins with Cd(II) since it can follow the ns exchange dynamics of H_2O molecules bound to the CadC metalloprotein.

Chapter 5

Nuclear Magnetic Resonance (NMR)

The Nuclear Magnetic Resonance (NMR) firstly applied in 1939 [**?**], is very a powerful spectroscopic technique used as a non-destructive analytical tool in chemistry. Is is widely used for probing molecular conformation in solutions and solids since it can provide detailed information about the structure of the nucleus under study. Moreover, NMR allows for studying the physical properties of the molecules such as the conformational dynamics and the diffusion.

Different systems often require different NMR approaches. Usually, the 1D NMR is used to describe the chemical structure of small organic molecules while for more complicated systems, like nucleic acids and proteins, the 2D techniques are preferred.

5.1 Ingredients of Nuclear Magnetic Resonance

All nuclei with a non-zero spin ($I>0$) have a magnetic moment (μ) given by Eq. 5.1

$$\mu = \gamma I \tag{5.1}$$

where γ is the gyromagnetic ratio, a characteristic constant of each nucleus (N), given by Eq. 5.2

$$\gamma = g\mu_N/\hbar \tag{5.2}$$

where μ_N is the nuclear magneton and g_n is the g-factor of the nucleus.

A spinning nucleus generates a magnetic field that is oriented along the spin rotation axis. When an external magnetic field, B_0, is applied the orientation of the precession of the nuclear spin will no longer be random, as illustrated in Fig. 5.1. The precession frequency around the magnetic field B_0 is called Larmor frequency and is given by Eq. 5.3.

$$\omega_L = \frac{\gamma B_0}{2\pi} \tag{5.3}$$

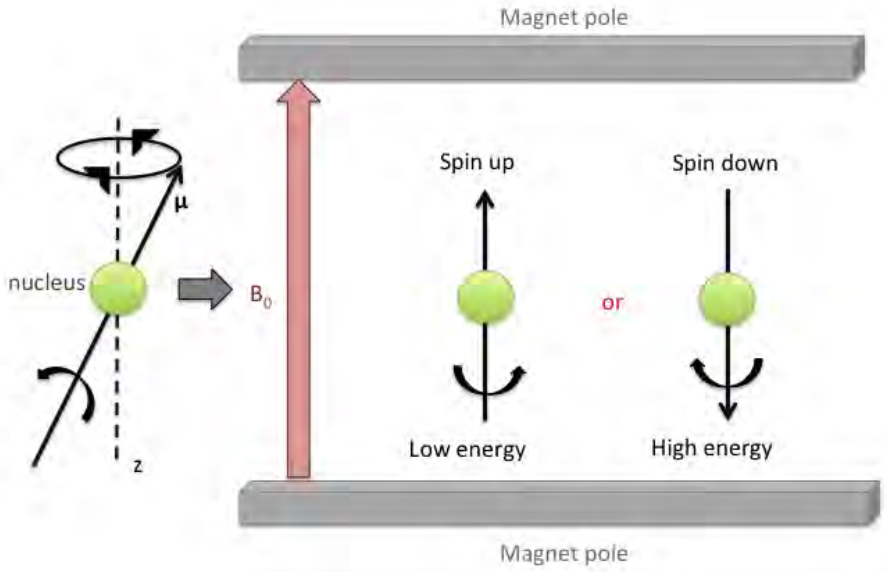

FIGURE 5.1: Orientation and precession of nuclear spins in a magnetic field in the case of single nucleus with I=1/2.

Most biologically interesting nuclei such as ^{1}H, ^{13}C, ^{15}N, ^{18}F and ^{31}P have I and $\mu > 0$. In these simple cases when a B_0 is applied, the nuclear spin energy levels are split in two populations, parallel and anti-parallel to the B_0 direction, due to the Zeeman Effect, as shown in Fig. 5.2. It is important to note that the some

common isotopes such as ^{12}C and ^{16}O do not have a nuclear spin and therefore NMR spectroscopy cannot be applied in such cases.

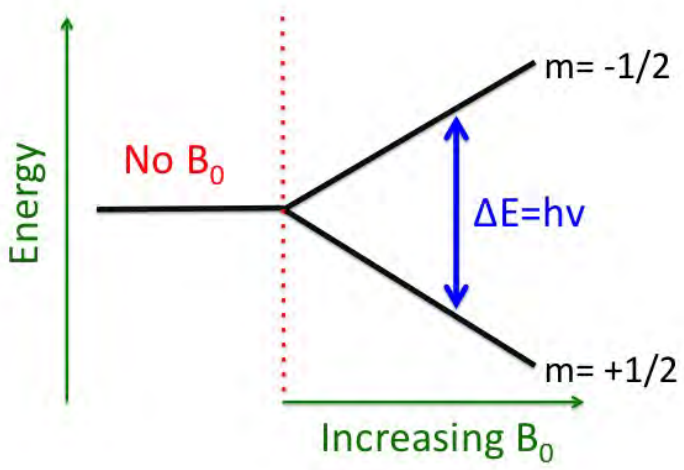

FIGURE 5.2: Zeeman energy splitting for nuclei with I=1/2 and $\mu > 0$ in an increasing magnetic field B_0.

According to the Boltzmann distribution, Eq. 5.4, when an ensemble of nuclei is immersed in a B_0, the population of spin energy states depend on the energy difference of the energy states and the temperature. The most favourable orientation of spin precession will be the one parallel to the magnetic field direction B_z .

$$\frac{N_{upper}}{N_{lower}} = e^{\frac{-\Delta E}{kT}} \tag{5.4}$$

Here N_{upper} and N_{lower} are the populations of nuclei in upper and lower states respectively, ΔE is the energy difference between the spin states as shown in Fig. 5.2, T is the absolute temperature in K and k is the Boltzmann constant. ΔE is related to the Larmor frequency of the nuclei and is given in Eq. 5.5.

$$\Delta E = \hbar\omega_{\mathrm{L}} \tag{5.5}$$

For recording an NMR signal we need to know precisely the Larmor frequency of the nuclei and to apply a secondary oscillating magnetic field perpendicular to

B_0. The applied radiofrequency (RF) should resonate with the ω_L of the nuclei in order to flip the nuclear spins. Once the resonance phenomenon takes place, the relaxation time and the way in which the nuclei consume the energy can give a lot of information regarding a variety of dynamic processes.

The resonance frequency depends on three parameters:

1. The type of the nucleus (^{1}H, ^{13}C, ^{25}Mg, ^{23}Na etc) that determines the nuclear magnetic dipole moment (μ) and thus the gyromagnetic ratio (γ).

2. The chemical environment close to the nucleus. Nuclei, in samples of any form, are surrounded by the electrons of the host material. When the NMR sample is in a strong magnetic field, the electrons' orbit generate a small magnetic field that opposes to the external B_0. The more the electrons surround the nucleus the more the opposing magnetic field to B_0 increases, thus the shielding that the nucleus experiences intensifies. As a consequence the nucleus "feels" a lower B_0 and a lower RF is needed to achieve the resonance phenomenon. This is known as the Nuclear Shielding phenomenon. If the electron density around the nucleus decreases the latter experiences higher B_0 and as a result a higher RF is necessary for reaching the resonance. This is called Nuclear Deshielding.

3. The magnetic field at the measurement region. Its homogeneity should always be high otherwise the resonance frequency varies depending on the spatial location of the nucleus. This parameter sets the basis of the Magnetic Resonance Imaging (MRI) where gradient fields are used and the Larmor frequency of the nuclei (e.g. ^{1}H, ^{129}Xe) vary as a function of the position [61, 62].

5.2 The NMR spectrometer

A diagram of a typical NMR spectrometer diagram is shown in Fig. 5.3 that consists of the following parts:

- A superconducting magnet, a permanent magnet or an electromagnet that provides a stable and homogeneous magnetic field.

- A probe for the liquid or solid state sample. The probe keeps the samples in the most homogeneous and strongest part of the magnetic field.
- A RF coil surrounding the probe, for inducing the RF pulses.
- A high-power radiofrequency (RF) transmitter.
- A sensitive RF receiver that amplifies the NMR signals.
- An analog-to-digital converter (ADC) that converts the NMR signals into a form suitable for storing in the computer.
- A pulse programmer for precise pulses and delays.
- A computer to control the hardware and process the NMR signals and spectra.

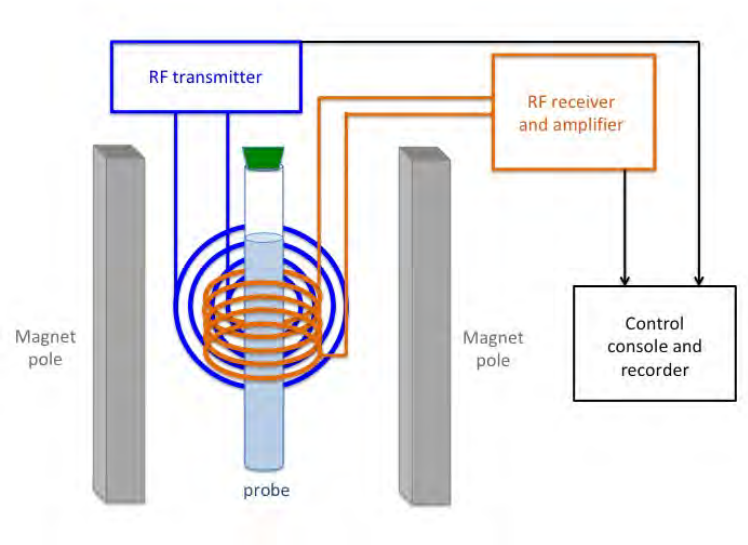

FIGURE 5.3: Schematic representation of a NMR spectrometer.

5.3 NMR spectroscopy: Pulsed NMR and Fourier Transform (FT)

To better describe the Fourier Transform (FT) and the Pulsed NMR (pNMR) one should picture the nuclear spins aligned with or against the B_0 as shown in Fig. 5.4 (a). The nuclear spins in the different energy levels precess around the B_0 z-axis

with the Larmor frequency. The NMR samples consist of a number of nuclei and the signal is the result of a combination of the individual magnetic moments μ of all the nuclei, the net magnetisation M_o=(N_{upper}-N_{lower})μ [63] (Fig. 5.4 (b)).

At thermal equilibrium the net magnetisation is aligned with the B_0 z-axis, hence $M_z = M_0$ is maximum and M_{xy}=0.

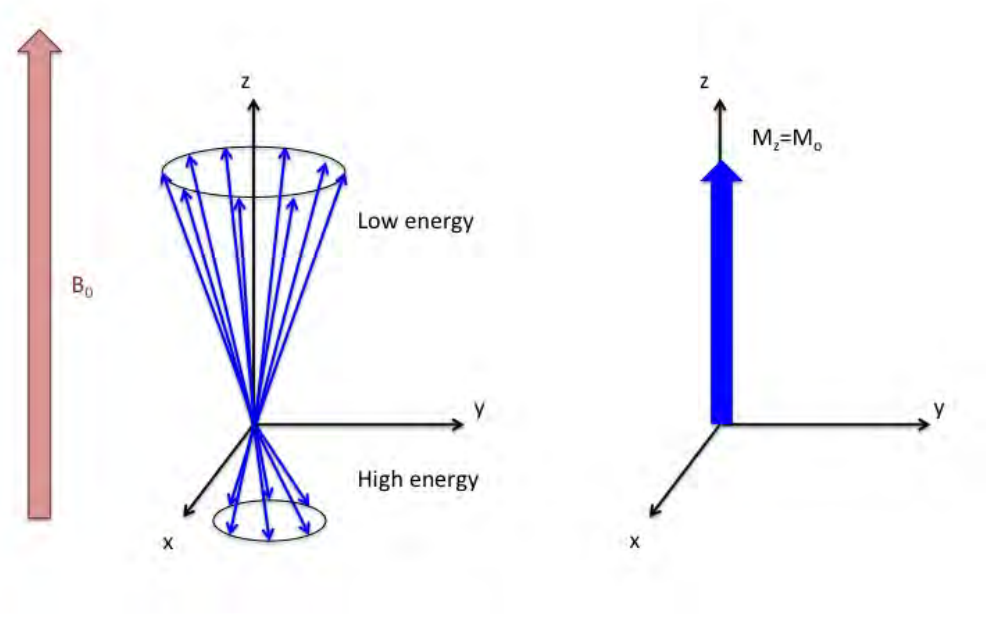

FIGURE 5.4: Nuclear spin alignment on the left and net Magnetisation on the right, *Mz*, when an ensemble of nuclei is in a B_0 magnetic field.

The overall net M_o initially lies along the z-axis. When a short and strong RF pulse, B_{rf}, is applied perpendicularly to the external magnetic field B_0, e.g along the x-axis, it interacts individually with every nuclear spin and causes a tilt of M_o towards the xy plane. The tilt angle of M_o depends on the time after the RF pulse (θ=γB_{rf}t). The magnetisation along the z, y and x axis at any time is given by Eq. 5.6.

$$\begin{aligned} M_x &= 0 \\ M_y &= M_o sin\theta \\ M_z &= M_o cos\theta \end{aligned} \tag{5.6}$$

In the quantum mechanical description, the difference between the two nuclear spin energy levels for the two different pulses is shown in Fig. 5.5. The effect of a $\pi/2$ pulse is the equalisation of the populations in the two energy states, while when a π pulse is applied we observe an inversion of populations.

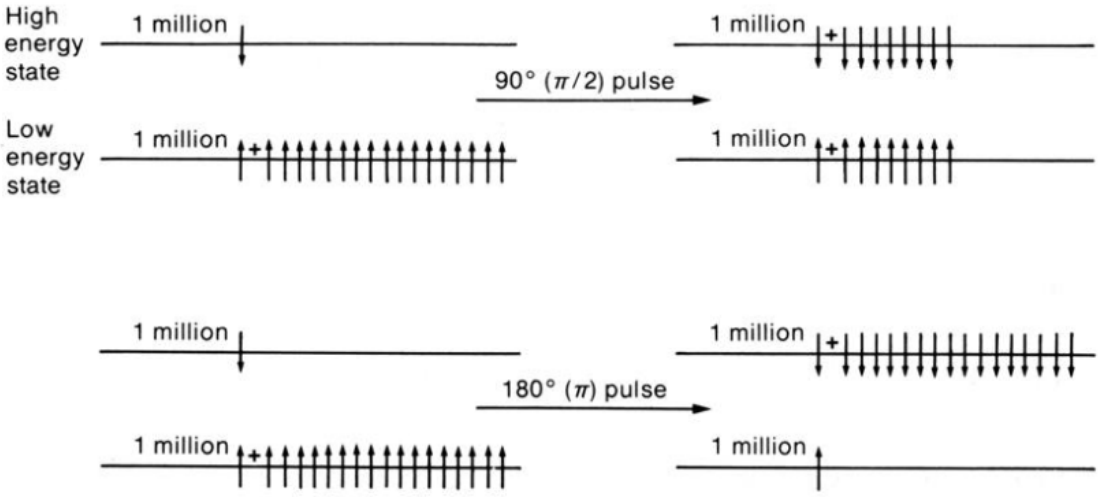

FIGURE 5.5: Effects of 90° and 180° RF pulses on the energy level populations in a sample of two million protons in a B_0=2.35 T [18]

.

Once the B_{rf} is turned off, the nuclear spins relax back to the z-axis. There are two magnetisation relaxation mechanisms, the T_1 spin-lattice or longitudinal relaxation along the z-axis and T_2 the spin-spin de-phasing of the magnetic moments away from the principal rotating x-axis, known as transverse relaxation along the x-y plane.

The receiver coil surrounding the sample, orange coil in Fig. 5.3, records the change in M_o generating a Free Induction Decay (FID). The FID after a 90° pulse is shown in Fig. 5.6 that diminishes over time.

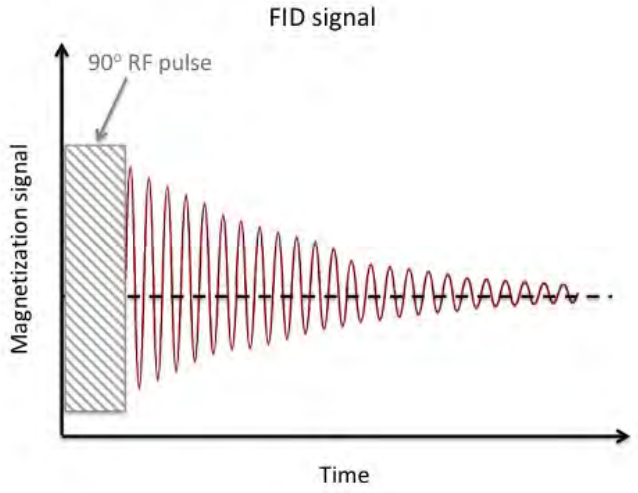

FIGURE 5.6: A typical Free Induction Decay (FID) signal.

The above description of the Pulsed NMR (pNMR) approach would be sufficient if only one frequency contributed to the signal. Most of the NMR experiments use a broad band width of frequencies that excite all the nuclei in a sample. The FID is the overlapping resonance signal generated by the precession of spins of all the excited nuclei in the xy plane and the resulting complex waveform is a time-dependent, f(t). For turning the FID signal into an actual NMR spectrum one has to Fourier Transform it (Fig. 5.7). The FT is given by Eq. 5.7.

$$f(\omega) = \int_{-\infty}^{\infty} f(t) \mathrm{e}^{-i\omega t} \, \mathrm{d}t \tag{5.7}$$

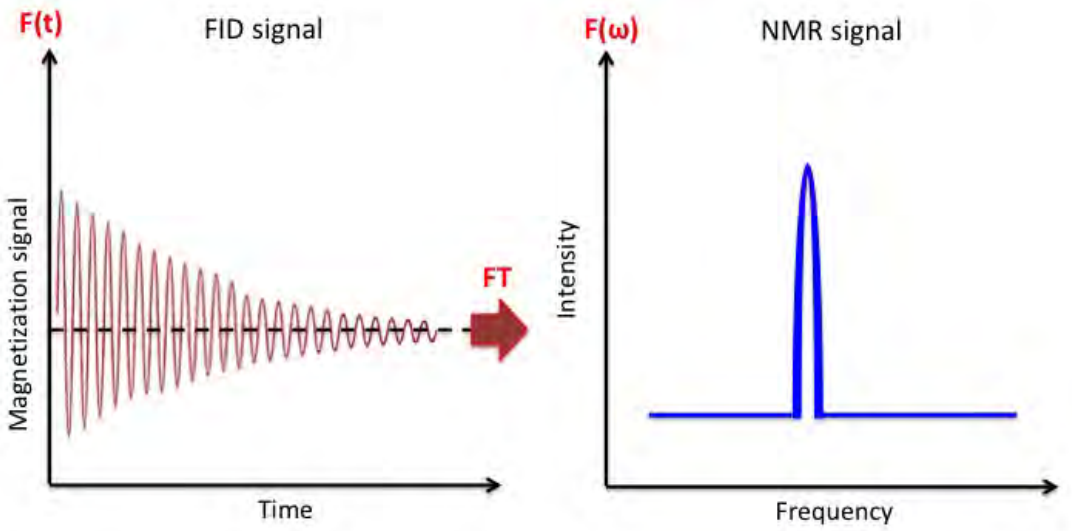

FIGURE 5.7: The Fourier Transformation (FT) of a FID.

The more quickly the FID signal decays, the broader the FT NMR signal becomes, since the FT treats less signal and the uncertainty of the true frequency is higher. In the case there are two or more frequencies overlapping, this appears as "beats" in the FID and only the FT will reveal which frequencies are present in the NMR signal.

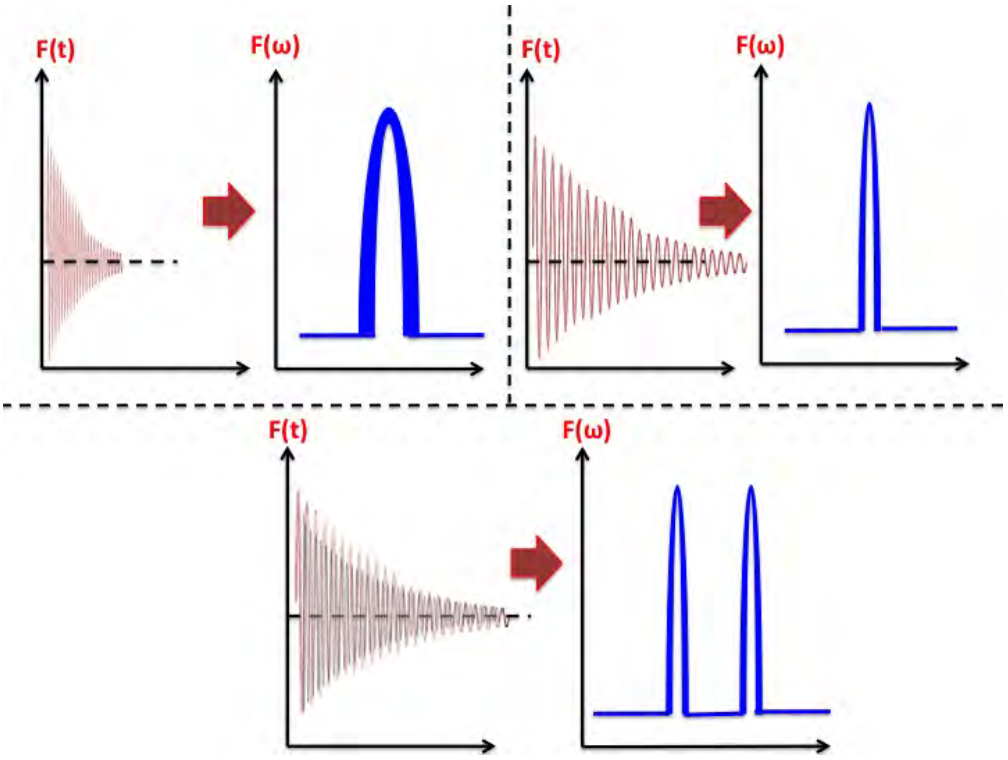

FIGURE 5.8: Effect of FIDs on FT NMR spectra.

5.4 The NMR relaxation mechanisms

In pulsed NMR, one can send different RF pulses. When a 90° RF pulse is applied, $M_z(o)(z)$ is rotated to the transverse x-y plane, and this magnetization is called transverse magnetization. Right after the 90° pulse $M_z(o)$ is zero while when the RF pulse is off the net M_o returns back to equilibrium along the z-axis. How fast the nuclear spins regain the Boltzmann equilibrium is a measure of the coupling between the excited nuclei with their neighbouring molecules (the lattice) is characterised by the time constant T_1, known as the spin-lattice or longitudinal relaxation time [64, 65]. The evolution of magnetisation with T_1 is given analytically in Eq. 5.8.

$$M_z(t) = M_z^{eq} + (M_z(o) - M_z^{eq})\mathrm{e}^{-t/T_1} \tag{5.8}$$

where $M_z(t)$ is the magnetisation as a function of time and M_z^{eq} the magnetisation at thermal equilibrium and $M_z(o)$ the longitudinal magnetisation at the start of the RF pulse.

T_1 is affected by the chemical environment and the applied magnetic field, B_0, Fig. 5.9. The Larmor frequency, ω_L, is directly proportional to B_0, as shown in Eq. 5.3. Changing B_0 will change the T_1 relaxation.

The nuclear spin flips are more efficient when the fluctuating magnetic field due to interaction with the neighbouring molecules are at or close to the Larmor frequency. This fluctuating magnetic field happens due to the molecular tumbling in the lattice. Materials of different forms and structures have different molecular tumbling that is described by the correlation time, τ_c.

As shown on the left side of Fig. 5.9, for nuclei in very mobile media with short τ_c (blue line) if the magnetic field is increased, the ω_L will increase but the fraction of molecules tumbling at the new frequency will not be affected considerably. However, for nuclei in media with slow or medium mobility, with medium to long ω_L (black and orange lines), shifting the ω_L to higher values will severely decrease the percentage of molecules resonating with the Larmor frequency. As a result the T_1 will decrease.

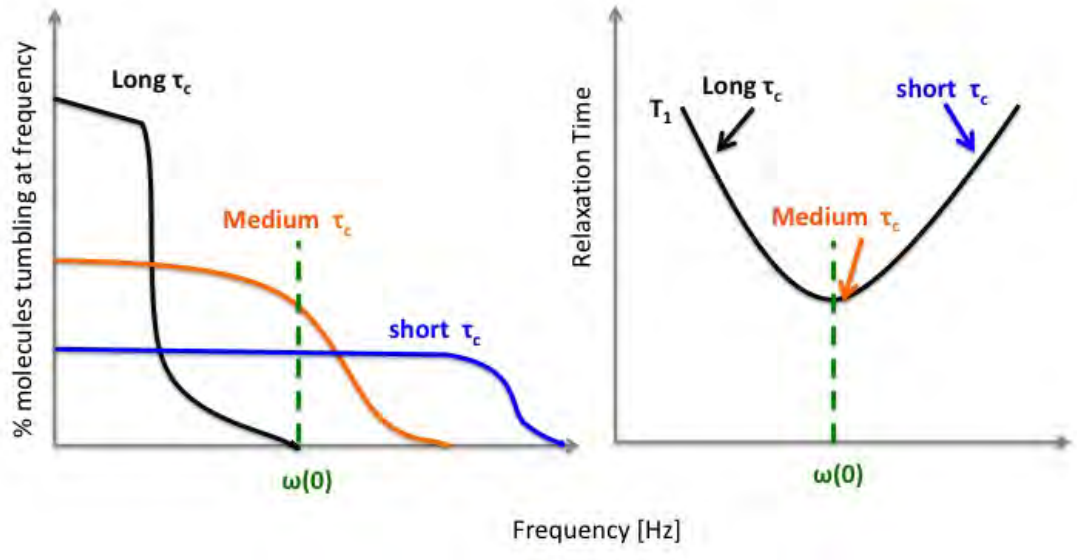

FIGURE 5.9: Schematic representation of T_1 longitudinal relaxation's dependence on the resonance frequency.

T_1 defines the delay time (recycle delay) between the applied pulses. The nuclear spin system must be allowed to relax back to equilibrium before the next pulse is applied and this time period is determined as d_1=10 T_1 [66].

5.4.1 The experimental method of determining T_1: The Inversion Recovery (IR)

A standard method for determining the T_1 is the Inversion Recovery (IR) technique, introduced and applied for the first time from Vold, Waugh, Klein and Phelps in 1968 [67]. This is the selected method of the current work for quantifying the T_1 relaxation of ^{25}Mg and ^{23}Na in different samples.

A typical IR pulse sequence starts with a 180° pulse that inverts the net magnetisation to the negative maximum value to the -z axis (-M_z). After the 180° pulse, the net magnetisation is allowed to relax until a second rf pulse of 90° is applied and tips the magnetisation from z to the x-y plane. At the end of the second RF pulse the FID can be acquired. The time between the two pulses is called the Inversion Time (TI). The amplitude and the sign of the NMR peaks in the IR spectrum depend on the longitudinal relaxation rate of each spin. The peak intensity as a function of TI is proportional to the value of M_z just before the second pulse. T_1 can be determined by fitting the graph shown in Fig. 5.10 [66]

In addition to the longitudinal magnetisation relaxation another relaxation process is present in the systems, namely the transverse spin-spin relaxation T_2. When a collection of nuclei in thermal equilibrium with $M_o(z)$ experiences a 90° pulse, M_o will flip to the xy-plane. Once in the xy-plane, the spins will start de-phasing since the magnetic moments of the nuclei interact with each other and the M_o will go back to the thermal equilibrium with the transverse relaxation time given by Eq. 5.9.

$$M_{xy}(t) = M_{xy}(0)e^{-t/T_2} \tag{5.9}$$

T_2 does not depend on the B_0. Fast T_2 leads to broad NMR peaks. $T_2 \sim 1\Delta v_{1/2}$.

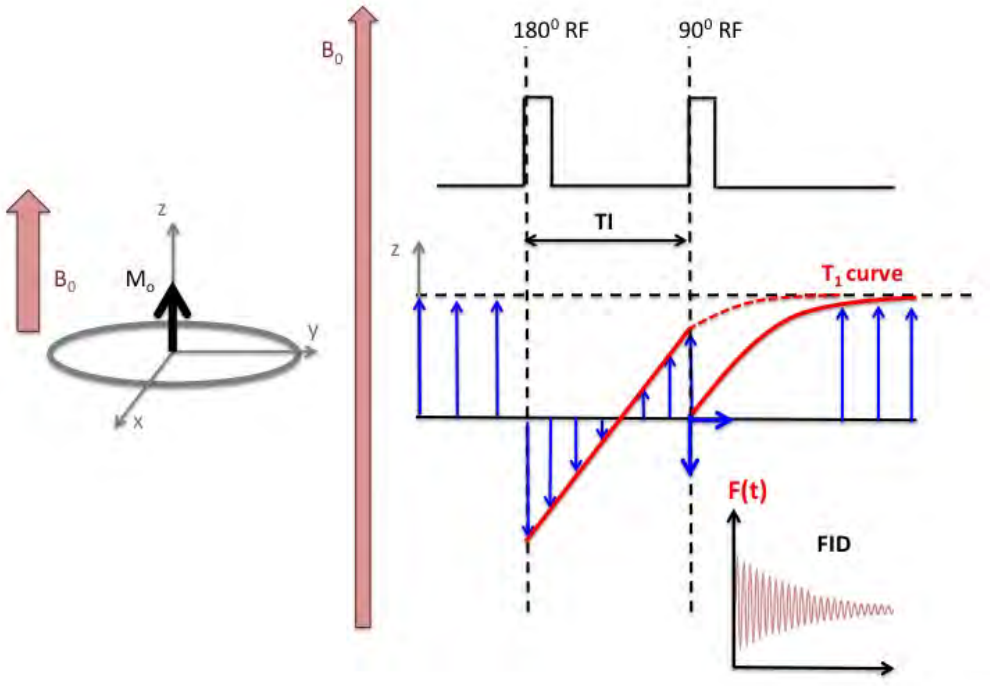

FIGURE 5.10: The $M_o(z)$ recovery following an inversion pulse. Each blue arrow corresponds to the intensity of the NMR signal.

5.5 Important NMR spectral parameters

The most important NMR spectral parameters for analysing the chemical systems of this work, are illustrated in a 1D NMR spectrum in Fig. 5.11.

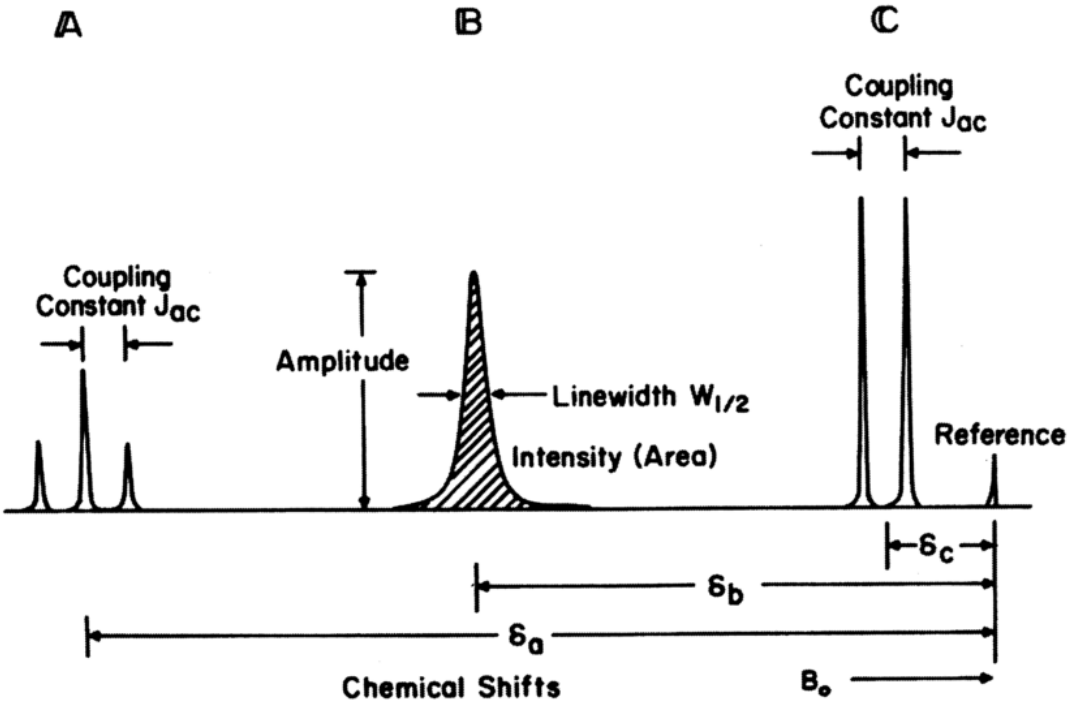

FIGURE 5.11: Typical NMR spectral parameters [19].

Chemical Shift

Nuclei of different elements in a given B_0 will resonate with different RF energies due to their different γ ratios, Eq. 5.3. However, also nuclei of the same isotope can resonate at slightly different frequencies, as a result of the shielding phenomenon due to differences in the local electronic environment. The induced magnetic fields are typically a million times smaller than B_o, meaning that if the Larmor frequency is in the order of MHz, the difference between the resonance frequencies of two different nuclei of the same isotope will be several Hz. For convenience we use a reference signal from a known compound to determine the relative positions of the different peaks. The difference between the reference signal (ν_{ref}) and the signal of interest (ν_{sample}) is called chemical shift, given by Eq. 5.10. It is expressed in terms of parts per million (ppm), a dimensionless quantity, and not in Hz, in order to decouple the chemical shift from the magnetic field strength.

$$\delta = \frac{\nu_{\text{sample}} - \nu_{\text{ref}}}{\nu_{\text{ref}}} 10^6 [ppm] \tag{5.10}$$

Here are some relevant typical ranges in chemical shifts for signals coming from biologically relevant nuclei:

^{1}H, 20 ppm; ^{13}C, 250 ppm; ^{15}N, 900 ppm; ^{23}Na, 70 ppm; ^{25}Mg, 70 ppm; ^{31}P, 430 ppm [68].

Linewidth

The NMR signal's linewidth, the Full Width of Half Maximum (FWHM), is at least as wide as specified by the Heisenberg Uncertainty Principle broadening due to inherent lifetime of spin states and is given by Eq. 5.11

$$FWHM = \frac{1}{\pi T_1} \tag{5.11}$$

and is related with the Heisenberg Uncertainty Principle broadening due to lifetime of spin coherence - gain and loss of magnetization in the x,y direction Eq. 5.12

$$FWHM = \frac{1}{\pi T_2} \tag{5.12}$$

Small T_2 leads to broad signals (big values of FWHM) while big T_2 to sharper lines.

Peak Intensity

The signal intensity is determined by the area of the peak and not its amplitude and is proportional to the number of magnetically equivalent nuclei contributing to the NMR signal. To be correctly determined, the delay time between the excitation and the FID recordings should be $\geq 4T_1$. If the concentration of the nuclei is known for a particular peak, it can be used as a standard.

Spin-Spin splitting: *J* coupling

Any nucleus with a magnetic moment is likely to interact with other nuclei in a sample. This interaction may lead to a mutual splitting of the NMR signal of each nucleus into a multiplet. Any signal can be split in $2nI+1$ components, where I is the nuclear spin and n is the number of the neighbouring nuclei interacting with a chosen nucleus.

There are two types of magnetic interactions between nuclei with a non-zero spin: the dipole-dipole coupling (D) and the scalar coupling (J). The D coupling makes difficult to get high-resolution NMR spectra in solid state NMR and in very viscous samples. NMR spectra in liquid crystals (where molecules are partially oriented and the dipolar coupling is only partially averaged) are very complex as well. In

liquid samples, due to the random motion of the molecules, the dipolar coupling is completely averaged and no direct effects are seen. Therefore, in the current work only the spin-spin J coupling was considered. The J coupling is a through-bond interaction. The spin of a nucleus polarises the spins of the surrounding electrons, which in turn polarise their neighbouring nuclear spins. The J coupling, always reported in Hz, is independent of the B_0 and is mutual for the different nuclei. The coupling effect is usually transmitted through the bonding electrons, as a result the magnitude of J falls off rapidly as the number of intervening bonds increases. Coupling over one (1J), two (2J) and three (3J) bonds usually dominates the fine structure of NMR spectra, but coupling across four (4J) and five (5J) bonds is also seen, especially through π bonds (double and triple bonds, aromatic carbons).

In Fig. 5.12 is illustrated the 1H NMR spectrum of 1,1,2-trichloroethane where the spin-spin slitting is enlarged in order to explain the J coupling phenomenon. The two H_a protons give rise to a peak at 3.96 ppm that is split into two subpeaks of equal amplitude and intensity, referred as a doublet. The Hb signal at 5.76 ppm is a triplet. The middle peak is higher than the two outside ones and its intensity is twice that of each of the lateral peaks [20].

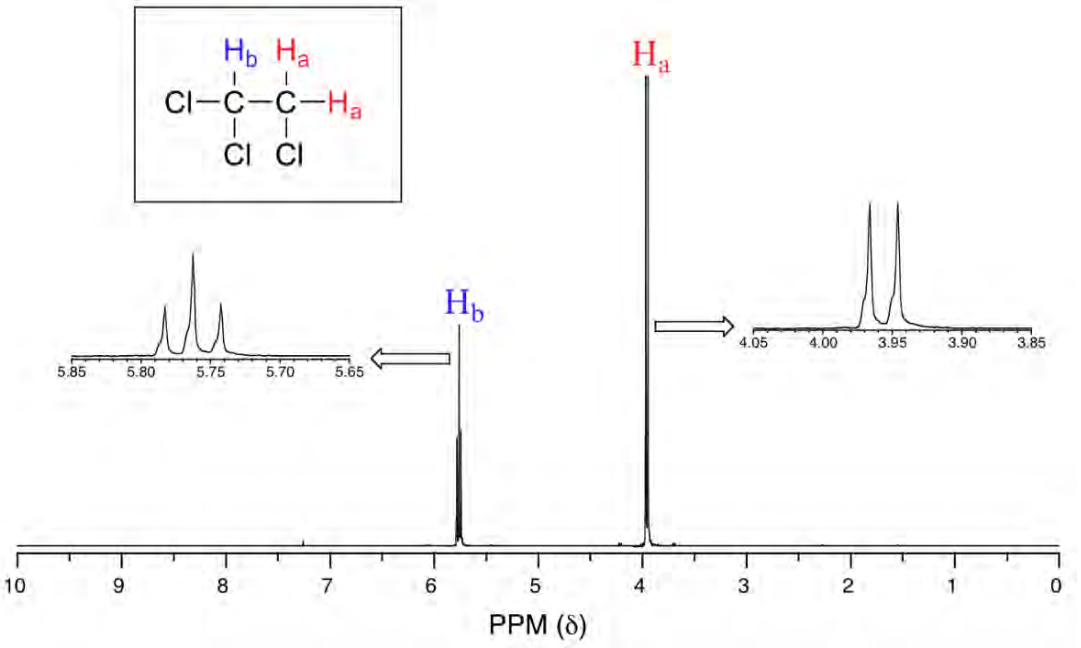

FIGURE 5.12: 1H NMR spectrum of 1,1,2-trichloroethane with enlargement of the individual signals due to J coupling [20].

To simplify the NMR spectrum and to improve the S/N ratio, the decoupling technique is often applied, especially with ^{13}C and ^{15}N NMR. The decoupling

causes a collapse of the multiplets into singlets [69].

5.6 Limitations of the NMR technique

Even though NMR is a very powerful technique it has certain limitations concerning the sensitivity and the detection efficiency of the NMR signal. These will be addressed in the present section.

Sensitivity and spin population distribution

The energy difference, ΔE Eq. 5.5, between the nuclear spin states depends on the strength of the external magnetic field and is always very small. For visualising the impact of B_0 increase on the population of nuclear spin states, the distribution of a small number (around two millions) of nuclei is presented in Fig. 5.13 for different B_0 strenghts. For a very high B0 of 18.8 T at thermal equilibrium the population ratio will be 0.999872. In other words for every 1,000,000 nuclei in the higher energy state there are 1,000,128 nuclei in the lower energy state. This small excess number of nuclei in the lower energy state is what creates the NMR signal and is the biggest limitation of NMR signalling in biological systems. A stronger magnetic field would increase the population ratio and would improve slightly the sensitivity but it should also be noted that other factors are important. For example,for macromolecules or small molecules that interact with macromolecules, increasing the magnetic field often increases the T_1 that can adversely affect the sensitivity.

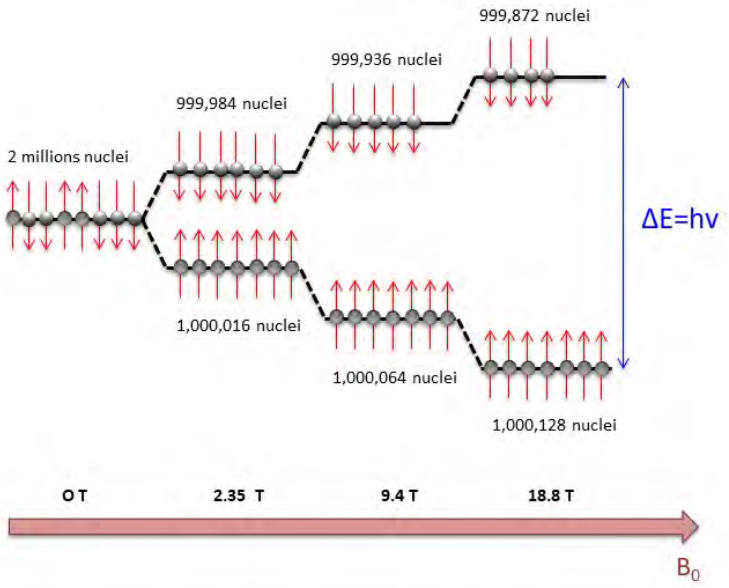

FIGURE 5.13: Separation of nuclear spin energy levels and relative populations as a function of B_0.

Sensitivity and gyromagnetic ratio

The sensitivity, also called receptivity R^x, is the measure of how easy one can acquire an NMR signal of a particular nuclide. The sensitivity of a nuclide X is given by Eq. 5.13

$$R^X = A * |\gamma^3| * I(I+1) \tag{5.13}$$

where A is the natural abundance, γ the gyromagnetic ratio and I the nuclear spin. The larger the γ and the natural abundance, the stronger the NMR signal is. This explains why for ^{13}C NMR more scans and more acquisition time is needed compared to ^{1}H NMR for getting the same quality of signals.

Every nucleus with $I \geq 1/2$ contributing to a NMR signal has a magnetic moment that is proportional to the gyromagnetic ratio (Eq. 5.1), which is characteristic for every nucleus.

Table 5.1 shows the most important NMR properties of selected biologically interested nuclei. The relative sensitivities of the nuclei are compared to ^{1}H NMR.

TABLE 5.1: NMR related properties of biologically relevant nuclei [30–32]

Isotope	Natural abundance (%)	I	Frequency relative to ^{1}H=100 (MHz)	Receptivity (R^X) related to ^{1}H=1.00	Gyromagnetic ratio γ (10^7 rad/T*s)	μ (μ_N) [70]	Q (mb) [70]	Linewidth factor (fm^4)
^{1}H	99.988	1/2	1	100	26.752	2.793	-	-
^{6}Li	7.59	1	14.72	6.45×10^{-4}	3.94	1.163	-0.808	0.033
^{7}Li	92.4	3/2	38.86	0.271	10.40	4.204	-40.1	21
^{13}C	1.1	1/2	25.15	1.7×10^{-4}	6.73	0.702	-	-
^{14}N	99.63	1	7.23	1.1×10^{-3}	1.93	0.404	0.020	21
^{15}N	0.37	1/2	10.14	3.85×10^{-6}	-2.71	0.283	-	-
^{23}Na	100	3/2	26.4519	0.0927	7.08085	2.86298	104	140
^{25}Mg	10.0	5/2	6.1216	2.68×10^{-4}	-1.63887	-1.0122	199.4	130
^{39}K	93.258	3/2	4.6664	4.76×10^{-4}	1.25006	0.50543	146.6	69
^{40}K	0.012	4	5.8020	6.12×10^{-7}	-1.55428	-1.4513	-73	5.2
^{41}K	6.73	3/2	2.5613	5.68×10^{-6}	0.68607	0.27739	71.1	67
^{43}Ca	0.135	7/2	6.7300	6.68×10^{-6}	-1.8030	-1.4940	-4.08	2.3
^{63}Cu	69.7	3/2	26.5155	0.0650	7.118	2.2236	-21.7	650
^{65}Cu	30.83	3/2	28.4037	0.0354	7.6053	2.3817	19.5	550
^{67}Zn	4.1	5/2	6.2568	1.18×10^{-4}	1.6768	0.8755	0.15	72

The linewidth factor, given by Eq. 5.14, is an indication of the amount of broadening of the NMR signal for I>1/2 nuclei. It is related to the nuclear spin, I, and the quadrupole moment, Q. The linewidth factor is zero for non-quadrupolar nuclei, I=1/2, as shown in Table 5.1.

$$LF = \frac{Q^2 * (2I + 3)}{I^2 * (2I - 1)} \tag{5.14}$$

Quadrupole coupling

Quadrupolar nuclei with I >1/2 interact strongly with the electric field gradient (EFG) generated by the surrounding electron clouds from the neighbouring nuclei leading to a faster T_1 relaxation. The quadrupolar coupling is predominantly an intramolecular interaction that involves both a nuclear property, Q, and a molecular property of the sample (the EFG). As a result, the nuclear quadrupole moments listed in Table 5.1 do not accurately reflect the typical magnitudes of the electric quadrupole interaction.

Metal nuclei with large quadrupole moments, such as ^{23}Na and ^{25}Mg, may have small quadrupole couplings if the nuclear environment is symmetric meaning that the local EFG is small.

5.7 Techniques to overcome the NMR limitations

The low sensitivity is one of the most severe limitations of NMR. Hense, it often complicates the analysis of spectra that belong to complex biomolecules in solutions. A number of key advances in NMR over the last decades led to remarkable improvements in sensitivity and the most common methods to increase the signal to noise (S/N) ratio for a given mass of sample in bio-molecular applications are :

1. Increase B_o
2. Average the signal
3. Increase the saturation of the sample
4. Reduce the temperature of the sample at the detection system
5. Reduce the volume in which the NMR signal is observed, to minimise the magnetic field fluctuations

(i) As the energy differences between the nuclear spin orientations is proportional to B_o, increasing its strength increases the absorption and the population difference between the two spin energy states an. So, the first way to improve the S/N would simply be to rise the strength of B_o (S/N $\sim {B_o}^{3/2}$) [71] to a current commercial maximum of 23.5 T (1000 MHz. Unfortunately, this is in many cases a prohibitively expensive way to improve the S/N ratio, as magnet costs increase rapidly with field strength increase.

(ii) S/N can be improved by averaging together many individual NMR spectra. But, while the signal increases as a function of the numbers of transients (the number of executions of the pulse sequence), n, the noise increases as a function of $\sqrt{n}$, meaning that the S/N increases as n/$\sqrt{n}$ or $\sqrt{n}$. A two-fold rise in S/N comes at a four-fold cost in time, which can soon become prohibitively long.

(iii) The full saturation of a sample is the equalisation of populations of nuclear spins in the up and down states. This can be achieved by applying a 90° rf pulse. After the saturation, the emitted rf photons are detected from the flip of the spins relaxing back to the ground state, restoring the original population difference between the two energy levels. The drawback of this technique is the long collection time needed for full saturation and full relaxation. An optimal balance between minimising run time and maximising the S/N ratio is often aimed, by applying pulses less than 90° allowing only partial relaxation.

(iv)There are two different ways in which one can reduce the temperature and increase the S/N. Either the temperature of the sample can be decreased [72], which leads to the increase of the M_o, although this is limited in liquid NMR by the temperature that the solvent freezes. Or one lowers the temperature of the equipment. The later can be achieved by using a cryoprobe that was first described by Styles et al [73] and has been used by several groups for structural biology studies [74, 75]. In such a case, NMR S/N ratios can be significantly improved by cooling the NMR RF detector and the preamplifier down to 20 K with liquid He. The resistance of the coil is significantly reduced and the thermal noise is decreased, leading to a corresponding increase in the S/N per scan, or for the same S/N a 16-fold reduction in acquisition time when compared to a normal probe.

(v) It is easier to have a homogeneous field over a small volume and acquiring sharp NMR peaks. That is why most commercial magnets have narrow bores of a few centimetres. For biological applications where sub-milligram samples need to be investigated, when the sample quantities are limited for biological reasons, microprobe NMR with samples of 1-200 nanomole range combined with microcoils can give a S/N ratio equal to the one acquired with cryoprobes [76, 77].

If all the parameters described are optimised and the sensitivity still needs to be enhanced, state-of-the-art techniques that shift nuclear spin populations away from the thermal equilibrium (hyperpolarisation) should be used. When a group of nuclei is hyperpolarised, the high energy nuclear level has much fewer spins than in thermal equilibrium. A representation of the hyperpolarisation concept is illustrated in Fig. 5.14.

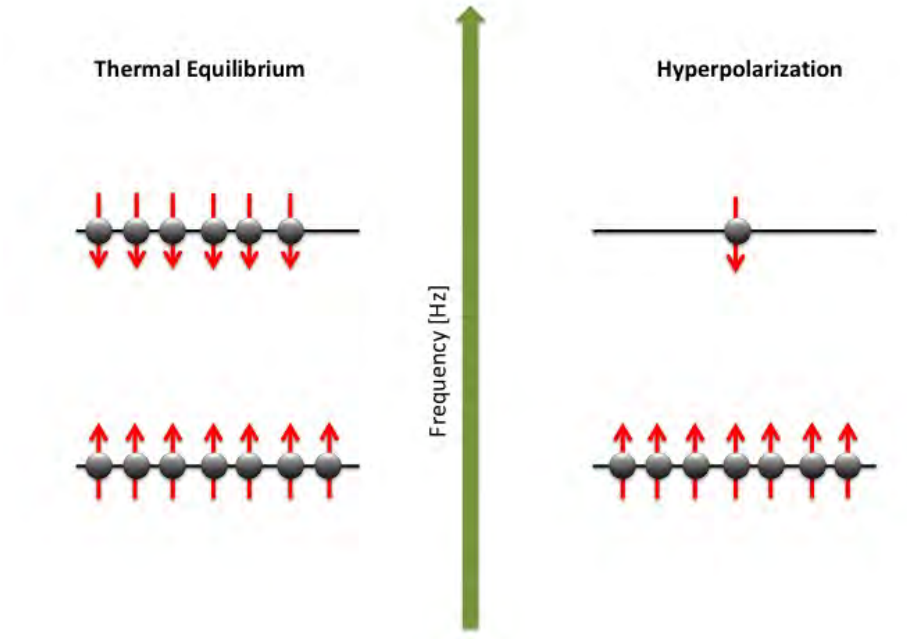

FIGURE 5.14: Spin distribution in the case of thermal equilibrium (left) and hyperpolarisation (right).

Several strategies for hyperpolarisation have been applied by many research groups

- The Dynamic Nuclear Polarization (DNP) that was first performed at low temperatures ($\sim 1K$) with low magnetic fields for solid state samples (metals) and is used to enhance the signal in solid state NMR [78, 79]. A new study [80] using DNP at 3 T at room temperature showed that a million-fold enhancement of liquid NMR signal can be achieved.

- The approach of Dissolution Dynamic Nuclear Polarization (DDNP) [81] is used for hyperpoplarizing water soluble biologically relevant samples. The enhancement of the NMR signal compared to conventional liquid NMR is 10,000 times at room temperature.

- The nuclear polarization can be observed in asymmetry of γ decay of radioactive nuclei. The approach has been already used in NMR [82] and has very recently been applied to Magnetic Resonance Imaging (MRI), combining the use of radioactive tracers emitting γ photons and using lasers for the hyperpolarization instead of strong B_0 [83].

- The technique of optical pumping, proposed by [84] for alkali metals, is a method of hyperpolarizing the ground or excited states of atoms or ions by absorption of circularly polarized light. It is also the method used in this work in combination with β-decay assymmetry since it allows for high degrees of polarization (theoretically even up to 100%). More details and the physics background of the technique will be given in Chapter 6.

The β detected NMR that has been applied successfully over the years in nuclear physics and solid state physics, has been very recently applied for the first time in liquid samples. The first liquid β NMR studies were initiated at ISOLDE/CERN using a low energy ^{31}Mg ion beam that was implanted in vacuum resistant Ionic Liquids (ILs) at room temperature [5]. Later, a high energy spin polarised ^{12}N beam was implanted in water at the National Institute of Radiological Sciences (NIRS) using the Heavy Ion Accelerator in Chiba (HIMAC) [85]. A more recent publications with direct observation of Mg^{2+} complexes in ionic liquid solutions by ^{31}Mg β-NMR spectroscopy can be found here [86]. These feasibility tests prove that β-decaying isotopes that are externally polarized and then implanted into the liquid samples retain their polarization and can give NMR signals that show a billion-fold (10^9) enhancement in the NMR sensitivity. In addition this technique opens the possibility to apply it to several elements across the periodic table that until recently were very difficult to be examined with conventional NMR, giving very poor to none resonances. The β-detected NMR technique is the core technique used in the current work and is going to be extensively discussed in Chapter 6.

Chapter 6

β-detected Nuclear Magnetic Resonance (β-NMR)

The initiative for establishing the β-NMR technique in liquids was triggered by the fact that conventional NMR is very limited in sensitivity. This makes difficult to apply NMR when small quantities of biological samples are available and is limited it to very abundant nuclei, those with high γ ratios such as ^{1}H and ^{13}C.

For isotopes that undergo a β-decay with half-lifes ($T_{1/2}$) of several ms to several s, a suitable way to observe the atomic and nuclear resonances is through the detection of the β-asymmetry when a polarized nuclear ensemble is stopped by a medium, solid or liquid.

The polarisation of an ensemble of nuclei with angular momentum I is defined by Eq. 6.1

$$P_{\mathrm{I}} = \frac{\langle I_{\mathrm{z}} \rangle}{I} = \frac{\sum_{m=-I}^{I} m N_{\mathrm{m}}}{I \sum_{m=-I}^{I} N_{\mathrm{m}}} \tag{6.1}$$

Nuclear spin polarisation with large population differences can be obtained by several methods that were mentioned in the previous section. Furthermore high nuclear polarisation can be achieved by nuclear reactions at selected emerging angles [85], reactions with polarised targets and particles [87, 88] and capture of

polarised thermal neutrons [89]. All these methods are versatile but are restricted only to fragmentation facilities. Another technique is the low-temperature nuclear orientation (LTNO) that has been used in combination with NMR [90, 91] but it cannot be applied to studies with liquids as it requires mK temperatures at the implantation site. Another approach under development is the polarisation via tilted foils that was used for β-NMR studies in measuring the nuclear magnetic moments [92, 93]. Finally, a widely used technique for achieving hyperpolarisation is the optical pumping through interactions with circularly polarised laser light. The latter method was applied in our ^{26,28}Na β-decay asymmetry and ^{26,27,28}Na β-NMR experiments, since it is suitable to be used for low-energy beams (30-60 keV) with a small energy spread, which are available at the ISOLDE facility at CERN. Optical pumping allows to obtain high degrees of polarisation ($\sim$ 60% for ^{28}Na) and gives the possibility to study the β-decay asymmetry, as well as the nuclear magnetic resonance, both interesting for our research.

Applying the optical pumping repetition technique, firstly we polarise the total atomic angular momenta F by inducing transitions between the m_F magnetic sublevels of the ground-state and the excited-state hyperfine multiplets, as shown in Fig. 6.1 for ^{28}Na atoms used in our first experiments.

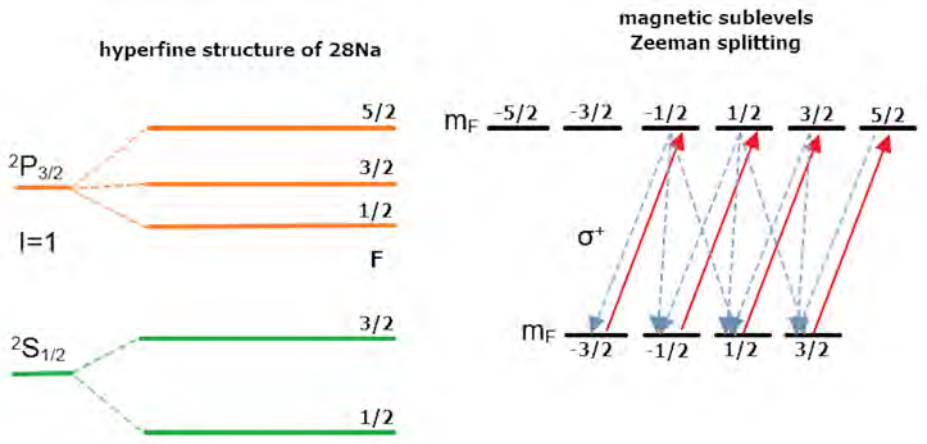

FIGURE 6.1: Optical pumping with σ^+ light for the $|\ F = 3/2\rangle \rightarrow |\ F' = 5/2\rangle$ component of the D2 line of ^{28}Na (I=1). Red lines correspond to excitations and the blue dashed lines show the decays to the ground-state.

The same atom/ion interacts with many photons, which subsequently transfer their angular momentum and as a result after many cycles the atom/ion is in the ground-state sublevel with maximum m_F if σ^+ light polarisation, or in the minimum m_F if σ^- polarisation is used. The mechanism of spin polarisation is based on

the selection rules for atomic dipole transitions. For σ^+ light only excitations with Δm_F=+1 while for σ^- only Δm_F=-1 are allowed towards higher m_F. The decays follow the rules Δm_F=-1, 0, +1. The theoretical 100% polarisation is lowered by the hyperfine pumping, in which the exited state decays to other ground-states F level, which cannot be excited by the same laser frequency.

Due to the hyperfine interaction between the atomic (electron) spin and the nuclear spin, polarisation of the atomic spins results also in the polarisation of the nuclear spins. After the atomic polarisation is achieved the nuclear and atomic spins are adiabatically decoupled when an increasingly strong magnetic field is applied, Fig. 6.2).

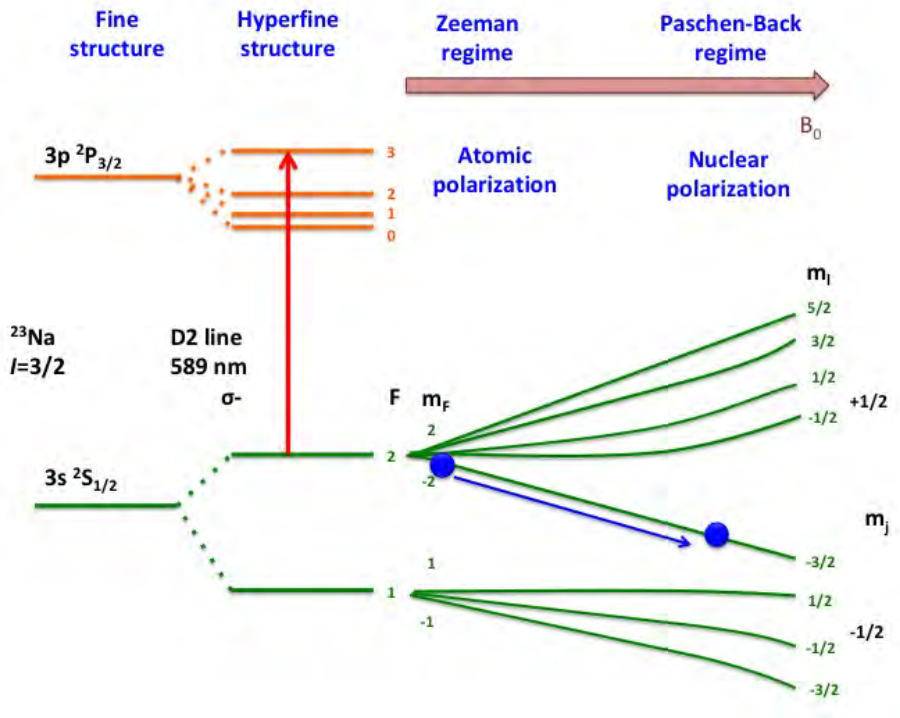

FIGURE 6.2: Adiabatic decoupling of the nuclear and atomic spins in a magnetic field on the example of ^{23}Na (I=3/2, μ>0) and F=2, m_F=-2 state which leads to m_I=-3/2.

Once the adiabatic decoupling of the nuclear and atomic spins is achieved, the emission asymmetry of β particles that are emitted from the polarised nuclei can be observed. Due to parity non-conservation, the β particles that are emitted from polarised nuclei, are emitted mainly along the nuclear spin [94]. The correlation between the angular distribution of the emitted β particles and the nuclear polarisation is given by Eq. 6.2

$$W(\theta) = 1 + \alpha \frac{v}{c} P_{\mathrm{I}} \cos\theta \tag{6.2}$$

where α is the nuclear asymmetry parameter (-1, 1) that depends on the initial and final nuclear spin involved in the β-decay process, v is the velocity of the β-particles (v/c is close to 1), $\mathrm{P_I}$ is the ensemble achieved polarisation and θ is the angle between the polarisation P_I and the emission direction of the β particles.

For acquiring an NMR signal the nuclear polarisation has to be destroyed. This can be achieved by applying a rf pulse at the Larmor frequency of the radioactive nuclei, around the stopping lattice. The signal detection is very efficient since it relies on the counting of β particles, Fig. 6.3) [28], which can be performed with around 10% efficiency (resulting from close to 100% detector efficiency and 10-20% detector opening angle) and not in the measurement of the rf absorption while there is a spin flip back to the thermal equilibrium.

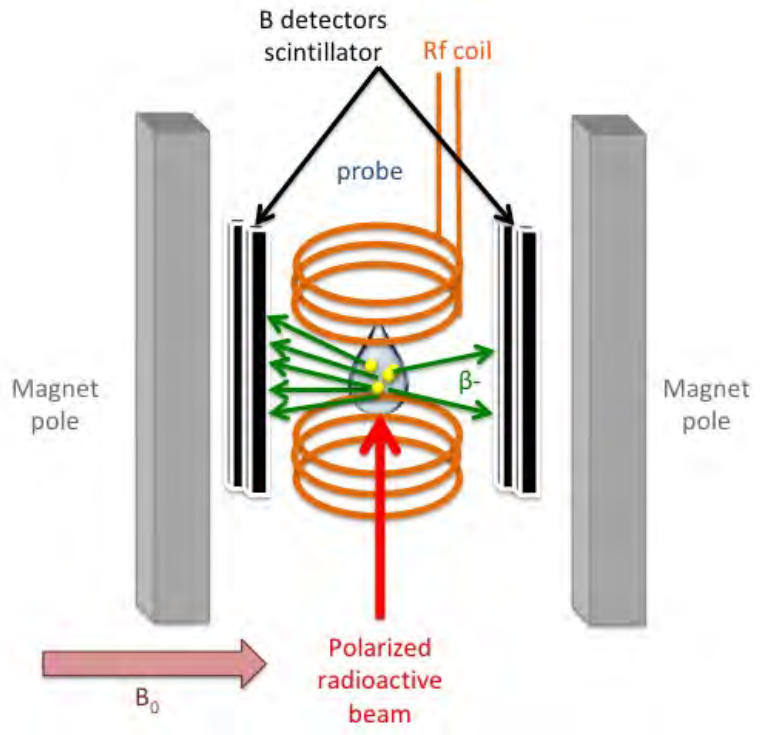

FIGURE 6.3: Principle of signal detection in β-NMR. Anisotropically emitted β particles are detected by two sets of β scintillator detectors.

We calculate the experimental asymmetry of β-particle detection. Eq. 6.3 is the normalised difference between the count rate of β-particles, N_β, recorded by detectors that are placed at angles θ_1 and θ_2.

$$A_{\text{exp}}(\theta_1, \theta_2) = \frac{N_\beta(\theta_1) - N_\beta(\theta_2)}{N_\beta(\theta_1) + N_\beta(\theta_2)} \tag{6.3}$$

The highest achieved experimental asymmetry is reached for detectors placed parallel (θ_1=0°) and antiparallel (θ_2=180°) to the direction of B_0. This is the geometry of detectors chosen for our experiments. The β-detectors can cover a certain solid angle and A can be connected to the polarisation via

$$A_{\text{exp}} = \frac{1}{2}\alpha\frac{v}{c}P_{\text{I}}(1 + \cos\theta) \tag{6.4}$$

Generally, the polarisation in presence of only a static magnetic field decreases with time as e^{-t/T_1}

$$A(t)_{\text{exp}} = A(0)e^{-t/T_1} \tag{6.5}$$

, where A(0) is the maximum asymmetry reached during the optical pumping process, which decreases with *T1* relaxation time. The average asymmetry for a total observation period, T, does not depend only on the longitudinal relaxation but also on the lifetime of the nucleus. For the same host, meaning same *T1*, nuclei with shorter lifetimes will give higher asymmetry at a given time since they emit more β-particles in the beginning of the measurement when the polarisation has little time to relax. For our experiments we neglected the polarisation relaxation in the NaF crystal, since the relaxation in this material is much longer than the $T_{1/2}$ of ^{26,28}Na.

A summary of the main differences between conventional NMR and β-detected NMR are presented In Table 6.1.

TABLE 6.1: β-NMR and conventional NMR properties

Property	**NMR**	**β-NMR**
Probe nuclei	**stable**: ^{1}H, ^{13}C, ^{15}N etc. $\sim 10^{17}$ in the sample	**radioactive**: ^{8}Li, ^{26,27,28}Na, ^{31}Mg etc $\sim 10^{7}$ per resonance
Samples	solids and liquids	solids and liquids with 1st liquid in 2012
Way of polarisation of probes	created **inside the sample** Boltzmann distribution in B_0 magnetic field	created **outside the sample** laser excitation via optical pumping
Achieved polarisation	normally 0.001%	1-100%
Observation of resonances	Change of magnetisation $\ll$100% detection efficiency	change in β-asymmetry Up to 100% efficiency
Type of experiment	off-line	on-line

The main differences between the conventional NMR and the β-detected NMR are lying on the way of polarising the spins (B_0 for NMR vs laser polarisation for β-detected NMR). This leads to degrees of polarisation between 1% and 100% for β-detected NMR compared to the very low polarization of conventional NMR (0.001%). This difference in the degree of polarization results to the enhancement of sensitivity up to 10^5 times for β-detected NMR compared to the normal NMR.

The detection method of the polarisation is a parameter that contributes the enhancement of the sensitivity. In β-detected NMR, the total magnetisation of an ensemble of nuclear spins is destroyed by a rf pulse that matches the Larmor frequency and radioactive particles are detected anisotropically in space in a predicted manner. The β particles detection is increasing the sensitivity of the NMR technique since the detection of RF photons is far less effective by 10^5 times. As a result, β-detected NMR can compete with conventional NMR since it is up to one billion times more sensitive.

6.1 The β-detected NMR technique as a new tool towards chemistry and biology

NMR has been a well established technique in wet chemistry and biology and is an indispensable analytical tool which is used for elucidating the structure and dynamics of large biomolecules, such as proteins and nucleic acids. However, the

limitations in sensitivity and applicability to a variety of elements that are biologically interesting lead to a recent initiative, started with a proof of principle experiment in 2012 at ISOLDE-CERN [5]. The β-NMR technique was applied for the first time in life sciences, biology and chemistry using laser spin-polarised radioactive beams. In 2016 we performed intensive design work and we installed a new permanent laser-polarisation setup at the low-energy part of the ISOLDE facility. Within this initiative the first stage of the beamline development is completed and radioactive atomic beams can be polarised via optical pumping with lasers, the β-decay asymmetry can be observed and quantified and β-NMR experiments can be performed.

The new beamline dedicated to laser polarised β emitted nuclei implanted in solid and liquid hosts, allowed for the signal detection originating from radioactive biologically important isotopes. Thousands of proteins require metal ions such as Na^{+}, Mg^{2+}, Ca^{2+}, Cu^{2+} and Zn^{2+} for their function, which with the conventional measuring tools are known to give poor to zero signal. Trying to overcome these signal limitations we applied the β-detected NMR technique for studying liquid samples of biological importance. The β NMR experiments in liquids were not trivial due to the technical challenge of the high vacuum (10^{-6} mbar) at the liquid sample interface at the end of the experimental setup. Within this PhD work three approaches were tested to overcome the low pressure challenge for liquids:

1. As a first step, we found and tested experimentally liquids that could be used as solvents for our biological samples that could remain liquids under high vacuum conditions.

2. We designed a differential pumping system that could allow for the good transmission of the radioactive atom/ion beam from the end of the beamline until the implantation site, maintaining the degree of the nuclear spin polarisation. The system should work from 10^{-6} mbar to 10 mbar for aqueous samples.

3. We tested thin foils in front of the liquid samples that could hold the sample in a certain place keeping at the same time the degree of polarisation and the transmission of the radioactive beam on the sample's surface.

Finally, the two first suggestions were retained by our ISOLDE β-NMR group and for both of them a vacuum chamber compatible with liquid samples was designed, built and tested.

6.1.1 Ionic Liquids (ILs) as the liquid hosts

In response to the need of using vacuum compatible-liquids with very low vapour pressure, different Ionic Liquids (ILs) were chosen and analysed extensively. ILs are considered as ideal solvents alternative to water, at least for the first steps towards the liquid bio-β-detected NMR. It has been widely acknowledged that the unique features of ILs originate from their dual ionic and organic nature since they are inorganic salts and organic solvents at the same time. Inheriting the advantages of both, they exhibit many superior properties allowing them to be environmentally friendly solvents, while pure organic solvents are usually volatile.

ILs are salts in a liquid state, combinations of cations and anions that are liquids at temperatures below 100 ^{o}C. Thus, usually they are described as Room-Temperature Ionic Liquids (RTILs) in order to differentiate them from traditional salts, which melt at much higher temperatures and are known as "molten salts". In contrast to conventional organic solvents, ILs usually have extremely low volatility, they are non-flammable and non-explosive. The vapour pressures for ILs are difficult to be found in the literature because they are extremely low (<1 Pa) and have to be obtained at high temperatures (400-500 K) [95]. They have other advantageous properties such as reasonable thermal stability, ability to dissolve a wide range of organic, inorganic and organometallic compounds. Furthermore, miscibility with water and other solvents, good solvation ability, low melting temperature, good conductivity, electrochemical stability, polarity, viscosity, density allow them to be used in many areas including chemistry and biology [96, 97].

Another interesting characteristic of ILs is that they are tunable. One can obtain the desired physico-chemical properties by selecting combinations of cations and anions. There is a vast number of different combinations of cation and anion of available ILs with a large variety of physical and chemical properties and one can in principle always find a suitable candidate to meet the requirement of a designated application. On the other hand, due to the numerous candidates it is unfeasible to determine the properties of all the ILs experimentally. For the purpose of this work several different ILs have been tested for finding the most appropriate candidate

that could best serve our goals towards the liquid β-detected NMR. Several NMR experiments have been conducted in order to characterise the different ILs used in this PhD work. The protocols of sample preparations and the NMR analysis and results are presented in Chapter 4.

6.1.2 β-NMR probe isotopes

A large number of β-decaying radioactive beams are available at ISOLDE but the ones that can actually be selected for the β NMR experiments are rather limited due to the following factors:

1. The half-life of the probe nucleus should be comparable or ideally slightly shorter than the spin-lattice relaxation time T_1. This would ensure that most of the β-particles detected come from polarised nuclei. In principle most isotopes studied so far have half-lifes between tens of ms and several seconds.

2. When measuring the relaxation time T_1, the half-life of the probe nuclei should be longer than T_1 in order to gather enough β-count statistics for characterising the decay asymmetry.

3. The production rate of the radioactive isotopes should be high enough (at least 10^5 ions/s) in order to obtain a spectrum with good S/N ratio within few minutes. The short measurement time helps to avoid observing long term drifts in the magnetic field that would lead to line broadening shifts in the resonance signal position and to keep a fresh sample being measured.

4. The degree of polarisation with optical pumping depends on the electronic structure of the atom/ion and the strength of the transitions accessible. The easiest pumping scheme should be chosen in order to achieve the highest degree of polarization. For example, atomic Na is much easier to be polarised than Na^+ and this is the reason why we used Na atoms in the current work.

5. The β-decay asymmetry parameter (α) that ranges between -1 and 1 and depends on the spin change during the nuclear decay, should be large in order to observe high asymmetries (A_{exp}).

6. The probe nuclei should have a small spin to avoid the broadening of the NMR peaks due to the interactions of their quadrupole moment (Q) with the host material.

Among almost 80 chemical elements that can be produced at ISOLDE, a dozen that can be spin-polarised with lasers are interesting in chemistry and biochemistry. The properties of the isotopes that have been already or will soon be tested and are suitable for β-detected NMR are summarised in Table 6.2.

TABLE 6.2: Properties of isotopes selected for β-detected NMR in liquids.

Nucleus	$T_{1/2}$	I	μ (μ_N)	Q (mb)	ISOLDE yield (ions/μC)	max β-asym.	Ref
^{8}Li	0.8 s	2	+1.6532(2)	+31.4(2)	6x10^{8}	4.5%	[98–101]
^{9}Li	0.18 s	3/2	+3.43678(6)	-30.6(2)	2x10^{7}	1.3%	[98–101]
^{26}Na	1.1 s	3	+2.851(2)	-5.3(2)	2.2x10^{7}	24*,32%	[33, 102, 103]
^{27}Na	0.3 s	5/2	+3.894(3)	-7.2(3)	3.1x10^{5}	30%	[102, 103]
^{28}Na	30 ms	1	+2.420(2)	+39.5(1.2)	1.4x10^{4}	40*%	[33, 102, 103]
^{29}Mg	1.2 s	3/2	+0.9780(6)	-0.16(4)	6x10^{6}	3%	[104, 105]
^{31}Mg	230 ms	1/2	-0.88355(10)	-	1.5x10^{5}	8%	[104, 105]
^{37}K	1.2 s	3/2	+0.2036(1)	100(30)	7.1x10^{6}	-	[106–108]
^{49}K	1.3 s	1/2	+1.3386(8)	-	2.4x10^{4}	-	[109]
^{39}Ca	0.8 s	3/2	+1.01216(2)	+36(7)	5x10^{5}	5.3%	[110, 111]
^{51}Ca	0.36 s	3/2	-1.0496(11)	+36(12)	5.5x10^{5}	-	[51]
^{58}Cu	3.2 s	1	+0.570(2)	-150(30)	3x10^{5}	0.25%	[112, 113]
^{74}Cu	1.6 s	2	-1.068(3)	+260(30)	5x10^{5}	-	[53]
^{75}Cu	1.2 s	5/2	+1.0062(31)	-269(16)	1x10^{5}	-	[53]
^{75}Zn	10 s	7/2	-	-	5.6x10^{7}	-	[101]
^{*75}Zn	5 s	1/2	-	-	5.6x10^{7}	-	[101]
^{77}Zn	2 s	7/2	-	-	7.1x10^{6}	-	[101]
^{*77}Zn	1.1 s	1/2	-	-	3x10^{4}	-	[101]

Nuclei in bold can be polarised rather easily at ISOLDE.

Nuclei in italics are those planned to be polarised and used for future β-detected NMR experiments at ISOLDE.

$^{29\text{-}31}$Mg have been already polarised

* maximum asymmetry achieved within this work.

The first isotope which has been used for a β-NMR study in liquids was ^{31}Mg [5]. It has been laser-polarised at ISOLDE and was implanted in an ionic liquid (1-Ethyl-3-methylimidazolium acetate, or else EMIMAc). ^{31}Mg was selected for the

proof-of-principle experiments for its suitable $T_{1/2}$=230 ms and its nuclear spin. I=1/2 is ideal since no quadrupole interactions exist to broaden the resonance signal or to lead to faster relaxation. It can be relatively easily polarised giving high degrees of asymmetry (up to 8%) and its production yields at ISOLDE are satisfactory (10^5 ions/s).

More recently at HIMAC [85] ^{12}N polarised through the p(^{12}C, ^{12}N)n reaction was implanted into water and a NMR signal was successfully acquired. Both Mg and N are biologically important, since Mg(II) is one of the most abundant elements in the human body. Mg participates in practically all storage and energy transport mechanisms and in the folding of RNA, while N is an essential building block of amino and nucleic acids.

The Cu and Zn isotopes indicated in Table 6.2 have not yet been laser polarised at ISOLDE, therefore ^{58,74,75}Cu and ^{75,75m,77,77m}Zn spin-polarisation and β-NMR feasibility tests have been proposed. The motivation for Cu and Zn studies is given by the fact that they are both present in a large number of enzymes involved in electron transfer and activation of oxygen, stabilisation of DNA, and for gene expression. From the physics point of view, polarising these isotopes and doing β-NMR experiments will help to measure with high precision the magnetic moments of the neutron-rich Cu isotopes and concerning ground and isomeric Zn states, to measure and assign the spins and nuclear moments.

The motivation for the Na β-NMR studies comes primarily from the fact that Na plays a key role in biology. Na is responsible for the regulation of blood volume, blood pressure and helps to maintain a stable pH. One of the most important roles of Na in living organisms is that it is essential for the neuron functioning and osmoregulation between the cells and the extracellular fluid that is regulated by the Na^+/K^+ pump. From the physics point of view Na studies can be easily performed by our group at ISOLDE/CERN since Na isotopes can be very well produced by the available targets, Na atoms can be very well polarised with lasers through the atomic D2 transition from the ground state and the degree of experimental asymmetry expected is very high due to the large β-asymmetry factors.

6.2 The new laser polarisation and β-detected NMR beamline at ISOLDE

A new beamline dedicated to laser polarisation and β-detected NMR studies was designed, built and commissioned in 2016 at ISOLDE/CERN at the time of this thesis. A 3D drawing of the experimental setup is shown in Fig. 6.4.

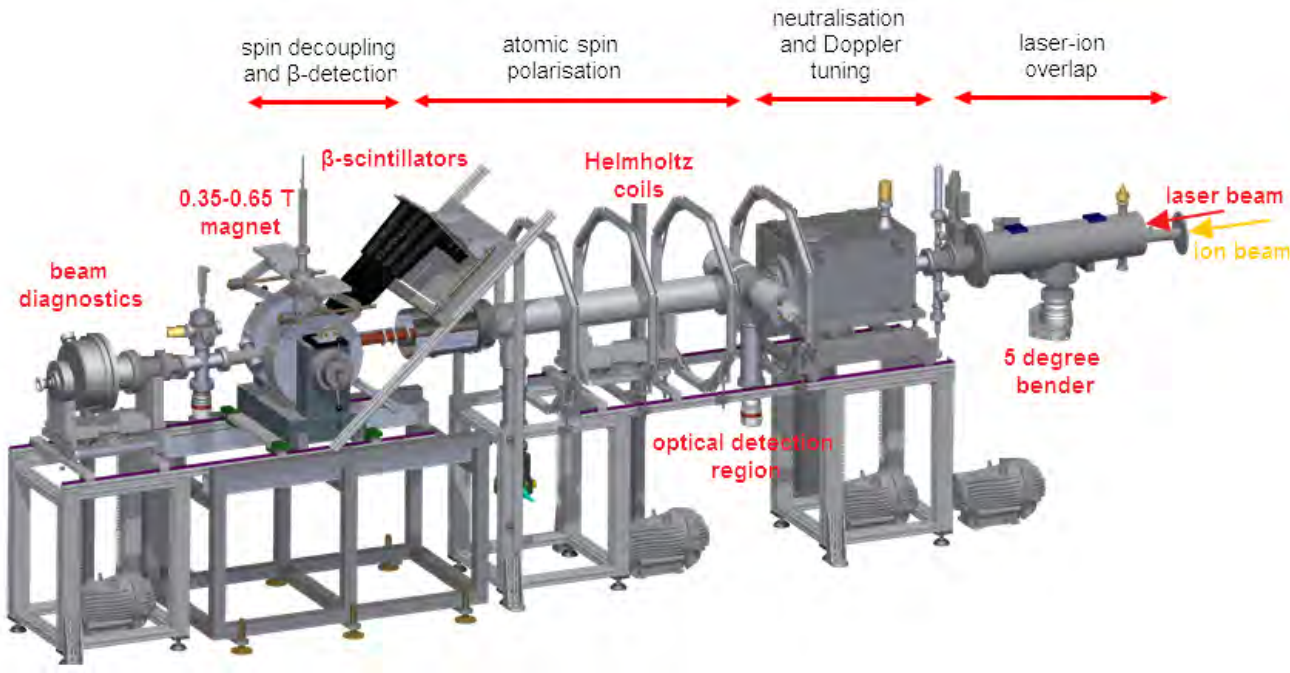

FIGURE 6.4: The laser polarisation and β-detected NMR setup at the new beamline at ISOLDE. 3D drawing courtesy of Dr. Frank Wienholtz.

The ion beam of interest is guided to the beamline after electrostatic deflection, to the right from the ISOLDE central beamline (Fig. 2.4). The first element that belongs to the new beamline is a quadrupole doublet (not shown in Fig. 6.4) that is used to properly focus the ion beam into the setup. The laser polarisation setup can be divided into four main areas from the right to the left.

1. **Laser-ion overlap region**: After the quadrupole doublet comes a 5° bender in which the ions are electrostatically deflected horizontally by 5°. At the bender the laser beam enters through a small quartz window and at the end of the bender the laser and ion paths get overlapped. Right after the 5°-bender, a beam diagnostics box is installed that hosts a variable aperture and a metal plate that is used for measuring the ion current.

2. **Neutralisation and Doppler tuning region**: The next element is the charge exchange chamber that hosts a Charge Exchange Cell (CEC), in which the ion beam can be neutralised, when it is needed for the optical pumping, by collisions with Na or K vapour. The CEC is used for the species which are polarised more efficiently as neutral atoms (e.g. Li, Na, Ar, Cu). The chamber hosts a set of acceleration/deceleration electrodes which can change the energy of the incoming beam by several keV in order to Doppler-tune them into resonance with the laser light. At the end of the chamber there is an electrostatic deflector that is used to separate the neutral atomic beam from the ions which were not neutralised. Right behind there is a chamber housing a photomultiplier which can be used to detect fluorescence light emitted by the excited atoms/ions. This allows for recording optical resonances of reference isotopes (usually stable ones, with production rates above 10^7 ions/s).

3. **Atomic spin polarisation section**: After the optical detection follows the optical pumping section where the atomic spins (F) are polarised. It consists of a long ($\sim$1.9 m) drift tube and four large Helmholtz coils surrounding it. The Helmholtz coils of 80 cm diameter, create a longitudinal magnetic field of 10-20 Gauss (1-2 mT) needed for maintaining the spin polarisation along the beam axis, since stray magnetic fields and magnetic materials in the neighbouring setups (e.g. REX-TRAP, REX-EBIS and the WISARD experiements) could cause polarisation losses. When the collinear laser light is in resonance with the atoms or ions, multiple absorption of circularly polarised photons allow to polarise the atoms/ions.

4. **Spin decoupling and β-detection region**: In the next section, the nuclear and atomic spin decoupling takes place when an increasing strong magnetic field is applied. As described in Section 6, the laser light polarises the atoms that pass the polarisation to the nuclei due to the hyperfine interaction between the atomic spin and the nuclear spin.

   After the atomic and nuclear spin decoupling, follows the implantation into a stopping medium (either solid crystal or liquid) that is placed in the centre of the NMR magnet where the homogeneity is highest. Then β-NMR detection takes place. The magnetic field of the electromagnet is perpendicular to the beam direction and the polarised nuclear spins have to be slowly rotated by 90°. The rotation of the nuclear spins is performed at the entrance of the

NMR magnet, where a set of small solenoids generate an increasing magnetic field, 80 Gauss and 180 Gauss (8 and 18 mT) respectively. The increasing magnetic field is matched with the perpendicular strong field of the 0.35-0.65 T commercially available Bruker magnet, inducing the adiabatic rotation of the nuclear spins with a minimum loss of polarisation.

The β-asymmetry detection that is translated to the NMR signal is measured by two pairs of β plastic scintillators of approximately 1 mm thickness each. The scintillators are placed between the β-windows of a vacuum chamber hosting the crystal or the liquid media.

5. **Beam diagnostics box:** hosting a faraday cup and a wire scanner used to maximise the beam transmission and to observe its profile.

The laser-polarisation setup in its initial configuration for β-asymmetry experiments with atoms as shown in Fig. 6.5.

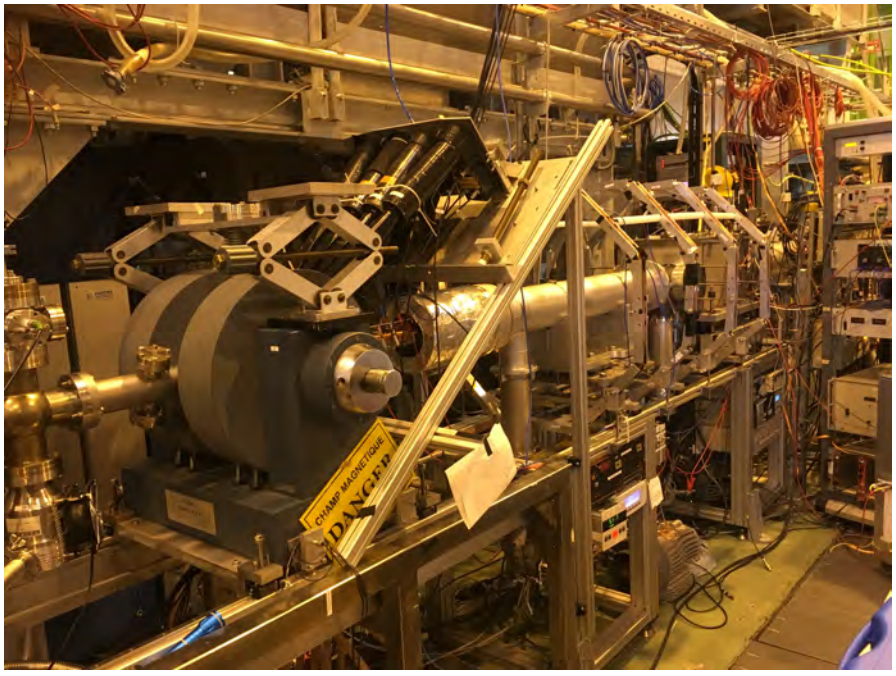

FIGURE 6.5: The new laser-polarisation setup's configuration at ISOLDE, as used for the β-asymmetry experiments during the commissioning campaigns.

6.3 The β-NMR chamber for liquids

For this PhD work a new β-NMR chamber for liquid hosts was designed and built. The major challenge has been to maintain a liquid sample in the same position at

the end of the beamline for time long enough to record a signal , while keeping the beam transport area at $\sim 10^{-6}$ mbar. This has been solved using a new differential pumping system as shown in Fig. 6.6. The system has been simulated and designed by Robert Harding within his PhD thesis. It consists of two 4-way crosses and three vacuum diaphragms (pinholes), which are as big as possible to allow a good transmission of the radioactive beam and as small as necessary to provide sufficient differential pumping power. Each region is connected to a powerful vacuum pump. In the end there is a cone nozzle that stops in front of the liquid host inside the chamber, where up to 10 mbar pressure should be feasible.

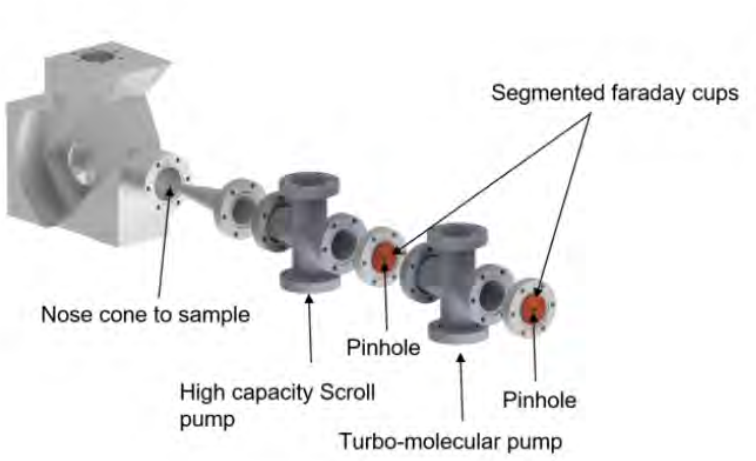

FIGURE 6.6: Cross section view of the differential pumping system. Courtesy of Robert Harding.

An NMR chamber dedicated to liquids has been designed with the following requirements: It should be made of a non-magnetic material, such as Al. It should host a capillary for the liquid dispensing, an RF coil, a sample holder for the reference measurements in crystals, at least one viewport and two thin Al windows letting β particles passing through. During the experiments presented in this work, the vacuum chamber belonging to the COLLAPS collaboration and the new β NMR chamber (as shown if Fig. 6.6) were used.

Chapter 7

Experimental results conventional NMR

7.1 Solution metal-based NMR experiments of ^{23}Na and ^{25}Mg in ionic liquids

Metal-centered NMR in solution is an important complement to the non-metal nuclei such as ^{1}H, ^{13}C, ^{31}P etc routinely used in the NMR characterisation of biological systems and organic, organometallic and coordination compounds. The chemical shifts of metal nuclei are frequently more sensitive to small changes in geometry and coordination number than those of ligands and can reveal subtle differences in the solution composition of complexes [32]. Na and Mg are two of the seven lightest metals (Z=11 and 12 respectively). Their stable isotopes, ^{23}Na and ^{25}Mg, with I different from 0 give NMR signals. They are both less commonly examined nuclei with NMR most probably because of their quadrupolar nature and the fact that their resonances can be extremely broad in asymmetric environments. Between these two nuclei there is a difference in NMR sensitivity that is proportional to their natural abundance and gyromagnetic ratio. Table 5.1 shows the most fundamental NMR properties for the light metals of interest for liquid NMR in analogy with our interest for β-NMR probe nuclei seen in Table 6.2.

Within this PhD work, ^{23}Na and ^{25}Mg NMR experiments were conducted in different ILs during the preparation of the β NMR experiments having the following goals:

1. Explore the solubility of Na and Mg salts in different IL environments and create sample preparation protocols for the ^{26,28}Na and ^{29,31}Mg β NMR experiments [86]. The sample preparation protocols can be found in Appendix B.

2. Analyse ^{1}H, ^{23}Na and ^{25}Mg NMR spectra of the different IL samples in order to find the most appropriate liquid host for the β NMR experiments. The main parameters of interest are chemical shifts and relaxation times. The goal was to find two solutions giving very different chemical shifts for preparing a mixture in which we could see both signals in one NMR spectrum. This could be used in order to test the resolution of our new liquid β NMR setup.

3. Determine ^{23}Na and ^{31}Mg chemical shifts for the different ILs chemical environments at the high magnetic field of 11.74 T. Then, predict the resonance frequencies at 0.6 T, which is the maximum magnetic field that can be achieved with the electromagnet at ISOLDE-CERN, available for the β NMR experiments of this work.

All ^{1}H, ^{23}Na and ^{25}Mg NMR experiments were carried out using a Bruker UltraShield Avance superconducting magnet at 500 MHz (11.74 T) and a 5 mm static variable-temperature probe. The spectrometer used, Fig. 7.1, is located at the Department of Food Science, University of Copenhagen (KU), under the supervision of Flemming Hofmann Larsen, Associate Professor of Department of Food Science in KU. The spectrometer can be fully automated by streamlining every aspect of NMR analysis, including sample submission, automatic probe tuning, data acquisition, processing and archiving making feasible the overnight automation that was needed for our measurements. The NMR data acquisition software was TopSpin, that includes comprehensive functionalities for processing, displaying and analysing single and multidimensional spectra. The NMR measurements were conducted under the supervision of F. H. Lassen and L. Hemmingsen, University of Copenhagen, Denmark.

FIGURE 7.1: Bruker UltraShield Avance spectrometer at University of Copenhagen, 500 MHz (11.74 T).

7.2 ^{23}Na NMR

Among the NMR active alkali metal nuclei, ^{23}Na is relatively easy to study because of its 100% natural abundance, relatively high γ ratio and receptivity (0.0927 relative to ^{1}H) and high resonance frequency (e.g 132.39 MHz at a magnetic strength of 11.7 T. However, the fact that ^{23}Na is also a quadrupolar nucleus (I=3/2 and Q=104 mb) causes difficulties not only on carrying out NMR experiments, but also on interpreting the experimental data. One of the major problems of liquid ^{23}Na NMR is related to its intrinsically poor resolution, a combination of the moderate chemical shift range (90 ppm) and large line width due to efficient ^{23}Na quadrupole relaxation.

Seven different samples were investigated with 1D ^{23}Na and ^{1}H NMR. All the ^{23}Na NMR experiments were performed at 70°C, unless stated otherwise. This approach was followed due to time limitations, based on preceding ^{25}Mg NMR experiments that showed narrower linewidths and better S/N ratio signals under this condition. The fact that temperatures above room temperature (RT) give better signals could be because the samples used for the experiments are highly concentrated and the ILs are very viscous at RT. Therefore, at 20°C slow tumbling of the molecules is observed that leads to fast *T2* relaxation due to the strong spin-spin interaction. Increasing the temperature to 70°C, the viscosity decreases and the overall molecular tumbling rate increases, making it easier to record a well resolved NMR signal.

In the following paragraphs the NMR experimental spectra acquired during the current work will be presented. The fitting and analysis of the experimental data were performed with Bruker Topspin 4.0.2.

The reference sample, 0.1 M NaCl dissolved 495μl H2O and 55 μl D_2O), was measured in the beginning of the ^{23}Na NMR experimental series. The reference linewidth is 6.5 Hz (0.049 ppm).

7.2.1 NaAc in EMIM_Ac and NaCl in EMIM_Ac

1-Ethyl-3-methylimidazolium acetate (EMIM_Ac) was the first IL selected to be studied, following the first successful ^{31}Mg β NMR experiments at ISOLDE [5]. The chemical structure of EMIM_Ac is presented in Fig. 7.2.

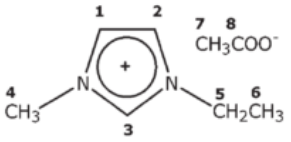

FIGURE 7.2: Chemical structure of EMIM_Ac with proton labelling according to [21].

^{23}Na NMR followed the ^{1}H NMR experiments D.1. Fig. 7.3 shows the ^{23}Na NMR spectra of 0.3 M NaAc dissolved in EMIM_Ac and 0.3 M NaCl dissolved in EMIM_Ac superimposed.

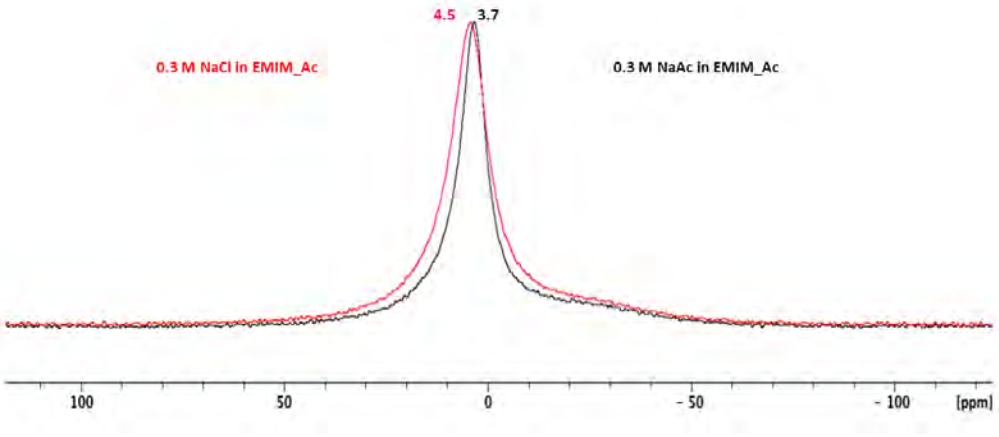

FIGURE 7.3: ^{23}Na NMR spectra of 0.3 M NaAc in EMIM_Ac and 0.3 M NaCl in EMIM_Ac.

There are minor differences between the chemical shift positions (<1 ppm) and the FWHM (3 ppm), see Table 7.2. Na^+ is expected to bind either at the CH_3COO^- site or be "free" in the bulk solution. Cl^- and Ac^- should be attracted by the positively charged ring of $EMIM^+$. The negligible differences between the two signals could mean that Na stays "free" Na^+ in the solution or the Na environment at the binding site is almost identical in both cases.

Na forms an ionic bond with Cl^- that has high electronegativity (3.16 according to Pauling electronegativity scale) while it forms an ionic bond with the one O of Ac (CH3COO) with electonegativity 3.44 (according to Pauling electronegativity scale). This could probably mean that when NaCl is dissolved in the ionic liquid,

the ionic bond between Na^+ and Cl^- breaks and Na^+ binds with the Ac^- of the IL, creating like this the same electronic environment. This could create the same shielding effect of Na and therefore the same chemical shift.

7.2.2 NaAc in EMIM_Ac and NaAc in BMIM_Ac

The second IL studied was the 1-Butyl-3-methylimidazolium acetate (BMIM_Ac) with chemical structure similar to EMIM_Ac with the addition of a CH_2CH_3, Fig. 7.4.

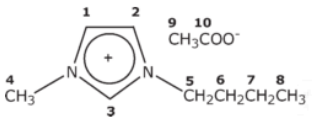

FIGURE 7.4: Chemical structure of BMIM_Ac with proton labelling according to [21].

In Fig. 7.5 the ^{23}Na NMR spectra of 0.3 M NaAc dissolved in EMIM_Ac and BMIM_Ac are superimposed.

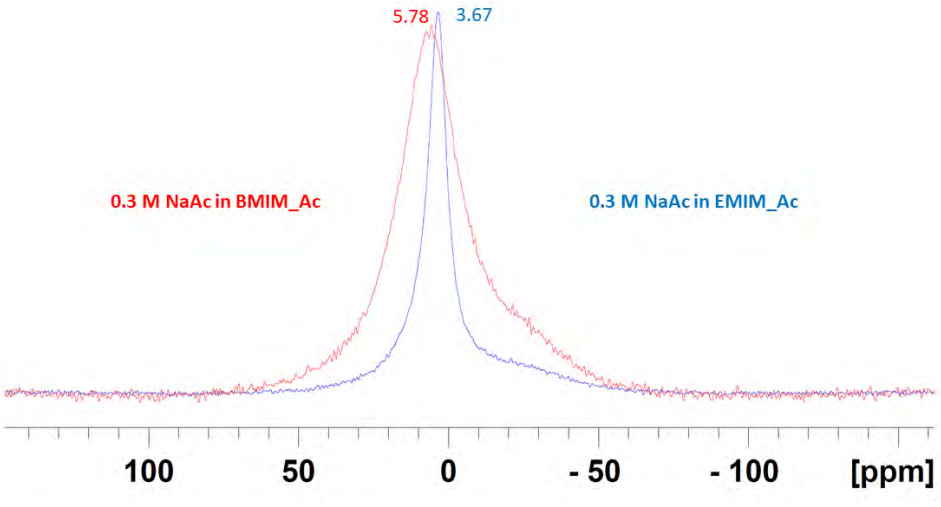

FIGURE 7.5: ^{23}Na NMR spectra of 0.3 M NaAc in EMIM_Ac and 0.3 M NaAc in BMIM_Ac.

Both measurements show one main signal and maybe a second very broad shoulder on the right, corresponding to a signal either from a binding site for Na or from

"free" Na^+ in bulk solution. There is a difference of ∼3 ppm between the two dominant signals (3.67 vs 5.78 ppm for EMIM and BMIM respectively) showing that Na is better shielded when EMIM is the cation of the ionic liquid solution. The FWHM of the dominant ^{23}Na signal in BMIM_Ac is three times broader than that of EMIM_Ac, 3300.8 and 1180 Hz respectively. This could probably mean higher asymmetry in the electronic environment of Na nuclei when BMIM is the cation.

According to literature, one of the possible explanations for seeing a second broader signal is that the ILs behaves like nematic liquid crystals (NLQ) and not as isotropic liquids [114]. Table 7.1 shows the rotational viscosity data ($\gamma 1$) as measured in the current work for BMIM_Ac in very good comparison with the literature data [114].

TABLE 7.1: Viscosity data for BMIM_Ac at different temperatures.

Temperature (K)	$\gamma 1$ (Pa*s)*	$\gamma 1$ (Pa*s) [114]
283	0.225	-
293	0.11	0.141
303	0.07	0.093
313	0.05	0.066
323	0.03	0.046
333	0.025	0.032
343	0.02	0.021
353	-	0.011

*results of current work

The linewidths of alkali signals in liquid crystals have been found comparable with the corresponding linewidths in aqueous solutions in the literature [115]. Sodium ions in liquids could exist in two environments, the "free" (unassociated) and bound (associated). "Free" Na^+ are mobile in the aqueous phase and normally have short correlation times, τ_c, while bound Na ions have a more restricted motion as a result of the ion binding or interacting with negatively charged functional groups (i.e. DNA, proteins, carbohydrates, etc).

Fig. 7.5 probably reflects a rapid exchange, relative to the relaxation scales, between the two different ion environments. This could explain why we observe one signal better because of the fast correlation time of the molecules due to the

elevated mobility as a result of the high temperature, 70 °C. We suggest that the narrow peak originates from the "free" Na^+ in the bulk solution since it is a Lorentzian lineshape, indicating that the quadrupole interaction is averaged by isotropic random motio. As a result and second peak may correspond to the bound Na^+, as suggested by several research groups using ^{23}Na NMR on biological gels and DNA solutions [116].

The magnitude of the second peaks' appearance could be affected by the B_0 strength and the Na concentration. When the sample is saturated (e.g. 0.3 M NaAc) the signal from the "free" Na^+ could be the predominant contribution "masking" the signal from the bound Na^+. Assuming that in both samples the dissolved Na^+ is equally binding to the Ac^- of BMIM and EMIM IL, when the solutions are less saturated the signal from the coordinated Na can contribute to a higher degree to the total ^{23}Na NMR signal of the sample, leading to the appearance of the second NMR chemical shift.

7.2.3 NaCl in EMIM_Ac and NaCl in BMIM_SCN

Another BMIM-based IL was studied, the 1-butyl-3-methylimidazolium thiocyanate (BMIM_SCN). The chemical structure of BMIM_SCN is shown in Fig. 7.6.

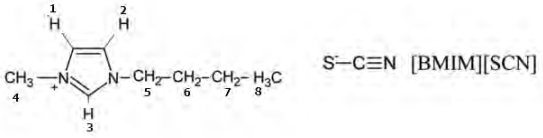

FIGURE 7.6: The chemical structure of BMIM_SCN with proton labelling according to [22].

Fig. 7.7 shows the ^{23}Na NMR spectra of NaCl dissolved in two different ionic liquids of different cation ($EMIM^+$ and $BMIM^+$) and different anion, acetate (Ac^-) and thiocyanate (SCN^-) superimposed.

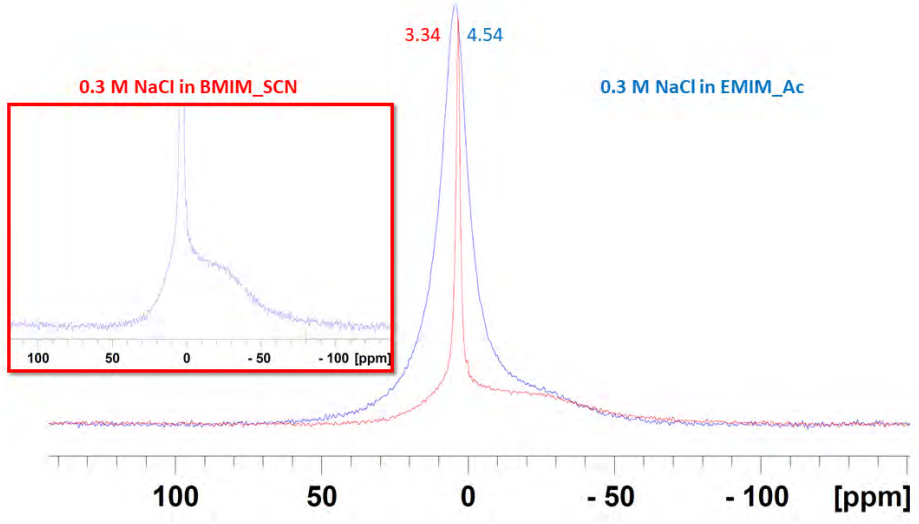

FIGURE 7.7: ^{23}Na NMR spectra of 0.3 M NaCl in EMIM_Ac and 0.3 M NaCl in BMIM_SCN.

The ^{23}Na NMR spectrum of NaCl in EMIM_SCN displays one predominant chemical shift at 3.34 ppm, with a sharp linewidth of 3.2 ppm (430 Hz), and a second very broad chemical shift with a linewidth estimated at around 52 ppm (6900 Hz), at ∼-18 ppm. This result indicates that the NMR spectrum consists from both the Na cation components, both the "free" Na^+ and bound Na^+ on SCN^-. Contrary, as have been discussed previously for the EMIM_Ac sample, the predominant signal is the one from "free" Na^+ that appears at δ=4.5 ppm with a FWHM=12 ppm (1602 Hz). The detailed results from the fitting procedure are summarised in Table. 7.2

7.2.4 NaCl in BMIM_SCN and NaSCN in BMIM_SCN

The ^{23}Na NMR spectra of 0.3 M NaCl in BMIM_SCN and 0.3 M NaSCN in BMIM_SCN are superimposed in Fig. 7.8. Both samples display two chemical shifts, a predominant peak at 3.34 and 3.84 ppm for NaCl and NaSCN respectively, with a linewidth of 3.2 and 2.6 ppm (430 and 340 Hz), and a second very broad chemical shift at ∼-18 ppm in both cases. The second chemical shift is much broader, with a linewidth of ∼52 ppm (6900 Hz) for NaCl and ∼34 ppm (4500 Hz) indicating the higher asymmetry of the electronic environment of the Na nuclei,

and with an amplitude 10 and 38 times lower than the one of the dominant site that is probably originating by the "free" Na^+ in the solution.

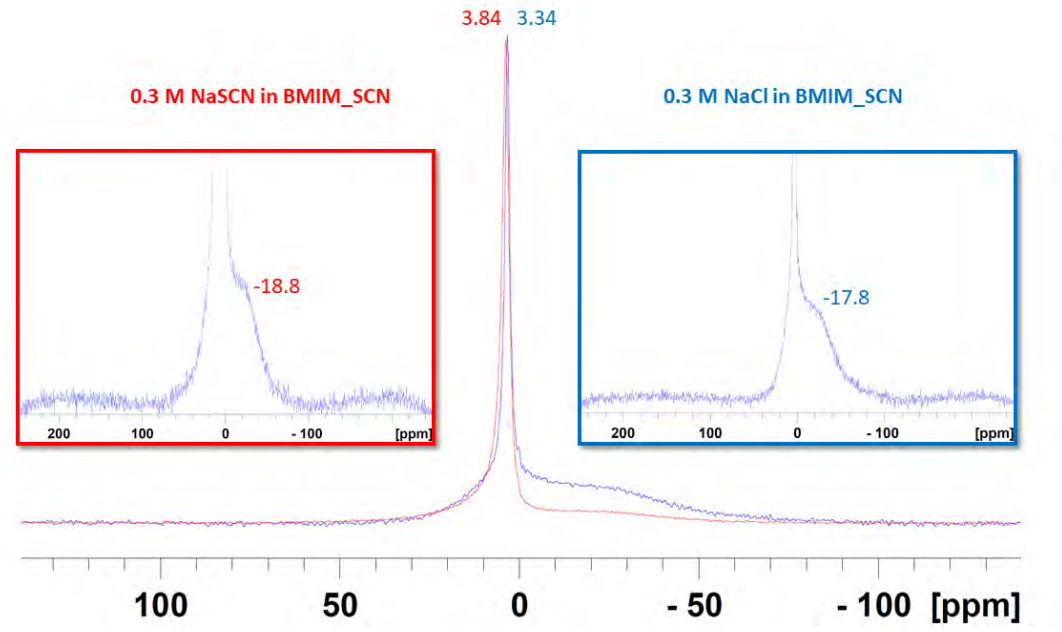

FIGURE 7.8: ^{23}Na spectra of 0.3 M NaCl in BMIM_SCN and 0.3 M NaSCN in BMIM_SCN.

The detailed results from the fitting procedure are summarised in Table. 7.2

7.2.5 NaSCN in BMIM_SCN and 15c5 ether in NaSCN_BMIM_SCN

During the time of the aforementioned ^{23}Na NMR experiments, after some primary analysis, we realised that there was not significant difference between the ^{23}Na chemical shifts (not more than 1 ppm), even though the ^{23}Na chemical shift span is expected to be as large as 70 ppm. Therefore, the idea of finding a molecule that could be easily dissolved and bound with the Na^+ was considered as a sensible step. After a short search in the literature, crown ethers were found to have attracted much interest as simple analogues for biological channels or diffusive carriers for alkali metals, such as Na and K [117–120].

A crown ether is a cyclic array of ether O atoms linked with organic spacers, usually $-CH_2CH_2-$ groups. 15-crown-5 is the crown ether chosen for the following experiment since it binds with high selectivity to Na^+ [121], Fig. 7.9.

FIGURE 7.9: 15-crown-5 ether with Na^+ captured in the middle of its plane.

.

Due to this selectivity we considered that it worth's testing if a known, previously measured sample would give a shifted peak when the 15-crown-5 is added. Theoretically, the NMR chemical shift was expected to decrease, since the Na^+ would be more shielded by the increase of the surrounding electronic cloud because of O2 atoms.

Fig. 7.10 shows the ^{23}Na NMR spectra with and without the 15-crown-5 ether ((C2H4O)5).

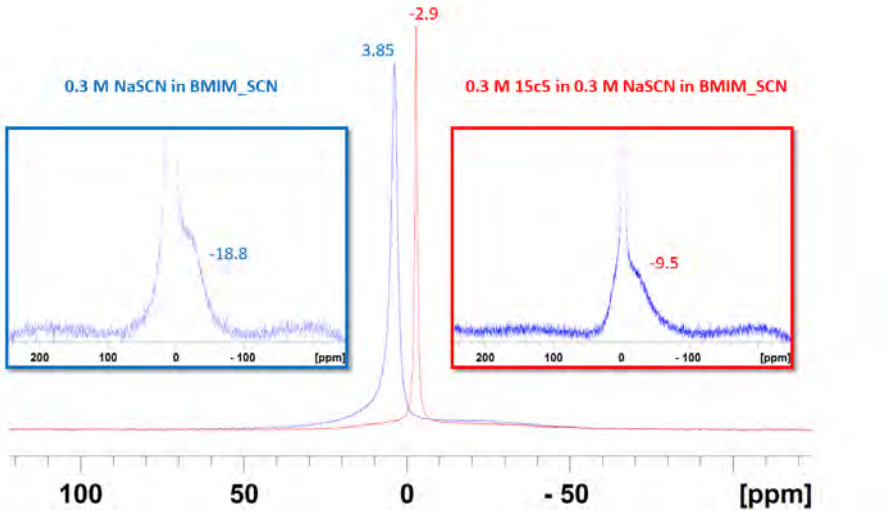

FIGURE 7.10: ^{23}Na spectra of 0.3 M NaSCN in BMIM_SCN and 0.3 M 15-crown-5 + 0.3 M NaSCN in BMIM_SCN.

When the crown ether dissolves in the BMIM_SCN solution with NaSCN, the chemical shift of the sharp signal moves upfield indicating that the electron density around the "free" Na^+ is higher when the crown ether is added. Also, the linewidth decreases approximately 3 times showing that the electronic environment is more symmetric compared to the sample without the 15-crown-5 ether. The chemical shift from 3.8 ppm moves to -2.9 ppm ($\Delta\delta$=6.7 ppm), a result that is consistent with previous experimental results from [122] where ^{23}Na resonance appeared at -3.6 ppm at 303 K and -5.7 ppm at 183 K for 15-crown-5 ether + NaSCN with respect to NaCl in D_2O. The addition of the crown ether in the solution lead to a decrease of the linewidth to 1/3, from 2.6 ppm to 0.9 ppm (340 Hz to 119 Hz).

On the other hand, the second broad peak moves downfield from -18.8 ppm to -9.05 ppm ($\Delta\delta$=9 ppm), and the linewidth increases from 34 ppm to 50 ppm (3.5 kHz to 6.65 kHz). This indicates that the Na nuclei that are bound with the IL through the SCN^-, have less electronic cloud around them and the environment becomes more asymmetric compared to the without crown ether sample.

7.2.6 Comparison of all the ILs tested

During the current work, four different ionic liquids were tested with ^{1}H and ^{23}Na NMR . There is a very long list of ILs that could have been tested, but due to time constraints and our limited knowledge of their behaviour with Na salts at that time, only four ILs were used. In this section the results of ^{23}Na measurements of BMIM_Ac, BMIM_SCN, EMIM_Ac and EMIM_DCA with the same cation Na salts are presented in Fig. 7.11. The same cations of the ILs and the Na salts were used for eliminating any possible interaction between the Na cation and the IL cation. ALl the presented spectra are referenced to the amplitude of the ^{23}Na signal of the BMIM_Ac measurement.

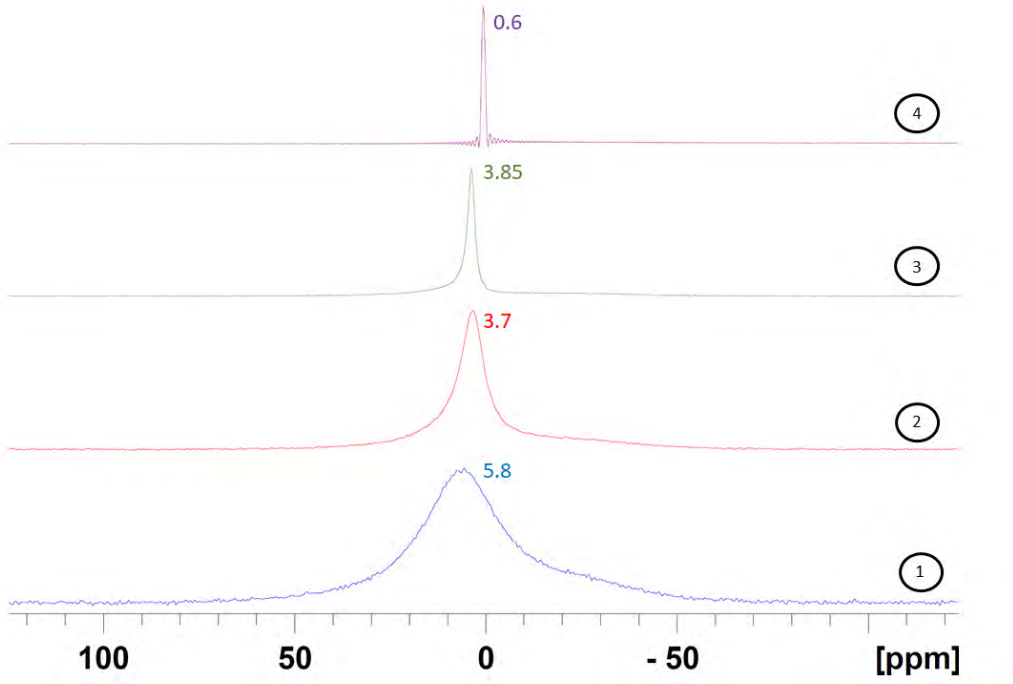

FIGURE 7.11: ^{23}Na NMR spectra of 1. 0.3 M NaAc in BMIM_Ac, 2. 0.3 M NaAc in EMIM_Ac, 3. 0.3 M NaSCN in BMIM_SCN and 4. 0.3 M NaDCA in EMIM_DCA.

As a general trend we see a strong dependence between the position of the signal and its linewidth with the IL used. The EMIM_Ac seems to give narrower signal than BMIM_Ac, $\sim$ 9 ($\pm$0.06) ppm compared to $\sim$ 25($\pm$0.09) ppm. The EMIM_DCA shows the more well defined NMR peak with FWHM 0.84($\pm$0.03) ppm at 0.6 ppm while BMIM_SCN has a linewidth of $\sim$ 2.6($\pm$0.02) ppm. For the detailed results of the analysis please refer to Table. 7.2.

TABLE 7.2: ^{23}Na NMR analysis of all the samples measured

sample	Peak position ppm	Peak Frequency Hz	FWHM ppm	FWHM Hz	Amplitude
0.3 M NaAc in EMIM_Ac	3.7 (0.02)	485.7 (2.6)	8.9 (0.06)	1180.4 (7.6)	14.4 (0.06)
0.3 M NaCl in EMIM_Ac	4.5 (0.01)	660.7 (1.9)	12.1 (0.04)	1602.3 (5.6)	14.6 (0.03)
0.3 M NaAc in BMIM_Ac	5.8 (0.03)	764.1 (4.2)	25.2 (0.09)	3330.8 (12.3)	14.5 (0.04)
0.3 M NaCl in BMIM_SCN	3.3 (0.01)	441 (1.8)	3.2 (0.04)	430 (5.9)	11.1 (0.09)
	-17.8 (0.65)	-2358.7 (86)	52.1 (1.8)	6900 (238.7)	1.1 (0.02)
0.3 M NaSCN in BMIM_SCN	3.85 (0.01)	508.5 (1.2)	2.57 (0.02)	340 (3.4)	14.5 (0.1)
	-18.8 (0.14)	-2485.3 (17.8)	34 (0.36)	4500 (47.6)	0.38 (fixed)
0.3 M NaSCN + 0.3 M 15c5 in BMIM_SCN	-2.9 (0.002)	-377.9 (0.04)	0.9 (0.001)	119.1 (0.14)	14.8 (0.01)
	-9.05 (0.28)	-1197.3 (37)	50.2 (0.65)	6646.1 (86)	0.25 (0.002)
0.3 M NaDCA in EMIM_DCA	0.61 (0.01)	81.3 (1.5)	0.84 (0.03)	111 (4.4)	16.6 (0.46)

Note 1. The chemical shifts were calculated using as reference compound the 0.1 M NaCl (aq) and D_2O.

Note 2. All the fits are performed with 100% lorentzian lineshapes.

7.2.7 T1 relaxation measurements of ^{23}Na signal from different ILs

For better characterising the different ILs, we attempted to measure the *T1* relaxation times with the Inversion Recovery (IR) technique. All the measurements were done at room temperature (300 K) and the repetition delay time, the Inversion Time (TI), varied to the following values: 1 ms, 2 ms, 4 ms, 8 ms, 16 ms, 32 ms, 64 ms, 128 ms, 256 ms, 512 ms and 1.024 sec.

From the ^{23}Na NMR spectra analysis we found that there are two sides where the Na^+ can reside, meaning two T1 components. The signal that originates from the "free" Na^+ has a long T1, longer than 1 s, and therefore could not be calculated with IR technique. While, the second component from the "bound" to Na^+ has a shorter relaxation time in the order of ms in most cases. The relaxation times T1 for the samples measured are shown in Table. 7.3.

TABLE 7.3: T1 relaxation time of bound Na^+ for IL samples

Sample	T1 [ms]
0.3 M NaAc in EMIM_Ac	40.5(±13)
0.3 M NaCl in EMIM_Ac	199(±71)
0.3 M NaDCA in EMIM_DCA	218(±37)
0.3 M NaAc in BMIM_Ac	$\sim$ 0.1
0.3 M NaCl in BMIM_SCN	368(±204)
0.3 M NaSCN in BMIM_SCN	99(±45)
0.3 M 15-crown-5 + NaSCN in BMIM_SCN	251(±95)

7.3 ^{25}Mg and ^{1}H NMR

Due to sensitivity problems caused by the relatively unfavourable characteristics of the ^{25}Mg nucleus for NMR experiments, such as the low natural abundance (10%), the small gyromagnetic ratio and the sizeable quadrupolar broadening because of the I=5/2, ^{25}Mg remains a largely under-explored nucleus. The main use of ^{25}Mg NMR is to measure the relaxation rates in order to detect the binding to biomolecules. Most commonly the observed chemical shifts are between -20 to 50 ppm and the quadrupolar effects dominate the ^{25}Mg spectra of Mg^{+} in non-cubic environments such as ILs.

In this work, we have recorded at high magnetic field, 11.7 T, ^{25}Mg liquid NMR spectra of several previously unreported non-aqueous IL solutions of Mg salts. The combination of high magnetic fields and high density solutions allowed ^{25}Mg NMR spectra with relatively good signal-to-noise ratio to be obtained and to indicate distinct Mg binding sites. In non-aqueous solvents the resonance frequency seems to be dependent on the solvent. In the following paragraphs the NMR experimental spectra of this work will be presented. The fitting and data analysis were performed with Bruker Topspin 4.0.4.

7.3.1 MgCl2 in BMIM_SCN and $MgCl_2$ in EMIM_Ac at 25 ^{o}C and 70 ^{o}C

The conventional ^{25}Mg NMR measurement series started with of 0.3 M MgCl2 dissolved in BMIM_SCN. We measured the same sample first at room temperature 25 ^{o}C and then at 70 ^{o}C. Fig. 7.12 shows that for the same number of scans the signal acquired with the high temperature measurement has better signal-to-noise-ratio (SNR) and a $\sim$ 19 ppm linewidth instead of 43 ppm for the dominant signal at $\sim$ 12 ppm. Due to this observation, it was decided to continue with all the ^{25}Mg NMR measurements at the high temperature of 70 ^{o}C while the 1H NMR measurements were done at 25 ^{o}C.

We repeated the different temperatures measurements for $MgCl_2$ anhydrous dissolved in EMIM_Ac at 25 ^{o}C and at 70^{o}C. Fig. 7.13 shows that for almost the same number of scans (24000 scans and 25000 scans respectively) the high temperature measurement shows a very well resolved signal. At 70^{o}C, there is a dominant

signal and a very broad shoulder, while at 25^{o}C there is one very broad peak that could represent the averaging of the two signals. In Table 7.4 there are the detailed results of the fit analysis. At 70^{o}C we see a narrow peak of FWHM 5 ppm and a broader one of 149 ppm, while the 25^{o}C measurement gives one broad signal of FWHM 169 ppm.

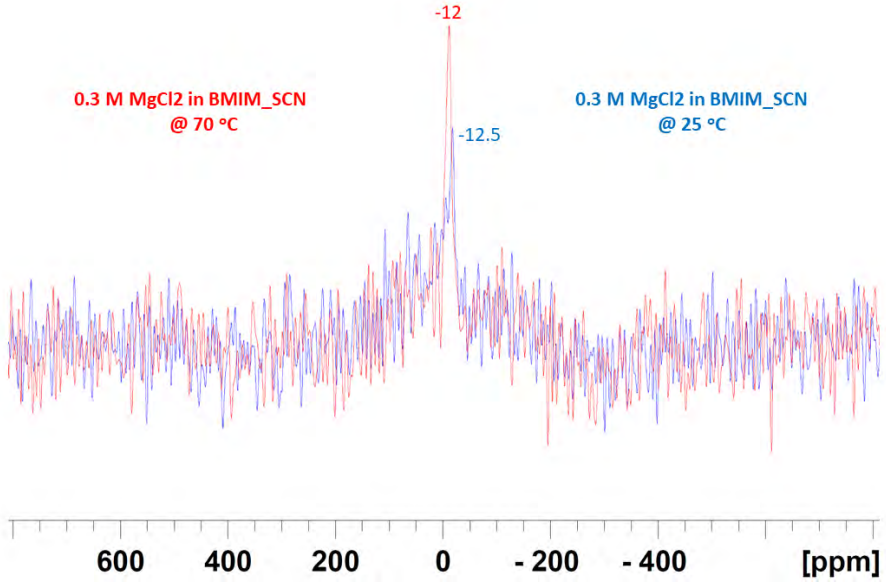

FIGURE 7.12: ^{25}Mg NMR spectra of 0.3 M $MgCl_2$ in BMIM_SCN at 70 ^{o}C and at 20 ^{o}C.

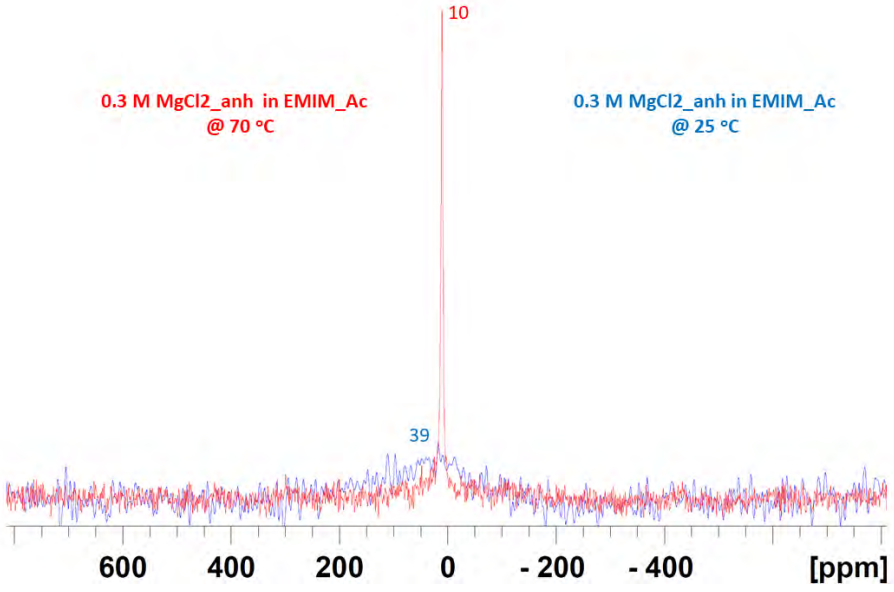

FIGURE 7.13: ^{25}Mg NMR spectra of 0.3 M MgCl2_anh in EMIM_Ac at 25°C and 70°C.

7.3.2 MgCl2 in EMIM_Ac and MgCl2 in EMIM_DCA

Aiming to probe differential chemical shifts of Mg^{2+} complexes with typical oxygen and nitrogen containing ligands, we tested two different ILs. 0.3 M $MgCl_2$ anhydrous were dissolved in EMIM_Ac and EMIM_DCA ILs, Fig. 7.14.

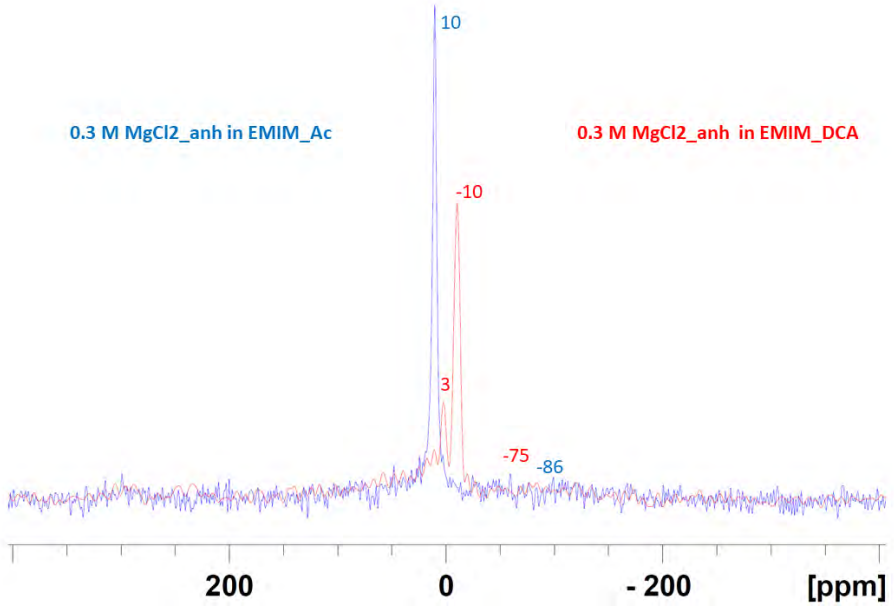

FIGURE 7.14: ^{25}Mg NMR spectra of 0.3 M MgCl2 anhydrous dissolved in EMIM_Ac and 0.3 M $MgCl_2$ anhydrous dissolved in EMIM_DCA.

The ^{25}Mg NMR spectrum of 0.3 M $MgCl_2$ anhydrous in EMIM_Ac displays a major resonance at 10 ±0.02 ppm and a shoulder consistent with an unresolved peak at -75 ±5 ppm. For 0.3 M $MgCl_2$ anhydrous dissolved in EMIM_DCA the main resonance is observed at -10 ±0.1 ppm while a second weaker signal is observed at 3 ±0.1 ppm. There is also a shoulder with an unresolved peak at -86 ±2 ppm. This indicates that with conventional NMR for the EMIM_DCA sample, there is a co-existence of at least two Mg^{2+} complexes with a third possible specie forming. For the EMIM_Ac sample there is a possibility of co-existance of two species. The fact that two or more resonances are observed indicates slow or no exchange between the coordination environments in the millisecond scale.

In comparison with the conventional ^{25}Mg NMR experiments conducted by collaborators at the University of Copenhagen [86] with the same initial conditions, i.e. magnetic field of 11.7 T and same temperature 70°C, but much different salt concentration (25 mM compared to 300 mM in the current work) in the current work

the spectral speciation was resolved. At the low concentrations of 25 mM only the major resonances at 10.2 ppm for EMIM_Ac and -13.3 ppm were observed showing that the higher the concentration of Mg^{2+} the easier to probe the coordination of Mg with the O and N ligands of EMIM_Ac and EMIM_DCA. On the other hand, with the ultrasensitive β NMR technique with a magnetic field 3.41 T and a MgO crystal as the reference compound, the same study [86] showed for Mg^{2+} implanted in EMIM-Ac one major resonance at -31.9 ±2.4 ppm and a shoulder with an unresolved resonance at -38.1 ±2.4 ppm at 25 mM that was reproduced at pM trace amounts of ^{31}Mg with the same technique. Leading to the conclusion that in order to resolve different Mg coordination environments with conventional NMR we need high concentrations compared to β NMR that can resolve different species with 100 lower ion concentrations proving that the β NMR technique is indeed more sensitive than the conventional equivalent spectroscopic technique.

Furthermore, with the β NMR technique the ^{31}Mg measurements in EMIM_DCA with concentration of 25 mM [86] showed two main resonances at -60.2 ±2.4 and -52.0 ±2.4. This could potentially confirm the chemical environments that gave two signals in ^{25}Mg NMR measurements of 0.3 M concentration, 3 ±0.2 ppm and -10 ±0.1 ppm.

7.3.3 MgCl2 in EMIM_Ac and $Mg(Ac)_2$*4H_2O in EMIM_Ac

In order to study the effect of Na salt added in EMIM_Ac, two different salts were tested, $MgCl_2$ anhydrous and $Mg(Ac)_2$ with four H_2O.

The 1H NMR measurements were followed by ^{25}Mg NMR measurements in both EMIM_Ac samples. Fig. 7.15 shows that the most dominant signals are identical in both cases, 9.8 (±0.016). with linewidth 4.1 (±0.04) and 9.8 (±0.016) with linewidth 5.1 (±0.04) for $MgCl_2$ and $Mg(Ac)_2$*4H_2O respectively.

On the other hand the $MgCl_2$ in EMIM_Ac shows a second unresolved signal at -37 ppm, a signal that is not observed when $Mg(Ac)_2$*4H_2O is dissolved in EMIM_Ac.

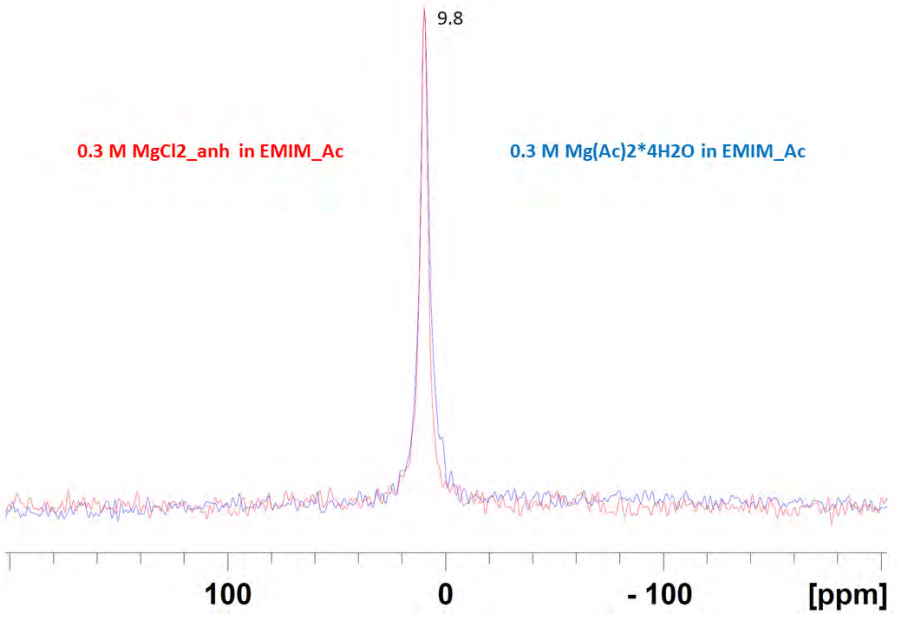

FIGURE 7.15: ^{25}Mg NMR signals of 0.3 M $MgCl_2$ in EMIM_Ac and 0.3 M $Mg(Ac)_2$*$4H_2O$ in EMIM_Ac.

7.3.4 MgCl2 in EMIM_Ac and MgCl2 in BMIM_SCN

Aiming to probe different chemical shifts of Mg^{2+} complexes with typical oxygen and nitrogen containing ligands, we tested two different ILs, EMIM_Ac and BMIM_SCN.

Following the 1H NMR measurements we did ^{25}Mg NMR experiments for the 0.3 M MgCl2 in EMIM_Ac and the MgCl2 in BMIM_SCN. Fig. 7.16 shows that the ^{25}Mg NMR spectrum of 0.3 M $MgCl_2$ in EMIM_Ac displays a major resonance at 10.5 ±0.01 ppm with FWHM 4.2 ±0.04 and a shoulder consistent with an unresolved peak at -47 ±5 ppm. For 0.3 M $MgCl_2$ dissolved in BMIM_SCN the main resonance is observed at -12.3 ±0.1 ppm with FWHM 12 ±0.4 and also shoulder with an unresolved peak at -93 ±2 ppm.

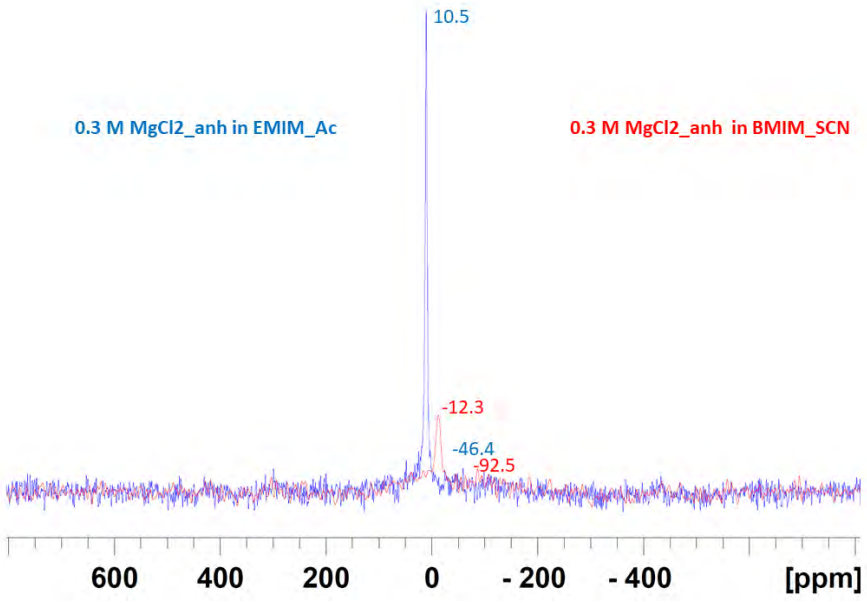

FIGURE 7.16: ^{25}Mg NMR signals of 0.3 M $MgCl_2$ in EMIM_Ac and 0.3 M $MgCl_2$ in BMIM_SCN.

This indicates that with conventional NMR we can distinguish between at least two different chemical Mg^+ environments when Ac and SCN are the anions. The difference between the two dominant signals observed is ∼23 ppm.

7.3.5 $MgCl_2$ in BMIM_SCN and Na2EDTA + $MgCl_2$ in BMIM_SCN

Trying to find a biologically interesting substance that could give a different chemical shift in conventional NMR and as a result in β-detected NMR, we prepared a sample with Ethylenediaminetetraacetic acid (EDTA). EDTA is a very effective Mg chelator and is commonly used in molecular biology. Mg^{2+} can form complexes with charged polydentate ligands, such as $EDTA^{4-}$, which are much more stable than the complexes formed with Na^+. The stability constants of EDTA with Mg^{2+} and Na^+ are 8.7 and 1.7 respectively [123] and it would be expected that Na^+ would be replaced by Mg^{2+} at the EDTA binding. It was expected that the Mg signals would differ in the absence and presence of the chelating EDTA.

Fig. 7.17 shows the ^{25}Mg NMR measurements of 0.3 M $MgCl_2$ dissolved in BMIM_SCN and 0.3 M Na_2EDTA + 0.3 M $MgCl_2$ dissolved in BMIM_SCN. The dominant signal in both cases is almost identical, at ∼-13 (0.1) ppm. Both

spectra show a broad unresolved peak at -29 (2.5) ppm without the EDTA and at -92.5 (2) ppm when EDTA is added in the solution. Even though the asymmetry around the Mg^{2+} seems not to differ significantly, when the EDTA is added, the broad chemical shift seems to move in less negative values, indicating that the electronic environment of Mg nuclei is more dense when the Na_2EDTA is added in the solution.

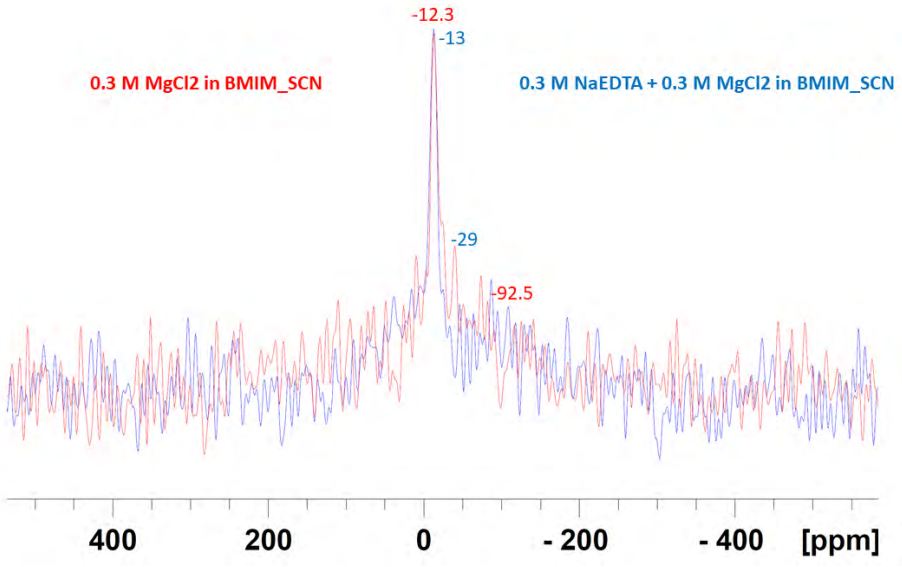

FIGURE 7.17: ^{25}Mg chemical shifts of 0.3 M $MgCl_2$ in BMIM_SCN and 0.3 M NaEDTA + 0.3 M $MgCl_2$ in BMIM_SCN.

It was expected that Mg^{2+} would bind stronger with the EDTA compared to SCN^- of BMIM. The $EDTA^{4-}$ donor atoms are the two N atoms and the four negatively charged O atoms. The electronegativity of SCN^- is known to be 2.67 according to [124] while O and N are more electronegative with 3.44 and 3.04 according to the Pauling scale. The most probable interpretation would be to assign the -29 ppm signal to the binding of Mg^{2+} with the EDTA molecule, while the -92.5 ppm signal is probably coming from MgSCN.

7.3.6 $MgCl_2$ in BMIM_SCN and Calcein + $MgCl_2$ in BMIM_SCN

Calcein is a highly negatively charged, water soluble fluorescein derivative, traditionally used for the fluorometric determination of Ca^{2+} and EDTA titration of Ca^{2+} in the presence of Mg^{2+}. This chemical reagent exhibits a yellow-green

fluoresence in the presence of certain metals ions, most notably Ca^{2+}. It has two methyleneiminodiacetic acid groups attached to the xathene portion of fluorescein. Each of these groups is equivalent to one half of the EDTA molecule. The structure of Calcein is shown in Fig. 7.18.

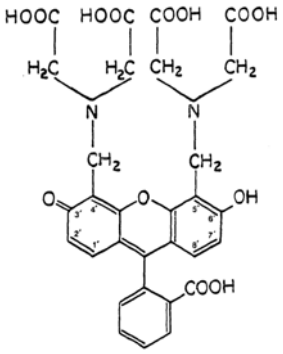

FIGURE 7.18: Calcein chemical structure.

The ^{25}Mg NMR measurements of $MgCl_2$ in BMIM_SCN and Calcein + $MgCl_2$ in BMIM_SCN show that dominant signal of Mg^{2+} shifts slightly to higher negative values. When the calcein is added in a sample with $MgCl_2$ dissolved in BMIM_SCN, the chemical shift moves upfield in more negative values, indicating that the electronic environment of Mg nuclei is more dense in the presence of calcein, as expected. Furthermore, the ^{25}Mg signal from the calcein sample seems to be more symmetric compared to one with only $MgCl_2$ in BMIM_SCN since the linewidth is smaller (FWHM= 14 ppm compared to 20 ppm). Both spectra show a second broad unresolved signal at -60 ppm. The detailed results of the ^{25}Mg NMR analysis are shown in Table 7.4.

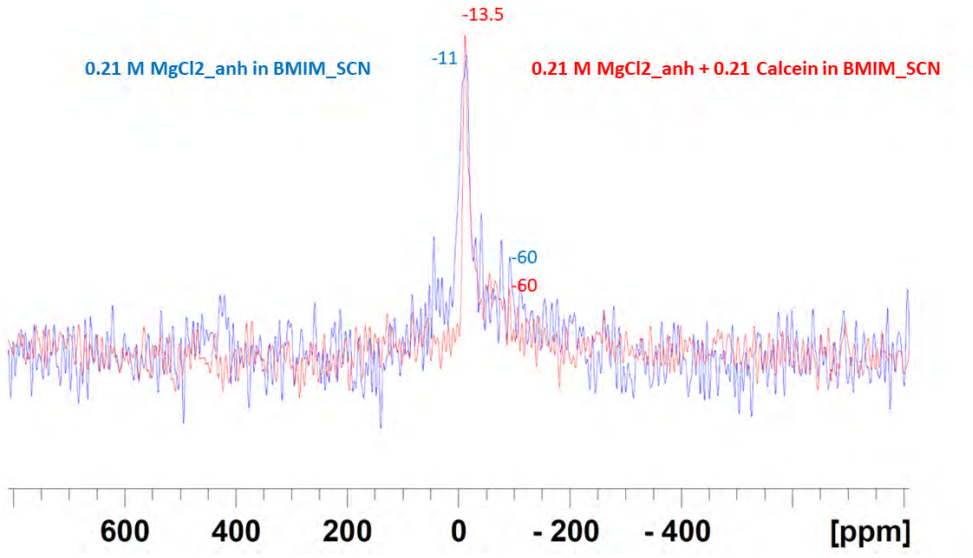

FIGURE 7.19: ^{25}Mg NMR chemical shifts of 0.21 M $MgCl_2$ in BMIM_SCN (red spectrum) and 0.21 M $MgCl_2$_anhydrous in 0.21 M Calcein solution in BMIM_SCN (black spectrum).

7.3.7 Comparison of all 25Mg NMR ILs spectra

During the current work, four different ILs were tested with ^{25}Mg NMR. In this section the results of ^{25}Mg NMR measurements of BMIM_SCN, BMIM_Ac, EMIM_Ac and EMIM_DCA with the same cation Mg salt (MgCl2) are presented in Fig. 7.20. All the presented spectra are referenced to the amplitude of the ^{25}Mg signal of the BMIM_Ac measurement.

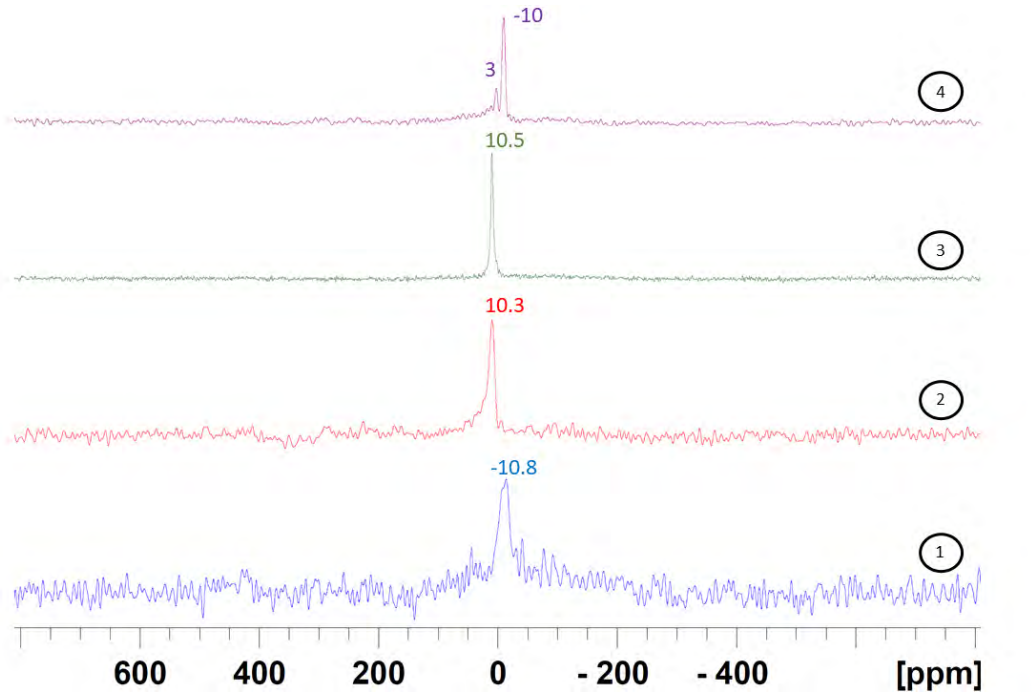

FIGURE 7.20: ^{25}Mg NMR spectra of 1. 0.3 M $MgCl_2$ dissolved in BMIM_SCN, 2. 0.3 M $MgCl_2$_anhydrous in BMIM_Ac, 3. 0.3 M $MgCl_2$_anhydrous in EMIM_Ac, 4. $MgCl_2$_anhydrous in EMIM_DCA.

As a first remark, we see that the dominant ^{25}Mg NMR signals from the BMIM_Ac and BMIM_SCN samples are 22 ppm away. In spectrum 2, we can see only signal at 10.3 ppm, while in spectrum 1 there is a dominant signal at -11 ppm and a second unresolved signal at around -60 ppm (see Table 7.4. This could probably mean that in BMIM_SCN, since SCN^- can bond with Mg^+ with both S and N, there are two electronic environments that contribute to the signal. On the other hand acetate has O as donors, creating one and symmetric environment around Mg^+. The difference between the linewidths of both spectra could be attributed to the possible fast dynamics and the exchange between the two S and N binding sites of SCN. Between the two acetate-bases ILs, the EMIM_A and BMIM_Ac, the dominant signal's position is identical. The linewidth of the EMIM_Ac ^{25}Mg signal is three times smaller that the signal from the BMIM_Ac sample, corresponding to a more symmetric electronic environment around Mg. Last, the EMIM_DCA sample shows at least two well resolved peaks, at 3 and at -10 ppm, therefore at least two coordination environments with slow dynamics and exchange in the ms scale. The linewidth of both signals is 6 ppm. For the detailed results of the analysis please refer to Table. 7.4.

TABLE 7.4: ^{25}Mg NMR analysis of all the samples measured

sample	Peak position ppm	Peak Frequency Hz	FWHM ppm	FWHM Hz	Amplitude
0.3 M MgCl2 in BMIM_Ac	10.3 (0.1)	314 (5)	13 (0.4)	391 (13)	983 (23)
0.3 M MgCl2_anh in BMIM_SCN	-10.8 (0.2)	-331 (6)	20 (0.0)	606 (27)	904 (20)
	-60 (6)	-1826 (171)	155 (11)	4747 (330	161 (9)
0.21 M MgCl2 + 0.21 M Calcein in BMIM_SCN	-13.5 (0.2)	-414 (7)	14 (0.7)	427 (22)	910 (32)
	-60 (1)	-1841 (34)	63 (3)	1907 (99)	197 (5)
0.3 M Na2EDTA + 0.3 MgCl2 in BMIM_SCN	-13 (0.1)	-411 (4)	9 (0.5)	287 (15)	798 (22)
	-26 (2.5)	-792 (77)	116 (6)	3578 (186)	245(11)
0.3 M MgCl2_anh + EMIM_Ac at 70°C	10.5 (0.01)	322 (0.5)	4.2 (0.04)	128 (1.4)	992.5 (1.4)
	-46.4 (5.5)	1419 (167)	99.5 (17)	3044 (520)	15 (1.5)
0.3 M MgCl2_anh + EMIM_Ac at 25°C	39 (1.5)	1190 (45)	169 (4)	5175 (130)	711 (12)
0.3 M MgCl2_anh + EMIM_DCA at 70°C	3 (0.2)	96 (7)	6 (0.7)	197 (23)	268 (19)
	-10 (0.06)	-310 (2)	6 (1)	171 (5)	1059 (20)
	-86 (2)	-2648 (55)	60 (6)	1839 (175)	34 (2)

Note 1. The chemical shifts were calculated using as reference compound the 11 M $MgCl_2$*$6H_2O$ in D_2O.

Note 2. All the fits are performed with 100% lorentzian lineshapes.

7.3.8 T1 relaxation measurements of ^{25}Mg signals from different ILs

For further characterising the different ILs, we attempted to measure the *T1* relaxation times with the Inversion Recovery (IR) technique. The measurements were done at 70°C (343 K) and the repetition delay time, the Inversion Time (TI), varied to the following values: 1 ms, 2 ms, 4 ms, 8 ms, 16 ms, 32 ms, 64 ms, 128 ms, 256 ms.

From the samples containing Mg^{2+} tested, due to the limited time of the NMR experiments, we measured only the T1 relaxation time for $MgCl_2$_anhydrous in EMIM_Ac and $MgCl_2$_anhydrous in BMIM_Ac. Table. 7.5 shows the analysis results. The T1 relaxation for the Mg2+ bound to Ac and SCN is fast, in the range of hundreds of μs.

TABLE 7.5: T1 relaxation time of bound Mg^+

Sample	T1 [us]
0.3 M MgCl2 in $EMIM_{Ac}$	230(±30)
0.3 M MgCl2 in $BMIM_{SCN}$	540(±30)

Chapter 8

Experimental results β-detected NMR

8.1 Commissioning of the new laser polarisation setup at ISOLDE with ^{26,28}Na

The goal of the online commissioning studies was to reproduce the degree of polarisation of ^{26,28}Na reported by the COLLAPS collaboration at ISOLDE [102]. This assured the reliable functioning of all the elements of the new laser-polarisation setup and helped us to optimise the different settings in order to maximise the degree of polarisation that is reflected in the observed β-decay asymmetry. The maximisation of the polarisation and the β-decay asymmetry is essential for observing the NMR signals from liquid biological samples. In this direction, several NaF, one $NaNO_3$ and one NaCl crystals were tested as the host material and were mounted on a sample holder as shown in Fig. 8.1 and Fig. 8.2.

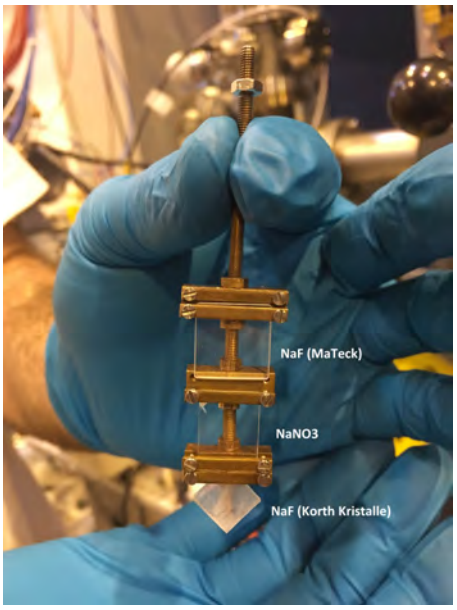

FIGURE 8.1: Sample holder arrangement of the first experimental campaign.

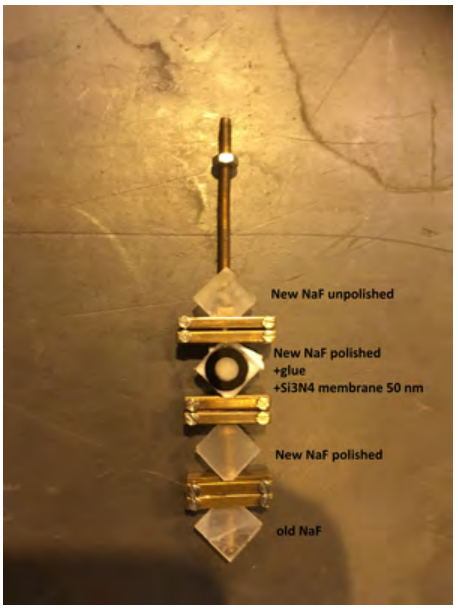

FIGURE 8.2: Sample holder arrangement of the second and third experimental campaigns.

The vacuum chamber for β-detected NMR experiments, provided by the COLLAPS collaboration, shown in Fig. 8.3, consists of four flanges, two thin 200μm Al windows for β particles and two pockets for hosting the β scintillator detectors. The flanges are one back CF type 63 flange that is connected with the beam diagnostics in the end of the beamline, one bottom non-standard KF type flange that is connected with with a bottom plate, one top CF 40 flange through to which we introduce the crystal holder system and one front CF 40 flange connected to the front of the beamline.

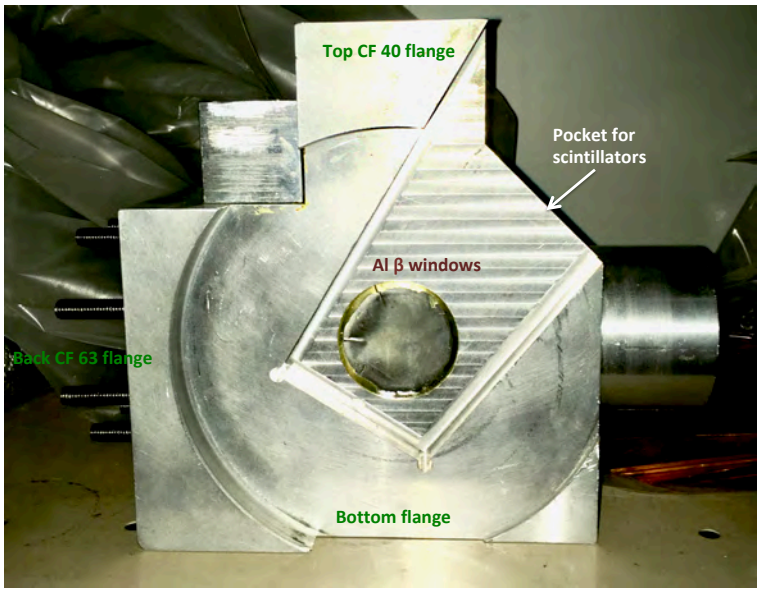

FIGURE 8.3: The COLLAPS β NMR chamber.

The crystal holder was screwed in an Al rod that was fixed on a CF blank flange. The rod and the flange are connected with a bellow system used to move the crystal holder in/out the centre of the NMR chamber (i.e. in and out of the beam path), as shown in Fig. 8.4.

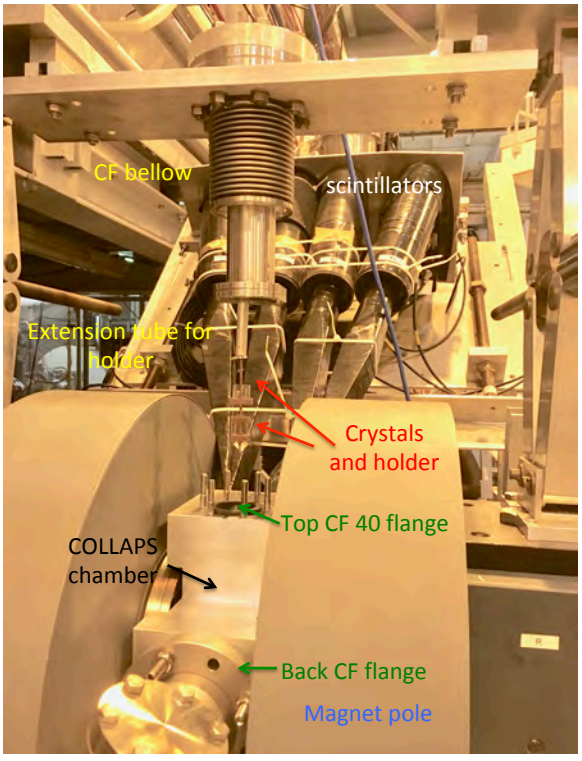

FIGURE 8.4: Magnet system with COLLAPS β-NMR chamber in place and CF bellow system with crystal holder.

8.2 ^{28}Na and ^{28}Na ions production

The Na isotopes were produced by a UC_x target with tungsten surface-ionisation source, the beam was accelerated to 30.2 keV and was mass-selected in the high resolution separator (HRS). The data acquisition triggered when a μs proton bunch from the CERN's Proton Synchrotron Booster (PS Booster) hit the target (this took place every 1.2 s or its multiples). For ^{26}Na the time between the consecutive proton bunches was selected to be 2.4 s or more while for ^{28}Na, due to its very short half-life, the proton bunch was accepted every 1.2 s. The produced ions were let into the new laser polarisation beamline for 2.3 s or 200 ms after the proton impact for ^{26}Na and ^{28}Na respectively. For nuclei with long-half-lives in the seconds range, the time between successive proton pulses must be programmed to optimise the effective beam intensity/count rate, while assuring a minimum overlap of beam bunches from different proton impact pulses. The aim is to perform a full cycle of polarisation-to-β-NMR measurement without contamination from the previous polarised beam bunch. This is achieved by proper programming the super-cycle of the booster, where the periodicity of the proton pulses is set and combined with the opening of the ISOLDE beam gate. Often, by delaying the opening of the ISOLDE beam gate after proton impact can be used to minimise the contamination of isobar species with half-lives much shorter than the element/isotope of interest.

The commissioning tests spread over three short runs, including changes in laser polarisation and laser power, change of the implantation crystal and changes in the strength of the guiding and the strong magnetic fields. During the first commissioning tests, different crystals were tested as shown in Fig. 8.1. At room temperature NaF turned out to be better than the $NaNO_3$ host, giving rise to higher β-decay asymmetry signals. Different NaF crystals were used during the commissioning tests of the new laser-polarisation setup. Two of the NaF crystals were polished in order to test the use of a sharp implantation surface and they were annealed up to 100°C for approximately 12 hours, in order to become moisture free as it was believed that absorbed water in the crystal could affect the T_1 relaxation. At room temperature NaF turned out to be superior to the other hosts, as it is known to have a long relaxation time of 37 s for Na .

8.2.1 Magnetic field mapping of the new beamline

Before the commissioning experiments the magnetic field mapping of the new beamline was done. In Fig. 8.5 the total magnetic field strength in the geometrical centre of the beamline is shown as measured by NMR probe.

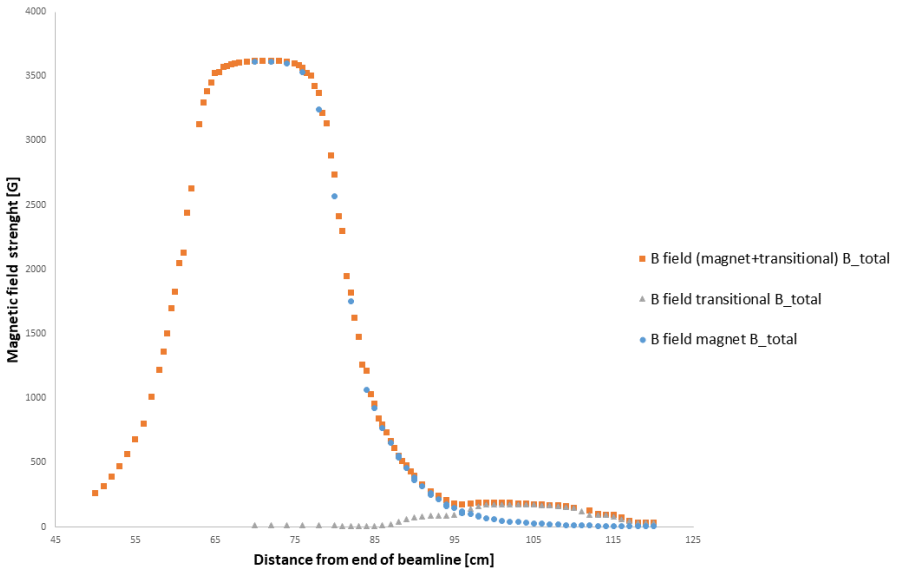

FIGURE 8.5: Magnetic field mapping from the end of the beamline (beam diagnostics) till the end of the CEC (beginning of the optical pumping region).

8.3 β asymmetry dependence on strong magnetic field B_0

The first test was to study the dependence of the polarisation degree on the strength of the magnetic field provided by the dipole electromagnet. Bellow we describe relevant parameters that were kept constant during these tests:

1. ^{26}Na atomic beam
2. NaF polished crystal as the host material
3. magnetic field of the optical pumping section was fixed at 1.7 mT
4. magnetic field of the big solenoid was fixed at 3 mT

5. small solenoid of the transition field at 17.4 mT
6. sign of the laser polarisation was σ^+
7. power of the laser light was at 150 mW
8. iris position at the beginning of the beamline was totally open and the atomic beam size was the maximum possible

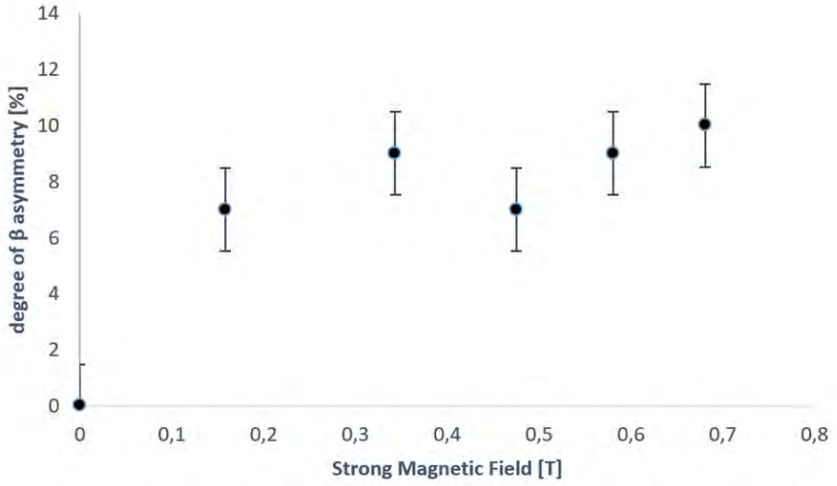

FIGURE 8.6: β-asymmetry of ^{26}Na atomic beam as a function of the magnetic field in the center of the magnet. The error bars correspond to the measurement uncertainty.

In Fig. 8.6 we can observe that the measured β-decay asymmetry and thus the polarisation doesn't change significantly with the change of the magnetic field strength. Only when no magnetic field is applied (I=0 A) the β-asymmetry is 0. This result indicates that the atomic and nuclear spins of ^{26}Na were fully decoupled even at lower fields used.

8.4 β asymmetry dependence on guiding magnetic fields along the beamline

We further studied the dependency of the polarisation and consequently the β asymmetry on the different magnetic fields applied along the beamline.

Starting from the magnetic field created by the Helmholtz coils around the optical pumping section, all the other parameters bellow remained unchanged:

1. ^{26}Na atomic beam
2. NaF polished crystal host material
3. magnetic field of the big solenoid was fixed at 5.1 mT
4. transitional field of the small solenoid was fixed at 17.4 mT
5. strong magnetic field of the electromagnet was fixed at 343 mT
6. sign of the laser polarisation was σ^+
7. power of the laser light was at 130 mW
8. iris opening at the beginning of the beamline was 15 mm

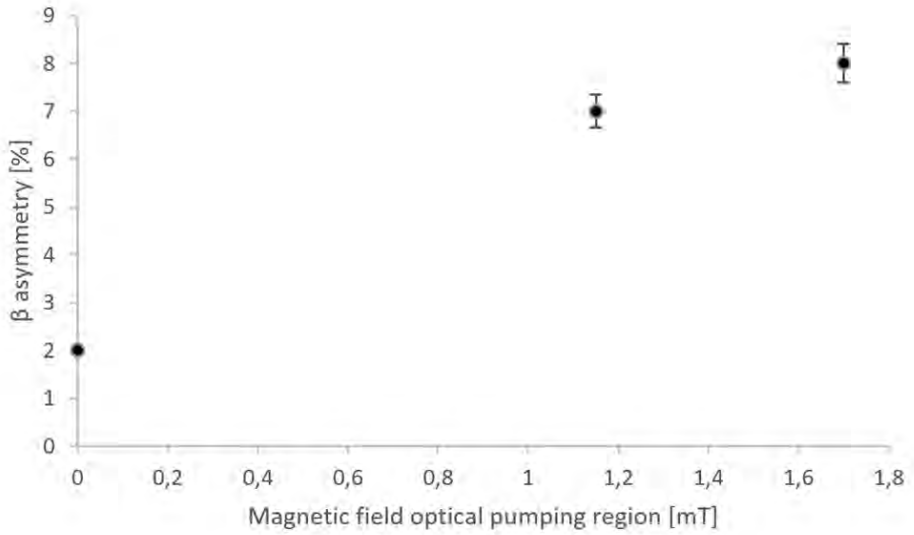

FIGURE 8.7: β-asymmetry of ^{26}Na atomic beam as a function of the guiding magnetic field created by the Helmholtz coils in the center of the magnet. The error bars correspond to the measurement uncertainty.

In Fig. 8.7 it is shown that the degree of polarisation depends on the magnetic field at the optical pumping region. The maximum β asymmetry is reached when the magnetic field created by the Helmholtz coils is 1.7 mT (I=6 A). At 0 T the beta asymmetry is only 2%. This indicates that the guiding magnetic field around the optical pumping region is necessary for maintaining the atomic polarisation achieved during the optical pumping procedure.

Next, we studied the dependency of the β asymmetry on the transitional magnetic field of the small solenoid, which served for the decoupling of the atomic and nuclear spins. The parameters bellow remained unchanged:

1. ^{26}Na atomic beam
2. NaF polished crystal as the host material
3. magnetic field of the optical pumping section was fixed at 1.7 mT
4. magnetic field of the big solenoid was fixed at 3.0 mT
5. strong magnetic field of the electromagnet was fixed at 680 mT

6. sign of the laser polarisation was σ^+
7. power of the laser light was at 150 mW
8. iris at the beginning of the beamline was fully open

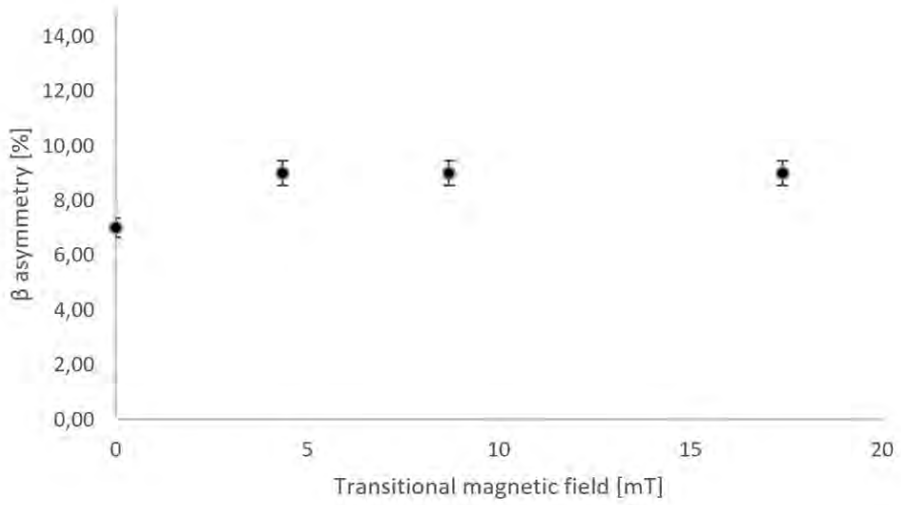

FIGURE 8.8: β-asymmetry of ^{26}Na atomic beam as a function of the transitional magnetic field created by the small solenoid. The error bars correspond to the measurement uncertainty.

Fig. 8.8 shows the degree of β asymmetry as a function of the transitional magnetic field created by the small solenoid infornt of the electromagnet. The β asymmetry does not show dependence on the strength of the small solenoid's magnetic field, meaning that the atomic and nuclear spins are being fully decoupled for any value higher than 5 mT.

As a result, the experimental β asymmetry (polarisation) of ^{26}Na atomic beam was found not to depend on the transitional and the strong magnetic field B_0 beyond the minimal values applied while it depends strongly on the guiding magnetic field of the optical pumping region.

8.5 Hyperfine structure (HFS) of ^{26}Na and ^{28}Na

During the commissioning tests the hyperfine structure of the atomic D2 line of ^{26}Na and ^{28}Na ($^2S_{1/2} \rightarrow {}^2P_{3/2}$ at 589 nm) with both right-handed (σ^+) and left-handed (σ^-) helicities of the laser light were recorded. We used a dye laser belonging to the COLLAPS collaboration pumped by an Nd:YAG laser.

8.5.1 Hyperfine structure of ^{26}Na

The HFS of ^{26}Na recorded for both helicities of the laser light (σ^+ and σ^-) is shown in Fig. 8.9. The experimental asymmetry was the highest (24%) for the σ^+ and corresponds to the strongest transition $|^2S_{1/2}{:}F{=}I{+}1/2\rangle \rightarrow |^2P_{3/2}{:}F'{=}I{+}3/2\rangle$. The degree of the β-asymmetry is comparable to the one reported earlier by the COLLAPS collaboration ($\sim$ 36%) [102], although somehow lower. The maximum experimental asymmetry allowed us to calculate the maximum achieved polarisation that is 28%, based on Eq. 6.4, taking into account that the opening angle of the β-detectors is 35° and the β-asymmetry parameter for ^{26}Na is -0.93(2) [103].

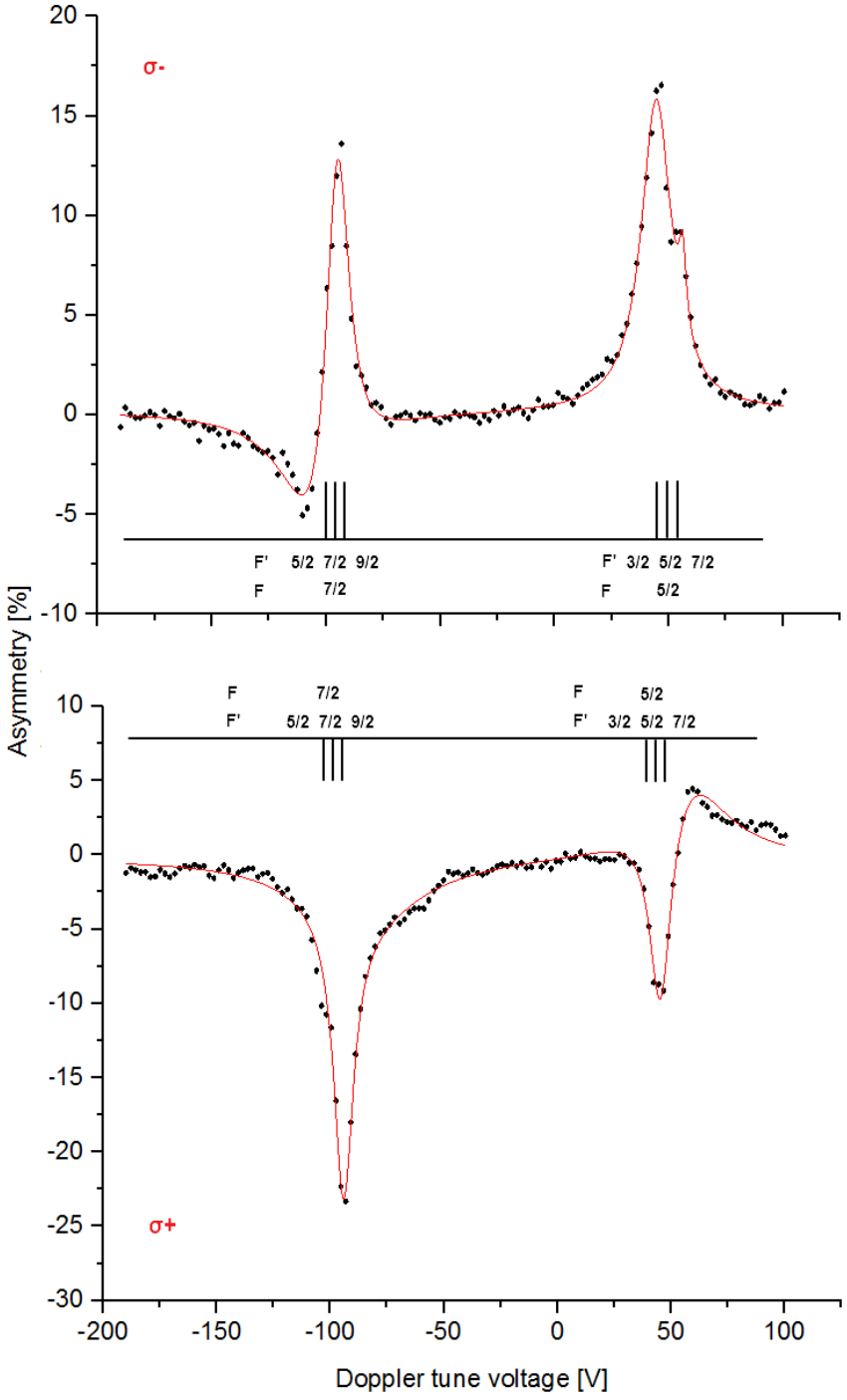

FIGURE 8.9: HFS of the D2 line in the atomic ^{26}Na as a function of the Doppler tune voltage observed in the β-decay asymmetry following excitation with σ^- (top) and σ^+ (bottom) light. Each point corresponds to experimental β counts recorded after only 1 proton pulse. Red line is the fitted multi-peak Lorentzian. Independent instrumental baseline was subtracted from all spectra. The statistical uncertainties in ^{26}Na spectra are smaller than the points [23].

8.5.2 Hyperfine structure of ^{28}Na

The HFS of ^{28}Na recorded again for both helicities (σ^+ and σ^-) is shown in Fig. 8.10. The highest experimental asymmetry (40%) is observed for the σ^+ polarised laser light and corresponds to the strongest transition $|^2S_{1/2}{:}F{=}I{+}1/2\rangle \rightarrow |^2P_{3/2}{:}F'{=}I{+}3/2\rangle$. The degree of the β-asymmetry is almost the same as the one reported earlier by the COLLAPS collaboration (44%) [102]. This result showed that the commissioning campaign was successful, since we managed to reproduce the degree of polarisation achieved before. The maximum polarisation was calculated 59%, as explained for ^{26}Na, taking into account that the β-asymmetry parameter for ^{28}Na is -0.75(1) [103].

For ^{28}Na we get a higher degree of polarisation than for ^{26}Na (as in previous study). This is due to the fact that ^{28}Na has a lower spin (I=1) compared to ^{26}Na (I=3) and the population of spins spreads in fewer substrates.

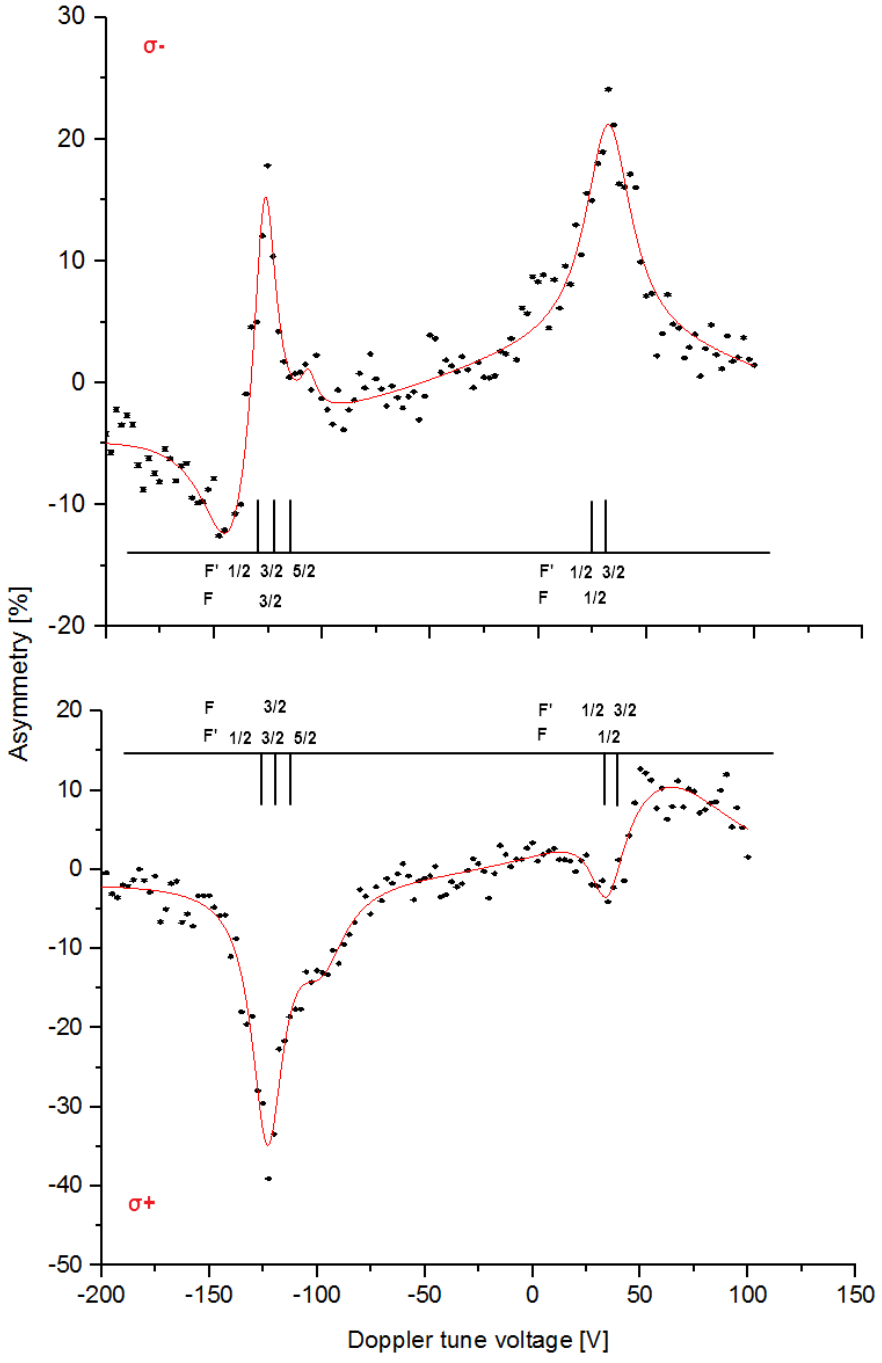

FIGURE 8.10: HFS of the D2 line in the atomic ^{28}Na as a function of the Doppler tune voltage observed in the β-decay asymmetry following excitation with σ- (top) and $\sigma+$ (bottom) light. Each point corresponds to experimental β counts recorded after only 1 proton pulse. Red line is the fitted multi-peak Lorentzian. Independent instrumental baseline was subtracted from all spectra. The statistical uncertainties in ^{26}Na spectra are smaller than the points. [23]

Table 8.1 summarises the results from the current experiments for the maximum

asymmetry and polarisation, compared with the ones achieved by the COLLAPS collaboration [102].

TABLE 8.1: Properties of ^{26,28}Na and β-decay asymmetry results for σ^+ light

	^{26}Na	^{28}Na
spin	3	1
half-life	1.1 s	30 ms
β-asymmetry parameter [103]	-0.93(2)	-0.75(1)
β-asymmetry of current work	24(4)%	40(9)%
β-asymmetry at COLLAPS [103]	36.6(12)%	44.2(7)%
nuclear polarisation of current work	28%	59%
nuclear polarisation at COLLAPS [103]	39(1)%	59(1)%

8.6 β NMR experiments with Ionic Liquids (ILs)

8.6.1 The liquid handling system

Moving from the solid state to liquid β-NMR experiments was not a trivial task. The first point addressed was the type of liquids that could be used at 10^{-6}mbar, which is the pressure that is required to transmit efficiently the ISOLDE low-energy radioactive beam. The water vapour pressure at room temperature is approximately 20 mbar, meaning that water would either evaporate or freeze immediately as experimentally observed once more during our first off-line tests. For that reason, room temperature Ionic Liquids (ILs) were considered as the best solution for the first feasibility tests of the liquid β NMR experiments, more specifically those bassed on 1-Butyl-3-methylimidazolium (BMIM).

The second point was the design of a system (referred from now on as the liquid handling system (LHS)) that would allow the controlled flow of the IL from the atmospheric environment inside the vacuum chamber and moreover, would allow to maintain the liquid sample in the centre of the magnetic field long enough for recording an NMR signal. Extensive tests under vacuum were performed. Some involved custom made borosilicate glass capillaries that we manipulated mechanically to get different tip shapes in order to find the optimised dimensions and conditions for forming the liquid drop. The inner diameter of the glass capillaries

was 3 mm and the glass wall thickness was 2 mm. The initial idea was to use a very short tip of 10 mm with a diameter 0.5 mm). The tip was designed with a thick wall (∼ 1 mm) since the drop could be held better by surface tension on the tip end.

In Fig. 8.11 one can see one of the glass tubes and an inner PTFE capillary used for guiding the liquid to the end of the glass capillary. Here one of the successful tests of this idea is shown, where a liquid drop of an IL was formed and was maintained in the same position almost for a day at 10^{-5} mbar. Unfortunately this behaviour was not easily reproducible and the idea of the drop formation was discarded while the idea of using a substrate was studied.

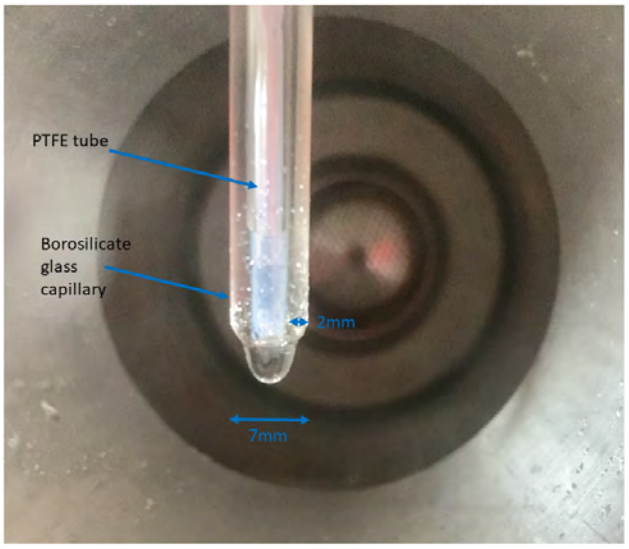

FIGURE 8.11: Successful test of the liquid drop formation.

The most effective way of controlling the ILs' dispensing on the substrate turned out to be a system made of several vacuum valves (Swadgelock type) connected with vacuum-tight tubes. As seen in Fig.8.12 it consists of four PFA (PerFluoroAlkoxy) vacuum tight-valves connected with 1/4" PFA tubes. Valve 1 was connected through a PFA 1/4" with the vacuum chamber. Valve 3 connected the LHS with the Ar bottle used to vent the chamber. Valve 4 was connecting the LHS with a dry prepump for degassing purposes. Valve 2 was used to insert the liquid sample (IL) into the LHS. This was done with a long syringe through a PFA inner plastic tube of 2 mm diameter while the system was vented with Ar, with the Valve 1 closed, in order not to vent the vacuum chamber. Once the liquid started flowing towards Valve 1, Valves 2,3 and 4 were closed. When the liquid

sample was observed close to Valve 1, Valve 4 was opened and vacuum was applied in the LHS allowing for degassing the sample for approximately 1h at 10^{-3}mbar in order to avoid inserting gas bubbles in the vacuum chamber that would potentially lead to the sample's removal from the substrate. When the liquid was well degassed (judged by absence of air bubbles coming out of it), Valve 1 was opened and the liquid started flowing in the inner 2mm PFA capillary until it reached the substrate's surface. Valve 4 was connected with a dry prepump to evacuate the LHS from air but also to help creating a backpressure that was expected to help the liquid drop to stay in place. During the experiments it was observed that the hydrophilicity of the substrate used played a very important role and the samples could stay at the same position long enough for the purpose of our experiments.

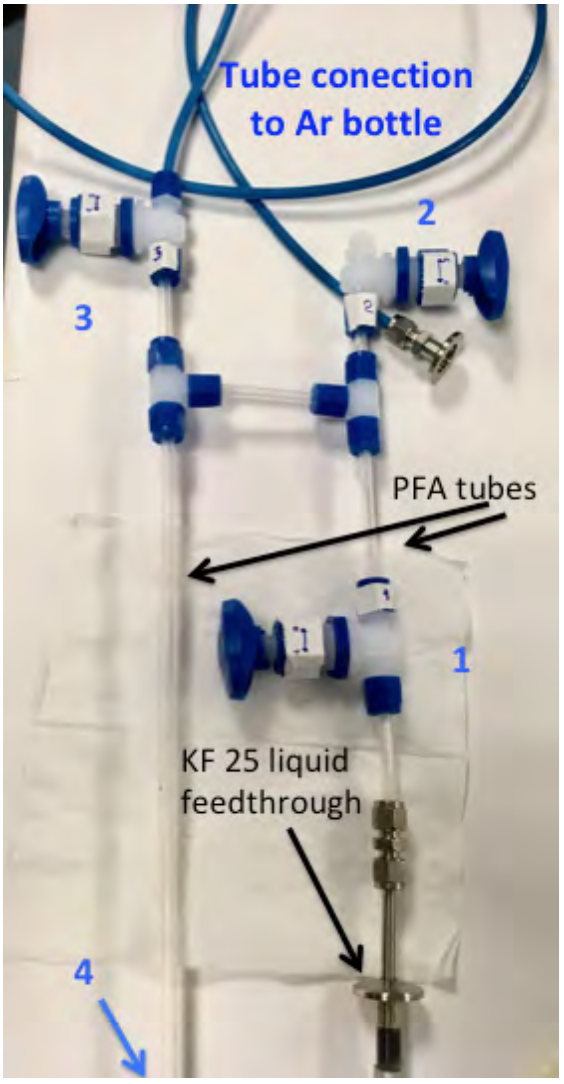

FIGURE 8.12: Liquid Handling System (LHS) based on PFA tubes and PFA Swagelok valves.

The polarised radioactive beam can be implanted in several hosts. Fig. 8.14 shows a custom-made glass capillary with 1 mm tip opening leading to the substrate that hosted the liquid samples for the β NMR measurements reported in this work. A mica substrate was placed at 45° relative to the beam axis, supported by a holder which was 3D printed from a vacuum-compatible resin. On the glass capillary, a 45° bend was made in order to place the NaF crystal needed for the reference measurements during the experiments. On top of the NaF crystal a second mica substrate was placed for measuring the background β asymmetry and β NMR signal that the substrate itself could possibly give.

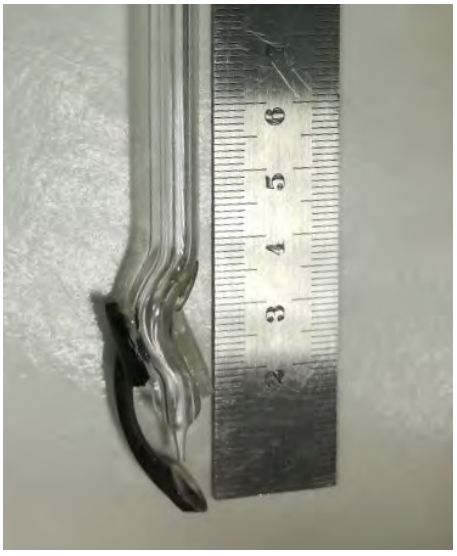

FIGURE 8.13: Glass capillary system side view for visualising the bend.

FIGURE 8.14: Glass capillary system front view, as the radioactive beam sees it.

The glass capillary system was attached to a CF 40 bellow that could be extended or shorthened with three long non-magnetic rods, for alignment purposes. The bellow was connected with the liquid feedthrough through an aluminium tube, Fig. 8.15.

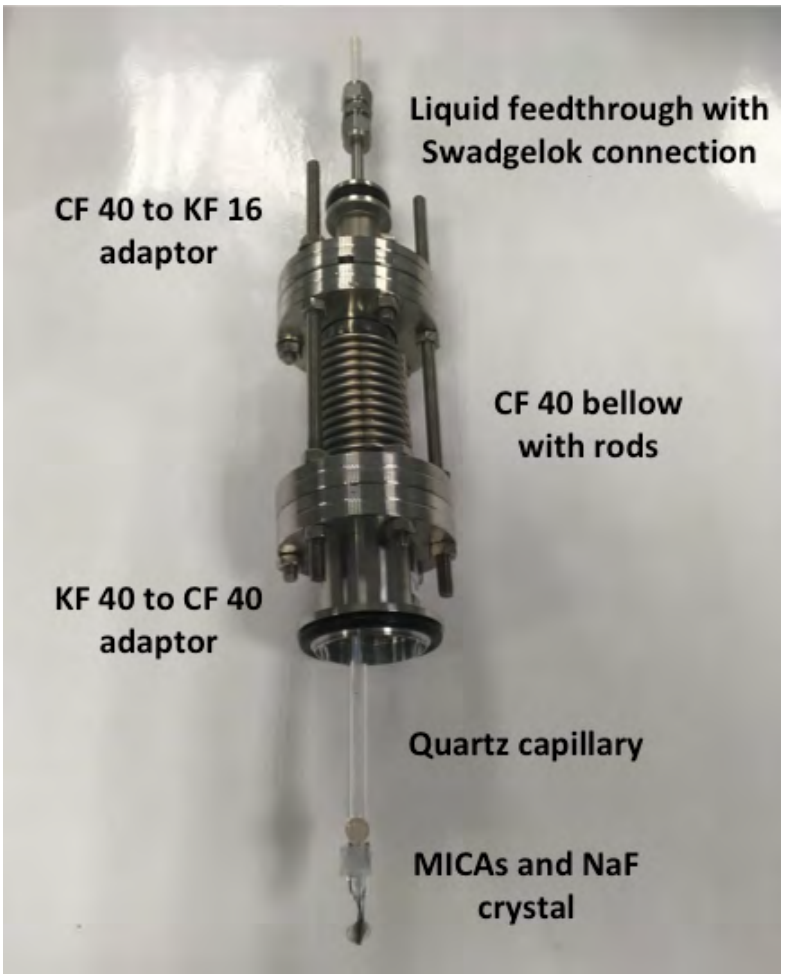

FIGURE 8.15: The glass capillary system connected with the liquid feedthrough and the bellow.

A view of the complete LHS system as used during the experiments is shown in Fig. 8.16. The LHS with the glass capillary system and the bellow were connected to the β NMR chamber.

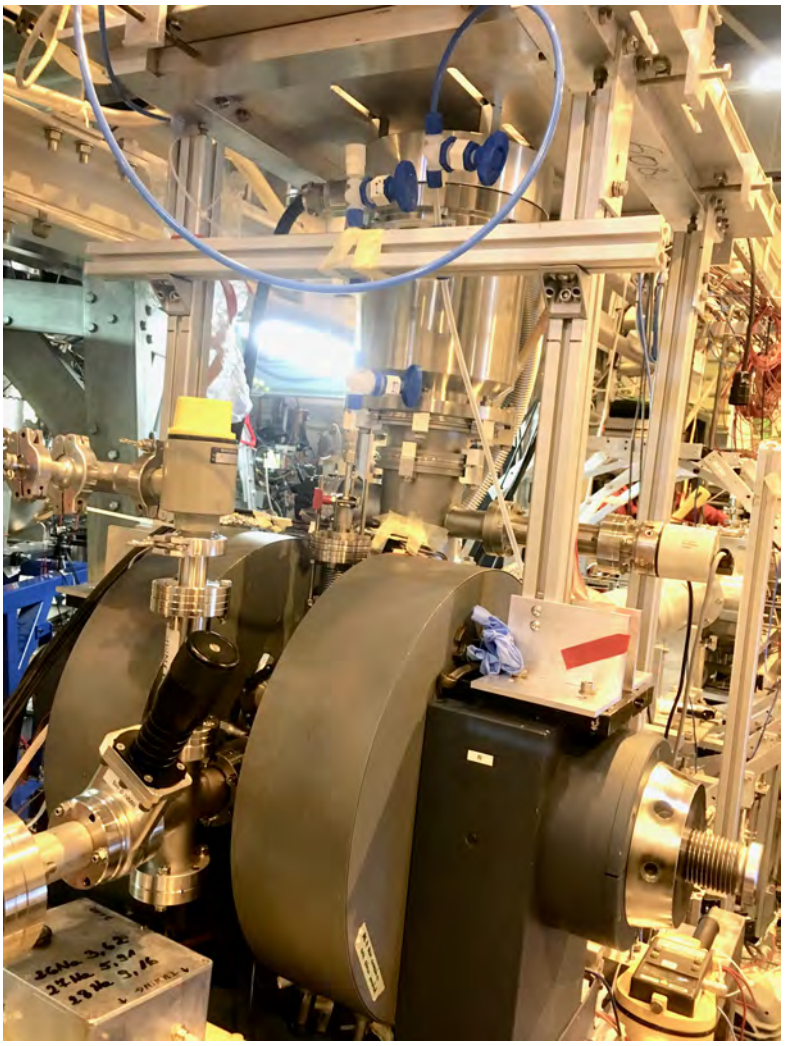

FIGURE 8.16: LHS and quartz capillary system connected with the β NMR chamber.

8.6.2 First β NMR results in NaF and ILs

The first β NMR spectrum at the new ISOLDE beamline was recorded successfully by implanting ^{26}Na atomic beam in the NaF crystal and several ILs. The strong magnetic field of the electromagnet was 0.6 T.

Fig. 8.17 shows the comparison between the signal of ^{26}Na in a NaF crystal and in 1-Butyl-3-methylimidazolium Formate (BMIM_HCOO) IL. At the top left we can see a zoom-in of the β NMR signal of BMIM_HCOO. Both spectra were acquired with 120 mV RF pulse amplitude. The ^{26}Na signal from the solid crystal has a FWHM of 7.0(5) kHz for a 7.2(1)% β-decay asymmetry, while the one from BMIM_HCOO has a FWHM of 48(5) Hz and almost the same asymmetry,

6.0(3)%. This much narrower resonance is due to the averaging of the ^{26}Na interactions with the molecules of the liquid host and is well known in conventional NMR.

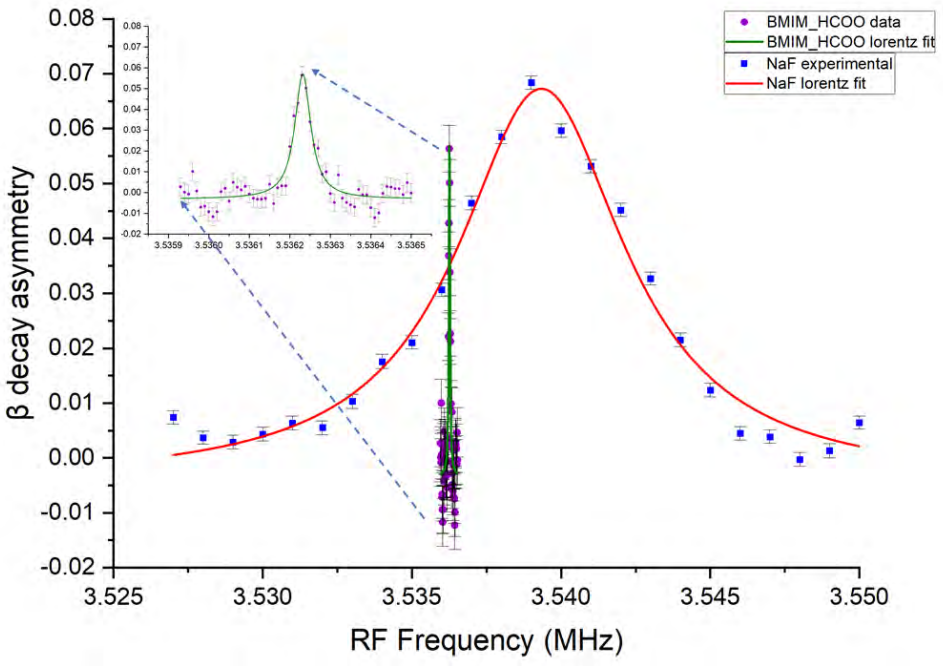

FIGURE 8.17: β NMR signals from ^{26}Na implanted into a NaF crystal and BMIM_HCOO IL.

Five different liquid samples were studied during the experiments, as described bellow:

- BMIM_Ac (1-Butyl-3-methylimidazolium Acetate) IL without any pre-dissolved $^{23}Na^{+}$
- BMIM_HCOO (1-Butyl-3-methylimidazolium Formate) IL without any pre-dissolved $^{23}Na^{+}$
- 0.1 M NaAC dissolved in BMIM_Ac
- 0.1 M NaAc dissolved in BMIM_HCOO
- 0.1 M double-stranded salmon DNA dissolved in BMIM_HCOO

Fig. 8.18 shows the resonance position in different liquid samples as a function of the start time of the first measurement. There is an increasing trend between each measurement showing that for different samples the magnetic field at the nucleus

gets shifted to higher values. At the time of the measurements there was no field stabilisation system for correcting the drift of the strong magnetic field, B_0. In order to verify if there was a B_0 drift or there was a real difference between the chemical shifts magnetic field stability at the measurement position was studied. The long-term stability measurements were repeated 2 times and they took place right after the experiments. They showed that there was an increasing drift of 1 ppm/h for the B_0 (during an observation time of 30 h). The dashed black line in Fig. 8.18 corresponds to this drift.

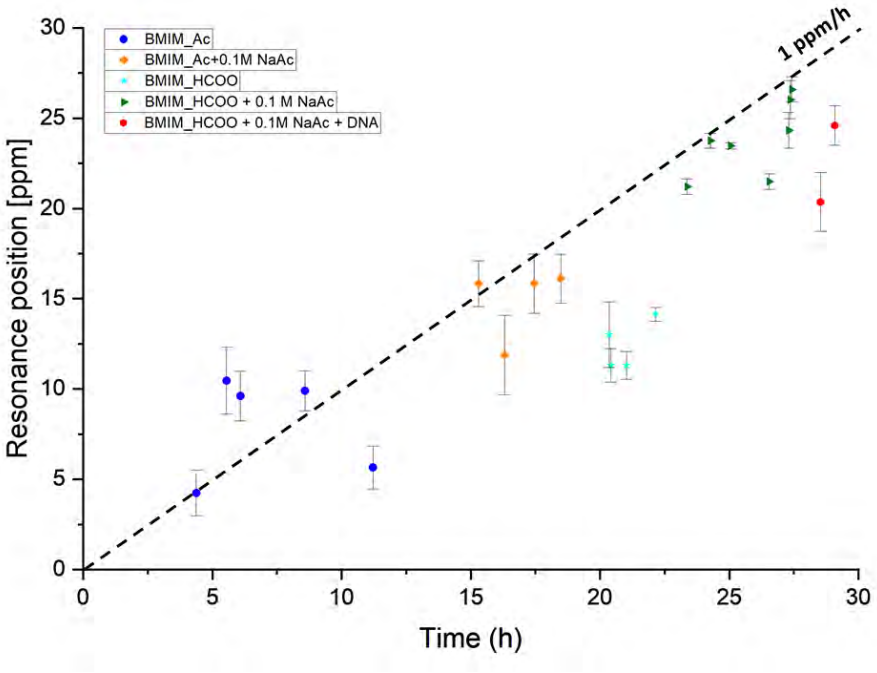

FIGURE 8.18: ^{26}Na NMR signal position in ppm from the start time of the first measurement. The chemical shifts in ppm were calculated using an arbitrary reference ν_f=3.536 MHz.

Fig. 8.19 shows the resonance position corrected for the above shift. It seems that there is no difference in the ^{26}Na resonance position between the BMIM_Ac samples, without salt and with a NaAc salt. We can see that there is a slight difference between the Na NMR signals in the two different ILs. More precisely, the Na signal coming from BMIM_HCOO is downshifted by ≈ 4 ppm compared to the one originating from BMIM_Ac. This could possibly mean that the Na atoms are less shielded when interacting with HCOO and more shielded by the acetone molecules. The Na NMR signals of BMIM_Ac + 0.1 M NaAc and BMIM_HCOO + 0.1 M NaAc seem to be the same. We can not say with big certainty that there is a difference in resonance position for the BMIM_HCOO + 0.1 M NaAc with

the salmon DNA. As B_0 was not recorded during the measurements, we cannot exclude that these chemical shifts are due to fluctuations and drifts in the magnetic field.

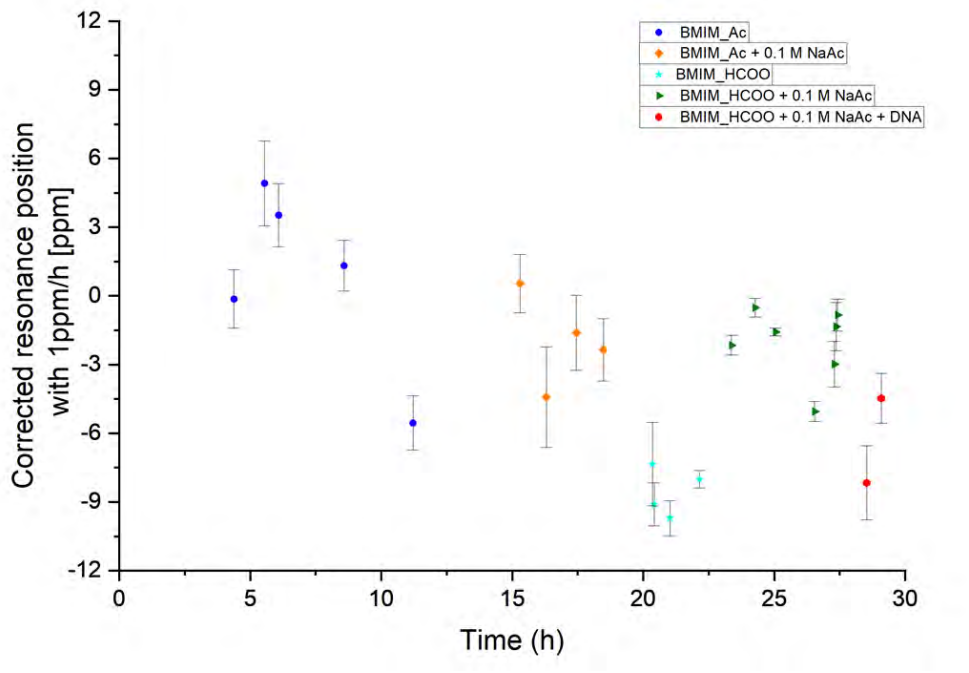

FIGURE 8.19: ^{26}Na NMR signal position corrected for 1 ppm/h drift from the measurements. 0 ppm corresponds to an arbitrary reference ν_f=3.536 MHz.

Unlike the position of the Na NMR signal, the FWHM of the different signals did not show any correlation with the continuously increasing B_0 during the experiments. Fig. 8.20 shows that independently of the time that the measurement took place and the samples, the FWHM of the resonances were very similar for the same RF pulse amplitude.

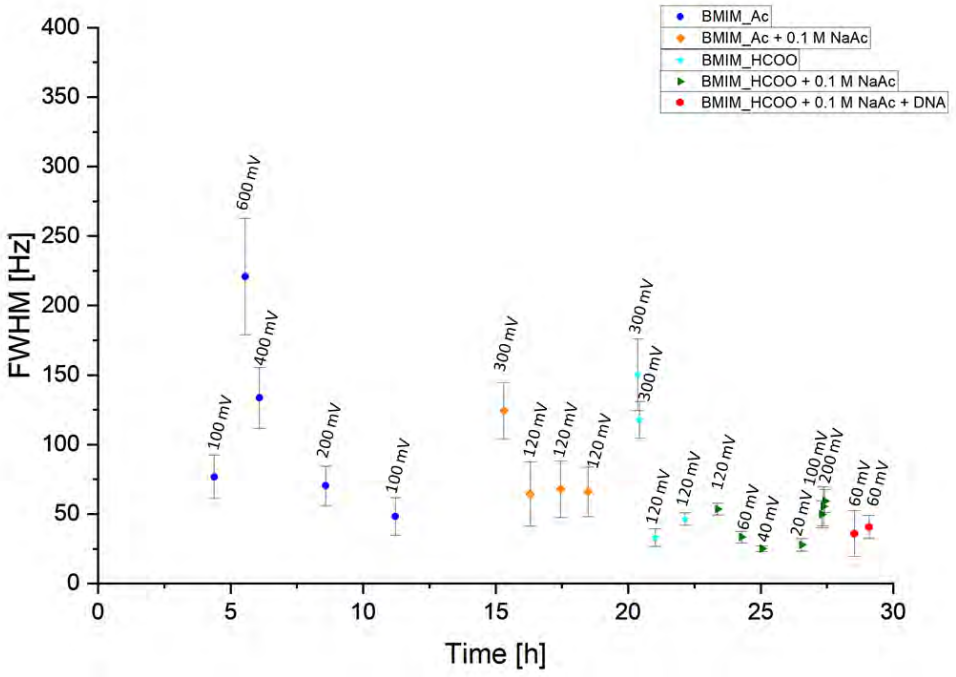

FIGURE 8.20: FWHM of ^{26}Na resonances presented also in Fig. 8.18 and Fig. 8.19.

The FWHM of the peak relates strongly with the RF amplitude of the RF pulse. The higher the RF amplitude the broader the peak is, independently the sample measured, due to the power broadening.

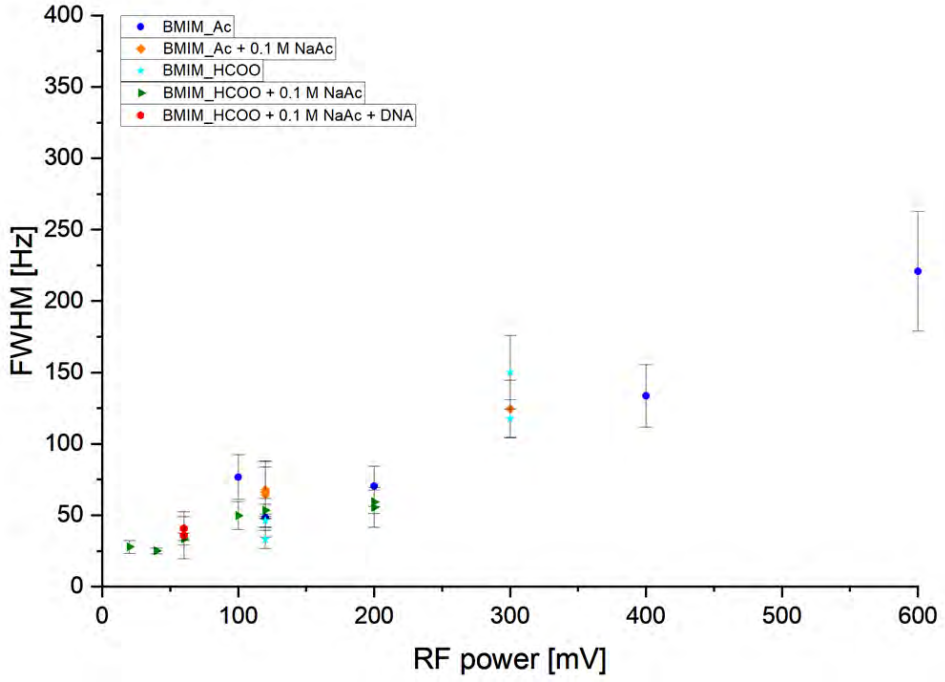

FIGURE 8.21: FWHM of ^{26}Na resonances as a function of RF pulse amplitude.

Summarising, we succeeded in recording for the first time at the new beamline at ISOLDE β NMR signals from different liquid samples and one containing DNA. As expected the resonances coming from liquids were much narrower compared to those coming from solid state samples (linewidths of Hz instead of kHz).

Chapter 9

Summary and Future prospects

This thesis constitutes a description of three nuclear techniques which can be applied to chemistry and biochemistry. The PAC spectroscpy, the NMR and β-detected NMR spectroscopies.

As has been presented in Chapter 4, a new PAC isotope, the ^{68m}Cu, can serve as a copper probe for PAC experiments. Due to the newly calculated quadrupole moment that is relatively small and the relatively short half life of the intermediate energy state, it seems difficult to use it as a PAC probe for elucidating Cu(I) coordination geometries in metalloproteins. On the other hand, after calculating the nuclear moments of the ^{68}Cu ground state, the ^{68m}Cu-^{68}Cu IT transition can be used for solid state physics experiments in order to study the magnetic and electric behaviour of different material of interest. To my knowledge, on-line ^{68m}Cu experiments at ISOLDE-CERN are being prepared by the SSP group to further exploit the capabilities of this new PAC probe.

In Chapter 4 it was presented the PAC spectroscopy as a tool for investigating the CadC metalloprotein structure and flexibility. With the PAC technique we managed to get important information about the type of arrangement of the Cd(II) metal ion binding site. The possibility of carrying out experiments at different physical states, pH and temperatures allow to mimic the natural environment of the metalloprotein and help us to study the real time dynamics of the biological samples. This is very crucial for understanding the kinetics of conversion between different species in solution that are very difficult to study with other conventional techniques as they are not responsive in the nanosecond time scale (0.1-100 ns).

During the current work, re-designing and building of a new experimental beamline took place at ISOLDE-CERN. A new vacuum compatible β NMR chamber and a new liquid handling system were tested off-line and with radioactive beams. The first successful ^{26}Na β NMR experiments in ILs are reported. The next step is to apply the β NMR technique in biologically interesting compounds and prove that the technique can contribute to the direct detection and investigation of the interaction of metal ions, such as Na^+.

It is stressed already how critical the role and the levels of biologically important metal ions are in living organisms when they interact with DNA/RNA and proteins, since their deficiency or over abundance could lead to serious health problems. A very representative example of the dysregulation and dyshomeostasis of the essential transition metals in traces amounts and in particular Cu and Zn, is the Alzheimer's disease (AD) [125].

In the end of the current thesis, the idea of testing the β-detected NMR technique for the first time on specific biological systems was developed and a proposal was formed and submitted to the ISOLDE and Neutron Time-of-Flight Committee in May 2017 [33]. The direct NMR detection of alkali metal ions at physiological concentrations is difficult or even some times impossible. One class of biological systems that we suggest to investigate using the β-detected NMR technique is the DNA guanine-quadruplexes, known as G-quadruplexes, interacting with K and Na. These systems have been studied until recently with solid state NMR and X-ray crystallography or with solution NMR but using indirect approaches using probes such as $NH4^+$ and Tl^+ due to the low small intensity and the unfavourable quadrupole spin relaxation properties of the stable Na and K isotopes. Compared to the aforementioned techniques it is much more difficult to study alkali metal ion binding to the G-quadruplexes in solutions. As a result, still little is known about the alkali metal cation dynamics in this class of DNA structures and we believe that the β-detected NMR technique could provide a new approach for direct observation of their interaction and dynamics with alkali metal ions in solution.

During this PhD thesis, several ILs were tested with conventional ^{25}Mg and ^{13}Na NMR. These measurements were used as the reference for the β-detected NMR measurements in the same ILs. More conventional NMR measurements at different B_0 and different temperatures are essential, since the dynamics can differ vastly with the magnetic field and the temperature increase. During the β-detected NMR experiments at ISOLDE-CERN, it was observed that the laser beam is directed on

the liquid sample during the optical pumping procedure, increasing the temperature of the samples in an uncontrolled way. Implementing a temperature control system would be essential for a better understanding the chemical behaviour of the samples. For a direct comparison of NMR and β-NMR results, the samples' preparation protocols should be adapted according to the experimental conditions of the β-detected experiments. Special vacuum tight NMR tubes should be used for reaching the high vacuum conditions during the experiments with radioactive ions and the high vacuum should be maintained during the conventional NMR measurements. The addition of the stable cations should therefore be done while the liquid host is under vacuum, possibly using a Schlenk line, since during the β-detected NMR experiments the ions are implanted after the insertion of the liquid host in the vacuum chamber.

Appendix A

Chemicals used for the NMR samples

A.1 Ionic Liquids (ILs)

A.1.1 1-ethyl-3-methylimidazolium acetate: EMIM_Ac

The 1-ethyl-3-methylimidazolium acetate, is a room temperature ionic liquid composed by the $EMIM^+$ and an Ac^-. It was provided by SigmaAldrich and its chemical properties are summarised in Table A.1.

Table A.1: Chemical properties of EMIM_Ac

EMIM_Ac chemical properties	
Molecular formula	$C_8H_{14}N_2O_2$ [24]
Molecular weight	170.21 [g/mol] [24]
Density	1.027 [g/cm^3] at 25°C [24]
Melting point	-20°C [126]
Flash point	164°C (327°F)
Viscosity	93 [mPas] at 25°C, 10 [mPas] at 80°C [126]
Sensitivity	Moisture sensitive
Solubility	Soluble in water, acetone, acetonitrile, dichloromethane

The chemical structure of EMIM_Ac is shown in Fig. A.1 [24]

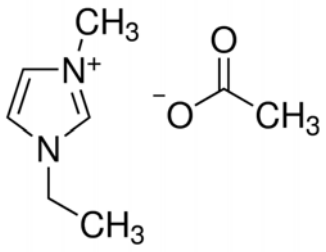

FIGURE A.1: Chemical structure of EMIM_Ac [24].

A.1.2 1-ethyl-3-methylimidazolium dicyanamide: EMIM_DCA

The 1-ethyl-3-methylimidazolium dicyanamide, is a room temperature IL composed by the $EMIM^+$ and an DCA^-. It was provided by SigmaAldrich, and its chemical properties are summarised in Table A.2.

TABLE A.2: Chemical properties of EMIM_DCA

EMIM_DCA chemical properties	
Molecular formula	$C_8H_{11}N_5$ [24]
Molecular weight	177.21 [g/mol] [24]
Density	1.06 [g/cm^3] at 25°C [24]
Melting point	-21°C
Flash point	164°C (327°F)
Viscosity	25.3 [mPa*s] at 21°C
Solubility	Soluble in water, acetone, acetonitrile, isopropanol

The chemical structure of EMIM_DCA is shown in Fig.A.2.

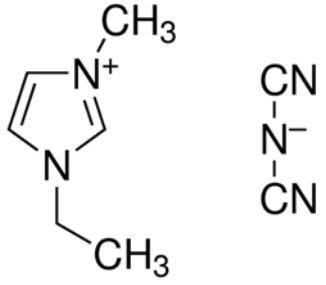

FIGURE A.2: Chemical structure of EMIM-DCA ionic liquid [24].

A.1.3 1-butyl-3-methylimidazolium acetate: BMIM_Ac

The 1-butyl-3-methylimidazolium acetate, is a room temperature IL composed by the $BMIM^+$ and an Ac^-. It was provided by SigmaAldrich and its chemical properties are summarised in Table A.3.

TABLE A.3: Chemical properties of BMIM_Ac

BMIM_Ac chemical properties	
Molecular formula	$C_{10}H_{18}N_2O_2$ [24]
Molecular weight	198.26 [g/mol] [24]
Density	1.0550 [g/cm^3] at 25°C and 1.0192 [g/cm^3] at 80°C [127]
Melting point	<-20°C [127]
Flash point	153°C (307.4°F) [25]
Viscosity	393.3 [mPa] at 25°C, 22.4 [mPa] at 80°C [127]
Sensitivity	air and water stable
Solubility	miscible in water and most CE solvents [128]

The chemical structure of BMIM_Ac is shown in Fig. A.3

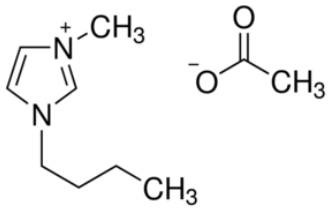

FIGURE A.3: Chemical structure of BMIM_Ac [24].

A.1.4 1-butyl-3-methylimidazolium thiocyanate: BMIM_SCN

The 1-butyl-3-methylimidazolium thiocyanate,BMIM_SCN), is a room temperature IL ia composed by the $BMIM^+$ and an SCN^-. Its most important chemical properties are summarised in Table A.4.

TABLE A.4: Chemical properties of BMIM_SCN Ionic Liquid.

BMIM_SCN chemical properties	
Molecular formula	$C_9H_{15}N_3S$
Molecular weight	197.3 [g/mol] [24]
Density	1.07 [g/cm^3] at 25°C
Melting point	<-20°C
Flash point	207°C
Viscosity	54 [mPas] at 25°C, 9 [mPas] at 80°C [126]

The chemical structure of BMIM_SCN is shown in Fig.A.4

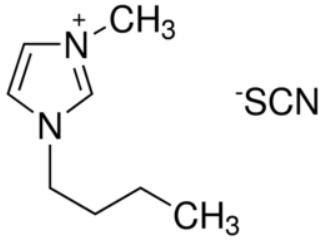

FIGURE A.4: Chemical structure of BMIM_Ac [24].

A.2 Other chemicals

A.2.1 15-crown-5 ether

Crown ethers are cyclic chemical compounds that consist of a ring containing several ether groups. The first number in a crown ether's name refers to the number of atoms in the cycle, and the second number refers to the number of those atoms that are oxygen. Crown ethers strongly bind certain cations, forming complexes. The oxygen atoms are well situated to coordinate with a cation located at the interior of the ring, whereas the exterior of the ring is hydrophobic. The resulting cations often form salts that are soluble in nonpolar solvents, and for this reason crown ethers are useful in phase transfer catalysis. The 18-crown-6 ether has high affinity for K^+ while 15-crown-5 for Na^+. Due to the high selectivity

to Na^+, 15-crown-5 was selected to be used in the current work. The 15-crown-5 (98% purity) was provided by SigmaAldrich, and its most important chemical properties are summarised in Table A.5.

TABLE A.5: Chemical properties of 15-crown-5 ether.

15-crown-5 chemical properties	
Molecular formula	$C_{10}H_{20}O_5$
Molecular weight	220.26 [g/mol] [26]
Density	1.113 [g/cm^3] at 20°C
Boiling point	93-96°C 0.05 mm Hg [25]
Flash point	>110°C (230°F) [25]
Sensitivity	Hydroscopic [25]
Solubility	miscible in water [25]
Stability	stable
	Incompatible with oxidising agents and strong acids
	Avoid exposure to water or moist air [25]

The chemical structure of 15-crown-5 ether is given in Fig. A.5

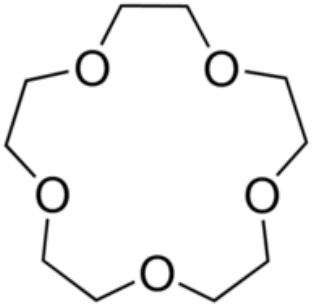

FIGURE A.5: Chemical structure of 15-crown-5 ether [25].

A.2.2 Calcein disodium salt

Calcein is yellow powder solid a calcium dependent fluoresent molecule and therefore is widely used for the fluorometric determination of calcium and EDTA titration of calcium. The calcein disodium salt with molecular weight 622.53 g/mol was provided by SigmaAldrich.

The chemical structure of Calcein disodium is given in Fig. A.6

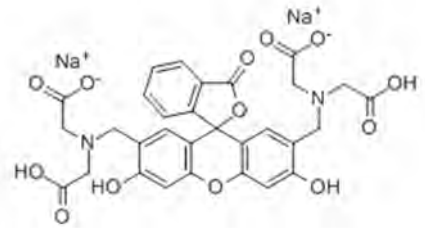

FIGURE A.6: Chemical structure of Calcein disodium [26].

A.2.3 Ethylenediaminetetraacetic acid disodium salt dihydrate, ($Na_2EDTA*2H_2O$)

Ethylenediaminetetraacetic acid disodium salt dihydrate, ($Na_2EDTA*2H_2O$ is a white powder solid and is widely used for molecular biology applications. an electrolyte supplementation ir a reagent in molecular biology. It was purchased from Fluka and its most important chemical properties are summarised in Table A.6.

TABLE A.6: Chemical properties of $Na_2EDTA*2H_2O$.

$Na_2EDTA*2H_2O$ chemical properties	
Molecular formula	$C_{10}H_{14}N_2Na_2O_8*2H_2O$ [25]
Molecular weight	372.2 [g/mol] [26]
Melting point	248°C [26]
Stability	Stable. Incompatible with strong oxidisers,halogens [25]
Sensitivity	Hydroscopic moisture sensitive [25]
Water solubility	11 g/100ml at 20°C [25]

The chemical structure of $Na_2EDTA*2H_2O$ is given in Fig. A.7

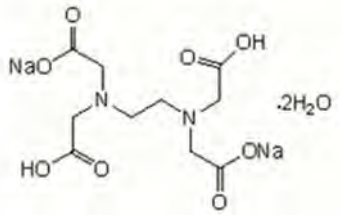

FIGURE A.7: Chemical structure of $Na_2EDTA*2H_2O$ [26].

A.2.4 Sodium Chloride ≥99%, NaCl

Sodium Chloride is one of the most common salts, called table salt, and it is an assembly of Na^+ and Cl^-. It is in crystal form since its atoms form a periodic anc symmetrical structure. Its most important chemical properties are summarised in Table A.7.

TABLE A.7: Chemical properties of sodium chloride (NaCl)

NaCl chemical properties	
Molecular formula	NaCl
Molecular weight	58.44 [g/mol] [26]
Melting point	801°C [26]
Vapour pressure	1.33 hPa at 865°C [26]
Water solubility	358 g/L at 20°C - soluble [26]

A.2.5 Sodium dicyanamide, 96%, (NaDCA)

Sodium dicyanamide, NaDCA, is a sodium salt with the appearance of white powder. The NaDCA (96% purity) was provided by SigmaAldrich, and its most important chemical properties are summarised in Table A.10.

TABLE A.8: Chemical properties of sodium dicyanamide (NaDCA)

NaDCA chemical properties	
Molecular formula	C_2N_3Na [25]
Molecular weight	89.03 [g/mol] [25, 26]
Melting point	300°C [25]
Sensitivity	Hydroscopic [25]
Water solubility	260 g/cm^3 at 30°C [25]

The chemical structure of NaDCA is given in Fig.A.8

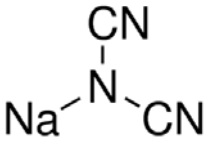

FIGURE A.8: Chemical structure of NaDCA [26].

A.2.6 Sodium thiocyanate, 99.99%, (NaSCN)

Sodium thiocyanate, NaSCN, is a colourless usually used in radio-pharmaceutical synthesis. salt with the appearance of white powder. The NaDCA (96% purity) was provided by SigmaAldrich, and its most important chemical properties are summarised in Table A.10.

TABLE A.9: Chemical properties of sodium dicyanamide (NaSCN)

NaSCN chemical properties	
Molecular formula	CNNAS [25]
Molecular weight	81.07 [g/mol] [25, 26]
Melting point	287°C [25]
Water solubility	1.000 g/cm^3 at 20°C-soluble [26]

The chemical structure of NaSCN is given in Fig.A.9

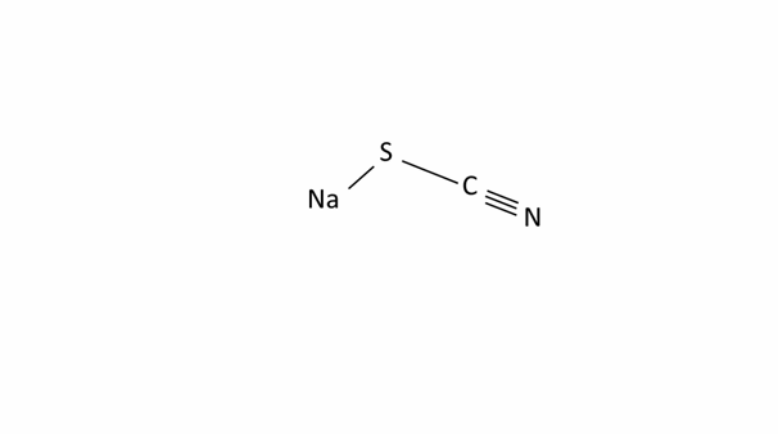

FIGURE A.9: Chemical structure of NaDCA [27]

A.2.7 Magnesium chloride anhydrous, ≥98%, ($MgCl_2$_anh)

Magnesium chloride anhydrous, $MgCl_2$, is a white powder salt with molecular wight 95.21 g/mol and is widely used as reagent in chemistry and biology as a source of magnesium ion. The $MgCl_2$ (≥98% purity) was provided by Sigma-Aldrich, and its most important chemical properties are summarised in Table A.10.

TABLE A.10: Chemical properties of magnesium chloride anhydrous ($MgCl_2$)_anh

$MgCl_2$ chemical properties	
Molecular formula	$MgCl_2$[25]
Molecular weight	95.21 [g/mol] [26]
Melting point	714°C [26]
Water solubility	100 mg/cm^3 at 20°C-soluble [26]

The chemical structure of $MgCl_2$ is given in Fig. A.10.

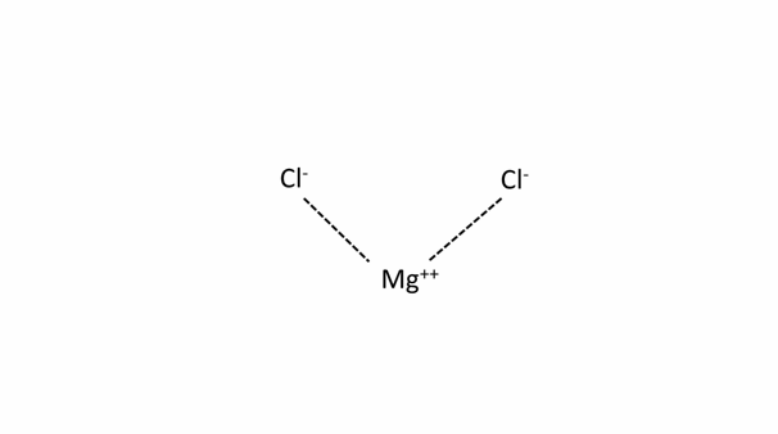

FIGURE A.10: Chemical structure of $MgCl_2$

A.2.8 Magnesium acetate tetrahydrate ≥99.99%, ($Mg(Ac)_2$*$4H_2O$

Magnesium acetate tetrahydrate, $Mg(Ac)_2$*$4H_2O$, is a solid hydrated acetate salt of magnesium. and is widely used as an electrolyte supplementation ir a reagent in molecular biology. It was provided by SigmaAldrich, and its most important chemical properties are summarised in Table A.11.

TABLE A.11: Chemical properties of magnesium chloride anhydrous ($Mg(Ac)_2$)*$4H_2O$

$Mg(Ac)_2$)*$4H_2O$ chemical properties	
Molecular formula	$C_4H_{14}MgO_8$[25]
Molecular weight	214.4 [g/mol] [26]
Melting point	80°C [25]
Water solubility	soluble [25]

The chemical structure of $Mg(Ac)_2$)*$4H_2O$ is given in Fig. A.11.

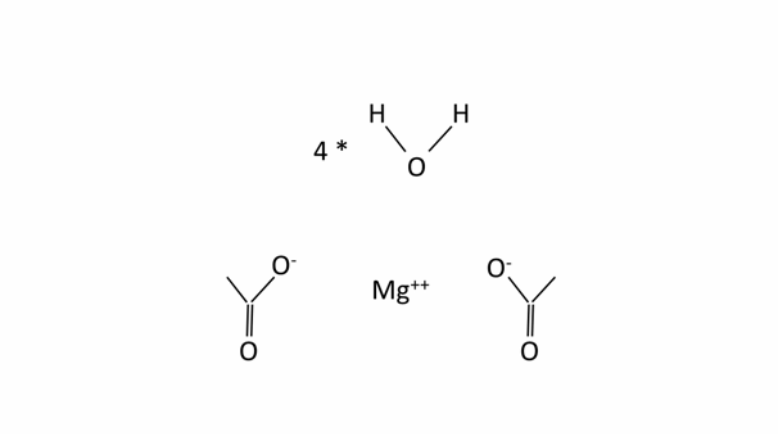

FIGURE A.11: Chemical structure of $Mg(Ac)_2$

Appendix B

Sample preparation protocols

The sample preparation protocoles were developed at the Chemistry department, University of Copenhagen, Denmark under the supervision of L. Hemminsgen.

B.1 0.3 M NaAc_anhydrous in EMIM_Ac

The sample was prepared by dissolving 98.4 mg sodium acetate (NaAc) anhydrous, with molecular weight 82.03 g/mol (purchased from Sigma-Aldrich, ≥99% purity) in 4 mL 1-ethyl-3-methylimidazolium acetate with molecular weight 170.21 g/mol (purchased from Sigma-Aldrich, ≥95% purity) leading to a final concentration of 0.3 M. The sample has been magnetically stirred with a stir bar for 7 h, no heating was used and no precipitation was apparent in the end of the mixing procedure. From the total of 4 mL, 550μL were used and transferred in an 5 mm NMR glass tube for the NMR experiments.

B.2 0.3 M NaCl in EMIM_Ac

The sample was prepared by dissolving 70 mg sodium chloride (NaCl), with molecular weight 58.44 g/mol (purchased from Sigma-Aldrich, ≥99% purity) in 4 mL 1-ethyl-3-methylimidazolium acetate with molecular weight 170.21 g/mol (purchased from Sigma-Aldrich, ≥95% purity) leading to a final concentration of 0.3 M. The sample has been magnetically stirred with a stir bar for 7 h. After the

stirring procedure ∼550μL were transferred in an 5 mm NMR glass tube for the NMR experiments.

B.3 0.3 M NaCl in BMIM_SCN

The sample was prepared by dissolving 70 mg sodium chloride (NaCl), with molecular wight 58.44 g/mol (purchased from Sigma-Aldrich, ≥99% purity) in 4 mL 1-butyl-3-methylimidazolium thiocyanate with molecular weight 197.30 g/mol (purchased from Sigma-Aldrich, ≥95% purity) leading to a final concentration of 0.3 M. The sample has been magnetically stirred with 2 stir bars for 7 h. There was no apparent precipitation in the sample and therefore ∼550μL were transferred in a 5 mm NMR glass tube for the NMR experiments.

B.4 0.3 M NaSCN in BMIM_SCN

The sample was prepared by dissolving 97 mg sodium thiocyanate (NaSCN), with molecular weight 81.07 g/mol (purchased from Sigma-Aldrich, ≥98% purity) in 4 mL 1-butyl-3-methylimidazolium thiocyanate with molecular weight 197.30 g/mol (purchased from Sigma-Aldrich, ≥95% purity) leading to a final concentration of 0.3 M. The sample has been magnetically stirred with 2 stirring bars for 5 h. There was no apparent precipitation in the sample and therefore ∼550μL were transferred in a 5 mm NMR glass tube for the NMR experiments.

B.5 0.3 M 15-crown-5 in 0.3 M NaSCN in BMIM_SCN

The sample was prepared by dissolving 117 μL (or 132.2 mg) of liquid 15-crown-5 ether (molecular weight mw=220.26 g/mol and density d=1.113 g/ml at room temperature) (purchased from Sigma-Aldrich, ≥98% purity) into the 2 mL solution of 0.3 M NaSCN in BMIM_SCN leading to a final concentration of 0.3 M 15-crown-5 in 0.3 M NaSCN in BMIM_SCN. The sample has been magnetically stirred with 2 stirring bars for more than 8 h and the solution looked well mixed. When the stirring was over, the solution was left for ∼2 h to relax in order to verify that the crown ether is well dissolved and there are not two phases in the solution.

After the 2 h, ∼550μL were transferred in a 5 mm NMR glass tube for the NMR experiments.

B.6 0.3 M NaDCA in EMIM_DCA

The sample was prepared by dissolving 80 mg of sodium dicyanamide (NaDCA) with molecular weight 89.03 g/mol (purchased from Sigma-Aldrich, ≥96% purity) in 3 mL of 1-ethyl-3-methylimidazolium dicyanamide (EMIM_DCA) with molecular weight 177.21 g/mol (purchased from Sigma-Aldrich, ≥98.5% purity) leading to a final concentration of 0.3 M. The solution was magnetically stirred with stir bars for 14 h but still precipitation was apparent in the sample. The sample was filtered with a membrane filter if 0.22 μm and the solution looked clear. ∼550μL were transferred in a 5mm NMR glass tube for the NMR experiments.

B.7 0.3 M NaAc_anhydrous in BMIM_Ac

The sample was prepared by dissolving 98.4 mg of sodium acetate anhydrous (NaAc) with molecular weight 82.03 g/mol (purchased from Sigma-Aldrich, ≥99% purity) in 4 mL of 1-Butyl-3-methylimidazolium acetate (BMIM_Ac) with molecular weight 198.26 g/mol (purchased from Sigma-Aldrich, ≥95% purity) leading to a final concentration of 0.3 M. The solution was magnetically stirred with stir bars and was simultaneously heated up to 40 °C for 1.5 h due to time constraints. ∼550μL were transferred in a 5 mm NMR glass tube for the NMR experiments.

B.8 0.17 M $MgCl_2$_anhydrous in EMIM_Ac

The sample was prepared by dissolving 143 mg magnesium chloride anhydrous ($MgCl_2$_anh), with molecular weight 95.21 g/mol (purchased from Sigma-Aldrich, ≥98% purity) first in 3 mL of 1-methyl-3-methylimidazolium acetate with molecular weight 170.21 g/mol (purchased from Sigma-Aldrich, ≥95% purity). Due to precipitation and after 3 h of magnetic stirring, 2 mL were further added. The final concentration of the solution reached was 0.17 M after 5 additional hours of

magnetic stirring. There was no apparent precipitation in the sample and ~550μL were transferred in a 5 mm NMR glass tube for the NMR experiments.

B.9 0.3 M $MgAc_2$*$4H_2O$ in EMIM_Ac

In 3 ml of 1-methyl-3-methylimidazolium acetate with molecular weight 170.21 g/mol (purchased from Sigma-Aldrich, ≥95% purity) were dissolved 193 mg magnesium acetate tetrahydrate ($MgAc_2$*$4H_2O$) with molecular weight 214.4 g/mol. For dissolving the salt, both an ultrasound bath and magnetic stirring were used for a total of 5 hours. ~550μL of the solution were transferred in a 5 mm NMR glass tube for the NMR experiments.

B.10 0.3 M $MgCl_2$_anhydrous in EMIM_DCA

The sample was prepared by dissolving 114 mg magnesium chloride anhydrous ($MgCl_2$_anh) with molecular weight 95.21 g/mol (purchased from Sigma-Aldrich, ≥98% purity) in 4 ml 1-ethyl-3-methylimidazolium dicyanamide (EMIM_DCA) wiwith molecular weight 177.21 g/mol (purchased from Sigma-Aldrich, ≥98.5% purity) leading to a final concentration of 0.3 M. After 15 hours of magnetic stirring, the solution got totally transparent meaning that there was no salt precipitation. A total of ~550μL of the solution were transferred in a 5 mm NMR glass tube for the NMR experiments.

B.11 0.3 M $MgCl_2$ in BMIM_SCN

The sample was prepared by dissolving 10 mg magnesium chloride anhydrous ($MgCl_2$_anh) with molecular weight 95.21 g/mol (purchased from Sigma-Aldrich, ≥98% purity) in 1.1 ml 1-Butyl-3-methylimidazolium thiocyanate (BMIM_SCN) with molecular weight 197.30 g/mol (purchased from Sigma-Aldrich, ≥95% purity) leading to a final concentration of 0.3 M. After several minutes of magnetic stirring, the solution got totally transparent meaning that there was no salt precipitation. A total of ~550μL of the solution were transferred in a 5 mm NMR glass tube for the NMR experiments.

B.12 0.3 M $Na_2EDTA*2H_2O$ + 0.3 M $MgCl_2$_anhydrous in BMIM_SCN

As a first step, 223 mg of ethylenediaminetetraacetic acid disodium salt dihydrate ($Na_2EDTA*2H_2O$) with molecular weight 372.24 g/mol (purchased from sigma Fluka), was dissolved in 2 ml 1-Butyl-3-methylimidazolium thiocyanate (BMIM_SCN) with molecular weight 197.30 g/mol (purchased from Sigma-Aldrich, $\geq$95% purity). After 2 hours of magnetic stirring the 2 ml of the solution were mixed with 2 ml of B.11. The new solution was magnetically stirred for 2 h and salt precipitation was persistent. A total of $\sim$550μL of the solution were transferred in a 5 mm NMR glass tube for the NMR experiments.

B.13 0.21 M Calcein + 0.21 M $MgCl_2$ in BMIM_SCN

Due to the limited remaining quantities of the BMIM_, 1 ml of 1-Butyl-3-methylimidazolium thiocyanate (BMIM_SCN) was used for dissolving 140 mg of Calcein disodium salt (purchased by Sigma-Aldrich) with molecular wight 665.5 g/mol. The solution was magnetically stirred for approximately 3 hours. At the same time, a 0.21 M solution of $MgCl_2$_anhydrous in of BMIM_SCN was prepared based on the same protocol with B.11, adjusting the quantinties for achieving the specific concentration. In the end, 1 ml of the 0.21 M calcein in BMIM_SCN and 1 ml 0.21 M $MgCl_2$_anhydrous in BMIM_SCN were mixed and magnetically stirred for approximately 4 hours. Finally $\sim$550μL of the solution were transferred in a 5 mm NMR glass tube for the NMR experiments. .

Appendix C

Detailed β NMR spectra and results

C.1 1-butyl-3-methylimidazolium acetate: BMIM-Ac

The same samples of BMIM-Ac was measured five times changing the number of scans and the RF power in each measurement. The NMR spectra are presented in Fig. C.1 and the detailed parameters and the experimental results acquired after the NMR analysis are presented at Table C.1.

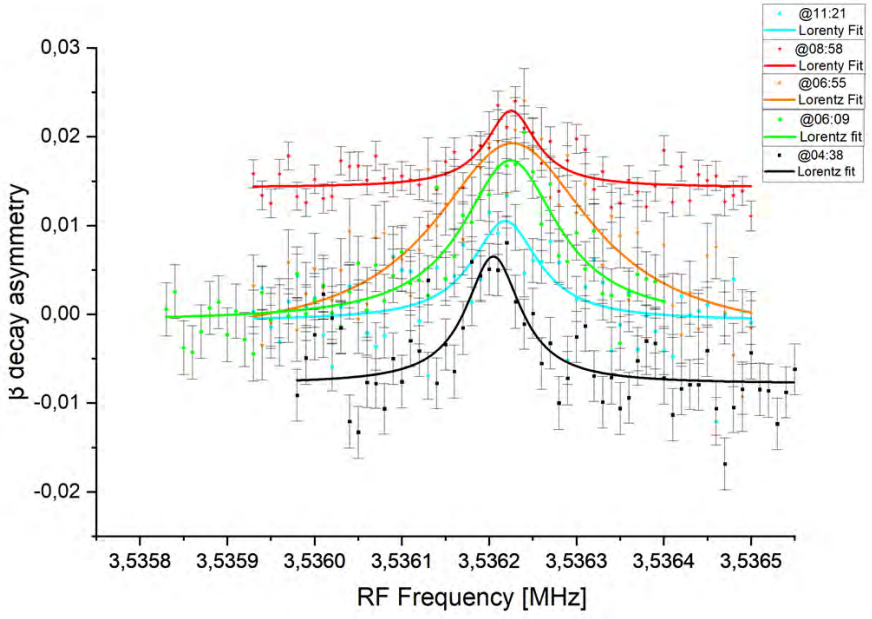

FIGURE C.1: ^{26}Na β-NMR experimental chemical shifts of BMIM-Ac IL at different starting measurement times.

TABLE C.1: Detailed NMR experimental parameters and results for BMIM-Ac IL

time	n_o scans [mV]	RF power [MHz]	NMR position [ppm]	NMR position [Hz]	FWHM [%]	Asymmetry
04:38	27	100	3.53620 (4.5E-6)	4.242 (1.3)	77 (16)	1.43 (0.17)
06:09	24	400	3.53622 (4.8E-6)	9.615 (1.4)	134 (22)	1.81 (0.14)
06:55	16	600	3.53623 (6.6E-6)	10.463 (1.9)	221 (42)	2.22 (0.18)
08:58	22	200	3.53623 (3.9E-6)	9.898 (1.1)	70 (14)	0.86 (0.09)
11:21	32	120	3.53621 (4.2E-6)	5.656 (1.2)	48 (13)	1.06 (0.18)

C.2 0.1 M Sodium Acetate dissolved in 1-butyl-3-methylimidazolium acetate: BMIM-Ac + 0.1 M NaAc

The same sample of 0.1 M NaAc dissolved in BMIM-Ac was measured four times changing the number of scans and the RF power. The NMR spectra are presented in Fig. C.2 and the detailed parameters and the experimental results acquired after the NMR analysis are presented at Table C.2.

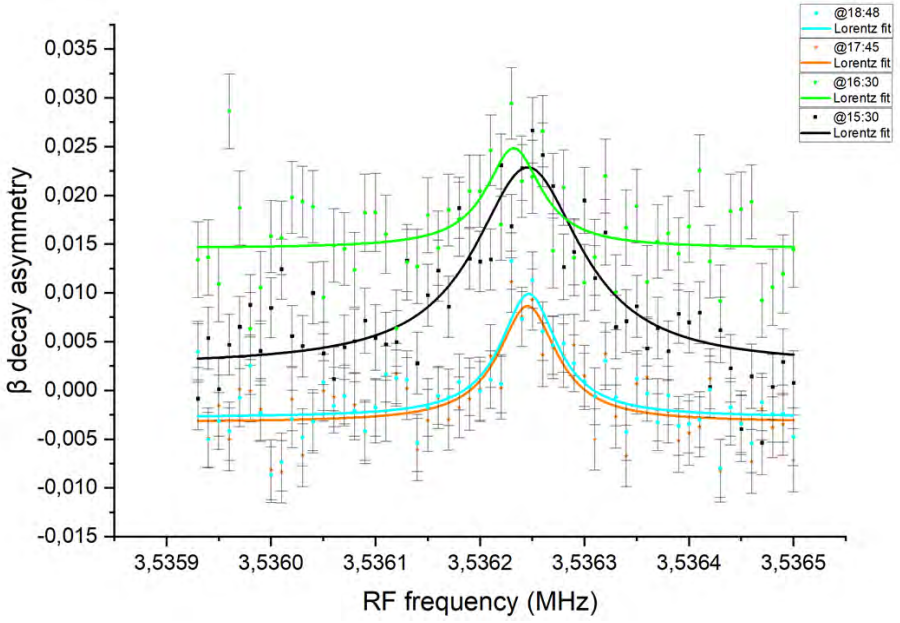

FIGURE C.2: ^{26}Na β-NMR experimental chemical shifts of 0.1 M dissolved in BMIM-Ac IL at different starting measurement times.

TABLE C.2: Detailed NMR experimental parameters and results for 0.1 M NaAc dissolved in BMIM-Ac IL

time	n_o scans	RF power [mV]	NMR position [MHz]	NMR position [ppm]	FWHM [Hz]	Asymmetry [%]
15:30	20	300	3.53625 (4.5E-6)	15.84 (1.3)	83 (20)	2.04 (0.16)
14:30	16	120	3.53623 (7.7E-6)	11.88 (2.2)	57 (23)	1.03 (0.23)
17:45	26	120	3.53625 (5.8E-6)	15.84 (1.6)	134 (20)	1.19 (0.19)
18:48	31	120	3.53625 (3.9E-6)	16.12 (1.4)	221 (18)	1.27 (0.18)

BMIMAcNaAvresultsNMR

C.3 1-butyl-3-methylimidazolium formate: BMIM-HCOO

The same sample of BMIM-HCOO was measured four times changing the number of scans and the RF power. The NMR spectra are presented in Fig. C.3 and the detailed parameters and the experimental results acquired after the NMR analysis are presented at Table C.3.

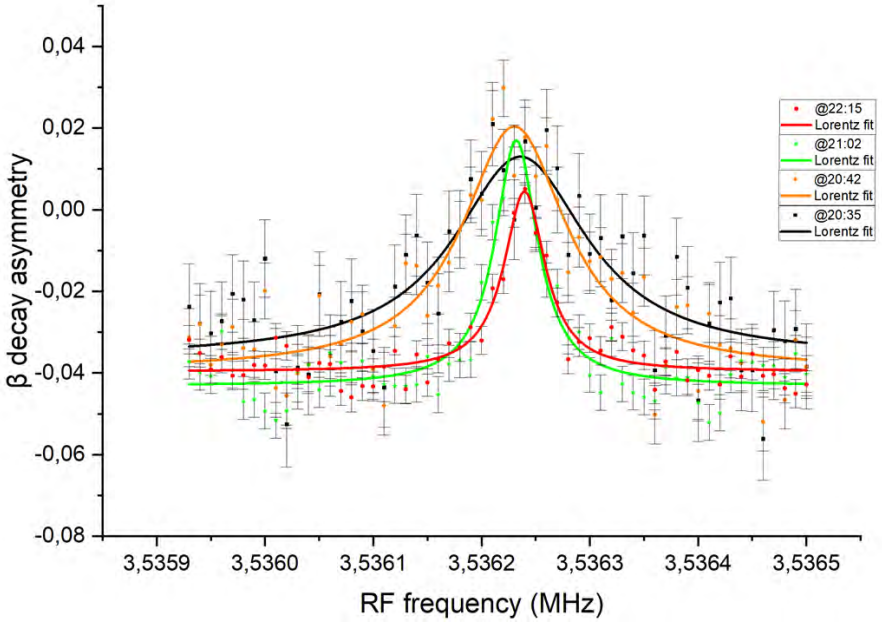

FIGURE C.3: ^{26}Na β-NMR experimental chemical shifts of BMIM-HCOO IL at different starting measurement times.

TABLE C.3: Detailed NMR experimental parameters and results for BMIM-HCOO IL

time	n_o scans	RF power [mV]	NMR position [MHz]	NMR position [ppm]	FWHM [Hz]	Asymmetry [%]
20:35	2	300	3.53624 (6.4E-6)	13.01 (1.8)	79 (26)	4.93 (0.45)
20:42	4	300	3.53623 (3.3E-6)	11.31 (0.9)	43 (13)	5.98 (0.34)
21:02	11	120	3.53623 (2.7E-6)	11.31 (0.8)	127 (6)	5.92 (0.81)
22:15	21	120	3.53624 (1.3E-6)	14.14 (0.4)	118 (4)	4.41 (0.26)

C.4 0.1 M NaAc dissolved in 1-butyl-3-methylimidazolium formate: BMIM-HCOO + 0.1 M NaAc

The same sample of 0.1 M NaAc dissolved in BMIM-HCOO was measured seven successive times changing the number of scans and the RF power. The NMR spectra are presented in Fig. C.4 and the detailed parameters and the experimental results acquired after the NMR analysis are presented at Table C.5.

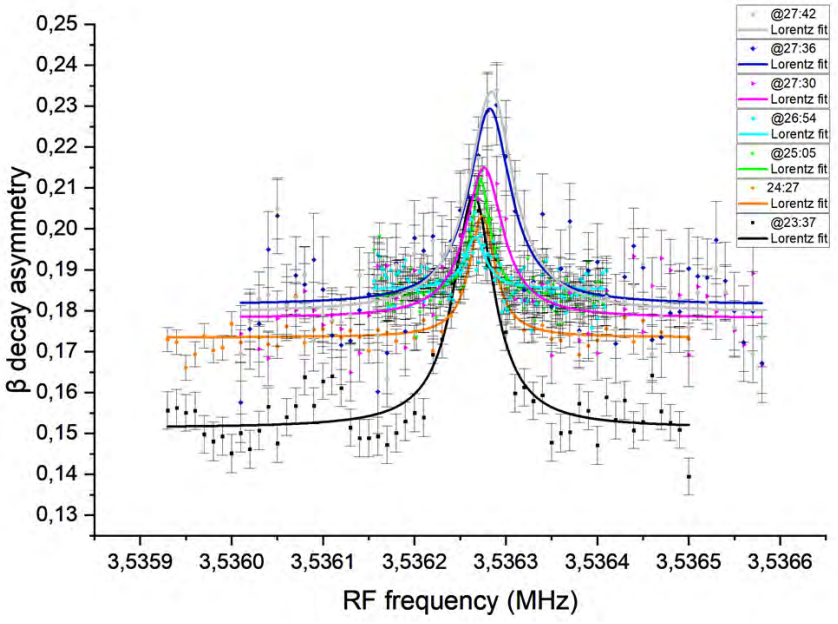

FIGURE C.4: ^{26}Na β-NMR experimental chemical shifts of 0.1 M NaAc dissolved in BMIM-HCOO IL at different starting measurement times.

TABLE C.4: Detailed NMR experimental parameters and results for BMIM-HCOO IL

time	n_o scans	RF power [mV]	NMR position [MHz]	NMR position [ppm]	FWHM [Hz]	Asymmetry [%]
23:37	10	120	3.53627 (1.5E-6)	21.0 (0.4)	73 (4)	5.69 (0.3)
24:27	22	60	3.53627 (1.5E-6)	23.7 (0.4)	52 (4)	2.98 (0.25)
25:05	8	40	3.53627 (6.2E-7)	23.5 (0.2)	25 (2)	2.83 (0.14)
26:54	8	20	3.53627 (1.5E-6)	21.5 (0.4)	27 (4)	1.28 (0.13)
27:30	4	100	3.53628 (3.5E-6)	24.3 (1.0)	21 (10)	3.67 (0.47)
27:36	2	200	3.53628 (3.7E-6)	26.1 (1.1)	32 (14)	4.79 (0.67)
27:42	4	200	3.53628 (2.5E-6)	26.5 (0.7)	16 (8)	5.39 (0.44)

C.5 0.1 M NaAc + 0.1 M DNA dissolved in 1-butyl-3-methylimidazolium formate: BMIM-HCOO + 0.1 M NaAc + 0.1 M DNA

The same sample of 0.1 M NaAc + 0.1 M DNA dissolved in BMIM-HCOO was two successive times changing the number of scans and the RF power. The NMR spectra are presented in Fig. C.5 and the detailed parameters and the experimental results acquired after the NMR analysis are presented at Table C.5.

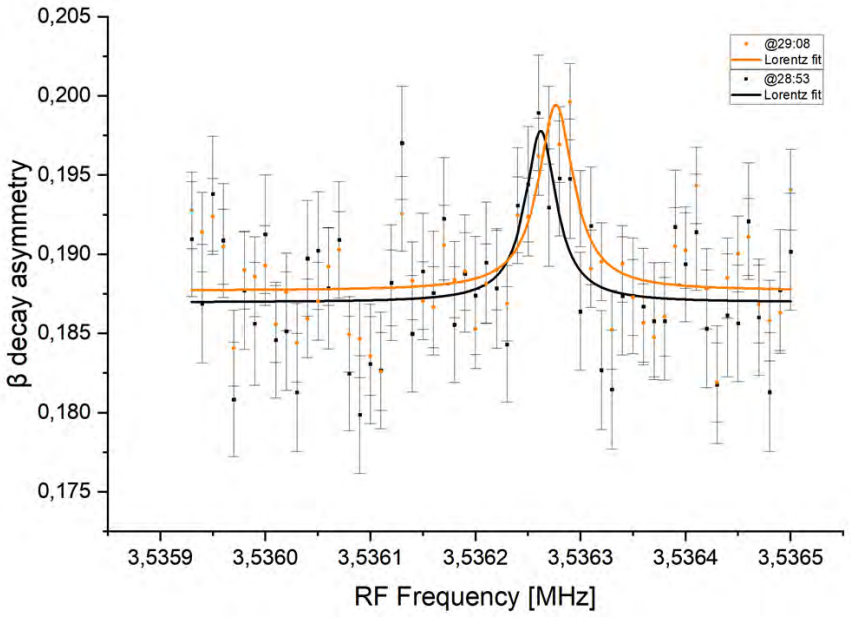

FIGURE C.5: ^{26}Na β-NMR experimental chemical shifts of 0.1 M NaAc + 0.1 M DNA dissolved in BMIM-HCOO IL at different starting measurement times.

TABLE C.5: Detailed NMR experimental parameters and results for 0.1 M NaAc + 0.1 M DNA in BMIM-HCOO IL

time	n_o scans	RF power [mV]	NMR position [MHz]	NMR position [ppm]	FWHM [Hz]	Asymmetry [%]
23:37	8	60	3.53626 (5.7E-6)	20.4 (1.6)	33 (16)	1.09 (0.3)
24:27	18	60	3.53628 (3.8E-6)	24.6 (1.1)	19 (8)	1.17 (0.2)

Appendix D

^{1}H NMR results

D.1 NaAc in EMIM_Ac and NaCl in EMIM_Ac

As a reference, ^{1}H NMR measurements were performed with plain EMIM_Ac at 25°C and at 70°C followed by measurements of 0.3 M NaAc dissolved in EMIM_Ac and 0.3 M NaCl dissolved in EMIM_Ac. In these experiments we only changed the Na salt for exploring the different behaviour between Cl^- and Ac^- in the solution. Table D.1 shows the expected values of the H chemical shifts of the EMIM_Ac, at RT, using a Bruker Avance 600 MHz (14 T) NMR spectrometer [21].

TABLE D.1: ^{1}H NMR chemical shifts of EMIM_Ac, 0.3 M NaCl in EMIM_Ac and 0.3 M NaAC in EMIM_Ac

Proton	H1	H2	H3	H4	H5	H6	H7
EMIM_Ac at 14 T [21]	7.90	8.07	10.14	3.60	3.92/3.89	0.64	1.09
					3.87/3.84	0.61	
						0.58	
*EMIM_Ac at 11.7 T	7.68	7.86	9.98	3.35	3.61/3.64	0.63	0.85
						0.61	
						0.59	
*NaCl in EMIM_Ac at 11.7 T	7.43	7.60	9.53	3.31	3.61/3.63	0.63	0.86
*NaAc in EMIM_Ac at 11.7 T	7.30	7.43	9.31	3.28	3.59/3.61	0.63	0.88

*results of current work

All the experimental chemical shifts differ less than 0.3 ppm compared to the one proposed by [21]. Therefore it was easy to assign the chemical shifts to each proton of the sample.

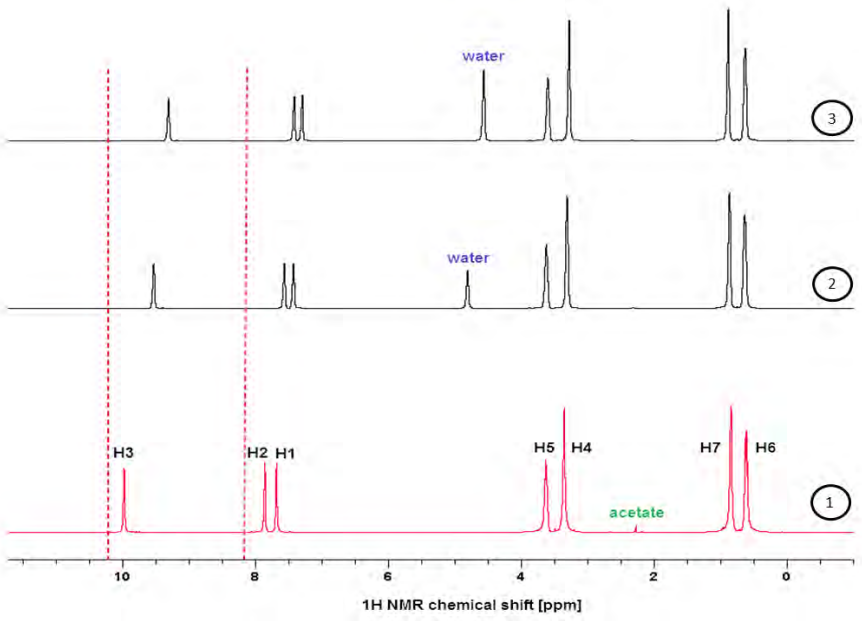

FIGURE D.1: ^{1}H NMR spectra of 1: EMIM_Ac, 2: 0.3 M NaCl in EMIM_Ac, 3: 0.3 M NaAc in EMIM_Ac.

We proposed that the small chemical shift at ∼2.3 ppm corresponds to the H of acetate (CH3COOH) [129] and the chemical shifts at ∼4.7 ppm to the H of water molecules [129]. The samples have not been outgased and traces of H2O were likely to be found in the samples.

Comparing the ^{1}H NMR spectra of the reference EMIM_Ac with the two EMIM_Ac samples containing Na salts, the proton resonances H4, H5, H6 and H7 were just marginally shifted (less than 0.1 ppm). The most significant shift occurred between the signals of H1, H2 and H3. Less than 0.4 ppm for H1 and H2, more than 0.5 for H3. The exact values of the chemical shifts can be found in Table D.1. Position 3 (H3), see Fig. 7.2, appears to be the most sensitive site of EMIM_Ac. H3 is more acidic and more sensitive than H1 and H2 since it is bonded to a carbon located between two more electronegative N atoms [21].

H1, H2 and H3 signals were shifted upfield, more upfield for the NaAc sample compared to the NaCl sample. According to bond theory, there are hydrogen-bond interactions between the acidic groups (H3) of the cation (EMIM) and the nucleophylic electron donor atoms of Ac^- and Cl^-. In both samples, the H3 of

EMIM interacted with the anion of the salts after the dissolution, forming ionic bonds leaving the Na^+ to form a bond with the Ac^- of the IL. Furthermore, the O from Ac^- shielded better the H3 of the $EMIM^+$ compared to Cl^- as it is more electronegative.

D.2 NaAc in EMIM_Ac and NaAc in BMIM_Ac

Fig. D.2 shows the ^1H NMR spectra of the reference plain ILs, EMIM_Ac and BMIM_Ac, and the the spectra from 0.3 M NaAc dissolved in EMIM_Ac and 0.3 M NaAc dissolved in BMIM_Ac. The main differences between the ^1H NMR spectra of EMIM_Ac and BMIM_Ac are the chemical shifts of protons from H6 to H9, as expected by their different chemical structures (see Fig. 7.2 and Fig. 7.4).

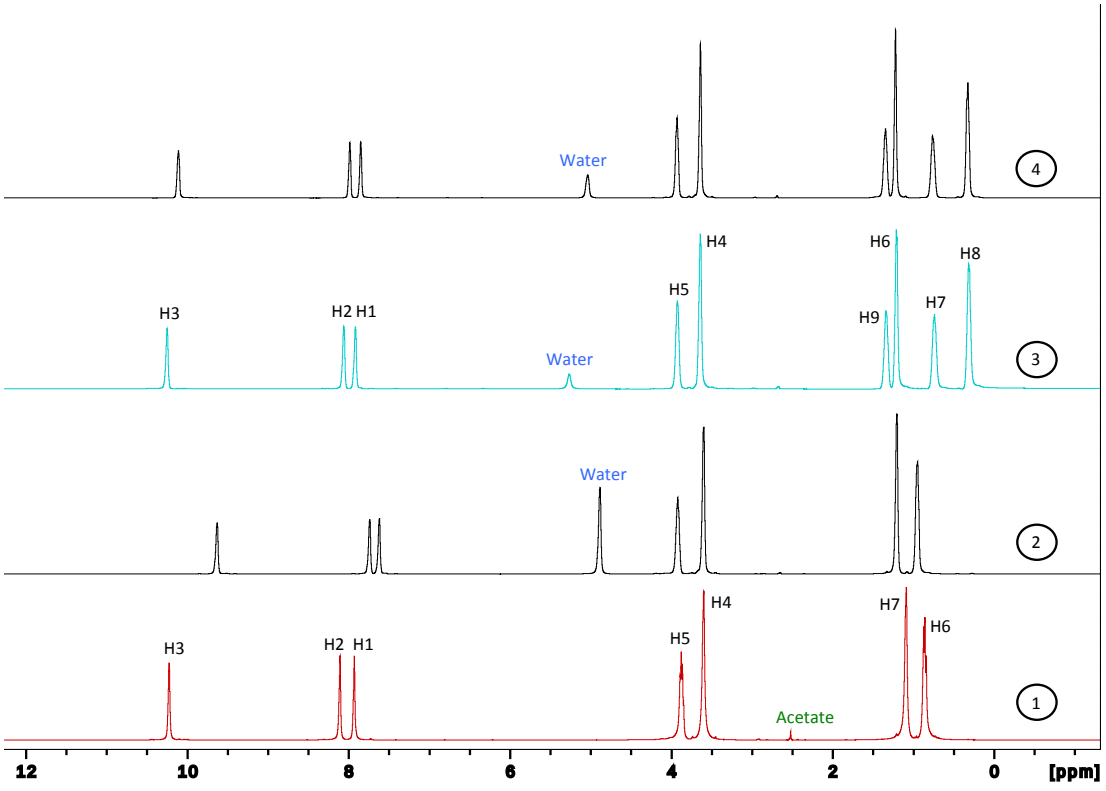

FIGURE D.2: ^1H NMR spectra of 1: EMIM_Ac, 2: 0.3 M NaAc in EMIM_Ac, 3: BMIM_Ac and 4: 0.3 M NaAc in BMIM_Ac.

When NaAc is dissolved in EMIM_Ac the most significant change is observed at the most acidic H3 proton (0.6 ppm upfield) and a smaller impact at H1 and

H2 protons (less than 0.4 ppm upfield). The same effect is observed when NaAc dissolved in BMIM_Ac, but with significantly smaller differences in the shifting of the H signals. Table D.2 shows that when NaAc is dissolved in BMIM_Ac, the H3 proton signal is shifted upfield by 0.14 ppm while H1 and H2 are shifted marginally (<0.1 ppm). This indicates that the CH_3COO^- (Ac^-) anion favours the formation of hydrogen bonds with hydrogen atoms of the aromatic protons in bulky cations $EMIM^+$ and $BMIM^+$ and especially with the most acidic H3.

TABLE D.2: ^{1}H NMR chemical shifts in ppm of EMIM_Ac, BMIM_Ac, and NaAc in EMIM and BMIM_Ac solutions

Proton	H1	H2	H3	H4	H5	H6	H7	H8	H9
EMIM_Ac at 14 T [21]					3.92/3.89	0.64			
	7.90	8.07	10.14	3.60	3.87/3.84	0.61	∼1.09		
						0.58			
*EMIM_Ac at 11.7 T						0.88			
	7.94	8.11	10.23	3.60	3.90/3.87	0.86	1.10		
						0.84			
*NaAc in EMIM_Ac at 11.7 T	7.62	7.74	9.63	3.60	3.93/3.90	0.95	1.20		
BMIM_Ac at 14 T [21]	7.99	8.14	10.31	3.64	∼3.91	∼1.29	∼0.69	0.27	∼1.46
*BMIM_Ac at 11.7 T	7.92	8.06	10.25	3.64	3.92	1.21	0.74	0.31	1.31
*NaAc in BMIM_Ac at 11.7 T	7.85	7.99	10.11	3.64	3.93	1.22	0.76	0.33	1.35

*results of current work

D.3 NaCl in EMIM_Ac and NaCl in BMIM_SCN

Fig. D.3 shows the ^{1}H NMR spectra of the ILs EMIM_Ac and BMIM_SCN. The ^{1}H NMR spectrum of BMIM_Ac was used as a "mediator" for the comparison of the two spectra. As found experimentally in the current work, confirming previous experiments in lower magnetic field of 5.9 T (250 MHz) [21], the H5 protons signals of EMIM_Ac and BMIM_Ac are found at almost the same position. For identifying the protons of BMIM_SCN, its H5 chemical shift was overlapped with the H5 chemical shift of BMIM_Ac and as a consequence with the one of EMIM_Ac.

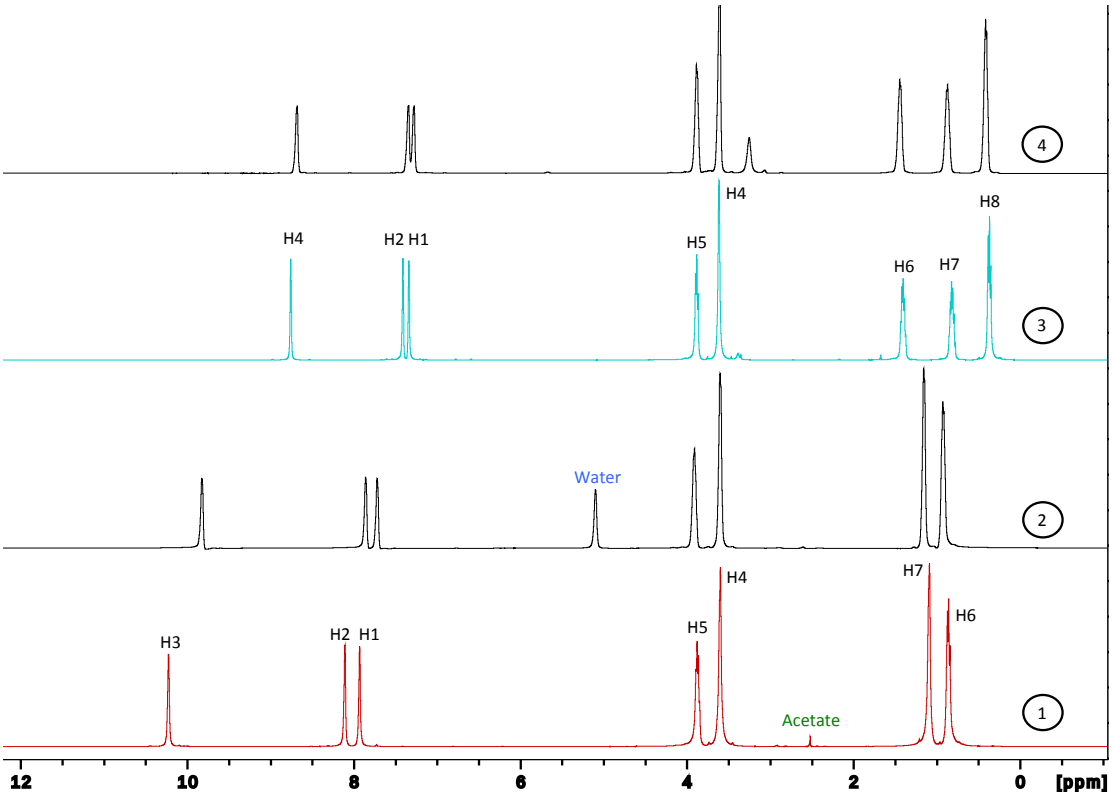

FIGURE D.3: ^{1}H NMR spectra of 1. EMIM_Ac, 2. 0.3 M NaCl in EMIM_Ac, 3. BMIM_SCN and 4. 0.3 M NaCl in BMIM_SCN.

The spectra 1 and 3 in Fig. D.3 correspond to the different structures of the ILs (Fig. 7.2 for EMIM_Ac and Fig. 7.6 for BMIM_CN). The exact values from the ^{1}H NMR analysis are shown in Table D.3.

TABLE D.3: 1H NMR chemical shifts in ppm of EMIM_Ac, BMIM_SCN, 0.3M NaCl in EMIM and 0.3 M NaCl in BMIM-SCN

Proton	H1	H2	H3	H4	H5	H6	H7	H8	
EMIM_Ac at 14 T [21]					3.92/3.89	0.64			
	7.90	8.07	10.14	3.60	3.87/3.84	0.61	∼1.09		
						0.58			
*EMIM_Ac at 11.7 T						0.88			
	7.94	8.11	10.23	3.60	3.90/3.87	0.86	1.10		
						0.84			
*NaCl in EMIM_Ac at 11.7 T	7.72	7.86	9.83	3.60	3.91	0.92	1.16		
BMIM_SCN at 7 T [22]	7.72	7.79	3.99	9.15	4.26	1.79	1.19	0.75	
*BMIM_SCN at 11.7 T					3.63	1.42	0.84	0.38	
	7.34	7.41	3.61	8.76	3.88	1.40	0.82	0.37	
					3.87	1.39	0.80	0.35	
*NaCl in BMIM_SCN at 11.7 T	7.02	7.09	3.35	8.43	3.63	1.19	0.62	0.16	3.00

*results of current work

The chemical shifts of the ring protons of EMIM_Ac (H3, H2 and H1) when NaCl is dissolved in it, are moving upfield indicating that these protons interact with Cl^-. Comparing the ^{1}H NMR spectra of the plain ILs the H3 and H4 protons chemical shifts are reversed. For BMIM_SCN the H3 proton's chemical shift is shifted upfield from ∼10 ppm to ∼3.6 ppm compared to EMIM_Ac, while the H4 signal was shifted downfield from ∼3.6 ppm to ∼8.8 ppm compared to the equivalent proton in EMIM_Ac.

The ^{1}H NMR analysis for 0.3 M NaCl dissolved in EMIM_Ac, have already been discussed previously, 7.2.1. The only effect is at the acidic protons H1, H2 and H3 with the bigger effect on the more acidic H3. It should be noted here that the EMIM_Ac ILs used for the different measurements are from different butches and the one used for the current measurements with NaCl had more traces of water. Since no dehydration procedures were performed before the NMR measurements, this could explain the new chemical shift observed at ∼5 ppm that could potentially correspond to H_2O [130]. Comparing the ^{1}H NMR spectra of the BMIM_SCN and its mixture with NaCl, no significant differences can be observed, except of the appearance of a new chemical shift at 3 ppm. This peak could perfectly correspond to the proton chemical shift of CH_3Cl [131].

D.4 NaCl in BMIM_SCN and NaSCN in BMIM_SCN

The 1H NMR spectrum of 0.3 M NaCl dissolved in BMIM_SCN when NaCl is dissolved has been discussed 7.2.3. For studying the effect of the SCN^- in the solution we dissolved 0.3 M NaSCN in BMIM_SCN and the 1H NMR spectra of both measurements are shown in Fig. D.4.

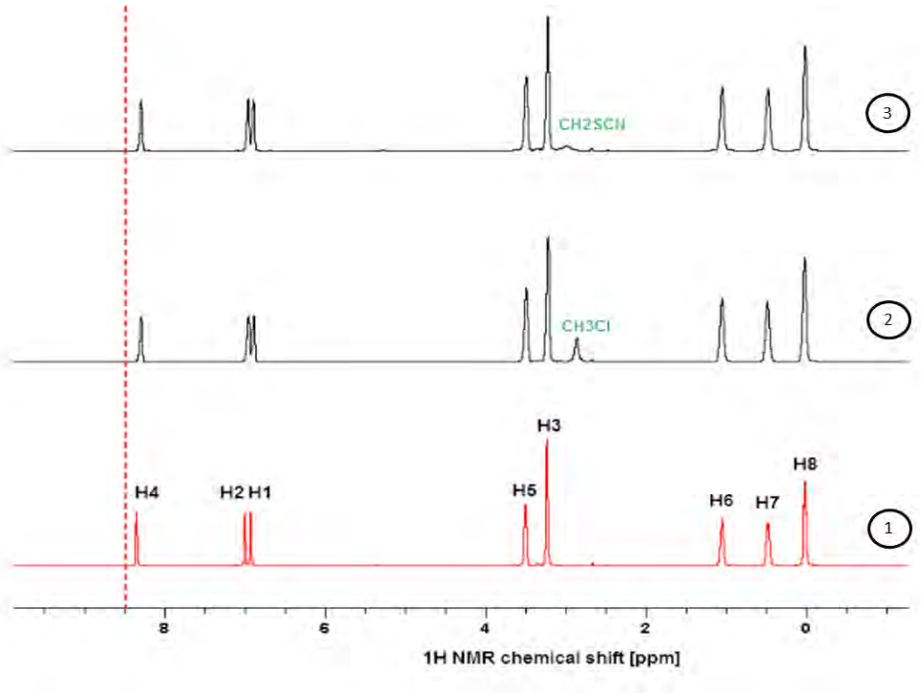

FIGURE D.4: ^1H NMR spectra of 1. BMIM_SCN, 2. 0.3 M NaCl in BMIM_SCN and 3. NaSCN in BMIM_SCN.

In Table D.4 the detailed values after the spectra analysis are shown. No difference in the the chemical shifts was observed when the NaSCN salt was dissolved in the BMIM_SCN. The main difference between the 1H NMR spectra is observed in the appearance of two different signals in the spectra. For the NaCl sample the new chemical shift at 3.0 ppm is assigned to CH_3Cl while at the NaSCN spectrum a chemical shift at 3.14 ppm could probably be assigned to CH_2SCN [132].

TABLE D.4: 1H NMR chemical shifts in ppm of BMIM_SCN, NaCl in BMIM and NaSCN in BMIM_SCN solutions

Proton	H1	H2	H3	H4	H5	H6	H7	H8	
BMIM_SCN at 7 T [22]	7.72	7.79	3.99	9.15	4.26	1.79	1.19	0.75	
*BMIM_SCN at 11.7 T	7.07	7.14	3.37	8.49	3.64	1.19	0.61	0.16	
*NaCl in BMIM_SCN at 11.7 T	7.03	7.10	3.36	8.43	3.64	1.19	0.62	0.16	3.00
*NaSCN in BMIM_SCN at 11.7 T	7.04	7.10	3.36	8.43	3.64	1.19	0.62	0.16	3.14

*results of current work

D.5 NaSCN in BMIM_SCN and 15c5 ether in NaSCN+BMIM_SCN

The ^{1}H-NMR spectra of 0.3 M NaSCN in BMIM_SCN and 0.3 M 15-crown-5 ether in 0.3 M NaSCN in BMIM_SCN are presented in Fig. D.5. The detailed spectral analysis results are shown in Table D.5.

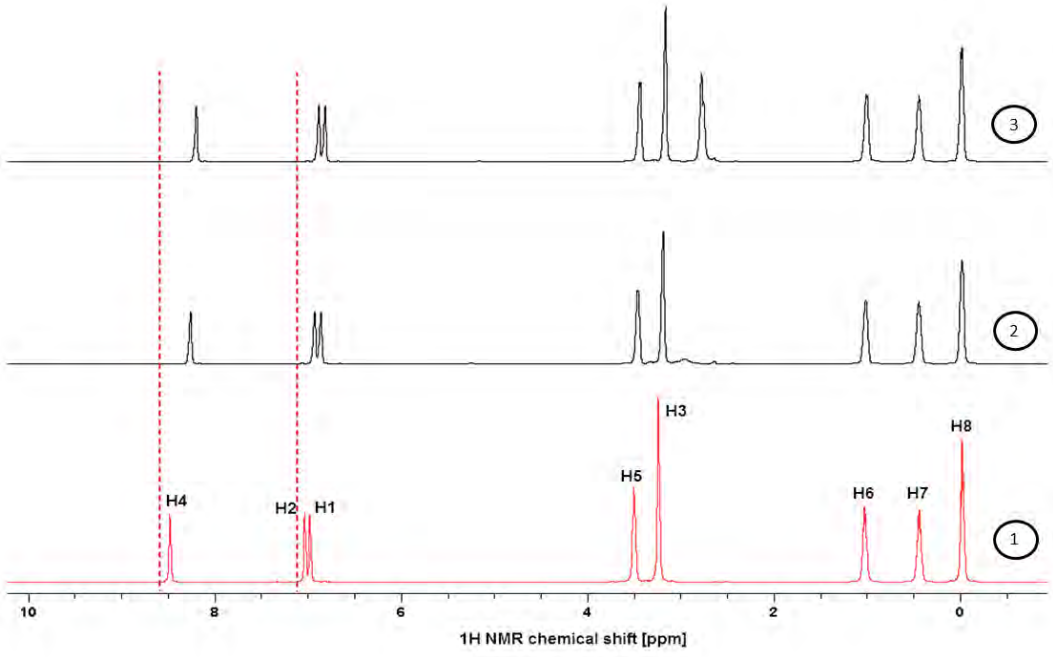

FIGURE D.5: ^{1}H NMR spectra of 1. BMIM_SCN, 2. 0.3 M NaSCN in BMIM_SCN and 3. 0.3 M NaSCN and 0.3 M 15-crown-5 in BMIM_SCN.

The addition of NaSCN in BMIM_SCN led to a small alteration of the chemical shift of the H4 proton of the methyl group and of the amide protons H1 and H2. This suggests that NaSCN is able to interact with both hydrophobic (CH3) and

charges groups. The further addition of the crown ether, made this phenomenon even stronger showing a higher shielding of the same protons. One can see a high intensity new chemical shift at ∼3 ppm when the crown ether is added that should come from the the protons of the C-CH_2-O groups.

TABLE D.5: 1H NMR chemical shifts in ppm of BMIM_SCN, NaSCN in BMIM_SCN and 15-crown-5 in BMIM_SCN solutions

Proton	H1	H2	H3	H4	H5	H6	H7	H8	
*BMIM_SCN at 11.7 T	7.07	7.14	3.37	8.49	3.64	1.19	0.61	0.16	
*NaSCN in BMIM_SCN at 11.7 T	7.04	7.10	3.36	8.43	3.64	1.19	0.62	0.16	3.14
*15c5 + NaSCN in BMIM_SCN at 11.7 T	7.00	7.06	3.34	8.38	3.61	1.19	0.62	0.16	2.95

*results of current work

D.6 MgCl2 in EMIM_Ac and $Mg(Ac)_2$*4H2O in EMIM_Ac

Fig. D.6 shows the 1H NMR spectra of EMIM_Ac, 0.3 M $MgCl_2$ anhydrous dissolved in EMIM_Ac and 0.3 M $Mg(Ac)_2$*$4H_2O$ dissolved in EMIM_Ac. The small chemical shift at ∼2.3 ppm in all spectra corresponds to the H of acetate (CH3COOH) [129] and the chemical shift at ∼4.7 ppm for the third spectrum containing H_2O corresponds to the H of water molecules [129].

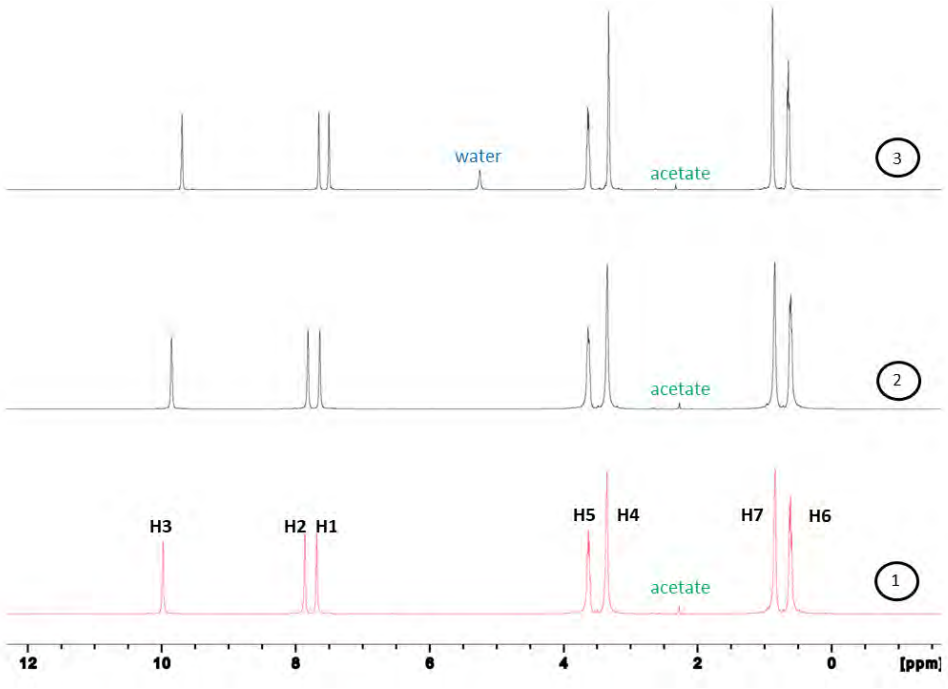

FIGURE D.6: ^1H NMR spectra of 1. EMIM_Ac, 2. 0.3 M $MgCl_2$ dissolved in EMIM_Ac and 3. 0.3 M $Mg(Ac)_2$*$4H_2O$ dissolved in EMIM_Ac.

Table D.1 shows the expected values of the H chemical shifts of EMIM_Ac, at RT, using a Bruker Avance 600 MHz (14 T) NMR spectrometer [21] and the experimental results of this work.

TABLE D.6: ^1H NMR chemical shifts of EMIM_Ac, 0.3 M $MgCl_2$ anhydrous in EMIM_Ac and 0.3 M $MgAc_2$*$4H_2O$ in EMIM_Ac

Proton	H1	H2	H3	H4	H5	H6	H7
EMIM_Ac at 14 T [21]	7.90	8.07	10.14	3.60	3.92/3.89	0.64	~1.09
					3.87/3.84	0.61	
						0.58	
*EMIM_Ac at 11.7 T	7.68	7.86	9.98	3.35	3.61/3.64	0.63	0.85
						0.61	
						0.59	
*$MgCl_2$ in EMIM_Ac at 11.7 T	7.64	7.81	9.85	3.35	3.61/3.64	0.62/0.60	0.85
*$Mg(Ac)_2$*$4H_2O$ EMIM_Ac at 11.7 T	7.50	7.65	9.69	3.33	3.61/3.64	0.66/0.63	0.88

*results of current work

Comparing the ^1H NMR spectra of the reference EMIM_Ac with the two EMIM_Ac samples containing Mg salts, the proton resonances H4, H5, H6 and H7 were just marginally shifted (less than 0.1 ppm). The most significant shifts occurred between the signals of H1, H2 and H3. The exact values of the chemical shifts can

be found in Table D.6. H3, see Fig. 7.2, appears to be the most sensitive site of EMIM_Ac. H3 is more acidic and more sensitive than H1 and H2 since it is bonded to a carbon located between two more electronegative N atoms [21].

H1, H2 and H3 signals were shifted upfield, more upfield for the $Mg(Ac)_2$ sample compared to the MgCl2 sample. In both samples, the H3 of EMIM interacted with the anion of the salts after the dissolution, forming ionic bonds leaving the Na^+ to form a bond with the Ac^- of the IL. Furthermore, the O from Ac^- shielded better the H3 of the $EMIM^+$ compared to Cl^- as it is more electronegative.

D.7 $MgCl_2$ in EMIM_Ac and $MgCl_2$ in BMIM_SCN

Fig. D.7 shows the ^1H NMR spectra of the EMIM_Ac, 0.3 M2 dissolved in EMIM_Ac, BMIM_SCN and 0.3 M $MgCl_2$ dissolved in BMIM_SCN. The ^1H NMR spectrum of BMIM_Ac was used as a "mediator" for the comparison of the spectra of EMIM_Ac and BMIM_SCN.

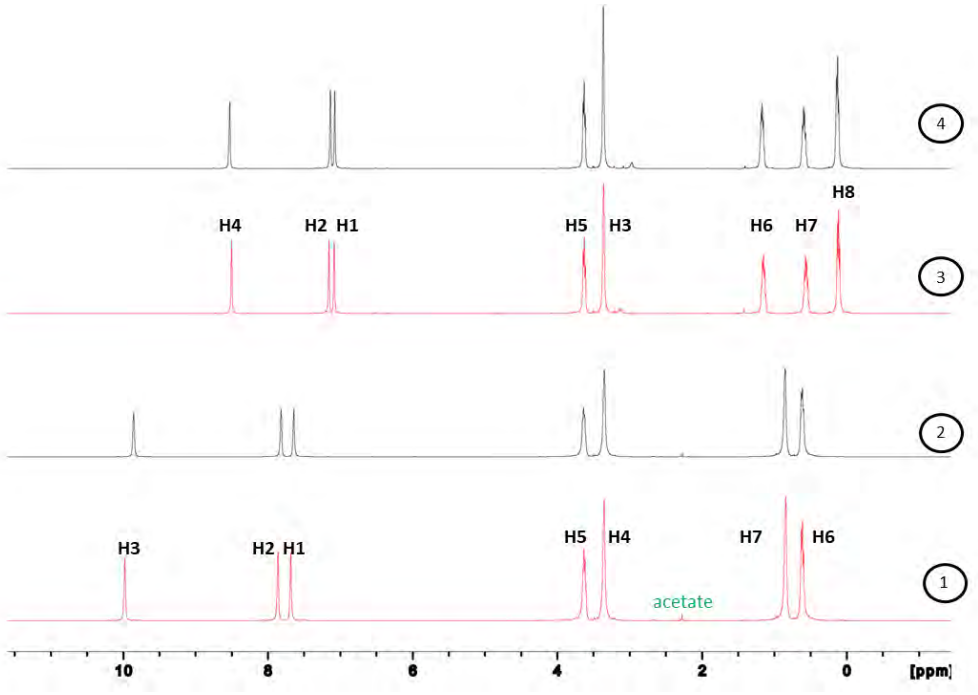

FIGURE D.7: ^1H NMR spectra 1. EMIM_Ac, 2. 0.3 M $MgCl_2$ in EMIM_Ac, 3. BMIM_SCN and 4. 0.3 M $MgCl_2$in BMIM_SCN.

The exact values from the ^1H NMR analysis are shown in Table D.7.

TABLE D.7: 1H NMR chemical shifts of EMIM_Ac and MgCl2 in EMIM_Ac

Proton	H1	H2	H3	H4	H5	H6	H7	H8
*EMIM_Ac	7.68	7.86	9.98	3.35	3.61/3.64	0.63	0.85	
						0.61		
						0.59		
*MgCl2 in EMIM_Ac	7.64	7.82	9.85	3.35	3.62/3.64	0.63	0.85	
						0.61		
						0.50		
*BMIM_SCN	7.06	7.13	3.36	8.48	3.63	1.18	0.60	0.14
*MgCl2 in BMIM_SCN	7.10	7.16	3.36	8.55	3.63	1.14	0.55	0.10

*results of current work at 11.7 T

The chemical shifts of the ring protons of EMIM_Ac (H3, H2 and H1) when $MgCl_2$ is dissolved are marginally moving upfield indicating that these protons interact with Cl^-. For MgCl2 dissolved in BMIM_SCN the main difference is observed at the H4 indicating that this proton interacts mainly with Cl. Comparing the ^{1}H NMR spectra of the plain ILs the H3 and H4 proton signals are reversed. For BMIM_SCN the H3 proton's chemical shift is shifted upfield from ∼10 ppm to ∼3.4 ppm compared to EMIM_Ac, while the H4 signal was shifted downfield from ∼3.3 ppm to ∼8.5 ppm compared to the equivalent proton in EMIM_Ac.

D.8 $MgCl_2$ in BMIM_SCN and Na2EDTA + $MgCl_2$ in BMIM_SCN

Fig D.8 shows the 1H NMR specrta of the plain BMIM_SCN, 0.3 M $MgCl_2$ dissolved in BMIM_SCN, 0.3 M NaEDTA dissolved in BMIM_SCN and 0.3 M $NaEDTA_d$issolved + 0.3 M $MgCl_2$ dissolved in BMIM_SCN. The results of the 1H NMR analysis are presented in Table D.8 and show no significant differences between the chemical shift positions.

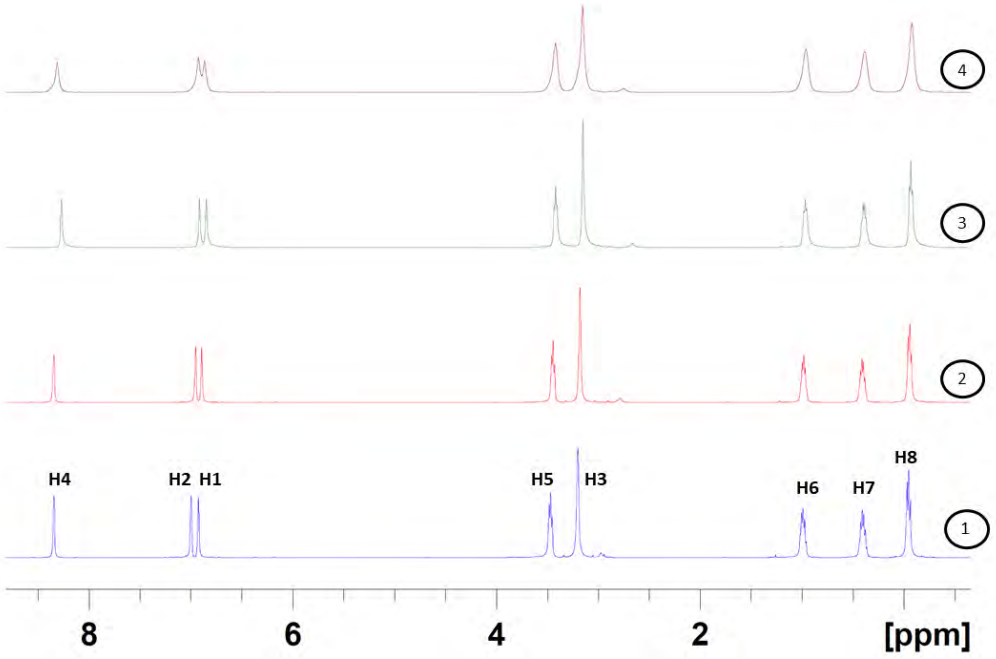

FIGURE D.8: ^1H NMR spectra of 1. BMIM_SCN, 2. $MgCl_2$ in BMIM_SCN, 3. NaEDTA in BMIM_SCN and 4. NaEDTA + $MgCl_2$ in BMIM_SCN.

TABLE D.8: 1H NMR chemical shifts of BMIM_SCN, 0.3 M $MgCl_2$ in BMIM_SCN, 0.3 M Na_2EDTA in BMIM_SCN and 0.3 M $MgCl_2$+ Na_2EDTA in BMIM_SCN

Proton	H1	H2	H3	H4	H5	H6	H7	H8
*BMIM_SCN	7.09	7.16	3.37	8.50	3.63	1.15	0.7	0.12
*MgCl2 in BMIM_SCN	7.08	7.14	3.37	8.53	3.63	1.17	0.60	0.13
*Na2EDTA in BMIM_SCN	7.06	7.13	3.36	8.48	3.63	1.18	0.61	0.15
*Na2EDTA + MgCl2 in BMIM_SCN	7.08	7.14	3.36	8.52	3.63	1.18	0.60	0.14

*results of current work at 11.7 T

D.8.1 $MgCl_2$ in BMIM_SCN and Calcein + $MgCl_2$ in BMIM_SCN

Fig D.9 shows the 1H NMR specrta of the plain BMIM_SCN, 0.3 M $MgCl_2$ dissolved in BMIM_SCN, 0.3 M Calcein dissolved in BMIM_SCN and 0.3 M Calcein + 0.3 M $MgCl_2$ dissolved in BMIM_SCN. The results of the 1H NMR analysis are presented in Table D.9 and show no significant differences between the chemical shift positions.

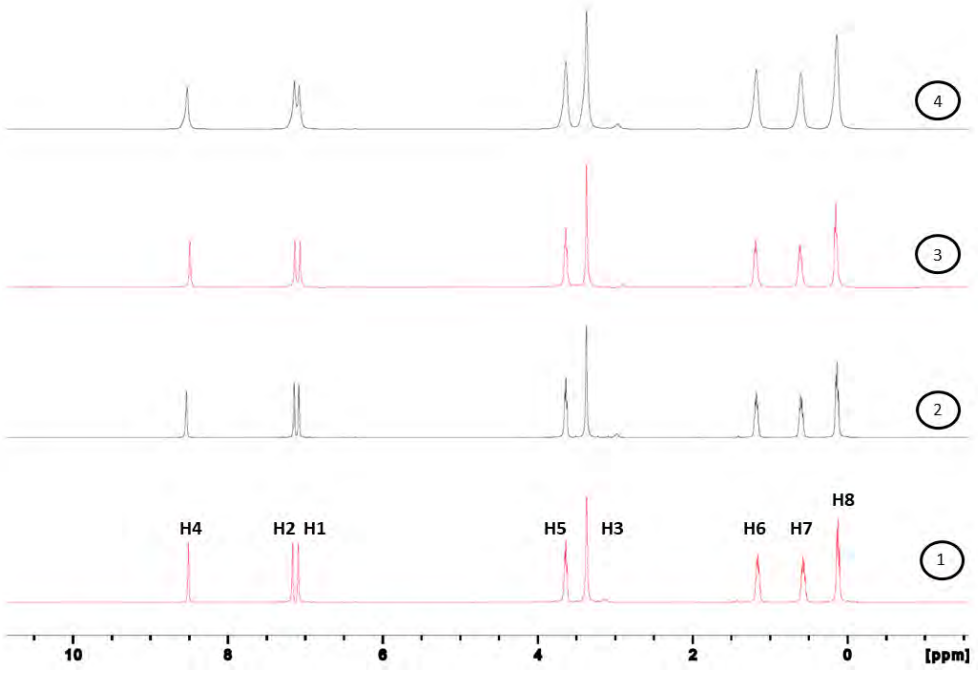

FIGURE D.9: ^{1}H NMR spectra of 1. BMIM_SCN, 2. $MgCl_2$ in BMIM_SCN, 3. Calcein in BMIM_SCN and 4. Calcein + $MgCl_2$ in BMIM_SCN.

TABLE D.9: 1H NMR chemical shifts of BMIM_SCN, 0.21 M $MgCl_2$ in BMIM_SCN, 0.21 M Calcein in BMIM_SCN and 0.21 M $MgCl_2$ + 0.3 M Calcein in BMIM_SCN

Proton	H1	H2	H3	H4	H5	H6	H7	H8
*BMIM_SCN	7.09	7.16	3.37	8.50	3.63	1.15	0.60	0.12
*$MgCl_2$ in BMIM_SCN	7.08	7.14	3.37	8.53	3.63	1.17	0.60	0.13
*Calcein in BMIM_SCN	7.06	7.13	3.37	8.49	3.63	1.18	0.60	0.15
*Calcein + $MgCl_2$ in BMIM_SCN	7.08	7.14	3.37	8.52	3.63	1.18	0.60	0.13

*results of current work at 11.7 T

Bibliography

[1] J. Anastassopoulou and T. Theophanides. *The Role of Metal Ions in Biological Systems and Medicine*. Springer, Dordrecht, 1995. ISBN 978-94-011-0255-1.

[2] L. Singh Thakur. Heavy metal cu, ni and zn: Toxicity, health hazards and their removal techniques by low cost adsorbents: A short overview. *International Journal of Plant, Animal and Environmental Sciences*, 3:143–157, 2013.

[3] K. N Sas L. Hemmingsen and E. Danielsen. Biological applications of perturbed angular correlations of γ-ray spectroscopy. *Chemical Reviews*, 104: 4027–4061, 2004. URL https://pubs.acs.org/doi/10.1021/cr030030v.

[4] A. Abragam and R. V. Pound. Influence of electric and magnetic fields on angular correlations. *Phys. Rev.*, 92:943–962, 1953. URL https://link.aps.org/doi/10.1103/PhysRev.92.943.

[5] M. Kowalska M. L. Bissell V. Arcisauskaite K. Blaum A. Helmke K. Johnston K. Kreim F. H. Larsen R. Neugart G. Neyens R. F. Garcia Ruiz D. Szunyogh P. W. Thulstrup D. Yordanov A. Gottberg, M Stachura and L. Hemmingsen. Billion-fold enhancement in sensitivity of nuclear magnetic resonance spectroscopy for magnesium ions in solution. *ChemPhysChem*, 15:3929–3932, 2014. URL http://dx.doi.org/10.1002/cphc.201402619.

[6] . URL http://isolde.web.cern.ch.

[7] U. Koster. Isolde target and ion source chemistry. *Radiochimica Acta*, 89:749–756, 2001. URL https://doi.org/10.1524/ract.2001.89.11-12.749.

[8] M. Breitenfeldt A. Dorsival G. J. Focker T. P. Gharsa T. J. Giles J-L Grenard F. Locci P. Martins S. Marzari J. Schipper A. Shornikov R. Catherall, W. Andreazza and T. Stora. The isolde facility. *Journal of Physics G: Nuclear and Particle Physics*, 2017.

[9] . URL http://isolde.web.cern.ch/isolde-logos-layouts-and-templates.

[10] S. Takács L. A. Hermanne, F. Tárkányi and Y. N. Shubin. Experimental determination of cross section of alpha-induced reactions on natpb. *Nuclear Instruments and Methods in Physics Research Section B: Beam Interactions with Materials and Atoms*, 229:321–332, 2005. URL http://dx.doi.org/10.1016/j.nimb.2004.12.126.

[11] URL http://tat.gu.se/collaborators/cyclotron-unit.

[12] URL https://cds.cern.ch/record/1953739/files/INTC-P-427.pdfv.

[13] K. Iwig M. Jäger and T. Butz. A user-friendly fully digital tdpac-spectrometer. *Hyperfine Interactions*, 198:167–172, 2015. URL https://doi.org/10.1007/s10751-010-0201-8.

[14] K. Iwig M. Jäger and T. Butz. A compact digital time differential perturbed angular correlation-spectrometer using field programmable gate arrays and various timestamp algorithms. *Review of Scientific Instruments*, 82:065105, 2011. URL https://doi.org/10.1063/1.3599417.

[15] J. G. Correia M. Stachura K. Johnston A. Gottberg A. Mokhles Gerami J. Röder H. Grawe B. A. Brown U. Köster T. M. Mendonça J. P. Ramos B. A. Marsh T. Day Goodacre V. S. Amaral L. M. C. Pereira M. J. G. Borge A. S. Fenta, S. Pallada and H. Haas. The 68mcu/68cu isotope as a new probe for hyperfine studies: The nuclear moments. *EPL*, 115:62002, 2016. URL https://doi.org/10.1209/0295-5075/115/62002.

[16] L. Hemmingsen A. G. Tebo and V. L. Pecoraro. Variable primary coordination environments of cd(ii) binding to three helix bundles provide a pathway for rapid metal exchange. *Metallomics*, 7:1555–1562, 2015. URL http://dx.doi.org/10.1039/C5MT00228A.

[17] U. Vetter J. G. Correia M. A. Nagl, M. B. Barbosa and H. C. Hofsäss. A new tool for the search of nuclides with properties suitable for nuclear

solid state physics based on the evaluated nuclear structure data files. *Nuclear Instruments and Methods in Physics Research Section A: Accelerators, Spectrometers, Detectors and Associated Equipment*, 726:17–30, 2013. URL https://doi.org/10.1016/j.nima.2013.05.045.

[18] T. L. James. *Fundamentals of NMR*. 1998. URL http://www.ias.ac.in/initiat/sci_ed/resources/chemistry/James.T.pdf.

[19] T. L. James. *Chapter 1: Fundamentals of NMR*. 1998.

[20] URL https://chem.libretexts.org/Textbook_Maps/Organic_Chemistry_Textbook_Maps/Map%3A_Organic_Chemistry_With_a_Biological_Emphasis_(Soderberg)/Chapter_05%3A_Structure_Determination_II/5.5%3A_Spin-spin_coupling.

[21] B. Kosan K. Schwikal S. Hesse-Ertelt, T. Heinze and F. Meister. Solvent effects on the nmr chemical shifts of imidazolium-based ionic liquids and cellulose therein. *Macromolecular Symposia*.

[22] F. Mutelet A. L. Revelli and J. N. Jaubert. Extraction of benzene or thiophene from n -heptane using ionic liquids. nmr and thermodynamic study. *J. Phys. Chem. B*, 114:4600–4608, 2010.

[23] M. Baranowski M. L. Bissell W. Gins R. D. Harding H. Heylen G. Neyens S. Pallada N. Severijns Ph. Velten M. Walczak F. Wienholtz Z. Y. Xu X. F. Yang M. Kowalska, P. Aschenbrenner and D. Zakoucky. New laser polarization line at the isolde facility. *Journal of Physics G: Nuclear and Particle Physics*, 44:084005, 2017. URL https://doi.org/10.1088/1361-6471/aa77d7.

[24] URL http://www.sigmaaldrich.com/content/dam/sigma-aldrich/docs/Aldrich/Brochure/al_chemfile_v6_n9.pdf.

[25] URL http://www.chemicalbook.com/ChemicalProductProperty.

[26] URL http://www.sigmaaldrich.com.

[27] URL https://pubchem.ncbi.nlm.nih.gov.

[28] A. Gottberg J. Schell M. Stachura D. Szunyogh S. Pallada D. C. Lupascu M. Kowalska A. Jancso, J. G. Correia and L. Hemmingsen. Tdpac and β-nmr applications in chemistry and biochemistry. *Journal of Physics G:Nuclear*

and Particle Physics, 44:064003, 2017. URL https://doi.org/10.1088/1361-6471/aa666b.

[29] L .E. Jørgensen E. Danielsen and P. Sestoft. Monte carlo simulations of pac-spectra as a general approach to dynamic interactions. *Hyperfine Interactions*, 141:607–626, 2002. URL https://doi.org/10.1023/A:1022494519185.

[30] J. Bothwell and J. Griffin. An introduction to biological nuclear magnetic resonance spectroscopy. *Biological Reviews of the Cambridge Philosophical Society*, 86:493–510, 2011. URL https://doi.org/10.1111/j.1469-185X.2010.00157.x.

[31] . URL https://www.webelements.com/.

[32] T. P. Hanusa. Solution nmr of the light main group metals. *Encyclopedia of Inorganic and Bioinorganic Chemistry*, pages 1–25, 2015. URL https://doi.org/10.1002/9781119951438.eibc2292.

[33] M. Baranowski L. Cerato M. Bissell W. Gins R. Grzywacz F. Gustafsson R. Harding L. Hemmingsen F. Hofmann H. Heylen A. Kanellakopoulos V. Kocman M. Kozak M. Madurga Flores G. Neyens S. Pallada J. Plavec N. Severijns D. Szunyogh K. Szutkowski P. Thulstrup M. Walczak F. Wienholtz J. Wolak X.F. Yang D. Zakoucky M. Kowalska, V. Araujo Escalona. Proposal to the isolde and neutron time-of-flight committee interaction of na ions with dna g-quadruplex structures studied directly with na β-nmr spectroscopy. pages 1–9, 2017. URL https://cds.cern.ch/record/2266838/files/INTC-P-521.pdf.

[34] M.Baranowski M.L.Bissell R.F.Garcia Ruiz M.Kowalska G.Neyens S.Pallada N.Severijns Ph.Velten F.Wienholtz Z.Y.Xu X.F.Yang D.Zakouckyg W.Gins, R.D.Harding. A new beamline for laser spin-polarization at isolde. *Nuclear Instruments and Methods in Physics Research Section A: Accelerators, Spectrometers, Detectors and Associated Equipment*, 925:24–32, 2019. URL https://doi.org/10.1016/j.nima.2019.01.082.

[35] V. Gabelica E. Largy, J.-L. Mergny. The role of alkali metal ions in g-quadruplex nucleic acid structure and stability. *Met. Ions Life Sci.*, 16:203–258, 2016. URL http://dx.doi.org/10.1007/978-3-319-21756-7_7).

[36] J. D. Roberts. Nuclear magnetic resonance spectroscopy. *J. Chem. Educ*, 38:581, 1961. URL https://doi.org/10.1021/ed038p581.

[37] J. Seliger. Mössbauer spectroscopy. *Nuclear Quadrupole Resonance, Theory*, pages 1672–1680, 1999. URL https://doi.org/10.1006/rwsp.2000.0211.

[38] T. E. Cranshaw. Mössbauer spectroscopy. *Journal of Physics E: Scientific Instruments*, 7:497, 1974. URL http://dx.doi.org/10.1016/0029-554X(70)90294-6.

[39] D. W. Cooke. A review of muon spin rotation with selected applications in solid state physics and chemistry. *AIP Conference Proceedings*, 69:1057, 1981. URL https://doi.org/10.1063/1.32881.

[40] P. W. Thulstrup N. J. Christensen K. Johnston L. Hemmingsen, M. Stachura. Selected applications of perturbed angular correlation of γ rays (pac) spectroscopy in biochemistry. *Hyperfine Interactions*, 197:255–267, 2010. URL https://doi.org/10.1007/s10751-010-0248-6.

[41] J. T. Pedersen A. Jancso J. G. Correia S. Chakraborty, S. Pallada and L. Hemminsgen. Nanosecond dynamics at protein metal sites: An application of perturbed angular correlation (pac) of γ-rays spectroscopy. *Acc. Chem. Res.*, 50:2225–2232, 2017. URL https://doi.org/10.1021/acs.accounts.7b00219.

[42] J. D. Baldeschwieler T. Leipert and D. A. Shirley. Applications of gamma ray angular correlations to the study of biological macromolecules in solution. *Nature*, 220:907–909, 1968. URL http://dx.doi.org/10.1038/220907a0.

[43] M. Deicher H. P. Gunnlaugsson A. S. Fenta E. David-Bosne A. R. G. Costa K. Johnston, J.Schell. J. G. Correia and D. C. Lupascu. The solid state physics programme at isolde: recent developments and perspectives. *Journal of Physics G: Nuclear and Particle Physics*, 44:10400, 2017. URL http://dx.doi.org/10.1088/1361-6471/aa81ac.

[44] S. R. De Groot. On the theories of angular distribution and correlation of beta and gamma radiation. *Physica*, 18:1201–1214, 1952. URL https://doi.org/10.1016/S0031-8914(52)80196-X.

[45] H. Frauenfelder and R. M. Steffen. Alpha-beta- and gamma-ray spectroscopy. *Angular Correlations*, page 997, 1965.

[46] HH Rinneberg. Application of perturbed angular correlations to chemistry and related areas of solid state physics. *At. Energy Rev.; (International Atomic Energy Agency (IAEA)*, 17:2, 1979.

[47] S. Zheng J.Autschbach and R. W. Schurko. Analysis of electric field gradient tensors at quadrupolar nuclei in common structural motifs. *Concepts in Magnetic Resonance Part A*, 36A:84–126, 2010. URL https://doi.org/10.1002/cmr.a.20155.

[48] A. W. Carbonari R. Domingues Mansano T. T. Dang J. Schell, D. C. Lupascu and R. Vianden. Implantation of cobalt in sno2 thin films studied by tdpac. *AIP Advances*, 7:055304, 2017. URL https://doi.org/10.1063/1.4983270.

[49] E. Danielsen and R. Bauer. Analysis of perturbed angular correlation spectra of metal ions bound to proteins with rotational correlation times in the intermediate region. *Hyperfine Interactions*, 62:311–324, 1991. URL https://doi.org/10.1007/BF023977.

[50] K. Johnston M. L. Bissell R. F. Garcia Ruiz J. Martins Correia-A. R. Granadeiro Costa M. Dehn M. Deicher A. Fenta L. Hemmingsen T. E. Molholt M. Munch G. Neyens S. Pallada M. R. Silva D. Zakoucky M. Stachure, A. Gottberg. Versatile ion-polarized techniques on-line (vito) experiment at isolde-cern. *Nuclear Instruments and Methonds in Physics Research Section B: Beam Interactions with Materials and Atoms*, 376:369–373, 2016. URL https://doi.org/10.1016/j.nimb.2016.02.030.

[51] A. Gottberg M. Stachura L. Hemminsgen G. Neyens N. Severijns R. F. Garcia Ruiz, M. L. Bissell and the VITO Collaboration. Perspectives for the vito beam line at isolde, cern. *EPJ Web of Conference*, 93:07004, 2015. doi: https://doi.org/10.1051/epjconf/20159307004.

[52] H. W de Wijn and J. L. de Wildt. Temperature dependence of nuclear quadrupole resonance in cuprous oxide. *Physical Review*, 150:200–201, 1966. URL https://link.aps.org/doi/10.1103/PhysRev.150.200.

[53] M. Avgoulea J. Billowes M. L. Bissell K. Blaum B.A. Brown B. Cheal M. De Rydt D. H. Forest Ch. Geppert M. Honma M. Kowalska J. Kramer A. Krieger E. Mane R. Neugart G. Neyens W. Nortershauser T. Otsuka M. Schug H. H. Stroke G. Tungate andD. T. Yordanov P. Vingerhoets, K.

T. Flanagan. Nuclear spins, magnetic moments and quadrupole moments of cu isotopes from n = 28 to n = 46: probes for core polarization effects. *Physical Review C*, 82:064311, 2010. URL https://link.aps.org/doi/10.1103/PhysRevC.82.064311.

[54] Y. Koi T. Kushida, A. H. Silver and A. Tsujimura. Nuclear resonance in ferromagnetic alloys. *Proceedings of the Seventh Conference on Magnetism and Magnetic Materials*, 33:1079–1083, 1966. URL https://doi.org/10.1007/978-1-4899-6391-8_21.

[55] P. Kroneck O. LutzH. H. Oehler. 63cu and65cu fourier transform nuclear magnetic resonance studies. *Zeitschrift für Physik A Atoms and Nuclei*, 288, 1978.

[56] D. P. Giedroc and A. I. Arunkumr. Metal sensor proteins:nature's metaloregulated allosteric switches. *Dalton Transactions*, 29:3107–3120, 2007. URL http://dx.doi.org/10.1039/B706769K.

[57] R. A. Scott B. P. Rosen M. D. Wong D. P. Giedroc L. S. Busenlehner, N. J. Cosper. Spectroscopic properties of the metalloregulatory cd(ii) and pb(ii) sites of s. aureus pi258 cadc. *Biochemistry*, 40:4426–4436, 2001. URL https://www.ncbi.nlm.nih.gov/pubmed/11284699.

[58] K. C. Kondapalli T. L. Stemmler B. P. Rosen A. Kandegedara, S. Thiyagarajan. Role of bound zn(ii) in the cadc cd(ii)/pb(ii)/zn(ii)-responsive repressor. *J. Biol. Chem.*, 284:14958–14965, 2009. URL http://www.jbc.org/content/284/22/14958.full.pdf.

[59] M. J. Bjerrum M. Zeppezauer H. W. Adolph G. Formicka E. Cedergren-Zeppezauer L. Hemmingsen, R. R. Bauer. Cd-substituted horse liver alcohol dehydrogenase: catalytic site etal coordination geometry and protein conformation. *Biochemistry*, 34:7145–7153, 1995. URL https://doi.org/10.1021/bi00021a028.

[60] M. K. Stachura. *PhD dissertation: Nuclear Techniques Using Radioactive Beams for Biophysical Studies*. 2012.

[61] M. E. Hayden and P. J. Nacher. *History and physical principles of MRI*, volume 1. CRC press, 2016. URL https://hal.archives-ouvertes.fr/hal-01191404.

[62] P. C. Lauterbur. Image formation by induced local interactions: Examples employing nuclear magnetic resonance. *Nature*, 242:190–191, 1973. URL https://doi.org/10.1038/242190a0.

[63] D. Mallin A. Vesci and C. Fiedler. Finding spin lattice and spin spin relaxation times using pulsed nmr. pages 1–4, 2011. URL https://pdfs.semanticscholar.org/95bc/0653725c415c112fafdede2437dd1b40dd72.pdf.

[64] R. Freeman and H. D. W. Hill. Fourier transform study of nmr spin–lattice relaxation by "progressive saturation". *The Journal of Chemical Physics*, 54 (3-4):3367–3377, 1971. URL https://doi.org/10.1063/1.1675352.

[65] Koch. Spin-lattice and spin-spin relaxation spin-lattice relaxation mechanisms. pages 1–10, 2015.

[66] I. Discussion X. Relaxation. Varian nmr user's guide. *Interactions*, 1:57–59, 2001.

[67] M. P. Klein R. L. Vold, J. S. Waugh and D. E. Phelps. Measurement of spin relaxation in complex systems. *The Journal of Chemical Physics*, 48:3832, 1968. URL http://dx.doi.org/10.1063/1.1669699.

[68] . URL http://chem.ch.huji.ac.il/nmr/techniques/1d/row2/c.html.

[69] N. H. Meyer and K. Zangger*. Simplifying proton nmr spectra by instant homonuclear broadband decoupling**. *Angew Chem Int Ed Engl*, 52:7143–7146, 2013. URL https://doi.org/10.1002/anie.201300129.

[70] URL http://magneticmoments.info/NUMOR/.

[71] Y. Okuno J. H. Lee and S. Cavagnero. Sensitivity enhancement in solution nmr: Emerging ideas and new frontiers. *Journal of magnetic resonance*, 241:18–31, 2014. URL http://www.ncbi.nlm.nih.gov/pmc/articles/PMC3967054/.

[72] R. Tycko. Nmr at low and ultralow temperatures. *Accounts of chemical research*, 46:1923—-1932, 2013. doi: https://doi.org/10.1021/ar300358z.

[73] C. A. Scott D. A. Crag F. Row D. J. White P. Styles, N. F. Soffe and P. C. J. White. A high-resolution nmr probe in which the coil and preamplifier are

cooled with liquid helium. *Journal of Magnetic Resonance*, 60:397–404, 1984. URL https://doi.org/10.1016/0022-2364(84)90050-7.

[74] J. M. McDonnell M. J. Goger and D. Cowburn. Using cryoprobes to decrease acquisition times of triple-resonance experiments used for protein resonance assignments. *Spectroscopy*, 17:161–167, 2003. URL http://dx.doi.org/10.1155/2003/462471.

[75] J. L. Griffin C. Richter D. Moskau J. C. Lindon H. C. Eun, O. Beckonert and J. K. Nicholson. Cryogenic probe 13c nmr spectroscopy of urine for metabonomic studies. *Analytical chemistry*, 74:4588–4593, 2002. URL http://dx.doi.org/10.1155/2003/462471.

[76] D. S. Dalisay and T. F. Molinski. Nmr quantitation of natural products at the nanomole scale. *Journal of natural products*, 72:739–744, 2009. URL https://doi.org/10.1021/np900009b.

[77] G. Goff D. Sakellariou and J. F. Jacquinot. High-resolution, high-sensitivity nmr of nanolitre anisotropic samples by coil spinning. *Nature*, 447:694–697, 2007. URL http://dx.doi.org/10.1038/nature05897.

[78] T. R. Carver and C. P. Slichter. Polarization of nuclear spins in metals. *Physical Review*, 92:212–213, 1953. URL https://doi.org/10.1103/PhysRev.92.212.2.

[79] H. Y. Carr and E. M. Purcell. Effects of diffusion on free precession in nuclear magnetic resonance experiments. *Physical Review*, 94:630–638, 1954. URL http://link.aps.org/doi/10.1103/PhysRev.94.630.

[80] N. Karschin G. Parigi C. Luchinat M. Bennati G. Liu, M. Levien. One-thousand-fold enhancement of high field liquid nuclear magnetic resonance signals at room temperature. *Nature Chemistry*, 2017.

[81] A. Gram G. Hansson L. Hansson M. H. Lerche R. Servin M. Thaning J.H. Ardenkjær-Larsen, B. Fridlund and Klaes Golmans. Increase in signal-to-noise ratio of $>$ 10,000 times in liquid-state nmr. *Proceedings of the National Academy of Sciences*, 100:10158–10163, 2003. URL https://doi.org/10.1073/pnas.1733835100.

[82] M. L. Pitt J. Clayhold W. Happer M. Kadar-Kallen M. Musolf G. Ulm K. Wendt T. Chupp J. Bonn R. Neugart E. Otten M. Kitano, F. P. Calaprice

and H. T. Duong. Nuclear orientation of radon isotopes by spin-exchange optical pumping. *Physical Review Letters*, 60:2133–2136, 1988. URL https://link.aps.org/doi/10.1103/PhysRevLett.60.2133.

[83] W. A. Tobias Y. Zheng, G. W. Miller and G. D. Cates. A method for imaging and spectroscopy using γ-rays and magnetic resonance. *Nature*, 537:652–655, 2016. URL http://dx.doi.org/10.1038/nature19775.

[84] A. Kastler. Quelques suggestions concernant la production optique et la détection optique d'une inégalité de population des niveaux de quantifigation spatiale des atomes. application à l'expérience de stern et gerlach et à la résonance magnétique. *J. Phys. Radium*, 11:255–265, 1950. URL https://doi.org/10.1051/jphysrad:01950001106025500.

[85] J. Shimaya K. Matsuta M. Fukuda J. Ohno M. Tanaka-S. Yamaoka K. Watanabe S. Iwakiri R. Yanagihara Y. Tanaka H. Du K. Onishi S. Kambayashi T. Minamisono D. Nishimura T. Izumikawa A. Ozawa Y. Ishibashi A. Kitagawa S. Sato M. Torikoshi T. Sugihara, M. Mihara and S. Momota. Nmr detection of short-lived β-emitter 12n implanted in water. *Hyperfine Interactions*, 238:20, 2017. URL http://dx.doi.org/10.1007/s10751-017-1401-2.

[86] V. L. Karner A. Chatzichristos T. Day Goodacre-M. H. Dehn L. Formenti D. Fujimoto A. Gottberg E. Kallenberg I. Kálomista R. F. Kiefl F. H. Larsen J. Lassen C. D. Philip Levy R. Li W. Andrew MacFarlane I. McKenzie G. D. Morris S. Pallada M. R. Pearson S. P. A. Sauer P. Schaffer P. W. Thulstrup L. Hemmingsen D. Szunyogh, R. M. L. McFadden and M. Stachura. Direct observation of mg2+ complexes in ionic liquid solutions by 31mg beta nmr spectroscopy. *Dalton Transactions*, 47:14431–14435, 2018. URL http://dx.doi.org/10.1039/C8DT02350F.

[87] R. J. Blin-Stoyle. Polarized nuclear reactions. *Proceedings of the Physical Society. Section A*, 64:700–711, 1951. URL http://stacks.iop.org/0370-1298/64/i=8/a=305.

[88] A. Lindner. Nuclear reactions with polarized particles of arbitrary spin. *Nuclear Physics A*, 155:145–160, 1970. URL https://doi.org/10.1016/0375-9474(70)90083-7.

[89] J. W. T. Dabbs L. D. Roberts, S. Bernstein and C. P. Stanford. Capture of polarized neutrons by polarized 149sm nuclei. *Physical review*, 95:105–110, 1954. URL http://journals.aps.org/pr/pdf/10.1103/PhysRev.95.105.

[90] N. J. Stone. Low temperature nuclear orientation and its application to magnetic systems. *Hyperfine Interactions*, 49:103–128, 1989. URL http://dx.doi.org/10.1007/BF02405138.

[91] N. J. Stone J. R. Stone C. Gaulard U. Köster-J. Nikolov G. S. Simpson T. Ohtsubo, S. Roccia and M. Veskovic. The on-line low temperature nuclear orientation facility. *Journal of Physics G: Nuclear and Particle Physics*, 44:1–13, 2017. URL http://dx.doi.org/10.1088/1361-6471/aa5f22.

[92] S. B. Dutta A. G. Martin W. F. Rogers, D. L. Clark. Beta-nmr magnetic moment measurement using on-line mass separation and tilted foil polarization. *Nuclear Instruments and Methods in Physics Research Section A: Accelerators, Spectrometers, Detectors and Associated Equipment*, 253:256–263, 1987. URL https://doi.org/10.1016/0168-9002(87)90712-1.

[93] Y. Nojiri. Tilted foil technique applied to beta-nmr studies. *Hyperfine Interactions*, 100:23–36, 1996. URL http://dx.doi.org/10.1007/BF02059928.

[94] R. W. Hayward D. D. Hoppes D. D. C. S. Wu, E. Ambler and R. P. Hudson. Experimental test of parity conservation in beta decay. *Physical Review*, 105:1413–1415, 1957. URL https://link.aps.org/doi/10.1103/PhysRev.105.1413.

[95] O. Rodríguez A. P. M.Tavares and E. A. Macedo. *New Generations of Ionic Liquids Applied to Enzymatic Biocatalysis*. 2013. URL http://dx.doi.org/10.5772/51897.

[96] D.Bankmann and R. Giernoth. Magnetic resonance spectroscopy in ionic liquids. *Progress in Nuclear Magnetic Resonance Spectroscopy*, 51:63–90, 2007. URL https://doi.org/10.1016/j.pnmrs.2007.02.007.

[97] F. V. Rantwijk and A. Sheldon. Biocatalysis in ionic liquids. *Chemical Reviews*, 107:2757–2785, 2007. URL http://dx.doi.org/10.1021/cr050946x.

[98] K. Blaum D. Borremans P. Himpe M. Kowalska P. Lievens S. Mallion G. Neyens N. Vermeulen R. Neugart, D. L. Balabanski and D. T. Yordanov. Precision measurement of ^{11}Li moments: Influence of halo neutrons on the ^{9}Li core. *Phys. Rev. Lett.*, 101:132502, 2008. URL https://doi.org/10.1103/PhysRevLett.101.132502.

[99] J. Billowes F. Buchinger K. H. Chow J. E. Crawford M. D. Hossein R. .F Kiefl C. D. P. Levy W. A. MacFarlane E. Mané G. D. Morris T. J. Parolin H. Saadaoui Z. Salman M. Smadella Q. Song A. Voss, M. R. Pearson and D. Wang. Nuclear electric quadrupole moment of 9 li using zero-field β-detected nqr. *Journal of Physics G: Nuclear and Particle Physics*, 38:075102, 2011. URL http://dx.doi.org/10.1088/0954-3899/38/7/075102.

[100] K. Blaum W. Geithner S. Gheysen P. Himpe M. Kowalska J. Lassen P. Lievens S. Mallion R. Neugart G. Neyens N. Vermeulen D. Borremans, D. L. Balabanski and D. Yordanov. New measurement and reevaluation of the nuclear magnetic andquadrupole moments of ^{8}Li and ^{9}Li. *Phys. Rev. C*, 72: 044309, 2005. URL https://link.aps.org/doi/10.1103/PhysRevC.72.044309.

[101] URL https://oraweb.cern.ch/pls/isolde/query_tgt.

[102] A. Klein R. Neugart M. Neuroth S. Wilbert P. Lievens L. Vermeeren B. A. Brown BA M. Keim, U. Georg and Isolde Collaboration. Measurement of the electric quadrupole moments of 26–29na. *The European Physical Journal A*, 8(1):31–40, 2000. URL https://doi.org/10.1007/s100500070117.

[103] A. Klein R. Neugart M. Neuroth S. Wilbert P. Lievens L. Vermeeren M. Keim, U. Georg and The ISOLDE Collaboration. Optical polarization of neutron-rich sodium isotopes and β-nmr measurements of quadrupole moments. *Hyperfine Interactions*, 97(1):543–550, 1996. URL http://dx.doi.org/10.1007/BF02150197.

[104] M. Kowalska. Phd. thesis: Ground state properties of neutron-rich mg. 2006.

[105] K. Blaum P. Himpe P. Lievens S. Mallion R. Neugart G. Neyens M. Kowalska, D. T. Yordanov and N. Vermeulen. Nuclear ground-state spins and magnetic moments of ^{27}Mg, ^{29}Mg, and ^{31}Mg. *Physical Review C*, 77:034307, 2008. URL https://link.aps.org/doi/10.1103/PhysRevC.77.034307.

[106] E. W. Otten H. J. Besch, U. Köpf and C. V. Platen. Nuclear magnetic moment of 37k. *Physics Letters B*, 26:721–722, 1968. URL https://doi.org/10.1016/0370-2693(68)90402-4.

[107] J. A. Behr, A. Gorelov, T. Swanson, O. Häusser, K. P. Jackson, M. Trinczek, U. Giesen, J. M. D'Auria, R. Hardy, T. Wilson, P. Choboter, F. Leblond, L. Buchmann, M. Dombsky, C. D. P. Levy, G. Roy, B. A. Brown, and J. Dilling. Magneto-optic trapping of β-decaying $^{38}K^m$, ^{37}k from an on-line isotope separator. *Phys. Rev. Lett.*, 79:375–378, 1997. URL https://link.aps.org/doi/10.1103/PhysRevLett.79.375.

[108] K. Minamisono J. Pereira J. Pinter R. Weerasiri, P. Mantica and J. Stoker. Implementation of a beta nqr system at the nscl for ground state quadrupole moment measurements. 2007.

[109] J. Papuga, M. L. Bissell, K. Kreim, K. Blaum, B. A. Brown, M. De Rydt, R. F. Garcia Ruiz, H. Heylen, M. Kowalska, R. Neugart, G. Neyens, W. Nörtershäuser, T. Otsuka, M. M. Rajabali, R. Sánchez, Y. Utsuno, and D. T. Yordanov. Spins and magnetic moments of ^{49}**K** and ^{51}**K**: Establishing the $1/2^+$ and $3/2^+$ level ordering beyond n=28. *Phys. Rev. Lett.*, 110: 172503, 2013. URL https://link.aps.org/doi/10.1103/PhysRevLett.110.172503.

[110] M. Fukuda T. Minamisono H. Akai M. Sasaki T. Yamaguchi T. Miyake K. Sato K. Minamisono F. Ohsumi Y. Muramoto S. Oui C. Ha K. Tanaka K. Kidera A. Morishita A. Kitagawa M. Torikoshi M. Kanazawa T. Nishio S. Koda T. Ohtsubo S. Fukuda Y. Nojiri S. Momota A. Ozawa K. Yoshida T. Suzuki T. Kobayashi I. Tanihata S. S. Hanna J. R. Alonso G. F. Krebs T. J. M. Symons K. Matsuta, T. Onishi. Electromagnetic moments of short lived β emitters 21f, 23mg, 27si and 39ca. *Hyperfine Interactions*, 120:673–677, 1999. URL http://dx.doi.org/10.1023/A:1017036009679.

[111] D. G. Mavis T.K. Saylor H. F. Glavish S. S. Hanna T. Minamisono, J. W. Hugg. Measurement of the magnetic moment of 39ca by use of a polarized proton beam and nmr detection. *Physics Letters B*, 61:155–157, 1976. URL https://doi.org/10.1023/A:10170360.

[112] J. Billowes M. L. Bissell K. Blaum B. Cheal M. De Rydt D.H. Forest Ch. Geppert M. Honma M. Kowalska J. Krämer K. Kreim A. Krieger R. Neugart

G. Neyens W. Nörtershäuser J. Papuga T. J. Procter M. M. Rajabali R. Sánchez H. H. Stroke P. Vingerhoets, K. T. Flanagan and D. T. Yordanov. Magnetic and quadrupole moments of neutron deficient 58–62cu isotopes. *Physics Letters B*, 703:34–39, 2011. URL https://doi.org/10.1016/j.physletb.2011.07.050.

[113] H. Ueno K. Matsuta D. Nishimura T. Nagatomo T. Moriguchi Y. Ito D. Nagae M. Fukuda A. Yoshimi K. Yamada M. Takechi Y. Ichikawa S. Momota Y. Hirayama T. Ohtsubo S. Suzuki T. Kubo Y. Namiki A. Ozawa Y. Ishibashi H. Oishi K. Suzuki I. HachiumaK. Namihira D. Horikawa T. Minamisono T. Yamaguchi T. Kuboki T. Suzuki K. Satohm Y. Kobayashi K. Asahi K. Matsukawa M. Mihara, T. Izumikawa and K. Shirai. Beta-nmr measurement of 58cu in si. *Hyperfine Interactions*, 197:143–147, 2010. URL http://dx.doi.org/10.1007/s10751-010-0249-5.

[114] O. Masahiro I. Masahiro, N. Hiroyoshi and A. Sugimura. Method for determination of rotational viscosity in nematic liquid crystals. *Japanese Journal of Applied Physics*, 33:L119, 1994. URL http://dx.doi.org/10.1143/JJAP.33.L119.

[115] 0. Lutz A. Nolle G. E. Siegloch W. Gauß, J. Kronenbitter. Quadrupole splittings of alkali nmr signals in decylammoniumchloride mesophases. *Physical Sciences*, 9:5–9, 1978. URL https://doi.org/10.1515/zna-1978-0201.

[116] Z. Yan Y. Huang W. Gang, I. C. M. Kwan and E. Ye. On the helical structure of guanosine 5'-monophosphate formed at ph 5: Is it left- or right-handed? *Journal of Nucleic Acids*, 2017:1–7, 2017. URL https://doi.org/10.1155/2017/6798759.

[117] J. A. Tossell. Na+ complexes with crown ethers: Calculation of 23na nmr shieldings and quadrupole coupling constants. *J. Phys. Chem. B*, 105:11060–11066, 2001. URL https://doi.org/10.1021/jp0115143.

[118] K. M. Larsson B. Eliasson and J. Kowalewski. Multinuclear nmr relaxation studies of crown ethers and alkali cation crown ether complexes. *J. Phys. Chem.*, 89:258–261, 1985. URL https://doi.org/10.1021/j100248a016.

[119] M. Hannu-Kuure M Lajunen A. Vendilo P. Oksman L. H. J. Lajunen K. Popov, H. Rönkkömäki. Stability of crown-ether complexes with alkali-metal ions in ionic liquid-water mixed solvents. *Journal of Inclusion Phenomena and Macrocyclic Chemistry*, 59:377–381, 2007. URL https://doi.org/10.1007/s10847-007-9340-1.

[120] W. M. Leevy G. W. Gokel and M. E. Weber. Crown ethers: Sensors for ions and molecular scaffolds for materials and biological models. *Chem. Rev.*, 104:2723–2750, 2004. URL https://doi.org/10.1021/cr020080k.

[121] D. Ray M. B. More and P. B. Armentrout. Intrinsic affinities of alkali cations for 15-crown-5 and 18-crown-6: Bond dissociation energies of gas-phase m+ - crown ether complexes. *J. Am. Chem. Soc.*, 121:417–423, 1999. URL https://doi.org/10.1021/ja9823159.

[122] M. Gielen-J. C. Martins V. Gramlich M. Kemmer, M. Biesemans and R. Willem. Complexation of triorganotin derivatives of [18]crown-6- and [15]crown-5-(benzo-4-carboxylate) with alkali thiocyanates. *Chemistry*, 7: 4686–4695, 2001. URL https://doi.org/10.1002/1521-3765(20011105)7:21<4686::AID-CHEM4686>3.0.CO;2-7.

[123] S. FLora and V. Pachari. Chelation in metal intoxication. *International Journal of Environmental Research and Public Health*, 7:2745–2788, 2010. URL https://doi.org/10.3390/ijerph7072745.

[124] W. Qingqei L . Huai and L. Lixin. An improvement of the formula for group electronegativity. *Journal of chemical education*, 69:783, 1992. URL https://doi.org/10.1021/ed069p783.

[125] C. W. Ritchie M. Sastre and N. Hajji. Metal ions in alzheimer's disease brain. *JSM Alzheimer's Disease and Related Dementia*, 2: 1014, 2015. URL https://spiral.imperial.ac.uk/bitstream/10044/1/23400/2/alzheimersdisease-2-1014-1.pdf.

[126] URL http://www.ilco-chemie.de/downloads/Ionic%20Liquid.pdf.

[127] T. E. Skrebets K. G. Bogolitsyn and T. A. Makhova. Physicochemical properties of 1-butyl-3-methylimidazolium acetate. *Russian Journal of General Chemistry*, 79:125–128, 2009. URL https://doi.org/10.1134/S1070363209010198.

[128] E. Kenndler. Organic solvents in ce. *Electrophoresis*, 30:101–111, 2009. URL https://doi.org/10.1002/elps.200900180.

[129] V. Kotlyar H. E. Gottlieb and A. Nudelman. Nmr chemical shifts of common laboratory solvents as trace impurities. *Organometallics*, 62:7512–7515, 1997. URL https://doi.org/10.1021/jo971176v.

[130] G. T. Whiteker* B. Canturk N. Choy L. C. Creemer C. V. De Amicis N. M. Hewlett P. L. Johnson J. A. Knobelsdorf F. Li B. A. Lorsbach B. M. Nugent S. J. Ryan M. R. Smith N. R. Babij, E. O. McCusker and Q. Yang. Nmr chemical shifts of trace impurities: Industrially preferred solvents used in process and green chemistry. *Org. Process Res. Dev.*, 20:661–667, 2016. URL https://doi.org/10.1021/acs.oprd.5b00417.

[131] Y. Muhammad M. AL-Jalali and Y. Mahzia. Effect of electronegative elements on the nmr chemical shift in somesimple r-x organic compounds. *IOSR Journal of Applied Physics*, 6:45–56, 2014. URL http://www.iosrjournals.org/iosr-jap/papers/Vol6-issue4/Version-3/G06434556.pdf.

[132] J. Roy. Phd thesis: synthese chimique et activité biologique d'agents stéroïdiens pour le traitement du cancer de la prostate et résumé. 2006.